Prospects for
Diffractive
and Forward Physics
at the LHC

The CMS and TOTEM
diffractive and forward physics
working group

Acknowledgments

Author List

M. Albrow[**1], G. Antchev[**3], M. Arneodo[**2], V. Avati[**3, **4], P. Bartalini[**5], V. Berardi[**6], U. Bottigli[**24], M. Bozzo[**7], E. Brücken[**8], V. Burtovoy[**9], A. Buzzo[**7], M. Calicchio[**6], F. Capurro[**7], M.G. Catanesi[**6], P. Catastini[**24], M.A. Ciocci[**24], R. Croft[**10], K. Datsko[**9], M. Deile[**3], J. De Favereau De Jeneret[**11], D. De Jesus Damiao[**12], E. Robutti[**7], A. De Roeck[**3], D. D'Enterria[**3], E.A. De Wolf[**13], K. Eggert[**3], R. Engel[**14], S. Erhan[**15], F. Ferro[**7], F. Garcia Fuentes[**8], W. Geist[**16], M. Grothe[**17, **18, **a], J.P. Guillaud[**19], J. Heino[**8], A. Hees[**3, **b], T. Hilden[**8], J. Kalliopuska[**8], J. Kaspar[**20], P. Katsas[**21], V. Kim[**22], V. Klyukhin[**3, **23], V. Kundrat[**20], K. Kurvinen[**8], A. Kuznetsov[**9], S. Lami[**24], J. Lamsa[**8], G. Latino[**24], R. Lauhakangas[**8], E. Lippmaa[**25], J. Lippmaa[**8], Y. Liu[**11, **c], A. Loginov[**3, **26, **d], M. Lokajicek[**20], M. Lo Vetere[**7], F. Lucas Rodriguez[**3], M. Macri[**7], T. Mäki[**8], M. Meucci[**24], S. Minutoli[**7], J. Mnich[**27], I. Moussienko[**28], M. Murray[**29], H. Niewiadomski[**3], E. Noschis[**8], G. Notarnicola[**6], S. Ochesanu[**13], K. Österberg[**8], E. Oliveri[**24], F. Oljemark[**8], R. Orava[**8,**30], M. Oriunno[**3], M. Ottela[**8], S. Ovyn[**11], P. Palazzi[**3], A.D. Panagiotou[**21], R. Paoletti[**24], V. Popov[**26], V. Petrov[**9], T. Pierzchala[**11], K. Piotrzkowski[**11], E. Radermacher[**3], E. Radicioni[**6], G. Rella[**6], S. Reucroft[**28], L. Ropelewski[**3], X. Rouby[**11], G. Ruggiero[**3], A. Rummel[**25], M. Ruspa[**2], R. Ryutin[**9], H. Saarikko[**8], G. Sanguinetti[**24], A. Santoro[**12], A. Santroni[**7], E. Sarkisyan-Grinbaum[**31, **e], L. Sarycheva[**23], F.P. Schilling[**3], P. Schlein[**15], A. Scribano Memoria[**24], G. Sette[**7], W. Snoeys[**3], G.R. Snow[**32], A. Sobol[**32, **f], A. Solano[**17], F. Spinella[**24], P. Squillacioti[**24], J. Swain[**28], A. Sznajder[**12], M. Tasevsky[**13, **g], C.C. Taylor[**4], F. Torp[**33], A. Trummal[**25], N. Turini[**24], M. Van Der Donckt[**11], P. Van Mechelen[**13], N. Van Remortel[**8], A. Vilela Pereira[**12], J. Whitmore[**33], D. Zaborov[**26]

**1: Fermi National Accelerator Laboratory, Batavia, Illinois, USA

**2: Università del Piemonte Orientale, Novara, ITALY and Sezione dell'INFN, Torino, ITALY

**3: CERN, European Organization for Nuclear Research, Geneva, SWITZERLAND

**4: Case Western Reserve University, Cleveland, USA

**5: University of Florida, Gainesville, Florida, USA

**6: INFN Sezione di Bari and Politecnico di Bari, Bari, ITALY

**7: INFN Sezione di Genova and Università di Genova, Genova, ITALY

**8: High Energy Physics Division, Department of Physical Sciences, University of Helsinki and Helsinki Institute of Physics, Helsinki, FINLAND

**9: State Research Center of Russian Federation - Institute for High Energy Physics, Protvino, RUSSIA

**10: University of Bristol, Bristol, UNITED KINGDOM

**11: Université Catholique de Louvain, Louvain-la-Neuve, BELGIUM

**12: Universidade do Estado do Rio de Janeiro, Rio de Janeiro, RJ, BRAZIL

**13: Universiteit Antwerpen, Antwerpen, BELGIUM

**14: Institut für Kernphysik, Forschungszentrum Karlsruhe, Karlsruhe, GERMANY

**15: University of California, Los Angeles, Los Angeles, California, USA

**16: Institut Pluridisciplinaire Hubert Curien, IN2P3-CNRS - ULP, UHA Mulhouse, Strasbourg, FRANCE

**17: Università di Torino e Sezione dell'INFN, Torino, ITALY

**18: University of Wisconsin, Madison, Wisconsin, USA

**19: Laboratoire d'Annecy-le-Vieux de Physique des Particules, IN2P3-CNRS, Annecy-le-Vieux, FRANCE

**20: Academy of Sciences of the Czech Republic, Praha, CZECH REPUBLIC

**21: University of Athens, Athens, GREECE

**22: Petersburg Nuclear Physics Institute, Gatchina (St Petersburg), RUSSIA

**23: Moscow State University - Institute for Nuclear Physics, Moscow, RUSSIA

**24: INFN Sezione di Pisa and Università di Siena, ITALY

**25: Estonian Academy of Sciences, Tallinn, ESTONIA

**26: Institute for Theoretical and Experimental Physics (ITEP), Moscow, RUSSIA

**27: Deutsches Elektronen-Synchrotron, Hamburg, GERMANY

**28: Northeastern University, Boston, Massachusetts, USA

**29: The University of Kansas, Lawrence, Kansas, USA

**30: University of Helsinki Faculty of Science High Energy Physics Division (SEFO), Helsinki, FINLAND

**31: University of Manchester, Manchester, UNITED KINGDOM

**32: University of Nebraska-Lincoln, Lincoln, Nebraska, USA

**33: Pennsylvania State University, University Park, USA

**a: This author is supported by the Italian Ministry for Education, University and Scientific Research under the program "Incentivazione alla mobilità di studiosi stranieri e italiani residenti all'estero"

**b: Now at Université Catholique de Louvain, Louvain-la-Neuve, BELGIUM

**c: Now at University of Science & Technology of China (USTC), Hefei Anhui, CHINA

**d: Now at Yale University, New Haven, Connecticut, USA

**e: Now at Universiteit Antwerpen, Antwerpen, BELGIUM

**f: On leave from State Research Center of Russian Federation - Institute for High Energy Physics, Protvino, RUSSIA

**g: Now at Institute of Physics, Academy of Sciences of the Czech Republic, Praha, CZECH REPUBLIC

Executive Summary

The CMS and TOTEM experiments intend to carry out a joint diffractive/forward physics program with an unprecedented rapidity coverage. The present document outlines some aspects of such a physics program, which spans from the investigation of the low-x structure of the proton to the diffractive production of a SM or MSSM Higgs boson.

Diffractive events are characterised by the fact that the incoming proton(s) emerge from the interaction intact or excited into a low mass state, with only a small energy loss. Diffractive processes with proton energy losses up to a few per cent are dominated by t-channel exchange with vacuum quantum numbers, the so-called Pomeron, now understood in terms of partons, primarily gluons, from the proton. For larger energy losses, mesonic exchanges – Reggeons and pions – become important. The topology of diffractive events is characterised by a large gap in the rapidity distribution of final-state hadrons due to the lack of colour and the effective spin of the exchange.

Events with a fast proton in the final state can also originate from the exchange of a photon. In particular, tagging a leading proton with small transverse momentum p_T allows one to select photon-proton events with known photon energy; likewise, tagging two leading protons with small p_T gives access to photon-photon interactions of well known centre-of-mass energy.

The physics interest of the program can be outlined as follows:

- At instantaneous luminosities small compared to that foreseen for the nominal LHC operation, i.e. $\lesssim 10^{30}\,\mathrm{cm}^{-2}\,\mathrm{s}^{-1}$, one can gain access to fundamental aspects of the strong interaction – the cross section for inclusive single diffraction ($pp \to pX$), the cross section for inclusive double-Pomeron exchange ($pp \to pXp$) and their t and mass dependences at the LHC centre-of-mass energy.

- Also at low luminosities, the low-x structure of the proton can be studied via e.g. the forward production of jets ($pp \to Xj$) and the production of forward Drell-Yan pairs ($pp \to Xl^+l^-$). This opens up the possibility of investigating the behaviour of QCD in the high-density, saturation regime already probed for the first time in heavy-ion collisions and at HERA.

- At higher luminosities, of the order of $10^{32}\,\mathrm{cm}^{-2}\,\mathrm{s}^{-1}$, the proton structure can be investigated via the diffractive processes $pp \to pX$ and $pp \to pXp$, where X includes a dijet system, vector bosons or heavy quarks. These reactions give access to the diffractive parton distribution functions, as well as to the so-called rapidity-gap survival probability. The latter is closely linked to soft rescattering and the features of the underlying event at the LHC.

- Central exclusive production ($pp \to p\phi p$) gives access to the generalised (or skewed) parton distribution functions. At the highest available luminosities, $\gtrsim 10^{33}\,\mathrm{cm}^{-2}\,\mathrm{s}^{-1}$, central exclusive production may become a discovery channel for particles with appropriate quantum numbers that couple to gluons. A case in point is the central exclusive production of a (SM or) MSSM Higgs boson.

- At all luminosities, a rich program of photon-photon and photon-proton physics can be pursued.
- The LHC centre-of-mass energy is approximately equal to the centre-of-mass energy of a 100 PeV fixed-target collision in air. This makes the forward detectors of CMS and TOTEM an ideal laboratory to test the models used to simulate the development of cosmic-ray showers in air.

We assess the combined acceptance of the two experiments for a number of different processes, both for standard, high-luminosity LHC optics and for a few special low-luminosity optics configurations. The measurement of the scattered proton kinematics is studied in detail.

At high luminosities, larger than $\approx 10^{32} \, \mathrm{cm^{-2} \, s^{-1}}$, two outstanding experimental problems need addressing: trigger and pile-up. We demonstrate that it is possible to operate a diffractive trigger stream up to luminosities of $\approx 2 \times 10^{33} \, \mathrm{cm^{-2} \, s^{-1}}$. We also assess, for a few analyses, the size of the diffractive pile-up background and discuss the tools to keep it under control.

Contents

x

Chapter 1

Introduction

Diffractive events are characterised by the fact that the incoming proton(s) emerge from the interaction intact, or are excited into a low mass state, with only a small energy loss. Diffractive processes, for proton energy losses up to a few per cent, are mediated by an exchange with quantum numbers of the vacuum, the so-called Pomeron, $I\!P$, now understood in terms of partons from the proton. For larger energy losses, mesonic exchanges – Reggeons and pions – become important. The topology of diffractive events is characterised by a gap in the rapidity distribution of final-state hadrons caused by the lack of colour and the effective spin of the exchanged object.

Events with a fast proton in the final state can also originate from the exchange of a photon. In particular, tagging one leading proton allows the selection of photon-proton events with known photon energy; likewise, tagging two leading protons gives access to photon-photon interactions of well known centre of mass energy. The average proton energy loss is larger and the proton scattering angle smaller in photon exchanges than for the diffractive case. This can be used to establish relative contributions of these two processes.

In the present chapter some of the key concepts at the basis of the current understanding of diffractive processes are reviewed. In addition, some of the main results from earlier experiments are summarised. We begin with the first pp collider, the CERN ISR, which made important discoveries in the field of diffraction. Later, the UA8 experiment at the CERN SPS $p\bar{p}$ collider was the first to see hard diffractive events and thus pave the way to describing diffractive events in terms of partons and structure functions. We then move on to HERA, where it became experimentally clear that QCD factorisation holds and that diffraction can be described in terms of diffractive parton distribution functions. The Tevatron data showed that diffraction in hadron-hadron collisions is more complicated and hard diffractive factorisation is broken by multiple interactions. These data are particularly enlightening since they are the closest to those expected at the LHC.

1.1 The interest of diffractive interactions

Building bridges between QCD and Regge theory has become a hot topic in recent years thanks to the study of hard diffractive processes, which combine high transverse momentum (p_T) scattering or heavy quark production with the features typical of soft diffractive events.

Ingelman and Schlein [1] were the first, in 1985, to build a model of hard diffractive scattering. This led the way to studying hard diffraction in a QCD-based framework; their model was basically confirmed by the first observation, in 1988, of hard diffractive events by the UA8 experiment at the CERN $p\bar{p}$ collider [2]. Early parton-model interpretations of the

1

Pomeron are discussed in references [3, 4].

There have been major advances in the field of diffractive interactions recently, largely driven by the study of diffraction at HERA and the Tevatron. There, the number of diffractive events, with the scattered proton remaining intact in a high-energy inelastic collision, is found to constitute a surprisingly large fraction of the entire rate. Measurements at HERA show that approximately 10% of the deep inelastic lepton-proton scattering cross section is diffractive. At the LHC the diffractive processes, including elastic scattering, are expected to represent about 50% of the total pp cross section[1].

The essential aspects of the recent results are discussed for instance in [5, 6], and can be summarised as follows:

- Many aspects of diffraction are well understood in QCD when a hard scale is present. In that case, perturbative techniques can be used and the dynamics of the events can be described in terms of quarks and gluons.

- A key to this success are factorisation theorems [7–10] in electron-proton scattering, which render part of the dynamics accessible to calculation in perturbation theory. The remaining non-perturbative quantities are the so-called diffractive parton distribution functions (dPDFs) and generalised (or "skewed") parton distributions (GPDs) – see e.g. [5, 6] and references therein. They can be extracted from measurements and contain specific information about small-x partons in the proton that can only be obtained in diffractive processes.

- Diffractive parton distributions are accessed in inclusive diffractive processes and can be interpreted as conditional probabilities to find a parton in the proton when the final state of the process contains a fast proton of a given four-momentum. Generalised parton distributions are accessed in exclusive diffractive processes; they quantify correlations between parton momenta in the proton. Their t-dependence is sensitive to the distribution of partons in the transverse plane.

- The description of hard diffractive hadron-hadron collisions is more challenging since factorisation is broken by rescattering between spectator partons [9]. The resulting suppression of the diffractive cross section is often quantified in terms of the so-called rapidity gap survival probability, S^2 [11, 12]. These rescattering effects are of interest in their own right because of their intimate relation with multiple scattering effects, which at LHC energies are expected to be crucial for understanding the structure of the underlying events in hard collisions.

  The dynamics of rescattering and multi-gap events is still not completely understood. The available data can be described in terms of an effective, non-linear Pomeron trajectory [13]; its variation with energy would be a consequence of multi-Pomeron exchange effects [14]. Other models, also testable at the LHC, have been proposed (see e.g. [15] and references therein). These topics can be pursued in more detail with the CMS-TOTEM data at the LHC.

- A fascinating link has emerged between diffraction and the physics of heavy-ion collisions through the concept of saturation, which offers a new window on QCD dynamics in the regime of high parton densities.

- Perhaps unexpectedly, the production of the Higgs boson, both in the SM and

---

[1]Excluding elastic scattering, diffractive processes are expected to contribute about 25% of the total pp cross section.

in the MSSM, in diffractive pp collisions, is drawing more and more attention as a clean channel to study the properties of a light Higgs boson or even discover it. The central exclusive reaction, $pp \rightarrow pHp$, appears particularly promising; however, the possibly small cross section represents an experimental challenge.

1.2 Diffraction: the current experimental status

1.2.1 The ISR Collider at CERN

The first proton-proton collider, the CERN Intersecting Storage Rings (ISR), made several important discoveries (see e.g. [16, 17]) in the field of diffraction. Elastic scattering beyond the Coulomb region showed an exponential slope followed by a clear diffraction minimum around $|t| \approx 1.4\,\mathrm{GeV}^2$, which moves to smaller $|t|$ as $\sqrt{s}$ increases. This was interpreted as a growth in the proton size. Beyond the dip, a power law $\frac{d\sigma}{dt} \approx |t|^{-8}$ appears. Elastic scattering was measured out to $|t| \approx 10\,\mathrm{GeV}^2$, a value much larger than has been reached at higher energy colliders. The ratio of the elastic to the total cross section, $\frac{\sigma_{el}}{\sigma_T}$, was found to be approximately 0.173, independent of energy through the ISR range. Antiprotons were also stored in the ISR and σ_T and $\frac{d\sigma}{dt}$ were measured for $p\bar{p}$; the diffraction minimum is largely filled in, demonstrating the presence of a crossing-odd amplitude.

Prior to the ISR, with $\sqrt{s}$ up to only 7.4 GeV, diffractive excitation was limited to the (N^*) resonance region $M \lesssim 2\,\mathrm{GeV}$. At the ISR the inclusive proton spectra ($p + p \rightarrow p+$ anything (X)) in the Feynman scaling variable $x_F = \frac{p_Z}{p_{beam}}$ showed a strong peak for $x_F \gtrsim 0.95$, independent of $\sqrt{s}$ (scaling). At a given energy the cross section shows a $\frac{1}{M^2}$ behaviour above the resonance region. Adjacent to the proton in rapidity is a gap $\Delta y \gtrsim 3$ with no hadrons ("rapidity gap"). This showed that the proton can be diffractively excited to masses M_X far above the resonance region, in fact up to about $M_X = \sqrt{s}\sqrt{1-x_F} = 0.22\sqrt{s} = 14\,\mathrm{GeV}$ at $\sqrt{s} = 63\,\mathrm{GeV}$. The single diffractive cross section for $(1 - x_F) \leq 0.05$ rises from about 6 mb to 7 mb through the ISR energy range. Subsequently it has been found that the approximate $\frac{M^2}{s}$ scaling behaviour continues through the Tevatron range, with $\sqrt{s} = 1960\,\mathrm{GeV}$ and M_X up to $\approx 450\,\mathrm{GeV}$, which is well into the domain of high E_T jets, W and Z bosons, and these are indeed diffractively produced. At the LHC the same "rule of thumb" implies that single diffractive excitation will extend to $M_X \approx 3\,\mathrm{TeV}$, well above the $t\bar{t}$ threshold and into the range where new "Beyond the Standard Model" physics is expected.

Evidence for Pomeron-single quark interactions and large Λ^0 polarisation in single diffractive events was also found [18, 19].

At the ISR the process known as "Double Pomeron Exchange" (DPE) was discovered [20]. This was predicted by Regge theory; both protons are coherently (diffractively) scattered, losing energy (up to about $0.05 \times E_{beam}$, as for single diffraction), and a hadronic state X is created in the central region (near rapidity $y = 0$), with two rapidity gaps of $\Delta y \approx 3$. The mass limit for X (symmetric case) is now $M_X(max) = (1 - x_F)\sqrt{s} = 0.05\sqrt{s} = 3.1\,\mathrm{GeV}$ at the top ISR energy. Exclusive[2] central states $\pi^+\pi^-, \pi^+\pi^-\pi^+\pi^-, K^+K^-$ and $p\bar{p}$ were measured to study this special diffractive process (sometimes called "diffractive excitation of the vacuum") and to search for glueballs, supposing that the exchanged Pomerons are glue dominated. At the ISR α-particles were also stored, and the process $\alpha\alpha \rightarrow \alpha + \pi^+\pi^- + \alpha$ measured, proof that the scattering is indeed coherent. The mass spectra are the same as in

---

[2]Exclusive means that all the produced particles are measured.

pp. The cross section $\sigma(pp \to p + \pi^+\pi^- + p) \approx 10\mu b$. The $\pi^+\pi^-$ mass spectrum shows no ρ°, which is forbidden in DPE, but exhibits interesting structures: $\sigma(600)$, $f_0(980)$ and higher mass structures [21, 22] which have not yet been explained, extending to about 3-4 GeV.

1.2.2 The SPS Collider at CERN

The UA8 experiment used Roman Pot spectrometers (with $|t_{min}| = 0.8\,\text{GeV}^2$) installed in both arms of the UA2 interaction region [23]. Clear dijet events were observed, constituting the first evidence for the partonic structure of the proton in diffractive collisions [24].

UA8 studied the distribution in the variable x(2–jet), shown in Fig. 1.1(a). This variable is the longitudinal momentum of the observed dijet system along the Pomeron direction in the Pomeron-proton centre-of-mass, normalised to its maximum possible value.
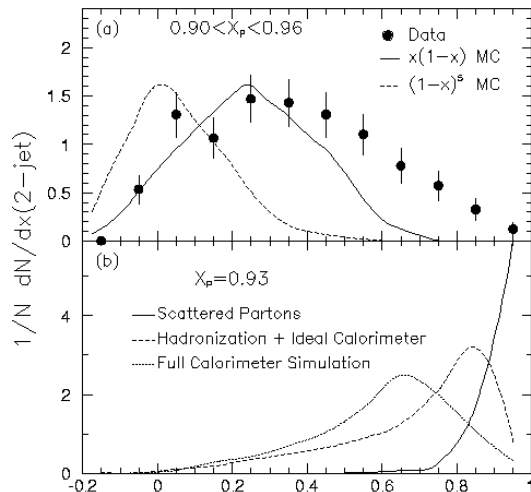
Figure 1.1: (a) x(2–jet) distribution (see text) compared to simulations assuming a soft (dashed) and hard (solid) Pomeron structure. (b) Expected "super-hard" x(2–jet) distribution at different levels of simulation (from [24]).

The x(2–jet) variable directly reflects the relative hardness of the Pomeron and proton structure functions. At parton level, before including the effects of hadronisation, jet-finding and detector efficiencies, x(2–jet) in a given event is related to the parton momenta in Pomeron and proton by x(2–jet) $= x$(Pomeron)$-x$(proton).

The curves in Fig. 1.1(a) indicate the results of MC simulations for a standard proton structure and either a soft ($x \cdot G(x) \propto (1-x)^5$) or a hard ($x \cdot G(x) \propto x(1-x)$) structure for the diffractive exchange. In the MC calculations, the scattered partons were hadronised and the simulated events were passed through the same full UA2 detector simulation and jet finding procedure as the data. A contribution harder than that of the hard Pomeron is seen for x(2-jet) > 0.7. These "super-hard" events were shown to be consistent with having the entire momentum of the Pomeron participating in the hard scattering [25]. Figure 1.1(b) shows the parton-level distribution for this case, x(2–jet) $= 1 - x$(proton), as well as the expected x(2-jet) distribution after hadronisation and full detector simulation. A combined fit of soft structure, hard structure and super–hard components to the experimental distribution in Fig. 1.1(a) yields 13%, 57% and 30%, respectively.

UA8 also made important contributions in the study of inclusive proton spectra [13] for
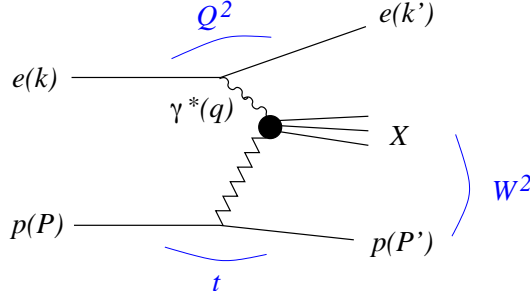
Figure 1.2: Schematic diagram of inclusive diffractive DIS, $ep \rightarrow eXp$. Four-momenta are indicated in parentheses.

$x > 0.90$, in the measurement of the cross section for diffractive dijet production [26] and in the study of inclusive Double-Pomeron-Exchange [27]. The diffractive dijet production study [26] did not require a rapidity gap in the trigger and obtained a Pomeron-proton coupling constant that agrees within a factor of two with that extracted by Donnachie and Landshoff from pp elastic scattering data. This result implies that the underlying cross sections for hard diffraction are not greatly influenced by multi-Pomeron-exchange effects which decrease the gap-survival probability. This result is at variance with that obtained later by CDF [28] and discussed in Sec. 1.2.4.

1.2.3 The HERA Collider at DESY

Figure 1.2 shows a schematic diagram of inclusive diffractive deep inelastic scattering (DIS). The following features are important:

- The proton emerges from the interaction carrying a large fraction x_L of the incoming proton momentum. Diffractive events thus appear as a peak at $x_L \approx 1$, the diffractive peak, which at HERA approximately covers the region $0.98 < x_L < 1$. The t distribution is exponential, similar to the case of elastic pp scattering. These protons remain in the beam-pipe and can only be measured with detectors located inside the beam-pipe.

- The collision of the virtual photon with the proton produces a hadronic final state X with the photon quantum numbers and invariant mass M_X. A large gap in rapidity (or pseudorapidity) is present between X and the final-state proton.

Diffractive ep scattering thus combines features of hard and soft scattering. The electron receives a large momentum transfer; in fact the photon virtuality Q^2 can be in the hundreds of GeV^2. In contrast, the proton emerges with its momentum barely changed.

1.2.3.1 Diffractive structure functions

The kinematics of $\gamma^* p \rightarrow Xp$ can be described by the invariants $Q^2 = -q^2$, $t = (P - P')^2$, and by the square of the centre-of-mass energy in the photon-proton system, $W^2 = (P + q)^2$, where the four-momenta are defined in Fig. 1.2. Also used are the scaling variables $x_{I\!P}$ (ξ in the Fermilab and LHC nomenclature) and β; the former is the fractional momentum loss of the incident proton, related as $x_{I\!P} \simeq 1 - x_L$ to the variable x_L introduced above. The variable β has the form of a Bjorken variable defined with respect to the momentum $P - P'$ lost by the initial proton instead of the initial proton momentum P. The usual Bjorken variable $x_{Bj} = Q^2/(2P \cdot q)$ is related to β and $x_{I\!P}$ as $\beta x_{I\!P} = x_{Bj}$.
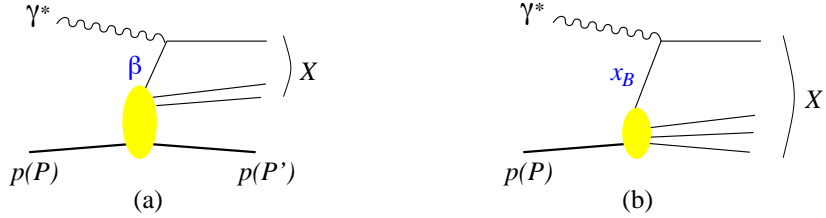
Figure 1.3: Parton model diagrams for deep inelastic diffractive (a) and inclusive (b) scattering. The variable β is the momentum fraction of the struck quark with respect to $P - P'$, and x_{Bj} its momentum fraction with respect to P.
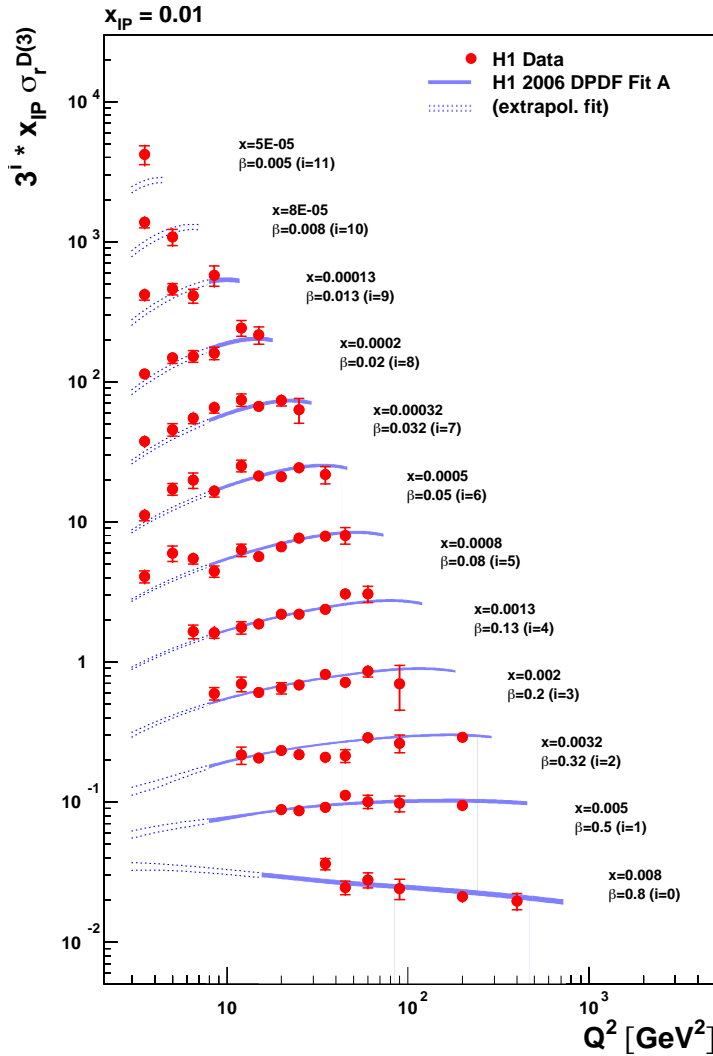
Figure 1.4: The reduced diffractive cross section $x_{I\!P}\sigma^{D(3)}$ as a function of Q^2 for different β bins at $x_{I\!P} = 0.01$ (from [29]). The reduced diffractive cross section $\sigma^{D(3)}$ is equal to the diffractive structure function $F_2^{D(3)}$ if $F_L^D = 0$. The curves are the result of a NLO QCD fit to the data.

The cross section for $ep \to eXp$ in the one-photon exchange approximation can be written in terms of the diffractive structure functions $F_2^{D(4)}$ and $F_L^{D(4)}$ as

$$\frac{d\sigma^{ep \to eXp}}{d\beta \, dQ^2 \, dx_{I\!P} \, dt} = \frac{4\pi\alpha_{\text{em}}^2}{\beta Q^4}\left[\left(1 - y + \frac{y^2}{2}\right)F_2^{D(4)}(\beta, Q^2, x_{I\!P}, t) - \frac{y^2}{2}F_L^{D(4)}(\beta, Q^2, x_{I\!P}, t)\right], \quad (1.1)$$

in analogy with the way $d\sigma^{ep \to eX}/(dx_{Bj} \, dQ^2)$ is related to the structure functions F_2 and F_L for inclusive DIS, $ep \to eX$. Here y is the fraction of energy lost by the incident lepton in the proton rest frame. The structure function $F_L^{D(4)}$ corresponds to longitudinal polarisation of the virtual photon; its contribution to the cross section is small in a wide range of the experimentally accessible kinematic region (in particular at low y). The structure function $F_2^{D(3)}$ is obtained from $F_2^{D(4)}$ by integrating over t.

In a parton model picture, inclusive diffraction $\gamma^* p \to Xp$ proceeds by the virtual photon scattering on a quark, in analogy to inclusive scattering (see Fig. 1.3). In this picture, β is the momentum fraction of the struck quark with respect to the exchanged momentum $P - P'$ (indeed the allowed kinematical range of β is between 0 and 1). The diffractive structure function describes the proton structure in these specific processes with a fast proton in the final state. F_2^D may also be viewed as describing the structure of whatever is exchanged in the t-channel in diffraction, i.e. of the Pomeron (if multiple Pomeron exchange can be neglected). It is however important to bear in mind that the Pomeron in QCD cannot be interpreted as a particle on which the virtual photon scatters (see e.g. Sec. 2.5 of [6]).

The data on $F_2^{D(3)}$ have two remarkable features:

- F_2^D is largely flat in the measured β range. Keeping in mind the analogy between β in diffractive DIS and x_{Bj} in inclusive DIS, this is very different from the behaviour of the "usual" structure function F_2, which strongly decreases for $x_{Bj} \gtrsim 0.2$.

- The dependence on Q^2 (see Fig. 1.4) is logarithmic, i.e. one observes approximate Bjorken scaling. The structure function F_2^D increases with Q^2 for all β values except the highest. This is reminiscent of the scaling violations of F_2, except that F_2 rises with Q^2 only for $x_{Bj} \lesssim 0.2$ and that the scaling violations become negative at higher x_{Bj}. In the proton, negative scaling violations reflect the presence of the valence quarks radiating gluons, while positive scaling violations are due to the increase of the sea quark and gluon densities as the proton is probed with higher resolution. The F_2^D data thus suggest that the partons resolved in diffractive events are predominantly gluons.

1.2.3.2 Diffractive parton distributions

The conclusion just reached can be made quantitative by using the QCD factorisation theorem for inclusive diffraction, $\gamma^* p \to Xp$. According to this theorem, the diffractive structure function, in the limit of large Q^2 at fixed β, $x_{I\!P}$ and t, can be written as [7–9]

$$F_2^{D(4)}(\beta, Q^2, x_{I\!P}, t) = \sum_i \int_\beta^1 \frac{dz}{z} C_i\left(\frac{\beta}{z}\right) f_i^D(z, x_{I\!P}, t; Q^2), \qquad (1.2)$$

where the sum is over partons of type i. The coefficient functions C_i describe the scattering of the virtual photon on the parton and are exactly the same as in inclusive DIS. In analogy

to the usual parton distribution functions (PDFs), the diffractive PDFs $f_i^D(z, x_{I\!P}, t; Q^2)$ can be interpreted as conditional probabilities to find a parton i with fractional momentum $z x_{I\!P}$ in a proton, probed with resolution Q^2 in a process with a fast proton in the final state (the momentum of which is specified by $x_{I\!P}$ and t).

Several fits of the available F_2^D data are available which are based on the factorisation formula (1.2) at next-to-leading order (NLO) in α_s [30, 31]. Figure 1.5 shows an example. As expected the density of gluons is larger than that of quarks, by about a factor 5–10.
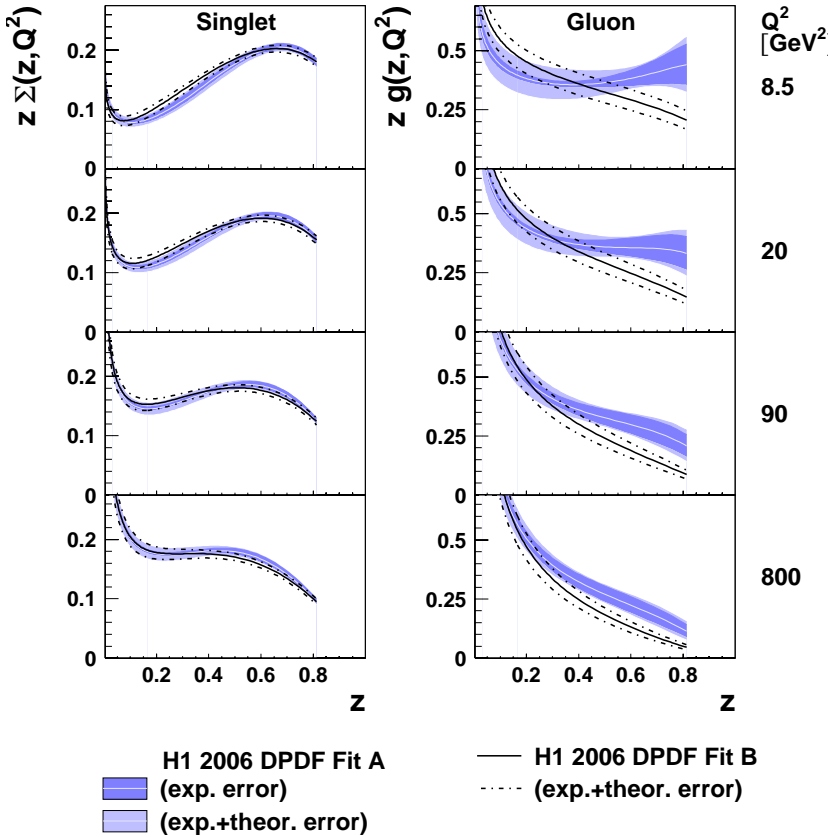
Figure 1.5: The proton diffractive PDFs, as determined in next-to-leading order (NLO) fits to F_2^D data by the H1 Collaboration, as a function of the parton fractional momentum z for different values of Q^2. Left panel: quark singlet distribution. Right panel: gluon distribution (from [29]).

1.2.3.3 Exclusive diffractive processes

HERA has also investigated exclusive processes in which the virtual photon dissociates into a single particle. Since diffraction involves the exchange of vacuum quantum numbers, this particle can in particular be a vector meson (which has the same J^{PC} quantum numbers as the photon) – in this case the process is sometimes referred to as "elastic" vector meson production. Another important case is deeply virtual Compton scattering (DVCS), $\gamma^* p \to \gamma p$.

A striking feature of the data taken at HERA is that the energy dependence of these processes becomes steep in the presence of a hard scale, which can be either the photon virtuality Q^2 or the mass of the meson in the case of J/Ψ or Υ production (see e.g. Fig. 15 of [6]).
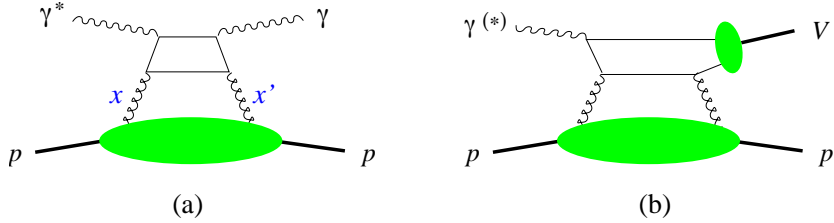
Figure 1.6: (a) Factorisation of deeply virtual Compton scattering, $\gamma^* p \to \gamma p$, which can be measured in the exclusive process $ep \to ep\gamma$. The blob represents the generalised gluon distribution, with x and x' denoting the momentum fractions of the gluons. (b) Factorisation of exclusive meson production. The small blob represents the vector meson wave function. In the collinear factorisation formalism, there are further graphs (not shown) involving quark instead of gluon exchange.

A theoretical analysis of DVCS and exclusive vector meson production at large Q^2 shows that factorisation holds [10]. In the limit of large Q^2 (at fixed Bjorken variable x_{Bj} and fixed t), the Compton amplitude factorises into a hard-scattering subprocess and a hadronic matrix element that describes the emission and reabsorption of a parton by the proton target (see Fig. 1.6a). As shown in Fig. 1.6b, the analogous result for exclusive meson production involves in addition the quark-antiquark distribution amplitude of the meson (often termed the meson wave function) and thus a further piece of non-perturbative input.

The hadronic matrix elements appearing in the factorisation formulae for exclusive processes tend to the usual PDFs in the limit in which the proton has the same momentum in the initial and final state. These matrix elements are more general functions than the usual PDFs and take into account the momentum difference between the initial and final state proton (or, equivalently, between the emitted and reabsorbed parton). These "generalised parton distributions" (GPDs) depend on two independent longitudinal momentum fractions instead of a single one, on the transverse momentum transferred to the proton (whose square is $-t$ to a good approximation at high energy), and on the scale at which the partons are probed. The scale dependence of the GPDs is governed by a generalisation of the DGLAP equations. The dependence on the difference of the longitudinal momenta (often called "skewness") contains information on correlations between parton momenta in the proton wave function.

The fact that the GPDs are approximately proportional to the usual PDFs squared explains the energy dependence of the cross sections mentioned above: this dependence reflects the x_{Bj} ($\propto 1/W^2$) and scale dependence of the gluon density in the proton, which grows with decreasing x_{Bj} with a slope becoming steeper as the scale increases.

1.2.4 The Tevatron Collider at Fermilab

As discussed in the previous section, an important question is to what degree hard diffractive processes obey QCD factorisation, i.e. whether the proton has universal, process-independent, diffractive parton distribution functions. In this case, the cross sections of hard diffractive processes could be written as a convolution of a parton-level cross section and process-independent diffractive PDFs. The results from HERA (see Sec. 1.2.3) show that QCD factorisation holds in diffractive deep inelastic scattering. However, single diffractive (SD) rates of W and Z-boson [32, 33], dijet [34, 35], b-quark [36] and J/ψ meson [37] production measured by CDF and DØ are about ten times lower than expectations based on the dPDFs determined at HERA, indicating a severe breakdown of factorisation in hard diffrac-
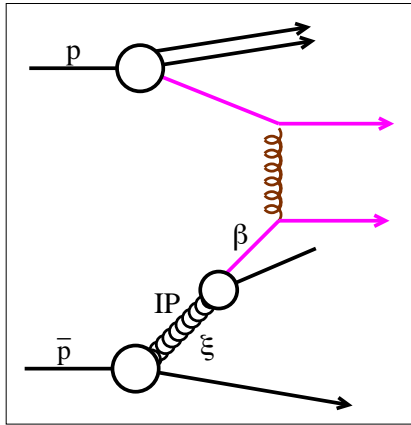
Figure 1.7: Single diffractive dijet production at the Tevatron.

tion between Tevatron and HERA. In general, while at HERA hard diffraction contributes a fraction of order 10% to the total cross section, it contributes only about 1% at the Tevatron.

In Run I (1992-96) diffractive events at the Tevatron were mostly tagged by their rapidity gaps. Since Run IC (1996) CDF has been equipped with near-beam detectors housed in Roman Pots to measure leading antiprotons inside the beam-pipe on one side of the interaction point. For the ongoing Run II, DØ has installed near-beam detectors on both sides of the interaction point. Tables 1.1 and 1.2 summarise the vast number of studies on soft and hard diffraction carried out at the Tevatron.

Table 1.1: The diffractive program of the Tevatron experiments, the methods for tagging diffractive events, and the kinematic coverage (t is given in units of GeV^2). SD stands for single diffraction, DD for double diffraction and DPE for double pomeron exchange.

Exp., Run	Tagging	Coverage	Physics
CDF IA,B [32, 34, 36–38]	rap. gap no RP	$\|\eta\| < 5.9$	soft SD, DD, DPE hard diffraction: dijets, W, b$\bar{\text{b}}$, J/Ψ
CDF IC [28]	rap. gap leading $\bar{\text{p}}$	$\|\eta\| < 5.9$ $-t < 1$ $0.03 < \xi < 0.1$	
CDF II [39]	rap. gap leading $\bar{\text{p}}$	$\|\eta\| < 7.5$ $-t < 2$ $0.02 < \xi < 0.1$	diffractive structure functions, search for exclusive DPE
DØ I [33, 35, 40]	rap. gap no RP	$\|\eta\| < 5.9$	hard diffraction: dijets, W, Z
DØ II [41]	rap. gap lead. p, $\bar{\text{p}}$	$\|\eta\| < 5.9$ $0.8 < -t < 2$ any ξ	all above with p, $\bar{\text{p}}$ tagging

Figure 1.7 shows a single diffractive dijet production diagram at the Tevatron according to a naive Pomeron-based model. The signature is a leading nucleon (an antiproton at CDF), which escapes the collision intact, losing only a small momentum fraction ξ to the diffractive exchange; a parton from the latter scatters with a parton from the other nucleon (a proton in the figure) resulting in two high E_T jets. The diffractive structure function $F_2^D(\beta)$ (see Sec. 1.2.3 for a definition of F_2^D) can be investigated by measuring the ratio of diffractive to non-diffractive dijet production rates as a function of the Bjorken variable $x_{Bj} = \beta\xi$ of

the struck parton in the nucleon. In leading-order (LO) QCD this ratio is the ratio of the diffractive to non-diffractive parton densities of the (anti)proton in dijet production. Figure 1.8(left) shows the discrepancy between $F_2^D = F_{jj}^D$ as extrapolated from the HERA measurements and the result from single diffractive (SD) dijet production at CDF in Run IC [28]. The F_{jj}^D function, integrated over the antiproton momentum loss ξ and four-momentum transfer squared t, was obtained as a function of β by measuring the ratio of diffractive to non-diffractive dijets rates and using the known leading order PDFs of the proton.
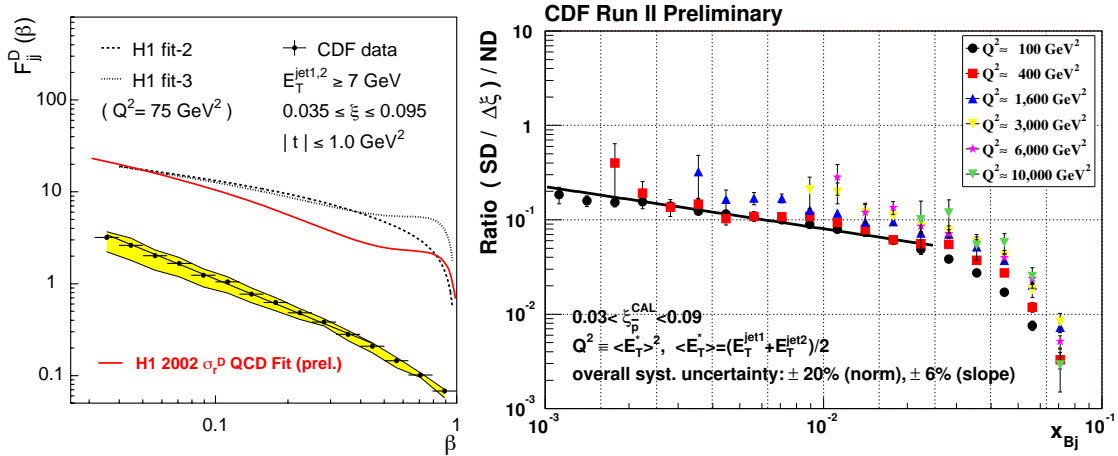
Figure 1.8: Left: Diffractive structure function $F_{jj}^D(\beta)$ of the proton as measured by CDF (points) and the expectations based on the dPDFs measured in diffractive DIS by H1. The continuous line is a fit to the data of the form β^{-n}. The band represents the sensitivity to the number of jets used in evaluating β. The normalisation uncertainty of the data is $\pm 25\%$ (from [28]). Right: Ratio of the diffractive dijet event rate per unit ξ to the non-diffractive dijet rate as a function of x_{Bj} of the parton in the antiproton, for different intervals in jet E_T. Q^2 is approximated as $Q^2 = \langle E_T \rangle^2$ [42].

A likely explanation of this breakdown is based on the different initial states in diffractive DIS and in $p\bar{p}$ diffraction. In the latter case, additional soft scattering between the two interacting hadrons can fill the rapidity gap and slow down and/or break up the (anti-)proton. The event no longer appears as diffractive. The effect of these soft re-interactions is quantified by the so-called "gap survival probability", S^2.

CDF Run I results were based on dijet events with relatively low transverse jet energies (E_T). In Run II further studies have been aimed at exploring the ratio of SD to non diffractive (ND) event rates at larger E_T, thanks to an improved particle coverage in the forward direction and to dedicated triggers.

In Fig. 1.8 (right), the ratio of diffractive to non-diffractive dijet production rates is plotted as a function of x_{Bj} of the struck parton in the antiproton. For each event, x_{Bj} is calculated from the E_T and the pseudorapidity η of the jets within $|\eta| < 2.5$. In LO QCD this ratio equals the ratio of the diffractive to non-diffractive parton densities of the antiproton in dijet production. Results from Run II are in good agreement with Run I measurements [28]. The results of Fig. 1.8 (right) show that the ratio does not depend strongly on $E_T^2 = Q^2$ in the range from $Q^2 = 100$ up to $Q^2 = 10,000 \, \text{GeV}^2$. This indicates that the Q^2 evolution of F_2^D is similar to that of the inclusive proton structure function F_2 [42].

A particularly interesting class of hard diffractive events is the exclusive central production through double-Pomeron-exchange (DPE), characterised by the presence of only one single particle or a dijet in the final state in addition to the two scattered protons. The selection rule on spin, $J_z = 0$, strongly suppresses the $gg \to q\bar{q}$ background for these events because of helicity conservation (see Sec. 7.2). This background would totally vanish at leading order (LO) for massless quarks. Table 1.2 lists some examples for exclusive production. CDF has seen candidates for exclusive dijet and χ_{c0} production, and set upper limits on the cross section that are useful for an extrapolation to the LHC [43].

Table 1.2: Examples of exclusive DPE processes (p + p → p + X + p). For cross sections see e.g. [44]. The numbers in square brackets are experimental upper limits from CDF, Run II [43].

Diffractive system	Decay channel	$\sigma(Tev.) \times$ BR	$\sigma(LHC) \times$ BR
dijet ($E_T > 10\,$GeV)	jj	0.97 nb [≤1.1 nb]	7 nb
χ_{c0} (3.4 GeV)	$\gamma J/\psi \to \gamma\mu^+\mu^-$	390 pb [≤204 pb][1]	1.8 nb
	$\pi^+\pi^- K^+ K^-$	12 nb	54 nb
χ_{b0} (9.9 GeV)	$\gamma Y \to \gamma\mu^+\mu^-$	≤ 0.5 pb	≤4 pb

[1] scaled from CDF's rapidity range ±0.6 to ±2.5 used by [44].
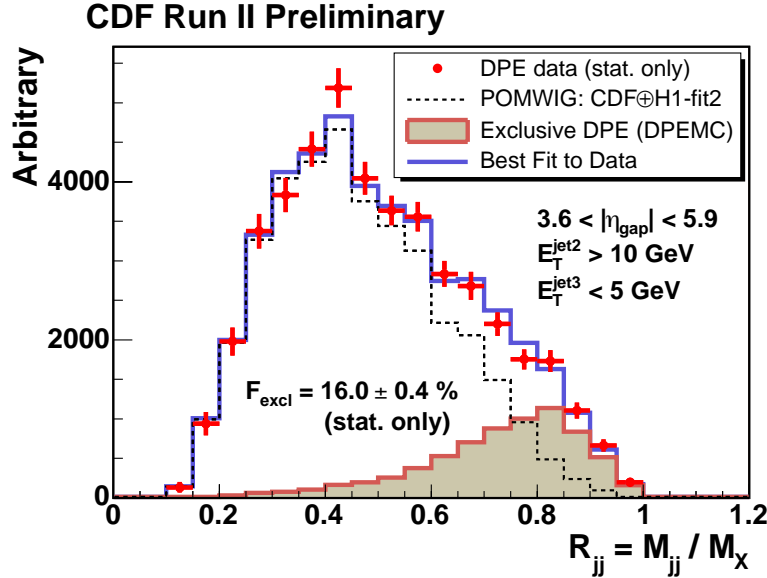
Figure 1.9: CDF data for $R_{jj} = M_{jj}/M_X$ compared to exclusive DPE production (shaded histogram) from DPEMC and a combination of inclusive DPE, SD and ND production (dotted histogram) from POMWIG [39].

Figure 1.9 shows the CDF result from the search for exclusive dijet events in about $430\,\text{pb}^{-1}$ of data collected between 2002 and 2005 with dedicated diffractive triggers [39]. A leading antiproton detected in the RP spectrometer and a rapidity gap on the proton side were required. The distribution of the dijet mass fraction, $R_{jj} = M_{jj}/M_X$, from the data, i.e. the

ratio of the invariant mass of the two leading jets to the total mass of the system reconstructed from the calorimeters, is compared to the distribution obtained with the inclusive POMWIG Monte Carlo [45]. The excess of data events towards $R_{jj} = 1$ is in agreement with exclusive DPE dijet production as modelled by the DPEMC Monte Carlo [46] (shaded area).

1.3 A survey of the processes investigated

In the following we give a brief survey of the processes that can be studied by CMS and TOTEM together. Some of these are presented in detail later in this document.

The accessible physics is a function of the integrated luminosity. We assume standard LHC optics with $\beta^* = 0.55$ m for the high-luminosity studies presented in Chapters 6 - 10. The low-luminosity ($\sim 10^{28} - 10^{30}$ cm^{-2} s^{-1}) studies presented in Chapter 5 would profit from running with $\beta^* > 0.5$ m, where the ξ coverage of the TOTEM Roman pot detectors at 220 m (see Chapter 2) is wider and the t resolution improves because of the lower transverse momentum spread of the beam. This is discussed in Chapter 3.

For $\beta^* = 0.55$ m, the detectors at 220 m have coverage for $0.02 < \xi < 0.2$, where ξ is the proton fractional momentum loss. Leading proton detectors at 420 m from the interaction point as suggested by the FP420 R&D project [47] would cover $0.002 < \xi < 0.02$ (see Chapter 2).

Inclusive single diffraction and double Pomeron exchange at low luminosity

At modest instantaneous luminosities, up to 10^{32} cm^{-2} s^{-1}, inclusive single diffractive (SD) events, $pp \to pX$, as well as inclusive double-Pomeron exchange (DPE) events, $pp \to pXp$, can be studied by requiring the presence of one or two rapidity gaps in the event. In the ξ range where the TOTEM detectors have acceptance, the scattered proton can be detected and the kinematics of the events fully measured.

The inclusive SD and DPE cross sections, as well as their M_X dependence, even in the absence of a hard scale, are important quantities to be measured at the LHC. Here M_X indicates the mass of the system X. These cross sections amount to approximately 15% and 1% of the total proton-proton cross section, respectively; their energy dependence is a fundamental parameter of (non-perturbative) QCD. In addition, since diffractive events constitute a major fraction of the pile-up events, their measurement is mandatory to be able to properly simulate and understand high-luminosity data, where, at instantaneous luminosities of 10^{34} cm^{-2} s^{-1}, approximately 35 pile-up events are superimposed, on average, to any hard event.

Some of the possible low-luminosity studies, also using special LHC optics, are detailed in Chapter 5.

SD and DPE production of dijets, vector bosons and heavy quarks

The study of SD and DPE events in which the diffractively excited state includes high-E_T jets, heavy quarks or vector bosons opens up the possibility of accessing dPDFs and GPDs. Some possible studies are presented in Chapters 5 and 7. The first priority here will be to repeat the measurements that have been carried out at the Tevatron (see Sec. 1.2.4).

Inclusive jet and heavy quark production are mainly sensitive to the gluon component of the dPDFs, while vector boson production is sensitive to quarks. The kinematic region covered expands that explored at HERA and Tevatron, with values of β as low as 10^{-4} and of Q^2 as

high as tens of thousands of GeV^2.

The extraction of the dPDFs and of the GPDs is complicated by the breakdown of QCD diffractive factorisation in hadron-hadron collisions discussed in Sec. 1.2: to access dPDFs and GPDs, it is necessary to establish by how much diffractive interactions are suppressed because of soft re-interactions of the spectator partons from the interacting hadrons. The comparison of the inclusive DPE and SD rates will help quantify this suppression: as a consequence of the factorisation breakdown, the diffractive structure function extracted from, say, SD jet production differs from that obtained from DPE jet production. The ratio of these two structure functions is sensitive to the rapidity gap survival probability.

Central exclusive production

As the delivered luminosity reaches tens of fb^{-1}, the central exclusive production process (DPE) becomes a tool to search for new physics.

By central exclusive, we refer to the process $pp \rightarrow p\phi p$, where there are large rapidity gaps between the outgoing protons and the decay products of the ϕ meson. There are three primary reasons why this process is attractive. Firstly, if the outgoing protons remain intact and scatter through small angles, then, under some general assumptions, the central system ϕ is produced in the $J_Z = 0$, C and P even state. Secondly, the mass of the central system can be determined accurately from a measurement of the transverse and longitudinal momentum components of the outgoing protons alone. This means an accurate determination of the mass irrespective of the decay mode of the centrally produced particle. Thirdly, the process delivers good signal to background ratios, due to the combination of the $J_Z = 0$ selection rule, the effect of colour and spin factors, the mass resolution, and the simplicity of the event in the central detectors. In addition, central exclusive production is sensitive to CP violating effects in the couplings of the object ϕ to gluons; these effects can be measured directly via the distribution of the azimuthal angle between the outgoing proton momenta.

Central exclusive production is generally an attractive way of searching for any new particles that couple to gluons. An example is the scenario in which the gluino is the lightest supersymmetric particle. In such models, there should exist a spectrum of gluino-gluino bound states which can be produced in the central exclusive channel. Likewise, central exclusive production of radions, the fields introduced in the Randall-Sundrum model of five-dimensional quantum gravity, has been studied.

The experimental prospects of studying the central exclusive production of a SM or MSSM Higgs boson are the subject of Sec. 7.2.

High-energy photon interactions

A significant fraction of events at the LHC involves photon interactions at energies above the electroweak scale. The protons radiating the photon often survive the collision intact and are scattered at angles comparable to the beam angular divergence. Detection of events of this type at the LHC will open up a new field of high-energy photon physics, which is outlined in Chapter 8. By requiring the detection of one or two forward protons, as done for diffractive interactions, photon-photon and photon-proton interactions can be selected. The photon fluxes, and the effective luminosities of photon-photon and photon-proton collisions are well known. The average proton energy loss is larger and the proton scattering angle smaller in photon exchanges than for the diffractive case. This can be used to establish relative contributions of these two processes.

Among the possible processes that can be studied, we discuss in Chapter 8 two-photon production of lepton and boson pairs, as well as photoproduction of single W bosons and associated WH photoproduction.

Low-x QCD: forward jet studies

Forward jet production at the LHC is an ideal process to investigate small-x QCD effects. The first part of Chapter 9 focuses on the measurement, in the forward hadron calorimeter (HF, 3< $|\eta|$ <5), of single inclusive jet cross sections and "Müller-Navelet" (MN) dijet cross section, where two jets with moderately high and similar p_T are produced with a large relative rapidity separation. The interest of the former measurement is based on the use of such relatively low E_T jets to constrain the proton PDFs (especially the gluon distribution) at fractional momenta of the order $x \approx 10^{-4}$. The interest of the second is based on the fact that the cross section for MN jets is a particularly sensitive measure of non-DGLAP small-x dynamics (BFKL and saturation evolution) in hadrons.

Low-x QCD: Drell-Yan

The study of forward production of low mass Drell-Yan lepton pairs at the LHC provides a unique opportunity to directly access low-x *quark* densities in the proton. This is presented in Chapter 9. In this process, the lepton pair originates from the annihilation of a quark-antiquark pair; the fractional momenta, x_1 and x_2, of the quark and the antiquark are related to the dilepton mass, M, and rapidity, y, of the lepton pair through

$$M^2 = sx_1x_2; \qquad x_{1,2} = \frac{M}{\sqrt{s}}e^{\pm y}, \qquad (1.3)$$

with $\sqrt{s} = 14\,\text{TeV}$, the centre-of-mass energy of the colliding protons. In order to access low x, a large imbalance in fractional momenta is required, boosting the lepton pair to large rapidities.

The CASTOR calorimeter (see Sec. 2) will cover the pseudorapidity range $5.3 < \eta < 6.6$ on one side of the interaction point, corresponding to x_{Bj} values down to 10^{-7}. With CASTOR and the T2 tracker (see Sec. 2), one can enhance the signal to background ratio by requiring tracks in association to the electromagnetic energy deposits. As T2 will measure both the azimuthal and polar angles of the tracks, a much more accurate measurement of the opening angle (and therefore of the dilepton mass) and a two-dimensional study in M^2 and x will become possible.

Rapidity gaps between forward jets

Experiments at the Tevatron and HERA have discovered events with a large rapidity gap between high E_T balancing jets. The four-momentum transfer squared $|t|$ across the gap can be as large as $1000\,\text{GeV}^2$. This could be a colour-singlet (BFKL) exchange between the scattering partons, or a normal gluon exchange followed by soft colour interactions to form the gap on a much longer space-time scale. As discussed in the last part of Chapter 9, we plan to study this early, when the luminosity is low enough to give single interactions (which is essential) but high enough to give high E_T jets separated by ~ 5 units of rapidity.

Validation of cosmic-ray generators

The correct simulation of the interaction of primary cosmic rays in the PeV energy range with the atmosphere is a key tool in the study of cosmic rays. The available generators differ

significantly in their predictions for the energy flow, multiplicity, hadronic energy fraction etc., in particular at high rapidities. These models can be tested at the LHC: a 100 PeV fixed-target collision in air corresponds to the centre-of-mass energy of a pp collision at the LHC. There are significant differences in the predictions, notably in the region covered by CAS-TOR, T1 and T2. A measurement of these features with CASTOR, T1 and T2 may thus be used to validate/tune these generators. More details are given in Chapter 10.

Chapter 2

Experimental Set-up

2.1 CMS

The CMS detector is described in detail elsewhere [48]. The main features of the apparatus are:

- Good muon identification and momentum resolution over a wide range of momenta in the region $|\eta| < 2.5$, good dimuon mass resolution ($\approx 1\%$ at $100\,\text{GeV}$), and the ability to determine unambiguously the charge of muons with $p_T < 1\,\text{TeV}$.
- Good charged particle momentum resolution and reconstruction efficiency in the inner tracker. Efficient triggering and offline tagging of τ's and b-jets, requiring pixel detectors close to the interaction region.
- Good electromagnetic energy resolution, good diphoton and dielectron mass resolution ($\approx 1\%$ at $100\,\text{GeV}$), wide geometric coverage ($|\eta| < 2.5$), measurement of the direction of photons and/or correct localisation of the primary interaction vertex, π^0 rejection and efficient photon and lepton isolation at high luminosities.
- Good missing energy and dijet mass resolution, requiring hadron calorimeters with a large hermetic geometric coverage ($|\eta| < 5$) and with fine lateral segmentation ($\Delta\eta \times \Delta\phi < 0.1 \times 0.1$).

An important aspect driving the detector design and layout is the choice of the magnetic field configuration for the measurement of the momentum of muons. Large bending power is needed to measure precisely the momentum of charged particles. This forces a choice of superconducting technology for the magnets.

At the heart of CMS sits a 13 m long, 5.9 m inner diameter, 4 T superconducting solenoid. In order to achieve good momentum resolution within a compact spectrometer without making stringent demands on muon-chamber resolution and alignment, a high magnetic field was chosen. The return field is large enough to saturate 1.5 m of iron, allowing 4 muon "stations" to be integrated to ensure robustness and full geometric coverage. Each muon station consists of several layers of aluminium drift tubes (DT) in the barrel region and cathode strip chambers (CSCs) in the endcap region, complemented by resistive plate chambers (RPCs).

The bore of the magnet coil is also large enough to accommodate the inner tracker and the calorimetry inside. The tracking volume is given by a cylinder of length 5.8 m and diameter 2.6 m. In order to deal with high track multiplicities, CMS employs 10 layers of silicon microstrip detectors, which provide the required granularity and precision. In addition, 3 layers of silicon pixel detectors are placed close to the interaction region to measure the impact parameter of charged-particle tracks, as well as the position of secondary vertices.

Primary vertices of pp-interactions are reconstructed in the CMS coordinate system with resolutions of $50\,\mu$m in the $r\phi$ and z coordinates, or better depending on the final states. More details can be found in [48]. The EM calorimeter (ECAL) uses lead tungstate (PbWO$_4$) crystals with coverage in pseudorapidity up to $|\eta| < 3.0$. The scintillation light is detected by silicon avalanche photodiodes (APDs) in the barrel region and vacuum phototriodes (VPTs) in the endcap region. A preshower system is installed in front of the endcap ECAL for π^0 rejection. The ECAL is surrounded by a brass/scintillator sampling hadron calorimeter with coverage up to $|\eta| < 3.0$. The scintillation light is converted by wavelength-shifting (WLS) fibres embedded in the scintillator tiles and channelled to photodetectors via clear fibres. This light is detected by novel photodetectors (hybrid photodiodes, or HPDs) that can provide gain and operate in high axial magnetic fields. This central calorimetry is complemented by a "tail-catcher" in the barrel region – ensuring that hadronic showers are sampled with nearly 11 hadronic interaction lengths. Coverage up to a pseudorapidity of 5.0 is provided by an iron/quartz-fibre calorimeter (HF). The Cerenkov light emitted in the quartz fibres is detected by photomultipliers. The forward calorimeters ensure full geometric coverage for the measurement of the transverse energy in the event.

The overall dimensions of the CMS detector are a length of 21.6 m, a diameter of 14.6 m and a total weight of $12\,500$ tons. The thickness of the detector in radiation lengths (X_0) is greater than 25 X_0 for the ECAL, and the thickness in interaction lengths (λ_I) varies from 7–11λ_I for the HCAL depending on η.

2.1.1 Forward Detectors

The central detector of the CMS experiment has an acceptance in pseudorapidity η of roughly $|\eta| < 2.5$ for tracking information and $|\eta| < 5$ for calorimeter information. The coverage in the forward direction will be extended by two calorimeters on both sides of the interaction region which will cover higher $|\eta|$ values, called CASTOR ($5.3 < |\eta| < 6.6$) and the Zero Degree Calorimeter (ZDC). They are described in detail in Chapter 7 of the CMS Physics Technical Design Report [48].

CASTOR is an electromagnetic/hadronic calorimeter, azimuthally symmetric around the beam and divided into 16 sectors ($\phi = 22.5$ degrees). It is also longitudinally segmented into 14 sections, the so called Reading Units (RU), in order to observe and measure the propagation of hadronic cascades (showers) along its depth. The calorimeter is a Cherenkov-light device, consisting of successive layers of tungsten plates, as absorber, and fused silica (quartz) plates, as active medium. The CASTOR calorimeter comprises 2 electromagnetic samplings, each consisting of 5 pairs of 5 mm tungsten plates and 2 mm quartz plates and a hadronic part that has 12 samplings, each consisting of 5 pairs of 10 mm tungsten plates and 4 mm quartz plates. The total depth of the EM section is about 20 radiation lengths (X_0) and the total depth is 10.3 interaction lengths (λ_I). It is situated in the collar shielding at the very forward region of CMS, starting at 1437 cm from the interaction point.

The ZDC is compact, fast, highly radiation resistant and with good energy and time resolution; it has acceptance for neutral particles originating from the interaction point and is intended to tag nuclear break-up in ion collisions. Tungsten is used as an absorber and the signal consists of Cherenkov light emitted in quartz fibres. This is also the basis of the HF. A similar design has proved very robust at RHIC [49, 50]. The design requirements for the ZDC are: width < 9.6 cm, length < 100 cm; energy resolution sufficient to resolve the 1 neutron peak; very high radiation tolerance; low sensitivity to induced radioactivity; rate capability

above 50 kHz (for Ar-Ar collisions); vertex resolution through timing of few cm, i.e. $\sigma_t \approx$ 100 ps. To measure forward going neutrons the calorimeter needs to be located at the end of the straight section surrounding the interaction point between the 2 pipes containing the counter-circulating beams. In CMS this occurs 140 m from the vertex at the so-called "pair of pants." This area is inside the Neutral Beam Absorber device (TAN) which shields the superconducting magnets from synchrotron radiation produced by the beams.

2.2 The TOTEM Detectors

The TOTEM experimental apparatus [51], placed symmetrically with respect to the Interaction Point 5 (IP5) and the CMS experiment, is optimised to measure the total pp cross-section and study elastic scattering and diffractive processes at the LHC in dedicated, special-optics runs. Two tracking telescopes T1 and T2, at distances between 7.5 and 14 m (Fig. 2.1), will measure the inelastic interactions in the forward region covering an adequate acceptance over a rapidity interval of $3.1 \leq |\eta| \leq 6.5$. Leading protons scattered elastically or quasi-elastically will be detected by silicon detectors placed in Roman Pot stations at distances of 147 m and 220 m from IP5. For a later stage a third Roman Pot position has been reserved at 180 m. The beam of the LHC being rather thin, with a $10\,\sigma$ envelope of about 1 mm, the detectors in the Roman Pot must have a very small dead zone at the mechanical edge facing the beam.
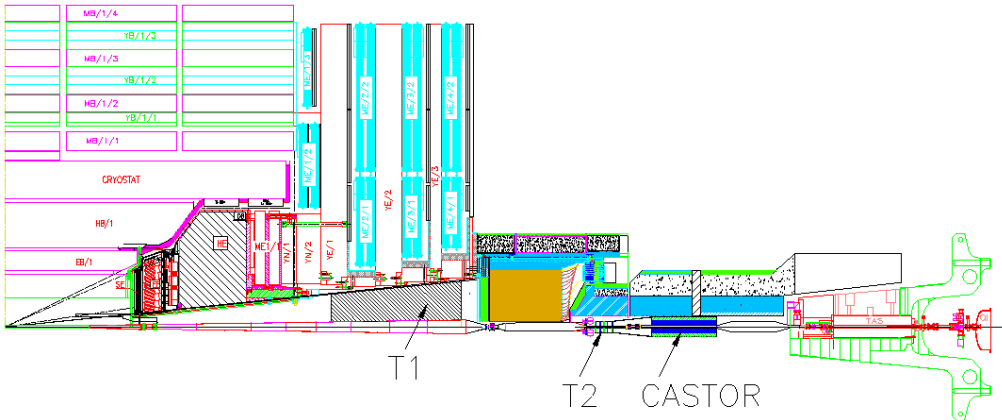
Figure 2.1: View of one quarter of the CMS detector with the TOTEM forward trackers T1 and T2. The CMS calorimeters, the solenoid and the muon chambers are visible. Note also the forward calorimeter CASTOR.

2.2.1 The Telescopes T1 and T2

At low luminosity, the T1 and T2 telescopes will provide a fully inclusive trigger for diffractive events and enable the reconstruction of the vertex of an event to disentangle beam-beam events from background. Each T1 arm will be installed in the End Caps of the CMS Magnet, covering the pseudorapidity range $3.1 < |\eta| < 4.7$, and will be composed of 5 planes of Cathode Strip Chambers (CSC) [52]. Each detector will measure three projections: one set of anode wires with a pitch of 3 mm measuring the radial coordinate and two sets of cathode strips with a pitch of 5 mm, rotated by $\pm 60^{\circ}$ with respect to the wires. The radial measurement will provide level-1 trigger information and will be used for vertex reconstruction in

order to suppress beam-gas background. Beam tests of final prototypes have shown a spatial resolution of 0.36 mm in the radial and 0.62 mm in the azimuthal coordinate.

For T2, which extends the acceptance into the range $5.2 < |\eta| < 6.5$, the Gas Electron Multiplier (GEM) technology [53], used successfully in COMPASS [54], has been chosen. GEMs are gas-filled detectors in which the charge amplification structure is decoupled from the charge collection and readout structure. Furthermore, they combine good spatial resolution with very high rate capability and a good resistance to radiation. The T2 telescope will be placed 13.5 m away from the IP5 and the GEMs employed will have an almost semicircular shape, with an inner radius matching the beam pipe. Each arm of T2 will have a set of 10 aligned detector planes mounted on each side of the vacuum pipe. To avoid efficiency losses, the angular coverage of each half plane is more than 180°. The read-out boards will have two separate layers with different patterns: one with 256 concentric circular strips, 80 μm wide and with a pitch of 400 μm, and the other with a matrix of pads varying in size from 2×2 mm^2 to 7×7 mm^2 (for a constant $\Delta\eta \times \Delta\phi = 0.06 \times 0.017\pi$). The pad information will also provide level-1 trigger information. Like the T1 chambers, the full size prototype GEM for T2 was successfully tested in 2004 at the X5 beam line.

With the above mentioned resolution for T1 and a resolution of $\sigma_R \cong 115\mu$m and $\sigma_\phi \cong$ 16 mrad for T2, Monte Carlo studies have shown the capability of reconstructing primary vertices well inside the beampipe with a resolution in the radial coordinate of $\sigma_{R_v} \cong 3$ mm within ± 5 cm from the IP5 along the beam axis. This vertex resolution is sufficient to discriminate beam-beam events from beam-gas background.

2.2.2 The Roman Pots

The Roman Pot detector system is optimised in view of measuring proton scattering angles down to a few μrad.

Each Roman Pot station (see Fig. 2.2 left) consists of two units separated by 4 m. Each unit has two vertical pots approaching the beam from the top and the bottom, and one lateral pot sensitive to forward protons. Furthermore, the overlap between the horizontal and the vertical pots (Fig. 2.2 right) will serve for measuring the relative distance of the vertical detectors. Each pot will contain 5+5 planes of Silicon detectors, their strips having orientations of ±45° with respect to the detector edge.

Given the challenging constraints of the LHC machine and the required physics performance of TOTEM, which needs to have active detectors at ∼1 mm from the 7 TeV beam, a special design has been developed [55]. A main issue has been the welding technology employed for the thin window that separates the vacuum of the machine and the Roman Pot – minimising the distance of the detector from the beam, with a thickness of less than 200 μm and a planarity better than 100 μm. A prototype of Roman Pot units with only the vertical pots has been successfully tested in the SPS ring with coasting beam in 2004 [56].

To detect leading protons in the Roman Pots two technologies of edgeless detectors have been retained: 1) planar Silicon detectors with a very narrow ($\sim 50\,\mu$m) current-terminating guard-ring structure (CTS) [57], and 2) planar Silicon detectors with active n$^+$ doped edges [58]. In both cases, the electrode pitch is 66 μm resulting in a spatial resolution of about 20 μm per plane.

The largest radiation, arising from diffractive protons, is on the edge (first few millimeters) of the horizontal detectors (see Fig. 4.4). It is about a factor 100 larger than on the vertical detectors. We estimated that the lifetime of these horizontal detectors is $\lesssim 1$ fb^{-1}. TOTEM is
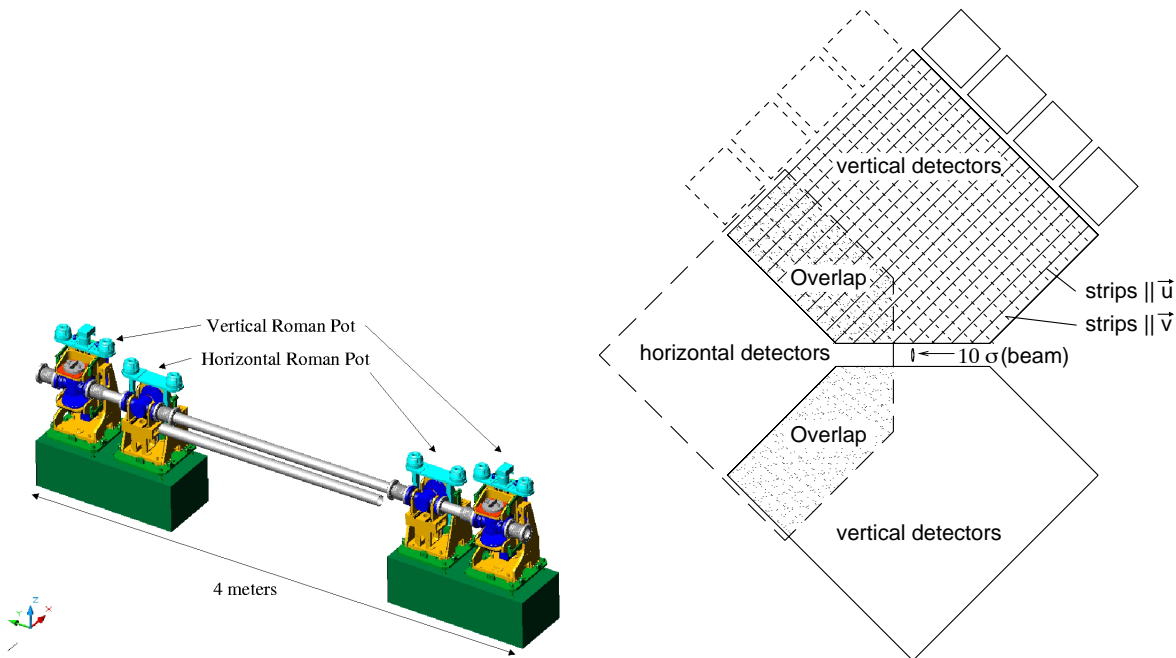
Figure 2.2: Left: Roman Pot station. Right: Arrangement of the detectors in the two vertical and the one horizontal Roman Pots of a station.

presently developing techniques which might increase in the future the above lifetime by a factor 10 [59].

In the planar edgeless detector the voltage applied to bias the device has to be applied also across the die cut via an implanted ring that runs along its physical edge. This external ring, called the current terminating ring, collects all the surface current from the cut avoiding its diffusion into the sensitive volume. Studies on samples irradiated up to 10^{14} "n"/cm^2 have shown that up to such fluences the radiation hardness of these planar edgeless detectors is equal to that of the standard planar detectors [57].

The 3D/planar edgeless detector instead exploits a new detector fabrication technique producing active edges by depositing doped polysilicon across the die cut. With this approach it has been shown in several measurements and test beams that the device is sensitive to within $10\,\mu$m from the physical edge [58].

Full-size detector prototypes have been successfully operated in the SPS test beams in 2004. The width of the efficiency transition from 10 % to 90 % was found to be around $50\,\mu$m.

The read-out of all TOTEM detectors will be based on the digital VFAT chips, enhancing the system uniformity from the point of view of the data processing chain.

The TOTEM triggers, combining information from the inelastic detectors and the silicon detectors in the Roman Pots can be incorporated into the general CMS trigger scheme, thus offering the ability to combine them with other CMS triggers. The digitisation of the TOTEM detectors and the data acquisition system are both fully compatible with the CMS DAQ thus enabling a common read-out of both detectors.

2.3 FP420

FP420 is a proposed magnetic spectrometer, consisting of detectors installed at ± 420 m from the interaction point [47]. The LHC magnets between the interaction point and the 420 m region bend out of the beam envelope protons that have lost a small fraction of their initial momentum. The FP420 detector consists of a system of moveable sensors which measure the spatial position as well as the arrival time of the outgoing protons at several points in a 10 m region around 420 m. A measurement of the displacement (and angle) of the outgoing protons relative to the beam allows the momentum loss and transverse momentum of the scattered protons to be reconstructed. The FP420 spectrometer is expected to operate with the standard high-luminosity LHC optics. It will have acceptance in the diffractive-peak region, $0.002 < \xi < 0.02$, giving access to central systems in the mass range $30 < M < 200\,\text{GeV}$ with an accuracy of a few GeV. This would complement and extend the reach of the TOTEM detectors, which cover $0.02 < \xi < 0.2$ in normal high-luminosity LHC running. A graphical representation of the expected coverage in ξ and t can be found in Fig. 3.4.

2.4 Running Scenarios

In this section we consider several operating conditions (running scenarios) for the LHC machine which provide different opportunities for diffractive physics in the common CMS/TOTEM program. These scenarios, summarised in Table 2.1, are mainly characterised by the betatron value β^* and the achievable luminosity [60].

Table 2.1: Diffractive Running Scenarios: k denotes the number of bunches; the stated luminosities assume a maximum of 10^{11} protons per bunch, except for scenario $\beta 05$ where lower proton densities are considered in the commissioning phase of the LHC.

Scenario	β^* [m]	k	$\mathcal{L}\,[\text{cm}^{-2}\,\text{s}^{-1}]$	Objectives
$\beta 05$	$0.55 - 2$	$936 - 2808$	$10^{32} - 2 \cdot 10^{33}$	hard diffraction
$\beta 18$	18	$936 - 2808$	10^{32}	hard diffraction
$\beta 90$	90	156	$3 \cdot 10^{30}$	(semi-) hard diffraction
$\beta 1540$	1540	156	$2 \cdot 10^{29}$	soft diffraction

The forward leading proton signature depends critically on the focusing scheme of the beams at the interaction point, i.e. the value of β^* which, in turn is related to the achievable luminosity. It is expected that the LHC will first be operated with reduced proton densities, reduced number of bunches and with betatron values corresponding to the injection optics or moderate values of $\beta^* = 2$ m [61]. With the maximum number of bunches at 43 to 156, the crossing angle will first be set to zero in order to reduce the risk of quenches in the superconducting magnets. Such conditions at moderate luminosities can be exploited for diffractive physics measurements. In particular the problem of multiple proton-proton interactions per bunch crossing (event pile-up) is reduced.

While the nominal LHC optics (β^*=0.55 m) and various low β^* optics developed for the run-in phase of the machine (β^*= 2 m etc) require the nominal "injection optics" β^*=18 m, the TOTEM optics ($\beta^* = 1540$ m [62]) requires a dedicated injection scheme and it is unlikely to be realised in the initial phase of the machine operation. An intermediate-β^* optics (90 m) [63] is therefore suggested that is based on the nominal injection scheme. In this scenario about 50% of the protons emerging from diffractive processes can be detected independently of their momentum loss, opening a wide range of measurements of diffractive events

for the CMS/TOTEM common program. The luminosity can be as high as $3 \cdot 10^{30}$ cm^{-2} s^{-1}, resulting in an integrated luminosity of 1 pb^{-1} in a few day run. Furthermore, the LHC luminosity and the total cross section can be measured in an early phase with a few per cent precision.

The nominal operation conditions for the first LHC phase are characterised by $\beta^* = 0.55$ and the maximum number of bunches $k = 2808$ with an increasing number of protons per bunch. For the measurement of hard diffractive processes and the search for new particles in exclusive central diffractive (CD) reactions, an integrated luminosity of $1 - 10$ fb^{-1} is required. This can be achieved with continuous running at luminosities of $10^{32} - 10^{33}$ cm^{-2} s^{-1} with low-β^* optics in one year of LHC operation. With low-β^* optics settings, diffractively scattered protons with a momentum loss larger than 2 % will be detected by RP stations at the $\pm$ 220 m location (see Chapter 3). The leading proton measurement can be extended by measuring rapidity gaps, provided the effect of pile-up events can be controlled.

Chapter 3

Measurement of Forward Protons

In this chapter, we describe the procedure, and its results, to determine the acceptance and momentum resolution for a proton leaving the interaction point with a given four-momentum.

To cover a maximal kinematic region in leading proton detection, several optics choices (see Sec. 2.4), complementary in their physics reach, have been analysed. We include results for the location of the TOTEM Roman Pot detectors at 220 m as well as for the 420 m location, where the FP420 R&D project considers installing detectors. Acceptance and resolution results for $\beta^* = 1540$ m and 90 m are used for the studies presented in Chapter 5, those for $\beta^* = 0.55$ m in Chapter 7. In some case studies are performed for $\beta^* = 2$ m which can be regarded as a good approximation of the $\beta^* = 0.55$ m case leading to similar results.

3.1   Principle of forward proton tracking

Protons emerging from diffractive scattering at LHC are characterised by their very small emission angles (10–150 μrad) and their small fractional longitudinal momentum loss ($\xi = \Delta p/p = 10^{-8} \div 0.1$). Hence they are very close to the beam and can only be detected in the RP downstream symmetrically on either side of the interaction point (IP) if their displacement at the detector location is sufficiently large to escape the beam halo.

The transverse displacement $(x(s), y(s))$[1] of a scattered proton at a distance s from the IP is related to its coordinates $(x^*, y^*, s = 0)$ and scattering angles $\Theta^*_{x,y}$ at the IP via the optical functions L^{eff}, v, D as:

$$
\begin{aligned}
y(s) &= v_y(s) \cdot y^* + L_y^{eff}(s) \cdot \Theta^*_y \\
x(s) &= v_x(s) \cdot x^* + L_x^{eff}(s) \cdot \Theta^*_x + \xi \cdot D(s)
\end{aligned}
\tag{3.1}
$$

where $v = \sqrt{\beta(s)/\beta^*} \cos \Delta\mu(s)$ is the magnification, $\mathrm{L}^{eff} = \sqrt{\beta(s)\beta^*} \sin \Delta\mu(s)$ the effective length, $\Delta\mu(s) = \int \frac{1}{\beta(s)} ds$ the phase advance and D the dispersion of the beam.

The optical functions $(L_{x,y}^{eff}(s), v_{x,y}(s), D(s))$ define the trajectory of a proton within the LHC lattice and depend on the initial coordinates of the produced particle at the IP. In order to optimise the kinematic range of forward proton detection, the LHC magnets can be powered in different ways to reach the optics conditions of Table 2.1.

---

[1] The reference system (x,y,s) defines the reference orbit in the accelerator; the s-axis is tangent to the orbit and positive in the beam direction; the two other axes are perpendicular to the reference orbit. The horizontal x-axis, in the bending plane, is negative toward the centre of the ring.

The proton acceptance in ξ, four-momentum transfer[2] t and azimuthal angle (ϕ) will depend on the choice of the LHC optics conditions.

In order to determine the acceptance, the protons are tracked through the accelerator lattice using the program MAD-X [64]. The transverse vertex position and the scattering angle at the IP are smeared assuming Gaussian distributions with widths given by the transverse beam size and the beam divergence, both determined by β^* and by the emittance ε (Table 3.1).

The minimum distance of a detector to the beam on one hand and constraints imposed by the beam pipe and beam screen size [65] on the other hand will determine the proton acceptance of a RP station. The detectors are assumed to be fully efficient at a distance from the beam which is proportional to the beam size $(10\sigma_{x(y)}(s))$ plus a constant (~ 0.5 mm) which takes into account the distance from the edge of the sensitive detector area to the bottom of the RP window.

As described in Chapter 2 the RP stations consist of detector doublets located at 145–149 m (RP150) and 216–220m (RP220) from the IP. For some studies, an additional detector doublet is considered at a distance of 420–430m (RP420).

Table 3.1: Parameters of the different optics settings at nominal emittance ε=3.75 μm·rad (ε=1 for β^*=1540). A beam energy spread of 10^{-4} is assumed.

β^* (m)	crossing angle (μrad)	IP offset in x (μm)	IP beam size (μm)	IP beam divergence (μrad)
1540	0.	0.	450	0.3
90	0.	0.	213	2.3
2	92	322	32	16
0.55	142	500	16	30

3.2   Acceptance

The design of the different optics (Table 2.1) is highly complementary:

- The high–β^* (1540 m) optics, optimised for very low t detection, is characterised by parallel-to-point focusing in both projections $[(x, s)$ and $(y, s)]$ at RP220 (i.e. $v_y \sim v_x \sim 0$), by a large $L_y^{eff}(220)$ and by a small beam divergence (0.3 μrad).

- The medium–β^* optics (90 m) is characterised by parallel-to-point focusing only in the vertical plane (y, s) at RP220, by a large $L_y^{eff}(220)$ and by a vanishing $L_x^{eff}(220)$: as a consequence, the horizontal displacement is proportional mainly to the momentum loss ξ and to the vertex.

- The nominal low-β^* (0.55÷2 m) optics is optimised for highest luminosities and not for forward proton detection, i.e. there are no particular settings at any detector location.

The main parameters of these optics are given in Table 3.1 and are used in the simulation. Figure 3.1 shows the hits distribution in the Si-detectors at RP220 for different scenarios.

The geometrical acceptance has been calculated for the following data samples:

---

[2]The Mandelstam variable t is defined as $t = (p_{\text{orig}} - p_{\text{scatt}})^2$, where $p_{\text{orig(scatt)}}$ is the four-momentum of the incoming (scattered) proton.
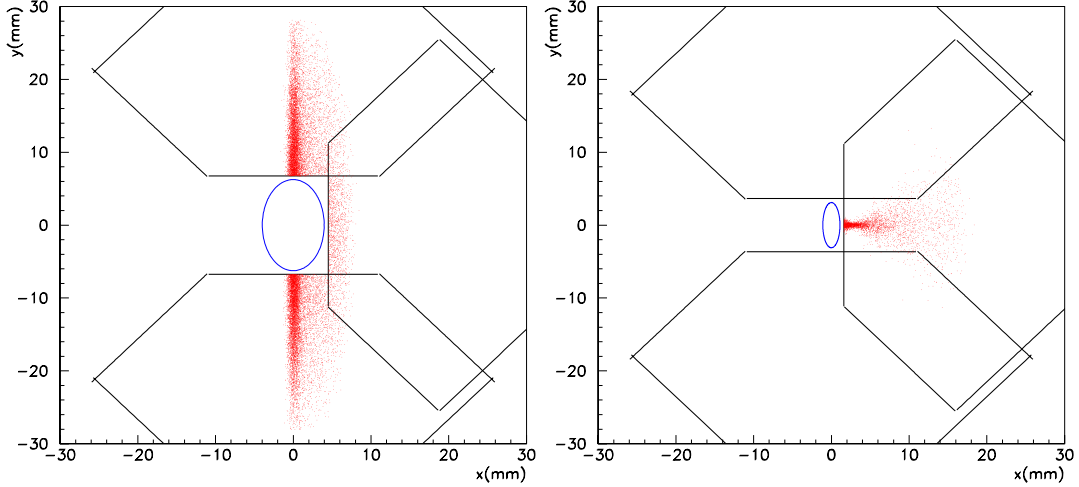
Figure 3.1: Hits distribution in the Si-detectors at RP220 for $\beta 90$ (left) and $\beta 05$ (right) scenarios.

1) a physics sample of protons from inclusive Double Pomeron Exchange was simulated with PHOJET [66] and later used for a complete physics study (Chapter 5). The protons are tracked along the beamline up to the RP220 station and a comparison of the acceptances, in the three scenarios mentioned above, is shown in the $\xi - t$ plane in Fig. 3.2 together with its projections (Fig. 3.3). In this case the nominal scenario chosen is β^*=2 m (early LHC scenario), which, from the point of view of the proton detection is very similar to the final optics β^*=0.55 m.

   In this scenario the protons only reach the horizontal detectors due to their momentum loss ξ (cf. Eq. 3.1), independently of the scattering angle. Hence just a small window in diffraction ($\xi >0.02$) can be seen.

   On the contrary, in the medium-(high-)β^* scenario protons are detected due to their scattering angle (cf. Eq. 3.1) mainly in the vertical detectors of the RP220 station. The acceptance starts at $|t|$ values as small as $3{\cdot}10^{-2}$ ($1{\cdot}10^{-3}$) GeV^2, almost independently of the proton momentum loss (ξ). This results in an acceptance of 50% (85%) for single protons from DPE events, averaged over all masses.

2) a physics process independent sample was generated with uniform distributions in the azimuthal angle ϕ, in Log(ξ) and in Log($-t$) in the kinematically allowed region of the ξ–t plane.[3] The protons are tracked along the beamline to the RP220 and RP420 stations, for the nominal scenario with β^*=0.55 m.
   Figure 3.4 show the acceptance in Log(ξ), Log($-t$) for RP220 and RP420 for the clockwise beam ("beam1"). The RP420 ξ-acceptance just overlaps with the acceptance at RP220 (Figure 3.5) but extends the ξ range down to $2{\cdot}10^{-3}$, which is important for the detection of centrally produced diffractive masses around 100 GeV.

---

[3]The scattering angle of the proton is physical when $t \geq t_0(\xi)$, where $t_0(\xi)$ is given by

$$t_0\left(\xi\right) = 2\left(P^2_{\text{orig}} + m^2_p\right)\left[\sqrt{1 + \left(P^2_{\text{orig}}\left[\xi^2 + 2\xi\right]\right)/\left(P^2_{\text{orig}} + m^2_p\right)} - 1\right] - 2\xi P^2_{\text{orig}}. \qquad (3.2)$$

More detailed about the acceptance calculation can be found in [67].
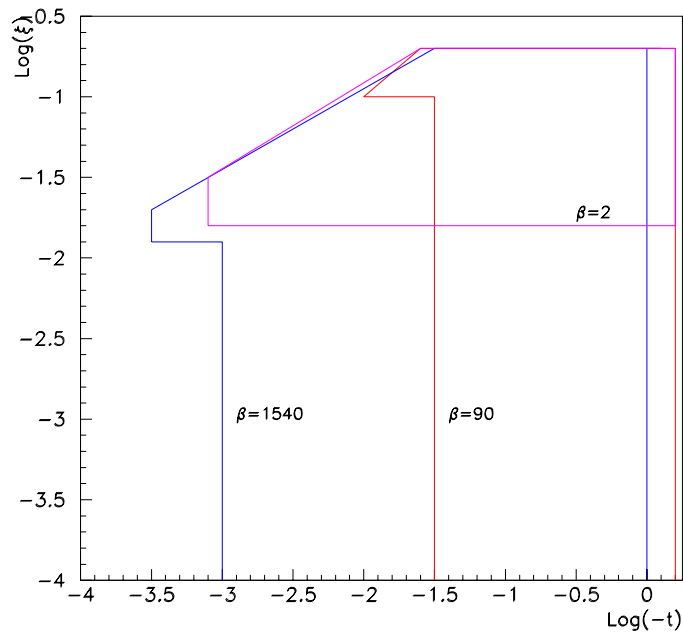
Figure 3.2: Log(ξ)-Log(-t) acceptance at different β^* at RP220 (the schematic contour plot refer to a minimum acceptance of 30%)
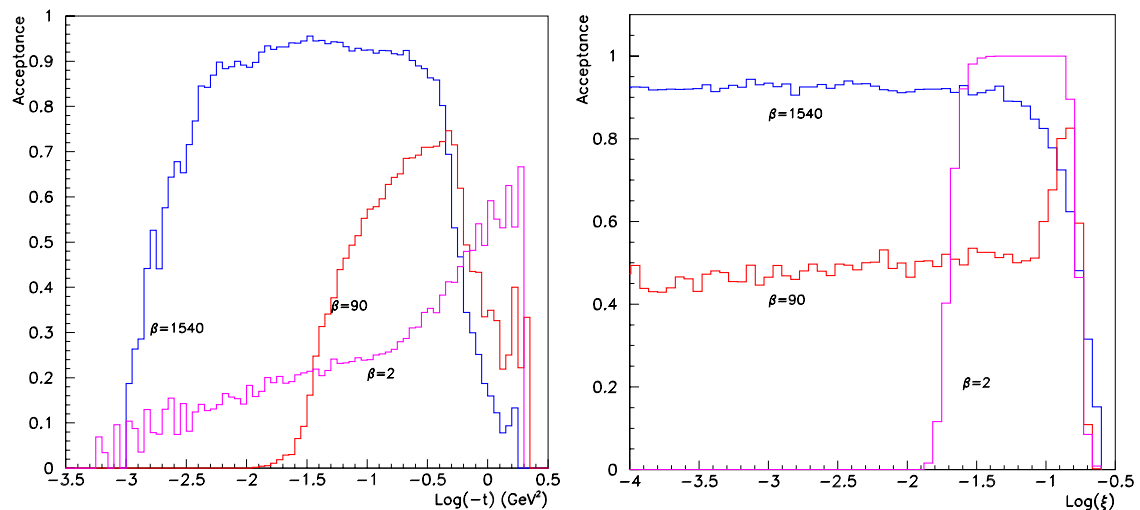
Figure 3.3: Single proton acceptance in Log(-t) (left) and Log(ξ) (right) at different β^* at RP220.
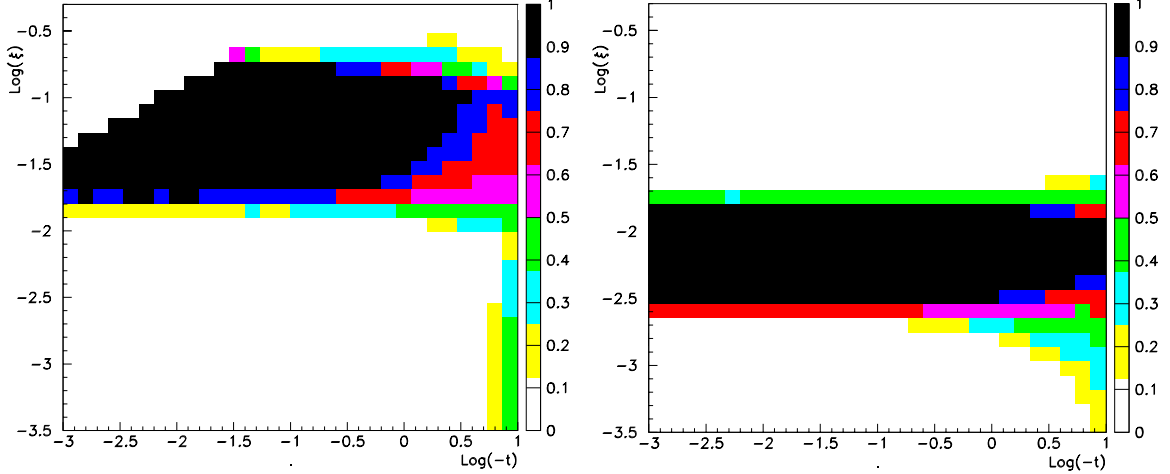
Figure 3.4: Log(ξ) vs Log($-t$) acceptance ($\beta 05$ scenario) [67] for beam1 at RP220 (left) and RP420 (right). The generated sample is described in the text.
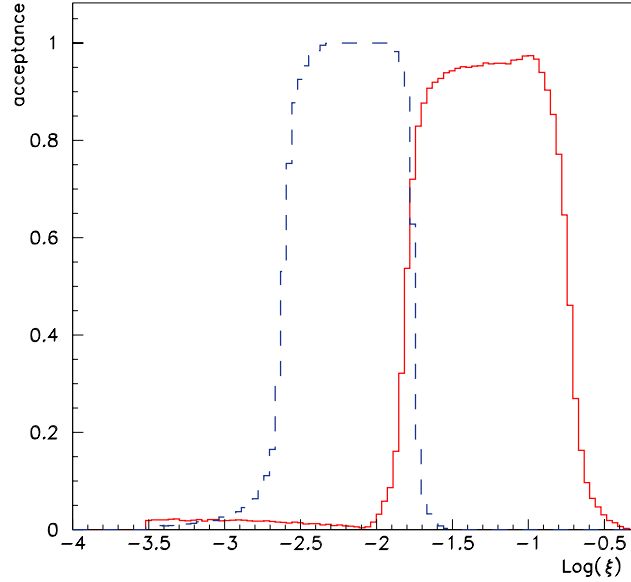
Figure 3.5: Log(ξ) acceptance ($\beta 05$ scenario) [67] for beam1 at RP220 (solid-red) and RP420 (dashed-blue).The generated sample is described in the text.

3.3 Proton Momentum Reconstruction

This section focuses on the systematic study of the precision of the momentum measurement of diffractively produced protons.

The final state protons are tracked along the beamline by MAD-X [64] with the beam related parameters as listed in Table 3.1 and the position and the angle are measured in the two sets of silicon detectors. From these two measurements, the initial parameters of the scattered protons ξ, $\Theta^*_{x,y}$ and $x^*(y^*)$ at the IP (see Eq. 3.1) can be deduced. As a consequence of the dispersion being mainly horizontal the ξ reconstruction only depends on the x-coordinate (Eq. 3.1).

A position reconstruction uncertainty is introduced by smearing the hit coordinates according to a Gaussian distribution with a σ of 10 μm per detector set.[4] The uncertainty of the beam position at the detector location is accounted for by smearing the hit coordinates by a correlated Gaussian distribution with a σ of 50 μm.

3.3.1 Nominal low–β^* Optics (β^*=0.55 m)

Since the runs in the nominal scenario will mainly focus on central diffraction, a sample of leading protons in exclusive diffractive processes ($p\,p \rightarrow p\,X\,p$) has been generated by two MC models (ExHuME [68], phojet [66]).

In the ξ-reconstruction procedure chosen, two x-measurements from a detector doublet are used to determine ξ and Θ_x^*, neglecting the x^* dependence, which will be treated as an independent source of uncertainty.

Each detector doublet yields two observables, the horizontal offset and angle with respect to the beam axis. The ξ dependence of these observables has been derived by fitting a functional form to the simulated average values of ξ, as a function of the values of these two observables [69].

The result is shown in Figure 3.6, where the relative resolution $\Delta\xi/\xi = (\xi - \xi_{rec})/\xi$ is plotted as a function of ξ in either RP220 or RP420 (protons circulating in the clockwise direction) [5]. Uncertainties due to the transverse vertex position, detector resolution, beam energy uncertainty and beam position at the detector location are shown separately. In both detector locations the main sources of uncertainty in the proton ξ resolution are the spread in transverse vertex position and detector resolution. In addition the uncertainty in the beam position at the detector location and the uncertainty on the beam energy also plays a significant role at the RP220 and the RP420, respectively.

The acceptance of the centrally produced mass, generated with the two Monte Carlo models, is shown in Figure 3.7 (left) for both leading protons detected at either $\pm$RP220 or $\pm$RP420. Separately shown is the case (sub-set of above) where both protons are within the acceptance of $\pm$RP420. The combinations of ξ-values building up the central masses as $M_X^2 \approx \xi_1\xi_2 s$, are due to the initial gluon (Pomeron) probability densities (pdf's). The ExHuME model tends to favour harder pdf's and yields, on the average, a more centrally produced diffractive system X, i.e. a higher acceptance.

The resolutions of the two leading protons are, in general, uncorrelated. The only source of correlation is due to their common origin at the IP, where the transverse position of the vertex point is determined by the r.m.s. spread of the beam ($\sigma_{beam}/\sqrt{2} = 11\mu m$). The vertex location will be independently measured by using the central tracking detectors [70]. In evaluating the central mass resolution, all other uncertainties of the two leading protons are assumed to be uncorrelated.

The mass resolutions for events with both protons within the acceptance of the $\pm$RP420, and for events with a combination of RP220 and RP420 on either side (labelled "asym." in the

---

[4]A detector set consists of five planes measuring each transverse coordinate: each plane provides a spatial resolution of 20μm. The assumption of a final resolution of 10μm is based on five independent measurements.This might not be true since the proton always hits the same strip in each plane due to its very small angle. Staggering of the individual planes to ensure independent measurements is under discussion.

[5]The ξ resolution of the protons circulating counter-clockwise is found to be similar to the clockwise one and therefore the same resolution is used for both directions.

figure) are shown as a function of the mass of the centrally produced system in Figure 3.7 (right). The values quoted in the figure are based on Gaussian fits to the reconstructed mass distributions. The two-proton acceptance requirement imposes a restriction on the allowed ξ_1–ξ_2 combinations; as a result the mass resolutions obtained with EXHUME and PHOJET are very similar.

If both protons are detected at the 220m location (not shown in the plot), the accepted mass of the central system is larger than 200 GeV and the relative resolution can be estimated to be around 2 %.

The results shown in [67] and in Section 3.3.1 have been included in FAMOS v1.4.0 [71] (CMS Fast Simulation) and have been used for the studies included in this document.

3.3.2 β^*=90 m Optics

As for the acceptance studies, the DPE events are generated with PHOJET [66] and the tracking follows the procedure described in Section 3.3.

With this optics setting, L_x has been forced to be close to zero at RP220. As a consequence the displacement of the proton with respect to the nominal beam axis in the horizontal coordinate mainly depends on the proton ξ and x^*-values (see Eq. 3.1). By using an independent measurement of the transverse coordinate of the vertex position at the IP, provided by the CMS central tracking detectors, a substantial improvement in leading proton measurement is achieved.

As in the case of low-β^* optics, the detector doublet yields two observables, the horizontal offset and the angle with respect to the beam axis (Figure 3.8). A ξ-surface is fitted in the plane spanned by the two above variables by using a set of unbiased input data generated without experimental uncertainties. To correct for the effects of a varying transverse position at the IP, a linear correction to the two variables is applied assuming that the transverse location of the vertex is measured by CMS with a precision of 30 μm.

It has been demonstrated [72] that the systematic uncertainty of the above ξ reconstruction method is small except for large ξ's ($\xi > 5$ %), where it becomes significant in comparison to the dominant experimental uncertainties.

The overall ξ resolution as shown in Fig. 3.9 is based on Gaussian fits to the distribution of the difference between the reconstructed and generated ξ. The uncertainties in the transverse vertex location, and in the beam position, dominate the overall resolution. The uncertainties in beam energy and angular divergence were also studied and found to be negligible in comparison. The overall resolution is about $1.6 \cdot 10^{-3}$ for low ξ values and decreases to about $1.2 \cdot 10^{-3}$ for ξ values about 5%.

The mass resolution of the centrally produced system, ($M_X^2 \approx \xi_{lower}\xi_{higher}s$), strongly depends on the ξ_{lower}–ξ_{higher} combination of the two outgoing protons, see Fig. 3.10.

The mass resolution is at its best (~ 15 GeV) for symmetric proton pairs ($\xi_{lo}/\xi_{hi} \approx 1$) and deteriorates ($\sim 60$ GeV) for processes in which the two protons are emitted with very different longitudinal momentum fractions ($\xi_{lo}/\xi_{hi} \leq 0.1$) .
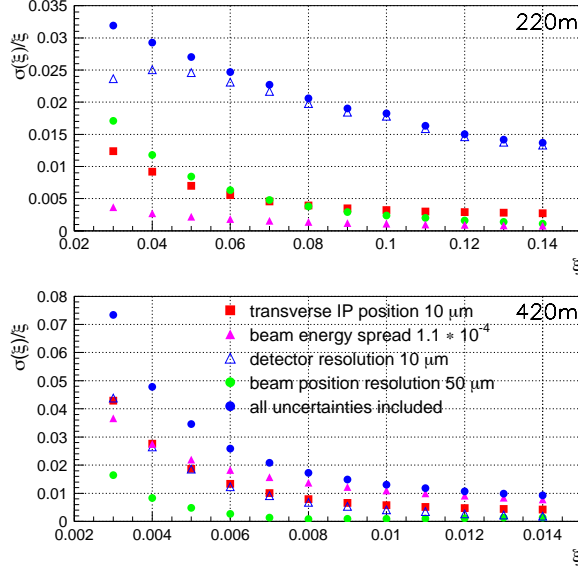
Figure 3.6: Summary of all effects studied contributing to the overall ξ resolution at RP220 (top) and RP420 (bottom) for the $\beta 05$ scenario. The t values of the protons used for each ξ bin is taken to be similar to the t distribution for central exclusive diffraction.
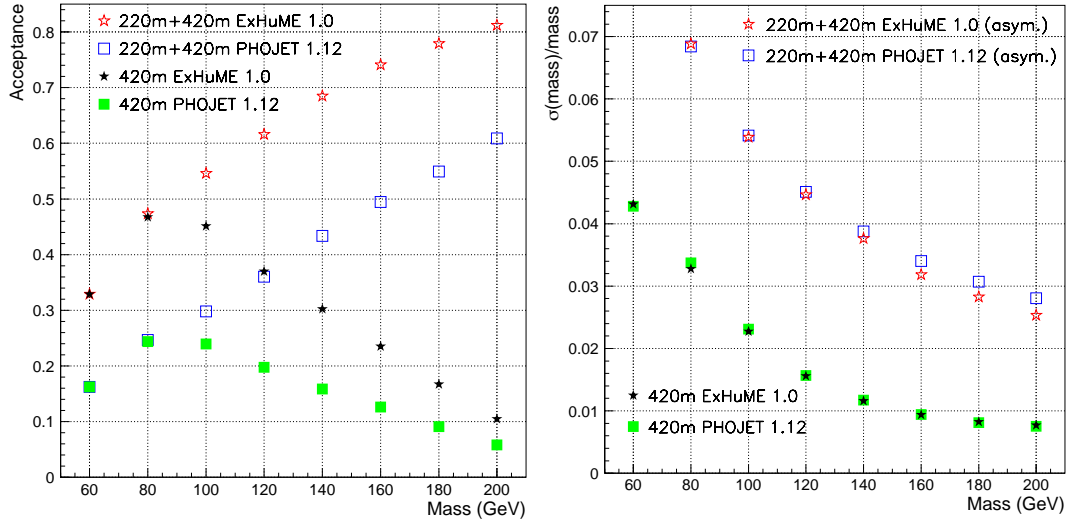
Figure 3.7: Left: Mass acceptance for events with protons within the acceptance of RP420 on each side of the IP ("420m"); and for events with protons within the combined acceptance of RP220 and RP420 on each side of the interaction point ("220m+420m"). Right: Mass resolution for events with protons within the acceptance of RP420 on each side of the IP ("420m"); and for events with one proton within the acceptance of RP220 on one side of the IP and the other proton within the acceptance of RP420 on the other side ("220m+420m (asym.)"). EXHUME or PHOJET denotes the generator used for producing the central exclusive diffractive events. Both plots refer to the $\beta 05$ scenario.
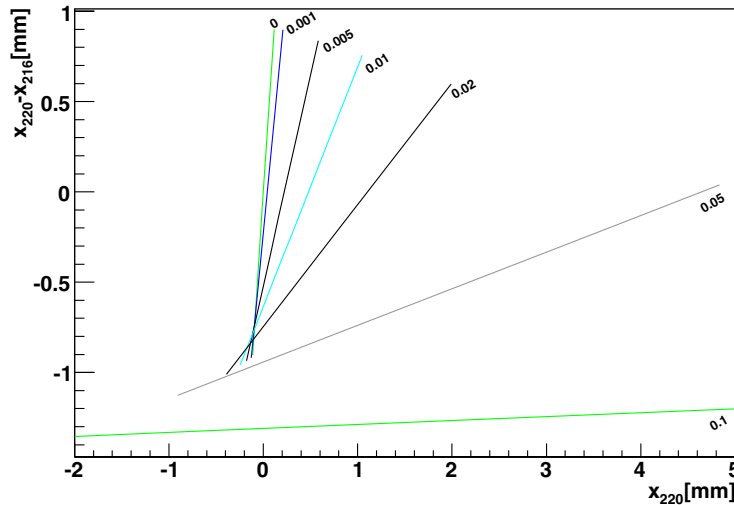
Figure 3.8: The difference of the horizontal offsets at 220 m and 216 m as function of the horizontal offset at 220 m for the $\beta^* = 90$ m optics for protons with a few fixed ξ values. The variation along the constant ξ lines is due to different horizontal scattering angle at the IP for the protons.
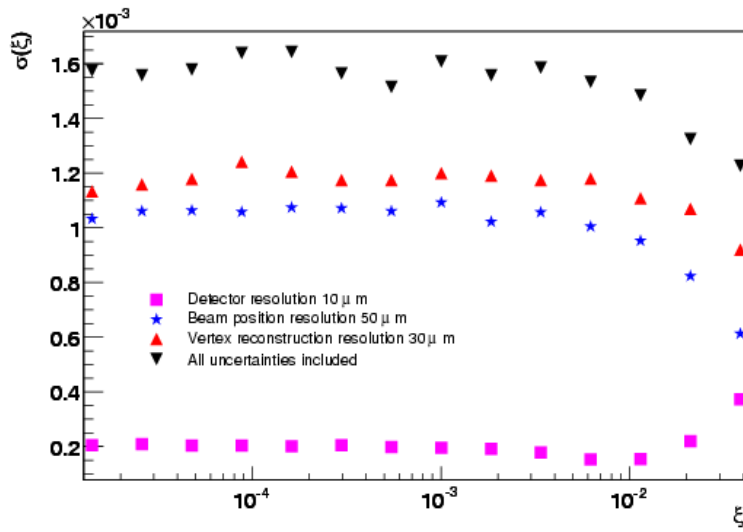
Figure 3.9: Summary of the uncertainties contributing to the overall ξ resolution at RP220 for the $\beta 90$ scenario as a function of ξ. The t-values assumed for the protons for each ξ bin correspond to the t-distribution expected from DPE.
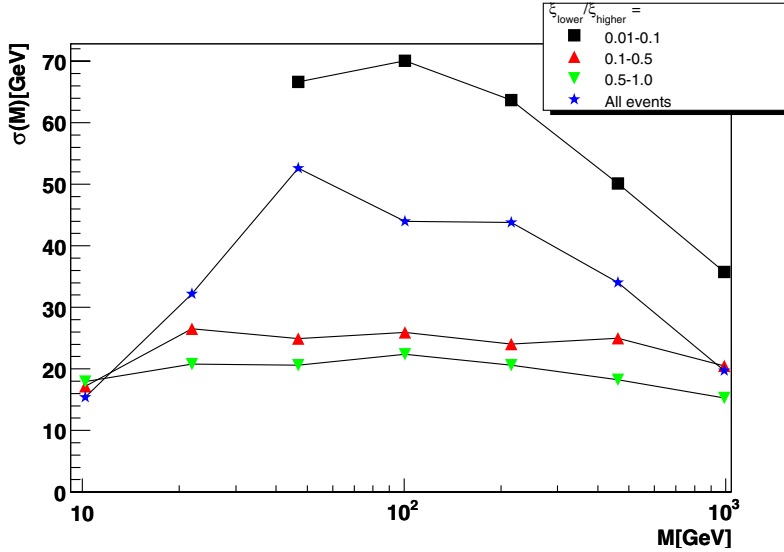
Figure 3.10: Mass resolution as a function of mass for DPE events for different ranges of the ratio of the two outgoing protons momentum loss ($\beta 90$, RP220).

3.3.3 β^*=1540 m Optics

The reconstruction procedure described in this section aims at the determination of the kinematics parameters $\Theta_{x,y}$, ξ of the proton. Since the large beam size at the IP, as characteristic of the β^*=1540 m optics, does not allow one to neglect the vertex contribution, we then consider (x^*, y^*) (see Eq. (3.1)) as additional free variables. To reconstruct the full parameter vectors

$$\vec{\Xi}_x \equiv \begin{pmatrix} \Theta_x \\ \xi \\ x^* \end{pmatrix} \text{ and } \vec{\Xi}_y \equiv \begin{pmatrix} \Theta_y \\ y^* \end{pmatrix} \tag{3.3}$$

of a given proton, at least three position measurements are needed. For this purpose, the two RP stations located at 145 m and 220 m are used, providing four measurements.

By means of a parametrisation of the optical functions [73], Eq. (3.1) can be written as:

$$\vec{x} = H_x(\vec{\Xi}_x)\,\vec{\Xi}_x + \delta\vec{x}\,, \tag{3.4}$$

$$\vec{y} = H_y(\vec{\Xi}_x, \vec{\Xi}_y)\,\vec{\Xi}_y + \delta\vec{y}\,, \tag{3.5}$$

where $\vec{x}$ ($\vec{y}$) is the vector of x- (y-) measurements x_i (y_i) at the position z_i. The transport matrices are given by

$$H_x(\vec{\Xi}_x) = \left(\vec{L}_x(\xi),\ \vec{D}(\Theta_x, \xi, x^*),\ \vec{v}_x(\xi)\right) \text{ and } \tag{3.6}$$

$$H_y(\vec{\Xi}_x, \vec{\Xi}_y) = \left(\vec{L}_y(\xi),\ \vec{v}_y(\xi)\right)\,, \tag{3.7}$$

where the vectors $\vec{L}_x$ etc. contain the optical functions at the measurement positions z_i. H_x and H_y depend on the kinematics, introducing non-linearity to the problem. The shifts $\delta\vec{x}$ and $\delta\vec{y}$ are caused by the finite measurement resolution. Additional smearing is caused by the beam energy uncertainty and the angular divergence as given in Table 3.1.

The knowledge of the beam width σ_{beam} at the vertex provides an additional constraint. The unbiased estimate $x_0 \equiv \hat{x}^* = 0$ with the (big) uncertainty given by the interaction width

$\sigma(x_0) = \sigma_{beam}/\sqrt{2} = 0.45\,\mathrm{mm}/\sqrt{2} = 0.32\,\mathrm{mm}$ (and analogously for y_0) can play the role of a measurement contributing another row to each of the matrix equations (3.4) and (3.5) with optical parameters $L_{x0} = L_{y0} = 0$, $D_0 = 0$, $v_{x0} = v_{y0} = 1$.

The reconstruction task consists in solving Eqs. (3.4) and (3.5) for $\vec{\Xi}_x$ and $\vec{\Xi}_y$. Without the dependence of the optical functions on the kinematics, this could be achieved analytically. The non-linearity was taken into account by minimising

$$\chi^2 = \sum_i \frac{\left(x_i - [H_x(\vec{\Xi}_x)\,\vec{\Xi}_x]_i\right)^2}{\sigma_{xi}^2} + \sum_i \frac{\left(y_i - [H_y(\vec{\Xi}_x, \vec{\Xi}_y)\,\vec{\Xi}_y]_i\right)^2}{\sigma_{yi}^2} \tag{3.8}$$

Single-Arm Reconstruction (for Single Diffraction)   The reconstruction of single arm protons has been evaluated using the units at 145 m, 149 m, 216 m and 220 m. In this case the tracks are measured before and after the dipole D2 which thus acts as a spectrometer, improving the resolution significantly as compared to the approach using only the RPs at 216 m and 220 m [74]. The drawback of requiring hits in all four RP units is the reduced acceptance in t. The overlapping acceptance of the two stations covers the range $0.02 < |t| < 1.2\,\mathrm{GeV}^2$ (at $\xi = 0$).

The resolution studies presented here were based on protons from 10000 DPE events generated with PHOJET and tracked through the machine with MAD-X. Only one arm was used for this study. The vertex positions, beam angles and momenta were distributed according to Table 3.1. Furthermore, the ideal hit positions in the detectors, as obtained from the simulation, were smeared with the detector resolution of 20 μm.[6] Then the reconstruction was done with a fit as described above, using the optics parameterisation. The resolutions in ξ and t were defined as the standard deviations of the distributions $\xi - \xi_{true}$ and $t - t_{true}$, respectively. They are shown in Fig. 3.11. For all the other kinematic variables see [74]. The difference in resolution between the horizontal directions $\phi = 0$ and π stems from the dependence of the dispersion on Θ_x.

The deterioration of the resolution at $\xi > 1\,\%$ is mainly due to the worse accuracy of the optics parameterisation in this parameter region. The distributions of parameter deviation $\xi - \xi_{true}$ or $t - t_{true}$ often have biases and strongly non-gaussian shapes whose widths cannot be sufficiently described by the standard deviations.

For comparison, a reference study was performed where the events were generated and reconstructed with the same optics parameterisation. In that ideal case, where the optics are perfectly known, a better resolution is obtained [74].

Double-Arm Reconstruction (for DPE)   Since both protons in a DPE event come from the same vertex (x^*, y^*) it is advantageous to reconstruct them both in a combined fit rather than separately. Indeed, the resolutions for combined double-arm reconstruction are better than for single-arm reconstruction.

The results from a reconstruction test based on simulated DPE events with protons tracked through the machine are shown in Fig. 3.12. For each proton, detector acceptance was required. The parameter space studied was defined by the diffractive mass M and the ratio between the lower and the higher ξ-value (leading and non-leading, respectively) of the two protons characterising the degree of momentum symmetry of the event. The other parameters, i.e. the t- and ϕ-values were averaged.

---

[6]Refer to the footnote at page 30.
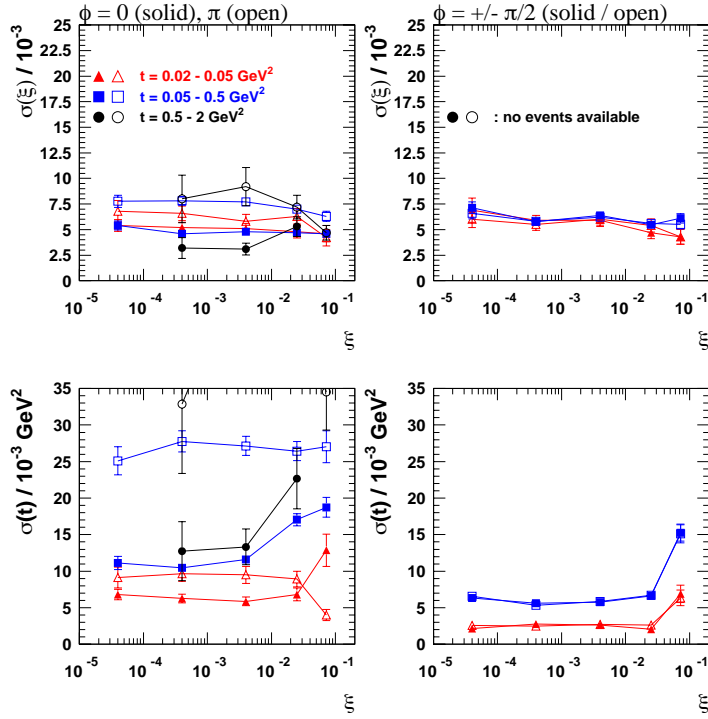
Figure 3.11: ξ and t resolution with tracked protons as a function of ξ for different t and azimuthal angles: $\phi = 0, \pi$ (left-hand plots), i.e. horizontal, and $\phi = \pm\pi/2$ (right-hand plots), i.e. vertical.
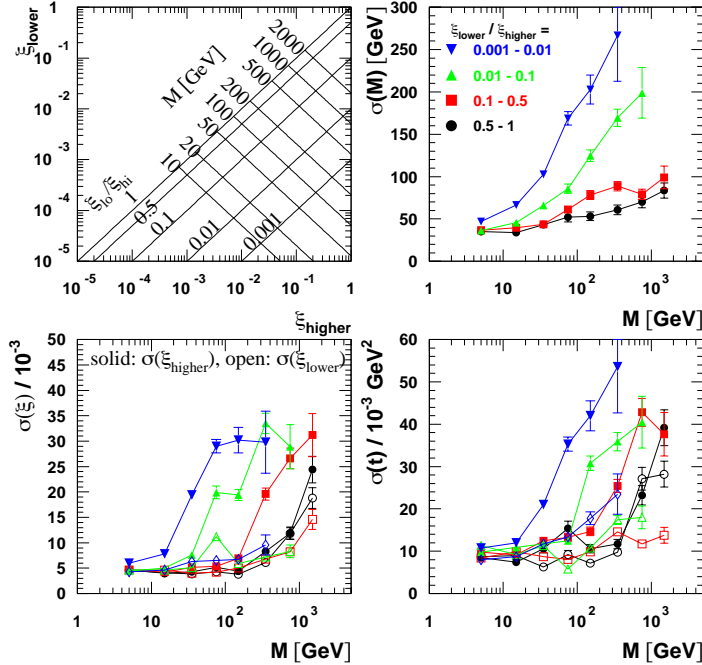
Figure 3.12: Resolution study for double-arm reconstruction of DPE events. Upper left: binning scheme for the other plots. Upper right: mass resolution for different ξ-ratios of the two protons. Lower left: ξ-resolution. Lower right: t-resolution.

Chapter 4

Machine induced background

The studies of machine-induced background rely on complex simulations taking into account the detailed machine geometry, collimation scheme, beam optics and bunch structure. Since most of these simulations or their analyses are still in progress, this document can only reflect the present understanding.

In the following sections, the backgrounds will be discussed first for the TOTEM inelastic telescopes and then for the Roman Pot stations.

4.1 Background in T1, T2

The background in the inelastic detectors T1 and T2 is mainly given by beam-gas interactions. There is also a component from the muon halo which is expected to be small but has not been evaluated quantitatively up to now.

The beam-gas interaction rate is calculated from the rest-gas densities ρ_i and the cross-section σ_i of proton-gas-molecule collisions as given in Table 4.1. For each of the two beams the rate per unit ring length is

$$dR/dl = \frac{k\,N\,c}{l_{LHC}} \sum_i \sigma_i\,\rho_i \,, \tag{4.1}$$

where $l_{LHC} = 26.7\,\text{km}$ is the length of the LHC ring.

Table 4.1: Nuclear proton-gas-molecule scattering cross-sections [75] and residual gas densities in IP5 [76] for $k = 156$ and $k = 2808$ bunches with N=1.15 $\times 10^{11}$ protons.

Gas	σ [mb]	ρ [molecules / m^3]	
	σ	$k = 156$	$k = 2808$
H_2	94	1.2×10^{11}	5.5×10^{11}
CH_4	568	1.2×10^{10}	2.8×10^{10}
CO	840	3.4×10^{8}	5.9×10^{10}
CO_2	1300	4.2×10^{8}	1.6×10^{11}

The ring segment to be considered for the production of beam-gas showers extends for each beam from the aperture-limiting upstream TAS at -20 m to the downstream T1 or T2 chamber, i.e. at most up to +14 m. This corresponds to a maximum segment length of 34 m. The results for different bunching parameters N and k are given in Table 4.2.

To obtain the T1/T2 trigger rates, the numbers given in Table 4.2 have to be modified by the T1/T2 probabilities for misidentifying beam-gas events as given in the TOTEM TDR [51]

Table 4.2: Beam-gas interaction rate for one beam per unit LHC ring length and integrated over the segment from the upstream TAS to the downstream T2 chamber.

Scenario	dR/dl [Hz / m]	$R_{TAS\,to\,T2}$ [Hz]	$\frac{R_{TAS\,to\,T2}}{k\,f_{LHC}}$ [per bunch]
$\beta^* = 1540\,\mathrm{m}$, $k = 156$, $N = 7.4 \times 10^{10}$, $L = 10^{29}\,\mathrm{cm^{-2}\,s^{-1}}$	0.26	8.8	5.0×10^{-6}
$\beta^* = 90\,\mathrm{m}$, $k = 156$, $N = 5.7 \times 10^{10}$, $L = 10^{30}\,\mathrm{cm^{-2}\,s^{-1}}$	0.20	6.8	3.9×10^{-6}
$\beta^* = 0.5\,\mathrm{m}$, $k = 2808$, $N = 4.0 \times 10^{10}$, $L = 10^{33}\,\mathrm{cm^{-2}\,s^{-1}}$	41	1395	44×10^{-6}

(Chapter 8.3). A rough calculation yields an average suppression factor of 0.6.

4.2   Background in the Roman Pots

The proton measurements in the Roman Pots are subject to three kinds of machine-induced background:

- The beam halo consists of beam protons that were lost from their design orbits and were not caught by the collimation system. These protons have very small angles and are thus indistinguishable from elastic or diffractive signal protons – at least at the level of one arm of the experiment. This background is reduced by requiring a coincidence between one Roman Pot arm and either the other Roman Pot arm or certain signatures in the central detectors.

- The beam-gas background consists of shower particles created by collisions between protons and gas molecules. Depending on the distance between the collision and the Roman Pot, the shower's angular distribution is wider or narrower. Suppression techniques for this background include cuts on the track angles and multiplicities.

- The p-p background is caused by generic inelastic proton-proton collisions in the IP5 producing a great number of particles dominantly in the forward direction. Some of these particles can travel as far as the RP station at 220 m and even further. On their way along the beam line they collide with machine elements creating secondary showers with randomised energies and track angles. Suppression relies on the same cuts as for beam-gas background.

4.2.1   Beam-Halo Background

Simulations of the collimation inefficiencies [77] have produced two-dimensional beam-halo profiles at various positions along the LHC ring, in particular at the RP stations at 150 m and 220 m. This is a refinement of earlier studies (used for estimates in [51]), where the halo profile was averaged over the ring. The quantity determined by the simulation is the probability $P_{hori(vert)}(x_n, y_n)$ to find a proton in the halo at the transverse position $(x_n, y_n) \equiv (x/\sigma_x, y/\sigma_y)$ (normalised by the beam widths along x and y at the Roman Pot) under the condition that it was lost from its design orbit, distinguishing horizontal and vertical losses. So far, the refined simulation results are only available for the optics with $\beta^* = 0.5\,\mathrm{m}$. However, the older simulations done for both $\beta^* = 0.5\,\mathrm{m}$ and 1540 m showed very little dependence of

$P(x_n, y_n)$ on the optics. Hence – while waiting for specific simulations for the other optics – the distributions from $\beta^* = 0.5$ m are used for all running scenarios, taking into account the different beam currents and the different detector-beam distances x_{min}/σ_x and y_{min}/σ_y. The profiles at 220 m are shown in Figure 4.1.

To obtain the total halo rate at a point (x_n, y_n), the horizontal and the vertical components have to be weighted by their loss rates:

$$f_{halo}(x_n, y_n) = f_{loss,\, hori} \, P_{hori}(x_n, y_n) + f_{loss,\, vert} \, P_{vert}(x_n, y_n) \quad . \tag{4.2}$$

The loss rates are determined by the beam lifetime contributions from different loss mechanisms (mainly elastic beam-gas collisions and intra-beam scattering):

$$f_{loss,\, hori} = \frac{k \, N}{\tau_{hori}} \, , \quad f_{loss,\, vert} = \frac{k \, N}{\tau_{vert}} \, , \tag{4.3}$$

with

$$\tau_{hori/vert}^{-1} = \sum_{\text{loss mechanism } i} \tau_{i,hori/vert}^{-1} \tag{4.4}$$

The differences between horizontal and vertical lifetimes are difficult to estimate. In all the following calculations, the estimate $\tau_{hori} \approx \tau_{vert}$ and $\tau_{tot} \approx 34$ h will be used, together with the average probability $P(x_n, y_n) = \frac{1}{2}[P_{hori}(x_n, y_n) + P_{vert}(x_n, y_n)]$.
The probability

$$P(\text{halo hit}) = \int_{detector} dx_n \, dy_n \, P(x_n, y_n) \tag{4.5}$$

for a lost proton to hit a Roman Pot detector was evaluated using the simulated halo protons together with the precise detector positions and geometries. The results are listed in Table 4.3 for the Roman Pot station 220 m.
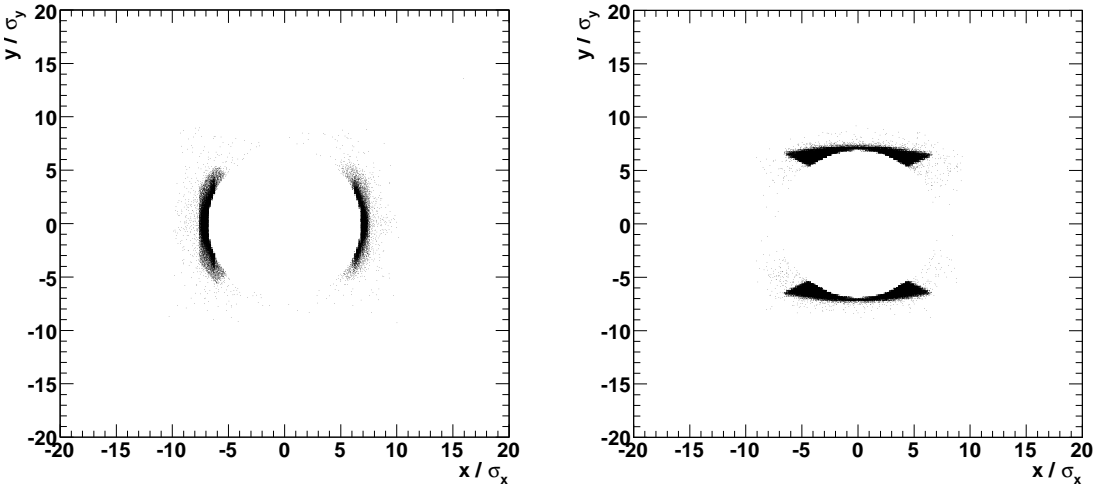
Figure 4.1: Beam-halo profiles for $\beta^* = 0.5$ m at 220 m for horizontal and vertical proton losses. The coordinates are normalised by the beam width.

Furthermore, $P(\text{halo hit})$ was evaluated as a function of $d/\sigma_{x(y)}$, the detector distance from the beam normalised to the beam width. The result given in Figure 4.2 shows that above $\sim 11\,\sigma$ the halo hit probability is of the order 10^{-6} and not very sensitive to the detector position.

Table 4.3: Halo at 220 m: Loss rates, halo hit probabilities $P(\text{halo hit})$ and halo rates (single arm) for the following detector configurations: the one horizontal detector of a RP unit; any one of the 2 vertical detectors; overlap areas between the horizontal and the vertical detectors.

		Scenario		
β^* [m]		1540	90	0.5
k		156	156	2808
$N/10^{10}$		7.4	5.7	4.0
$\mathcal{L}$ [cm^{-2} s^{-1}]		10^{29}	10^{30}	10^{33}
f_{loss} [MHz]		94	73	918
hori. det.:	x_{min}/σ_x	23.0	11.1	16.9
	$P(\text{halo hit})$ [10^{-6}]	1.40 ± 0.57	1.52 ± 0.59	1.40 ± 0.57
	f_{halo} [Hz]	132	111	1285
	[10^{-5} / bunch]	7.5	6.3	4.2
2 vert. det.:	y_{min}/σ_y	16.6	10.9	10.9
	$P(\text{halo hit})$ [10^{-6}]	0.36 ± 0.29	0.82 ± 0.43	0.82 ± 0.43
	f_{halo} [Hz]	34	60	753
	[10^{-5} / bunch]	1.9	3.4	2.4
overlap:				
	$P(\text{halo hit})$ [10^{-6}]	0.24 ± 0.23	0.59 ± 0.37	0.47 ± 0.33
	f_{halo} [Hz]	22	43	431
	[10^{-5} / bunch]	1.3	2.5	1.4

4.2.2 Beam-Gas Background

A detailed simulation of beam-gas background has been performed only for the RP station at 220 m and a running scenario with the $\beta^* = 1540$ m optics and a bunch structure with $k = 156$, $N = 1.15 \times 10^{11}$. The simulation method is explained in [78]. In a nutshell, beam-gas collisions are generated along beam 1 in the range between the TAS upstream of IP5 and the Roman Pot station at 220 m downstream of IP5 (see Figure 4.3). More distant events, i.e. upstream of the TAS, are neglected considering that the TAS acts as the dominant aperture limitation.

The particles generated in a collision are weighted with a probability taking into account the rest-gas density map [76]. Then each particle is tracked along the ring creating secondary showers with a certain probability whenever machine elements are hit. In the same way, all daughter particles are tracked until a scoring plane at $s = 220$ m is reached. There, all arriving particles are recorded with their identity, energy, transverse position, track angles and statistical weights from which hit rates in the 220 m RP unit are obtained. The angular information is exploited to perform cuts on the track angle in two stages (see Table 4.4). First, a simple coincidence between the detector planes in the 216 m and the 220 m RP unit is required, which already reduces the trigger rate, in particular for electrons/positrons and gammas whose angular distributions are very broad. Then the angular selection is refined by imposing a trigger-road as described in the inset of Figure 4.3. In practice, the trigger rates will be further reduced by multiplicity cuts on the number of hits per detector plane and finally on the number of accepted track candidates. However, since the simulation at hand does not contain any information on the time structure or correlations of the arriving particles, such cuts have not been studied yet.
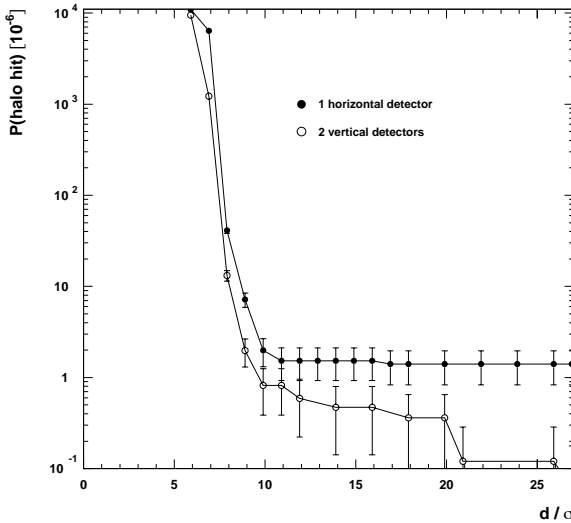
Figure 4.2: Halo hit probability per lost proton for the horizontal and the vertical detectors in the RP station at 220 m, evaluated for $\beta^* = 0.5$ m and not expected to depend strongly on the optics until availability of more simulation results. To obtain the halo hit rate, these numbers have to be multiplied by f_{loss} in Table 4.3.
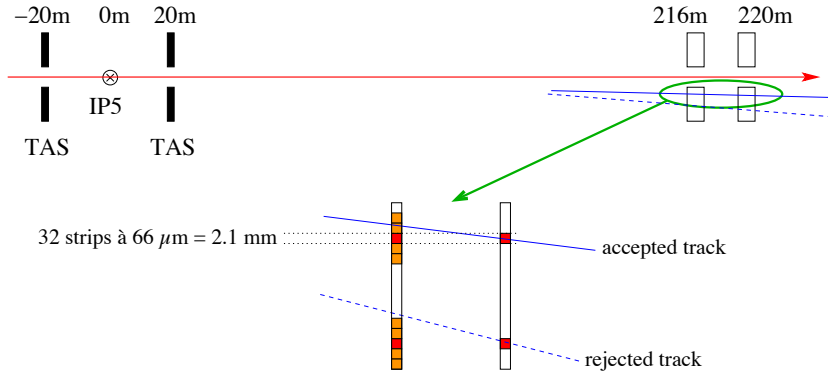
Figure 4.3: Schematic sketch of the LHC section included in the beam-gas background simulation (not to scale). The inset describes the angular selection with trigger roads: For each hit in a given 2.1 mm strip group at 220 m, a hit at 216 m is required either in the same strip or in one of the first or second neighbours. This criterion is applied to both projections u and v of the detectors.

To obtain the final hit rates for neutral particles (neutrons and photons), an energy-dependent detection efficiency has been estimated based on the probability of interaction in the detector silicon or in the window material (stainless steel) with creation of charged secondary particles mimicking tracks [79]. This leads to a strong suppression.

Rates for other running conditions can be obtained by scaling with the beam current $\propto k\,N$. A comparison is shown in Table 4.5.

Table 4.4: Single-arm beam-gas event rate evolution for $k = 156$ and $N = 7.4 \times 10^{10}$ (scaled from the original results for $N = 1.15 \times 10^{11}$) with angular cuts and – last column – with inclusion of an estimated detection efficiency for the neutral particles. The rates given have been integrated over the 2 vertical and 1 horizontal detector of a RP unit, without double-counting of the overlap zone.

Particle	Rate [Hz]			
	RP 220	RP 216 x RP 220	within trigger road	with det. effic.
p	221	198	195	195
n	112	84	83	0.3
π^+	396	308	248	248
π^-	261	186	142	142
e^+	2979	48	14	14
e^-	2163	79	9	9
γ	60950	6544	2510	174
Sum	67082	7447	3201	782.3

Table 4.5: Total single-arm beam-gas rates at 220 m.

		Scenario		
β^* [m]		1540	90	0.5
k		156	156	2808
$N/10^{10}$		7.4	5.7	4.0
$\mathcal{L}$ [cm^{-2} s^{-1}]		10^{29}	10^{30}	10^{33}
without cuts:	f_{b-g} [kHz]	67	52	653
	[10^{-4} / bunch]	382	295	207
with cuts:	f_{b-g} [kHz]	0.78	0.60	7.6
	[10^{-4} / bunch]	4.5	3.4	2.4

4.2.3 Background from pp Collisions in the IP

At present, only very approximate estimates about pp-induced background at the RPs are available. Recently, a new detailed simulation has been done [80] but the analysis of the effectiveness of RP trigger algorithms is still in progress.

The present numbers are based on an older study [81] for $\beta^* = 0.5$ m, $k = 2808$ and $N = 0.4 \times 10^{11}$ (leading to $L = 10^{33}$ cm^{-2} s^{-1}), where beam-gas and pp-induced backgrounds were treated together. At each of the RP stations at 150 m and 220 m the particle fluxes for charged hadrons, neutrons, electrons and photons are available, averaged over the area of the silicon detectors. In addition, it was noted that at the given running conditions a fraction between 0.001 and 0.01 of the background is caused by beam-gas interactions. This information allows us to isolate the pp-induced component (Table 4.6).

The charged hadron contribution to the horizontal RP contains diffractive protons which belong to the signal and hence have to be subtracted from the background rates. In the hadronic flux map at 220 m (Figure 4.4), a peak due to diffractive protons can be identified at $|y| < 3$ mm and approximately subtracted. This yields a remaining background rate of about 4 MHz or a diffractive proton rate of 2 MHz.

Since no distributions of particle energies or track angles are provided, the evaluation of the
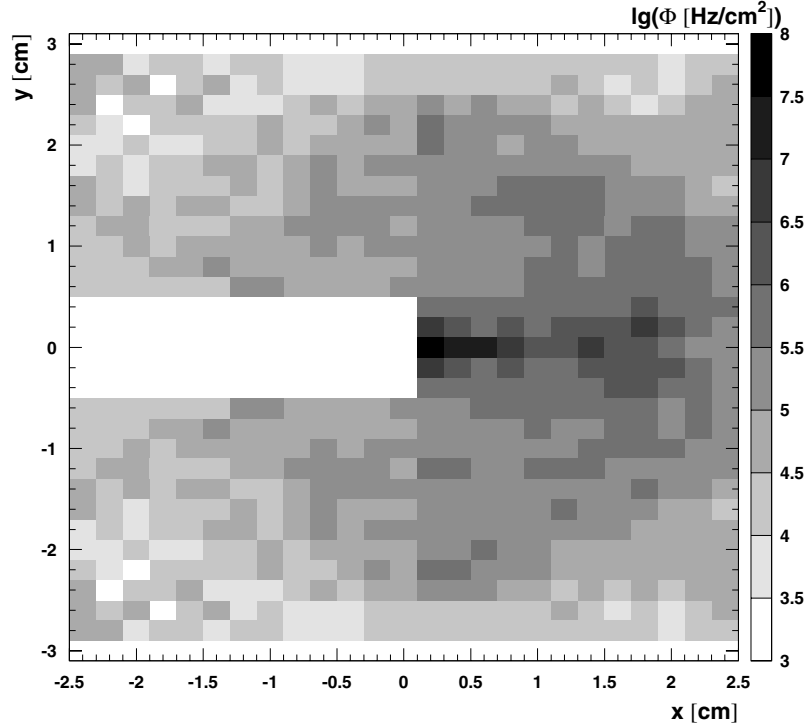
Figure 4.4: Map of the flux of charged hadrons (adapted from [81]) over an area corresponding approximately to the RP detectors at 220 m.

Table 4.6: Single-arm pp-induced background rate for $\beta^* = 0.5$ m, $k = 2808$ and $N = 0.4 \times 10^{11}$ ($\mathcal{L} = 10^{33}$ cm^{-2} s^{-1}) before application of any cuts, integrated over one RP silicon detector.

Particle	Rate [MHz]			
	RP 145 (vert.)	RP 149 (vert.)	RP 220 (vert.)	RP 220 (hori.)
charged hadr.	8.0	3.1	0.6	7.1 (incl. 3.4 diff. p)
n	3.9	1.4	0.4	1.5
$e^{\pm}$	121.9	29.7	12.7	19.1
γ	1494.6	295.7	85.9	155.8

cut efficiencies is very difficult. Two approximate approaches have been taken whose rate reductions are listed in Tables 4.7 and 4.8. The total rates for the different running scenarios are summarised in Table 4.9.

1. The assumption that the efficiency of the angular cuts is the same as for beam-gas background leads to the rate reduction in Table 4.7 and the upper limits in Table 4.9. This approach is pessimistic because pp-induced background lacks the forward boost of the beam-gas collisions and hence tends to be softer with wider angular distributions which respond better to cuts.

2. Angular distributions are available at the TAN entrance [82]. Assuming that the shower particle track angles at the RPs are at least as much randomised as at the TAN, one can

use those angular distributions to estimate the cut efficiencies (see Table 4.8 and the lower limits in Table 4.9).

In both cases, the events remaining after the cuts are dominated by the charged hadron component which has a high uncertainty from the crude subtraction of signal protons.

Scaling the background rates from the $\beta^* = 0.5\,\mathrm{m}$ scenario to the higher β^* running conditions is not straightforward because the effect of the optics is difficult to predict without dedicated simulations which are currently missing. For $\beta^* = 0.5\,\mathrm{m}$, charged particles with TeV-scale energies – being transported similarly to diffractive protons – are predominantly found in the horizontal detector. At the high-β^* optics with their bigger effective length L_y, they might be displaced into the vertical detectors. Approximate numbers can be obtained under the – rather uncertain – assumption that the total particle flux integrated over the active area of all detectors does not strongly depend on the optics, and thus scales with the luminosity. Hence, for $\beta^* = 1540\,\mathrm{m}$ and 90 m, Table 4.9 lists the sum of fluxes in the one horizontal and the two vertical detectors without double-counting the overlap zones. These numbers can be considered as upper limits for the background trigger rates in one horizontal or two vertical detectors.

In summary, due to pp-induced background, between 0.5 % and 3.2 % of all minimum bias events have a fake proton signature in the Roman Pot trigger of one given arm of the experiment. Accounting for the two arms and avoiding the double-counting of coincidences, a total fraction of 1.0 % to 6.3 % of all events have a fake proton in any arm.

Table 4.7: Single-arm pp-induced background rate before and after cut for $\beta^* = 0.5\,\mathrm{m}$ and $\mathcal{L} = 10^{33}\,\mathrm{cm}^{-2}\,\mathrm{s}^{-1}$ for one horizontal or vertical detector in the RP station at 220 m assuming the same cut efficiency as for beam-gas background.

Particle	Rate before cut [MHz]		reduction factor from beam-gas	Rate after cut [MHz]	
	hori.	vert.		hori.	vert.
charged hadr.	3.7	0.6	0.67	2.48	0.40
n	1.5	0.4	0.0027	0.004	0.001
$e^\pm$	19.1	12.7	0.0045	0.09	0.06
γ	155.8	85.9	0.0029	0.45	0.25
total	180.1	99.6		3.02	0.71

Table 4.8: Like Table 4.7 but using angular information from the TAN position.

Particle	Rate before cut [MHz]		det. effic.	angular cut	Rate after cut [MHz]	
	hori.	vert.			hori.	vert.
charged hadr.	3.7	0.6	1	0.15	0.56	0.092
n	1.5	0.4	0.004	0.15	0.0009	0.0002
$e^\pm$	19.1	12.7	1	0.002	0.038	0.025
γ	155.8	85.9	0.015	0.002	0.005	0.0026
total	180.1	99.6			0.60	0.12

Table 4.9: Total single-arm (one side) p-p induced background rates before and after cuts at 220 m for one horizontal or vertical detector. The minimum bias event rate f_{mb} is based on the assumption $\sigma_{tot} = 110$ mb. "o." stands for the overlap zone of a horizontal ("h.") and a vertical ("v.") detector.

	Scenario			
β^* [m]	1540	90	0.5	
k	156	156	2808	
$N/10^{10}$	7.4	5.7	4.0	
$\mathcal{L}\,[\,\mathrm{cm}^{-2}\,\mathrm{s}^{-1}\,]$	10^{29}	10^{30}	10^{33}	
f_{mb} [kHz]	11	110	110×10^3	
detector	h. + 2 v. − 2 o.	h. + 2 v. − 2 o.	h.	v.
before cuts:				
f_{p-p} [kHz]	31	310	180×10^3	100×10^3
f_{p-p}/f_{bx} $[10^{-4}/\mathrm{bx}]$	177	1767	5.7×10^4	3.2×10^4
after cuts:				
f_{p-p} [kHz]	0.07 − 0.35	0.66 − 3.47	604 − 3024	120 − 710
f_{p-p}/f_{bx} $[10^{-4}/\mathrm{bx}]$	0.38 − 1.98	3.76 − 19.8	191 − 958	38 − 225
f_{p-p}/f_{mb} [%]	0.6 − 3.2	0.6 − 3.2	0.5 − 2.7	0.1 − 0.6

4.2.4 Conclusions on Machine-Induced Background

At this point in time, a reliable estimation of machine-induced background is a very difficult task. The initial studies discussed above are based on the best available tools which however require extrapolations and assumptions to evaluate trigger and background rates in the detectors. These estimates are therefore subject to large uncertainties, and more refined studies are ongoing to consolidate these results and improve our understanding of the machine-induced background.

Chapter 5

Diffraction at low and medium luminosities

Diffractive final states will comprise almost 50% of all final states at the LHC. Their study will shed light on the proton structure and will help in understanding the transition between the non-perturbative regime of low-t elastic scattering and that of hard diffraction, where rapidity gaps and forward protons co-exist with large p_T final states. The present chapter focusses on the studies that can be performed at "low" luminosity, $\mathcal{L} \lesssim 10^{30}\,\mathrm{cm}^{-2}\,\mathrm{s}^{-1}$, and at "medium" luminosity, $\mathcal{L} = 10^{32}\,\mathrm{cm}^{-2}\,\mathrm{s}^{-1}$, where pile-up is negligible. The luminosity that can be integrated without pile-up is probably going to be $\lesssim 1\,\mathrm{fb}^{-1}$.

At low and medium luminosities inclusive single diffractive (SD) events, $pp \rightarrow pX$, as well as inclusive double-pomeron exchange (DPE) events, $pp \rightarrow pXp$, can be studied by requiring either the presence of fast forward protons or of one or two rapidity gaps in the event. Special optics runs at low luminosities are particularly well suited for these studies because of the excellent ξ coverage and the very good t resolution, allowing a multitude of analyses of soft diffractive events. The integrated inclusive SD and DPE cross sections, as well as their M_X and t dependences are important quantities to measure at the LHC; their energy dependence is a fundamental parameter of non-perturbative QCD. These measurements are presented in the first part of this chapter, after a discussion on triggering at low luminosities.

In standard optics runs with medium luminosities, diffractive studies can be extended to lower cross section processes involving a hard scale. The first priority here will be to repeat the measurements that have been carried out at the Tevatron (see Sec. 1.2.4). Among them, SD and DPE production of dijets, of W and Z bosons as well as of heavy flavours. These measurements open up the possibility of accessing the diffractive structure functions and hence the diffractive PDFs. Diffractive PDFs can be interpreted as conditional probabilities to find a parton in the proton when the final state of the process contains a fast proton of a given four-momentum. They are accessible in inclusive hard diffractive processes in ep scattering and, modulo the understanding of the rapidity gap survival probability, in pp scattering. Diffractive production of jets and heavy quarks is sensitive to the gluon content of the dPDFs. Conversely, vector boson production is sensitive to the quark content of the dPDFs. The comparison of the diffractive structure functions extracted from SD and DPE events can give information on the degree to which hard diffractive factorisation is broken, and hence on the rapidity gap survival probability. This chapter presents a few examples of possible studies – SD production of dijets, DPE inclusive production of W bosons, as well as SD and DPE production of B mesons.

5.1 Diffractive trigger in low-luminosity runs

Since special optics runs will be carried out at low luminosities, it is worthwhile to investigate trigger strategies specific for these runs. Trigger strategies for runs with nominal LHC optics and higher luminosities are discussed in Chapter 6.

Diffractive trigger scenarios at low and medium luminosities benefit from the excellent ξ acceptance with special optics. In the $\beta 90, \beta 1540$ scenarios, the acceptance as a function of ξ is large and nearly independent of the mass of the diffractive system. In single diffractive (SD) events, the proton fractional momenta are efficiently measured for diffractive masses $M_X >3$ GeV; in the DPE events central masses of $M_X <1$ TeV are covered with varying resolution.

We assume a level-one (L1) trigger rate of $\mathcal{O}(1)$ kHz, which might be further reduced at the High Level Trigger (HLT). For the special optics runs the data taking rate is limited to 100 Hz, while for the nominal optics runs the maximal rate of data taking has to be $\mathcal{O}(1)$ Hz, i.e. $\sim 1\%$ of the over-all CMS event rate (Chapter 6).

In Tabs. 5.1– 5.2 the cross sections, acceptances, trigger rates and expected number of events are summarised for different physics processes and running scenarios. The trigger and event rates are scaled according to the L1-trigger constraints given above. The background rate is given at the end of each Table; it includes the pile-up, as well as the fake tracks caused by the forward energy flow from the IP, simulating a diffractive proton. The machine induced background due to beam-gas interactions and beam-halo protons was estimated to be negligible (see Chapter 4).

DPE Trigger The DPE trigger is based on the requirement of a forward-backward pair of leading protons detected at $\pm$RP220, along with charged tracks detected in the T1 and/or T2 telescopes. The latter requirement discriminates against the elastic events that could fake the DPE events.

- The trigger scheme of the $\beta 90$ scenario at a luminosity of 10^{30} cm^{-2} s^{-1} is summarised in Table 5.1. The high coincidence rate estimated for the simultaneous elastic scattering and pile-up events (~ 1 kHz) can be suppressed by applying an anticollinear cut in the vertical coordinates of the two protons. This selection reduces the elastic rate from ~ 20 kHz to a few Hz, whereas it retains about 90% of the DPE events. Pile-up of two simultaneous SD events yields a background of 10 Hz. This has to be compared to the rate of 40 Hz due to the "fake protons" resulting from p-p interactions (probability of $\sim 2\%$ for each arm).

  Given that the trigger efficiency for DPE events is approximately 20%, the L1 trigger rate of 200 Hz (with a background event rate of 60 Hz) has to be prescaled in case the HLT is not available. Nevertheless, some 10^7 events, containing a sizable sample of dijet events with $p_T^{jet} >10$–20 GeV (shown in bracket in the Table), will be collected within a few days. Due to the lower cross section, dijet events could profit from a dedicated trigger stream with jet information.

  At this stage of the study no detailed information is available on the trigger and reconstruction efficiency of low–p_T (<20 GeV) jets in the central calorimeter; further studies will address the problem and will investigate the possibility of lowering the p_T threshold. In the following analysis, it is assumed [83] that the jet reconstruction efficiency increases from 50% at $p_T > 20$ GeV to 100% at $p_T > 50$ GeV (given in square brackets in Table 5.1). Since the L1 rate remains below the pre-

defined limit, the jet information is assumed to be available at HLT. In Table 5.1 the notation $(jets)_{HLT}$ refers to the DPE final state where at least one jet above threshold is reconstructed at higher level trigger stages.

- The $\beta1540$ scenario at a luminosity of about $10^{29}\,\mathrm{cm}^{-2}\,\mathrm{s}^{-1}$ (Table 5.2) allows diffractive protons to be detected with an acceptance 3 times larger compared to the $\beta90$ scenario. This means that the same number of diffractive events can be collected with both high-β run options. However, in case of $\beta1540$, the pile-up event rate is a factor 10 lower. As a consequence, the backgrounds due to simultaneous pairs of SD events (with the diffractive protons pointing to opposite directions) or elastic scattering together with a minimum-bias event are strongly suppressed. The maximum background rate for the events with two fake protons and a minimum bias event is estimated to be 4 Hz.

  As in the previous scenarios, dijet events will be collected too, but due to the lower luminosity and the lower cross section, a dedicated trigger on high-p$_T$ jets is not as useful.

- In the nominal scenario at luminosity of about $10^{32}\,\mathrm{cm}^{-2}\,\mathrm{s}^{-1}$, the available trigger bandwidth on data storage should not exceed 1 Hz and a high p$_T$ jet trigger is therefore mandatory. Hard DPE will be studied with jet transverse momenta up to a few hundred GeV. The $\xi > 2\%$ cut makes the trigger efficient for central masses larger than $\sim300\,\mathrm{GeV}$, which yields central jets with p$_T$ $>50\,\mathrm{GeV}$. While the trigger rate for these events is low, there are a number of background processes that have rates exceeding a few Hz.

  A signature based on a proton on one side and a rapidity gap on the other may increase the acceptance at lower central masses. More detailed studies on triggers based on central high p$_T$ jets L1-selection and one leading proton can be found in Chapter 6.

Single diffraction trigger   In triggering on single diffraction (SD), the approach can be similar to that of the DPE event selection (see Tables 5.1– 5.2). In this case, a leading proton is required to be detected on either side of the IP at $\pm$RP220 together with inelastic activity within the T1/T2 spectrometer or forward jets on the opposite side.

- Due to the large cross section, the L1 rate for the SD event candidates will significantly exceed the available bandwidth in the $\beta90$ scenario. Since the background rate due to fake protons and elastic pile-up events is expected to be at least 50% of the signal rate, a large prescaling factor is required. Requiring high p$_T$-jets in the hemisphere opposite to that of the scattered proton will reduce signal and background to a level of a few Hz.

- No prescaling is needed with the $\beta1540$ scenario. Here, the proton acceptance is substantially larger and the background smaller by a factor 10 due to the negligible pile-up probability. However, the ξ resolution is worse compared to the previous scenario which is optimised for good ξ resolution. Also in this case, approximately 10^4 events with p$_T^{jet}$ $>20\,\mathrm{GeV}$ can be collected.

- A large data sample with high p$_T$-jets will be accumulated in the $\beta05$ scenario where the rate should not exceed $\mathcal{O}(1)$ Hz. The main background is due to the pile-up events causing a proton signal on either side of the IP with a probability of 4%. This could generate an event rate in excess of a few Hz. A relatively high p$_T$ threshold (up to 50 GeV) is needed for suppressing this source of background.

Further studies on this source of background are being pursued. In general, a diffractive event sample of higher purity could be obtained by requesting a rapidity gap on the side of the leading proton. A gap of three units in $\Delta\eta$ could be requested by using the T1/T2 spectrometers as a veto.

β^*=90 m ; $\mathcal{L}$=10^{30} cm^{-2} s^{-1}; $\int \mathcal{L}$dt = 0.3 (pb^{-1})					
Process	σ	Acceptance	Trigger rate (Hz)	Scale factor	N events
		$(2p\times T1/T2)_{L1}\times[jets]_{HLT}$			
pp→p X p	1 mb	0.24 × 0.86	200	0.25	1.5·10^7
($E_T^{jet} > 10$ GeV)	1μb	0.26 × 0.99			(2·10^4)
($E_T^{jet} > 20$ GeV)	60 nb	0.26 × 0.99			(1·10^3)
pp→p j j X p					
$E_T^{jet} > 20$ GeV	60nb	0.26 × 0.99×[0.5]	7·10^{-3}	1.	2·10^3
$E_T^{jet} > 50$ GeV	1.5nb	0.26 × 0.99×[1.]	4·10^{-4}	1.	120
		$(1p\times T1/T2)_{L1}\times[jets]_{HLT}$			
pp→p X	14 mb	0.52× 0.82	6000	0.008	1.5·10^7
($E_T^{jet} > 10$ GeV)	20μb	"			(2·10^4)
($E_T^{jet} > 20$ GeV)	1μb	"			(1·10^3)
pp→p j j X					
$E_T^{jet} > 20$ GeV	1μb	0.52× 0.82×[0.5]	0.2	1.	6·10^4
$E_T^{jet} > 50$ GeV	30nb	0.52× 0.82×[1.]	0.013	1.	4·10^3
Background DPE		$(2p\times T1/T2)_{L1}$			
pp→(pp)$_{elast}$ + NSD		0.0037×0.99	3.6	0.25	
SD + SD		0.52×0.82	10	0.25	
NSD+2p("fake")			40	0.25	
Background SD		$(1p\times T1/T2)_{L1}$			
NSD+p("fake")			4000	0.008	

Table 5.1: An example of trigger scheme at β^*=90 m. The condition $(2p)_{L1}$ includes a cut on the RP hit coordinates as described in the text. The number of events in parenthesis refer to the process specified and they are collected with the trigger condition indicated. "Scale factor" indicates the required L1 prescale factor.

5.2 Inclusive and semihard Double Pomeron Exchange (DPE)

The direct measurement of the momentum loss (ξ) depends on the machine optics and will only cover a small range in ξ. The rapidity gap method ($\Delta\eta = -\ln\xi$) allows one to extend the measurement to smaller ξ-values but with a rather limited resolution. A third method, using the energy of the calorimeters, allows one to determine ξ and the diffractive mass. DPE events have been used to calibrate these different techniques.

Soft inclusive DPE events for the present studies were generated with the PHOJET [66] Monte Carlo, and hard inclusive dijet DPE events ($p_T >$20 GeV) with the DPEMC [46] Monte Carlo. The status of these studies will be summarised in this section.

β^*=1540 m ; $\mathcal{L}$=10^{29} cm^{-2} s^{-1}; $\int \mathcal{L}$dt = 0.03 (pb^{-1})					
Process	σ	Acceptance $(2p\times T1/T2)_{L1}\times(\text{jets})_{HLT}$	Trigger rate (Hz)	Scale factor	N events
pp→p X p	1 mb	0.76×0.86	65	0.75	$1.5\cdot10^7$
($E_T^{jet} > 10\,$GeV)	1μb	0.76×0.99			$(1.7\cdot10^4)$
($E_T^{jet} > 20\,$GeV)	60 nb	0.76×0.99			$(1\cdot10^3)$
pp→p j j X p					
$E_T^{jet} > 20\,$GeV	60nb	$0.76 \times 0.99 \times 0.5$	0.0025	1.	$0.7\cdot10^3$
		$(1p\times T1/T2)_{L1}\times(\text{jets})_{HLT}$			
pp→p X	14 mb	0.87×0.82	1000	0.2	$1.5\cdot10^7$
($E_T^{jet} > 10\,$GeV)	20μb	"			$(2\cdot10^4)$
($E_T^{jet} > 20\,$GeV)	1μb	"			$(1\cdot10^3)$
pp→p j j X					
$E_T^{jet} > 20\,$GeV	1μb	$0.87\times 0.82\times 0.5$	0.03	1.	$1\cdot10^4$
Background DPE		$(2p\times T1/T2)_{L1}$			
pp→$(pp)_{elast}$ + NSD		0.95×0.99	9		
NSD+2p("fake")			4		
Background SD		$(1p\times T1/T2)_{L1}$			
NSD+1p("fake")			440		

Table 5.2: An example of trigger scheme at β^*=1540 m. The condition $(2p)_{L1}$ doesn't include a cut on the RP coordinates. The number of events in parenthesis refer to the process specified and they are collected with the trigger condition indicated. "Scale factor" indicates the required L1 prescale factor.

5.2.1 Measurement based on the leading protons

DPE processes will be investigated in a so far unexplored kinematical region with the central masses extending from a few GeV to a few TeV.

In the special optics scenarios, $\sim$ 50% (β90) and $\sim$ 90% (β1540) of the leading protons will be detected independently of ξ over the entire diffractive ξ region (see Fig. 3.3 right). As a consequence, a wide range of central diffractive masses can be covered (Fig. 5.1, left). This is not the case for nominal runs (β05) where the ξ acceptance starts at ξ =0.02 and hence the central diffractive masses will be restricted to M_X >300 GeV, unless detectors at 420 m from the interaction point are used.

In Fig. 5.1(right), the generated mass distribution (A=1) for DPE events is plotted together with the acceptance corrected distributions for the three run options. The total DPE cross-section is of the order of 1 mb, allowing the accumulation of large statistics even at TeV masses with special optics runs.

The resolution on the central mass in DPE processes depends on the symmetry in ξ of the pair of diffractively scattered leading protons; the more symmetric the two protons are, the better is the achieved resolution. For the β90 scenario, the mass resolution is about 15 GeV, almost mass independent, for the symmetric case $\xi_{low}/\xi_{high} \sim 0.5$, worsening to 60 GeV for the highly asymmetric cases with $\xi_{low}/\xi_{high} \sim 0.01$.

The measurement of the DPE diffractive mass distribution over a large mass interval will allow decisive comparisons with different model predictions. Figure 5.2 shows the generated and reconstructed mass distribution for soft and hard ($E_T > 20$ GeV) DPE events. Due to the jet requirement, there is a mass cut in the plot on the right. Together with the CMS calorimeter and tracker information, comprehensive studies of the topology of soft DPE events and of the gluon jet content in the hard events can be performed with good statistics (see Table 5.1). Extension of the study to larger jet E_T (> 50 GeV) can be performed with the standard optics. The mass cut of 300 GeV given by the ξ acceptance will not be important in this case, since the masses will be larger due to the dijets in the event.

It is of great importance to measure the t-dependence for different topologies of DPE events. At small t, diffractive cross sections show an exponential behaviour with a slope related to the size of the interacting region. A more complicated structure, with dips, has been observed for larger $|t|$. With increasing DPE masses, the t-distribution becomes flatter, as can be concluded from Fig. 5.3, which shows the t-distribution for low (10 GeV), medium (100 GeV) and high mass (1 TeV). Adding a hard scale by means of the requirement of dijets with given transverse energy will allow one to change the size of the proton interaction radius. As a consequence, the hard scale will influence the diffractive t-distribution. This has been demonstrated by the HERA results in exclusive vector meson or photon production which exhibit a decrease of the slope with the photon virtuality Q^2 or with the mass of the heavy quark [84].

The diffractive t-distribution for DPE with dijet production as predicted in [85] is displayed in Fig. 5.4 for two dijet masses (30 and 200 GeV). The required statistics of at least 10,000 events can only be accumulated with normal run conditions and negligible pile-up. The trigger would contain two high p_T jets, a proton on one side and a large rapidity gap on the other, e.g. no activity in T2.
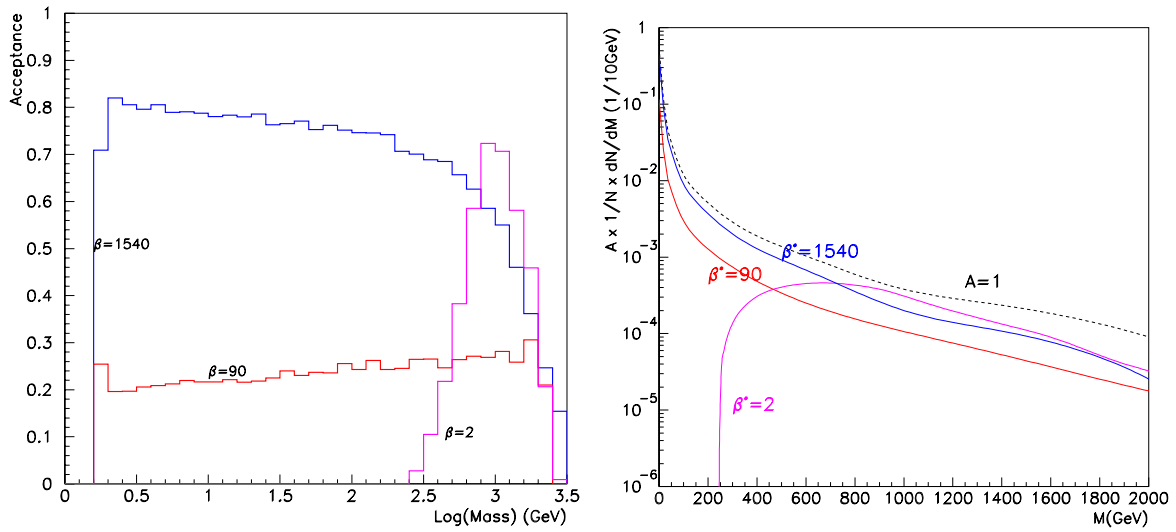
Figure 5.1: Left: Acceptance of soft DPE final states with mass M, double arm proton trigger, at different β^*. Right: Differential cross section of DPE with (solid) and without (dashed) the proton acceptance, for different optics.
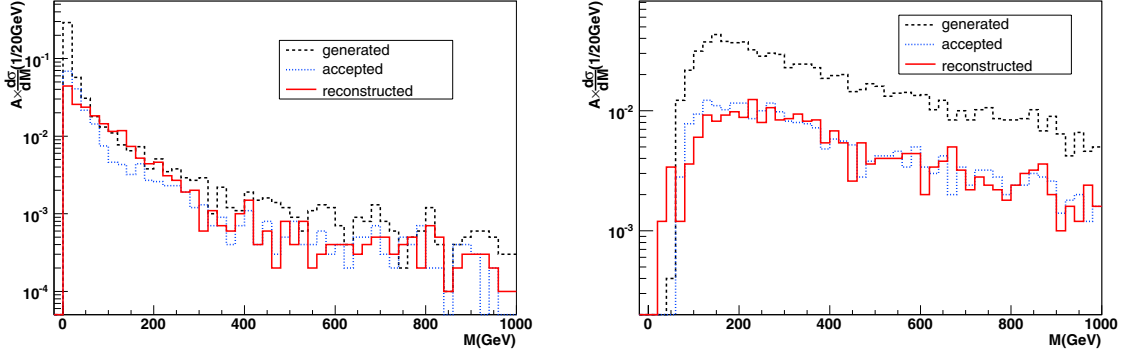
Figure 5.2: Reconstructed mass distribution for soft DPE(left), and for DPE dijets of $E_T >20\,$GeV at $\beta^* =90\,$m (right).
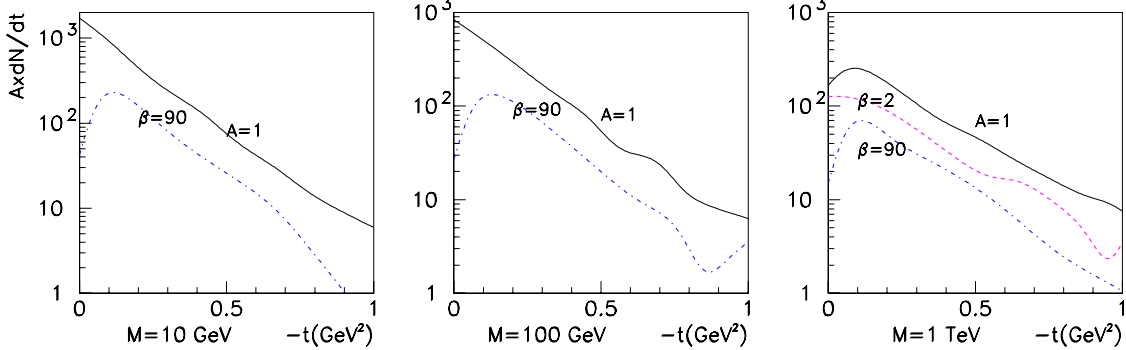
Figure 5.3: Generated t-distribution for different masses in DPE events (A=1) and after acceptance for two scenarios (β90 and β2).
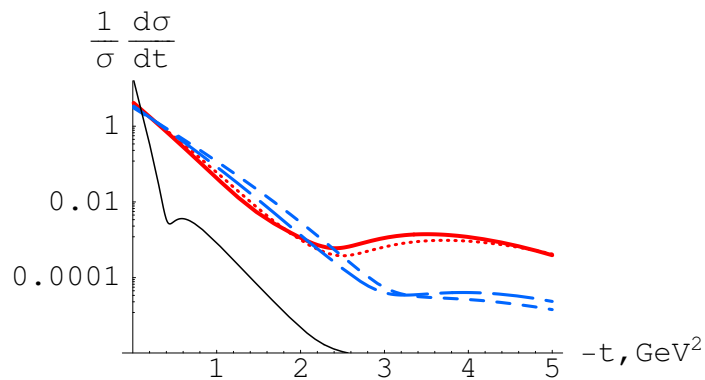
Figure 5.4: Normalised cross section for exclusive dijet production according to [85] as a function of t for $M_X = 30\,$GeV (the solid and long-dashed curves correspond to the LHC and Tevatron energies, respectively) and $M_X = 200\,$GeV (the dotted and short-dashed curves correspond to the LHC and Tevatron energies, respectively). The left curve corresponds to the elastic scattering at the LHC.

5.2.2 Reconstruction of event kinematics with the CMS calorimeter

An alternative method for reconstructing the fractional momentum loss, ξ, of a diffractively scattered proton is based on energy-momentum conservation [86]:

$$\xi_P^{\pm} = \frac{\Sigma_i E_T^i e^{\pm \eta_i}}{\sqrt{s}}, \tag{5.1}$$

where "+" refers to the outgoing proton direction and "-" to the opposite direction, and the sum is over all the particles in the event, except the forward protons. In practice, Eq. (5.1) is applied to the calorimetric energy depositions, provided that appropriate care is taken of the noise and undetected particles in the event. The method has been successfully used by the CDF [87] and D0 [35] experiments and provides a complementary way of measuring small ξ-values ($< 10^{-2}$) which are not directly accessible.

For validating the Monte Carlo calculations, Eq. (5.1) was first used at the particle level, without any simulation of the calorimeter response. The calorimeter coverage up to pseudorapidities of η= 5.0 (without CASTOR) allows the proton fractional momentum to be reconstructed in the range $10^{-4} < \xi < 10^{-1.5}$ without any substantial bias from the limited geometrical acceptance.

At the calorimeter level, an approach similar to the one used by D0 [35] was adopted by considering only electromagnetic calorimeter cells with energy deposition above 100 MeV (barrel) and above 500 MeV for the very forward calorimeter [88]. In such a way, the information from the noisier hadron calorimeter is not used in the ξ evaluation while keeping the full calorimeter coverage up to $|\eta| \sim 5$.

The ξ reconstruction based on the sum over the calorimeter energy depositions has to be corrected for: (i) detector inefficiencies, (ii) energy deposited within the hadron calorimeters, (iii) particles depositing energies below the threshold, and (iv) the charged low-p_T particles missing the calorimeters due to the magnetic field of the CMS solenoid.

To take into account the above effects, a correction factor K=ξ^{true}/ξ^{rec} was applied which was found to be independent of ξ. The correction is, however, different for min bias- (K$\sim$6.7) and dijet- (K$\sim$3.6) DPE events ($p_T > 20$ GeV). This can be understood in terms of the harder p_T spectrum in dijets events and hence the correction factor must be dependent on the dijet p_T. After applying the correction factor, the relative ξ difference ($\Delta\xi/\xi = (\xi^{true} - \xi^{rec})/\xi^{true}$) is as shown in Fig. 5.5 as a function of ξ. The error bars indicate the relative ξ reconstruction error: 100% for soft and 40% for dijet DPE events.

A cross-calibration of the ξ determination by the calorimeter method can be done by comparing the mass reconstructed from the calorimeter cells (whose energy has been corrected according to the energy scale correction factor K define above) to the mass calculated from the momentum losses of the two protons.

The result of the mass reconstruction is given in Figs 5.6- 5.7. The relative error in the mass is around 30% independent of ratio of ξ_{min}/ξ_{max} (Fig. 5.6, left); this was not the case for the direct proton measurement. The calibration of the mass determination depends slightly on the mass (Fig. 5.6,right). It has been demonstrated at the particle levels that this is due to acceptance effects.

In order to study the interplay between inclusive and exclusive DPE events, the dijet mass was compared (for events with $\xi < 0.1$) to the total central mass as shown in Fig. 5.7. The ratio of these two distributions should exhibit a peak around 1 for exclusive DPE events.

This distribution is fundamental for QCD studies which should describe the transition from inclusive to exclusive events.
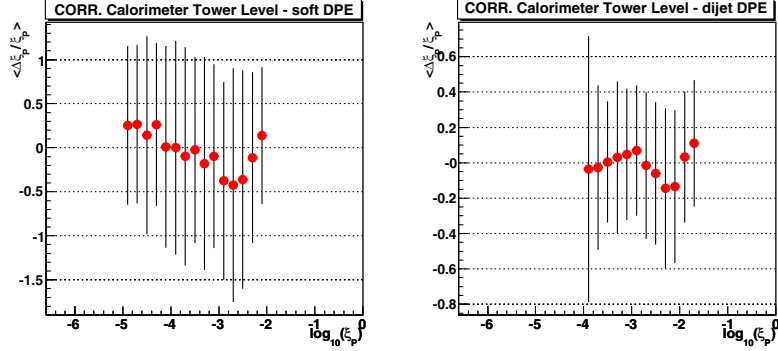
Figure 5.5: ξ reconstruction at calorimeter level according to Eq. 5.1 in soft (left) and dijet (right) DPE events after applying average correction factors. Shown errors are the rms of the $\Delta\xi/\xi$ distributions for each bin, found to be gaussian-like.
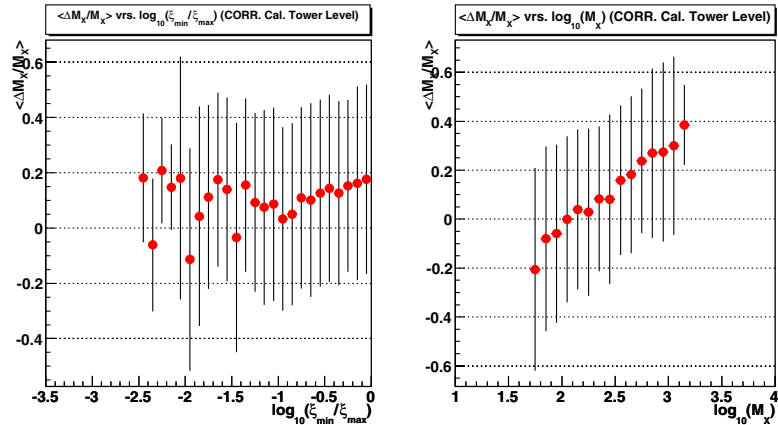
Figure 5.6: Mass resolution as function of ξ_{min}/ξ_{max} and as a function of mass for DPE dijet events ($p_T > 20\,\text{GeV}$)

5.2.3 Reconstruction of event kinematics with rapidity gaps

The CMS and TOTEM detectors, taken together, cover a rapidity range of about 14 units. Besides the typical SD events with a single large rapidity gap between the leading proton and the diffractive system, and DPE events with two rapidity gaps separating the central diffractive systems from the pair of leading protons, multi-gap events will be studied in detail. The rapidity gap $\Delta\eta$ is defined as the difference between the rapidity of the diffractively scattered proton and that of the hadron closest to it in (pseudo)rapidity. In the following analysis $\eta_p = 10$ has been assumed for the rapidity of the scattered proton.

The rapidity gap and the proton momentum loss ξ are related by

$$\ln\xi = -\Delta\eta. \tag{5.2}$$

Using the ξ value from the proton measurement, relation (5.2) can be calibrated over a large
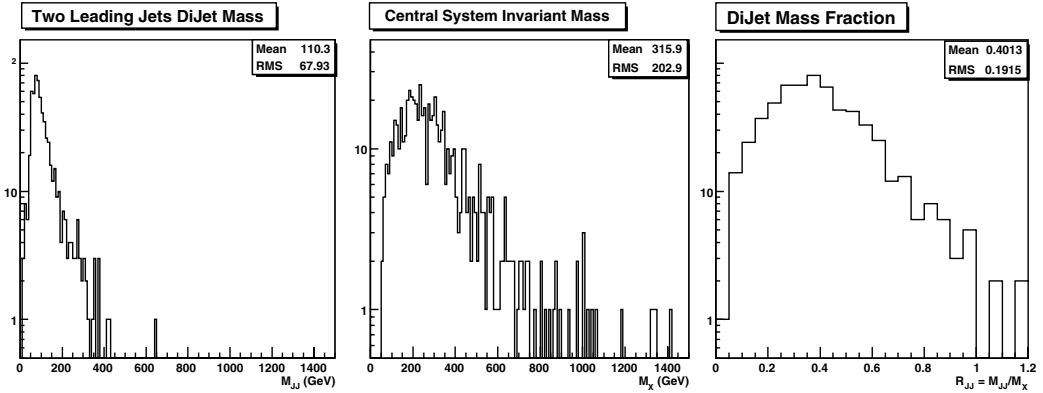
Figure 5.7: From left: Mass of "calibrated" jets system ($p_T > 20\,\text{GeV}$, $|\eta| < 3$); central mass corrected with the same method used for ξ; ratio of the two distributions.

ξ range. This calibration can then later be used at higher luminosities for which the proton can only be detected in a small ξ range ($\xi > 0.02$).

Two samples of events were generated: (1) soft inclusive DPE events with the PHOJET [66] Monte Carlo, and (2) hard inclusive dijet DPE events ($p_T > 20\,\text{GeV}$) with the DPEMC [46] Monte Carlo. In order to evaluate the accuracy with which the rapidity gaps can be measured by the CMS/TOTEM detectors, the events were analysed by using the full simulation of the TOTEM T1 and T2 spectrometers (OSCAR [89]) and the CMS fast simulation (FAMOS [71]) for the CMS calorimeters.

To define the maximum rapidity in each event, the reconstructed tracks in the T1 and T2 spectrometers and the energy deposits in the Barrel and EndCap electromagnetic calorimeters were considered. An energy threshold of 100 MeV was assumed for the Barrel and of 450 MeV for the EndCaps.

In Fig. 5.8, the rapidity gap sizes are plotted separately for the two protons, as a function of the simulated ξ-value for soft DPE events at generator level (top panels) and after reconstruction in the detectors (bottom panels). The coverages of the forward detectors do not fully overlap; this explains the acceptance gaps in the reconstructed distribution. Figures 5.9 and 5.10 show the predicted linear correlation between the gap sizes and $\ln \xi$, allowing ξ to be measured by the size of the rapidity gap. This may become important in cases where the direct leading proton measurement by the Roman Pots is impossible. Moreover, with a combined measurement, an optimised ξ-resolution would be achieved, notably in the very low ξ-region ($\xi < 10^{-3}$) where the resolution from the direct measurement is poor.
The achievable resolution in ξ ($\sigma(\xi)/\xi \sim 80 - 100\%$) is shown in Fig. 5.11 for soft and dijets events.

5.2.4 Inclusive DPE production of W bosons, $pp \rightarrow pXWp$

Inclusive DPE production of W bosons, $pp \rightarrow pXWp$, can be used to probe the dPDFs of the proton; unlike the production of dijets and heavy quarks, it is mainly sensitive to the quark component of the dPDFs. This process is relatively abundant and can be studied at instantaneous luminosities where pile-up is small. The present study was restricted to the W leptonic decay modes, $W \rightarrow e\nu$, $W \rightarrow \mu\nu$.

The reaction was simulated with the DPEMC generator v2.4 [46]. The generated events were
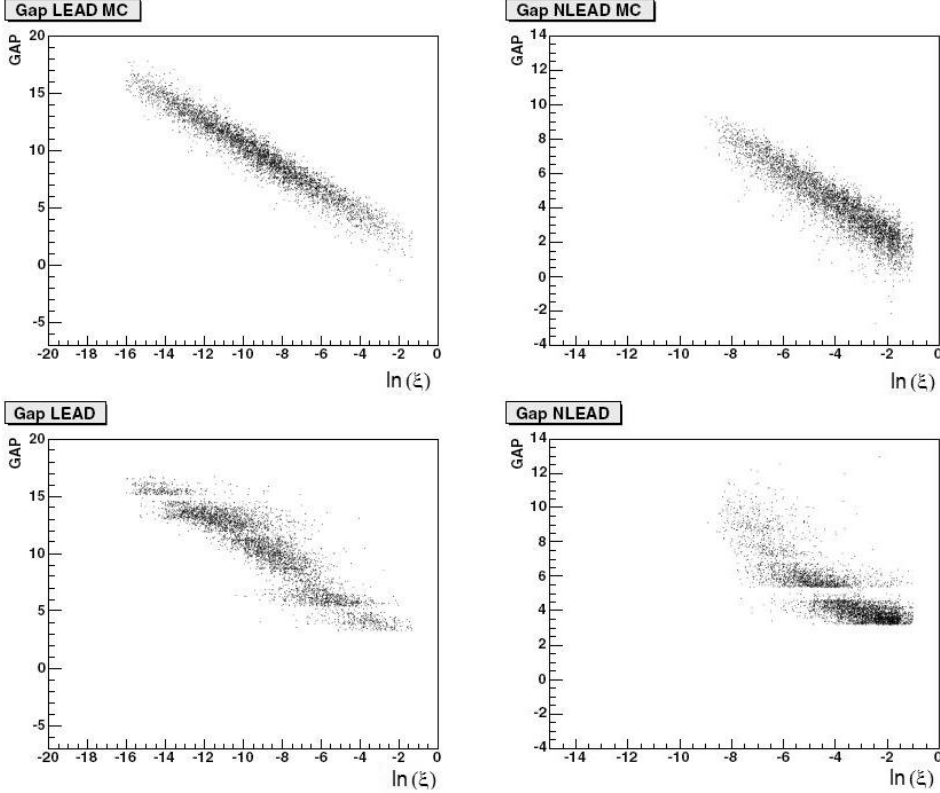
Figure 5.8: Soft DPE: gap (leading and non-leading proton side) vs $\log(\xi)$, generator level (MC) and after reconstruction. "Leading" is the proton with minimum ξ.
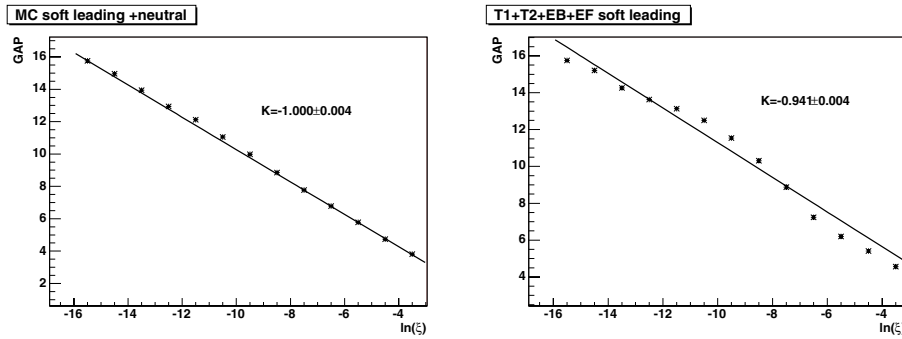
Figure 5.9: Soft DPE: linear fit of the gap mean value vs ξ, measured on the side of the leading proton at generator level (left) and after reconstruction (right) level.

passed through the fast simulation of the CMS detector, FAMOS version 1.2.0 [71], which includes the acceptances of the TOTEM RP detectors and of the FP420 detectors. The so-called "H1 fit 2" diffractive PDFs were used [90], in which the gluon distribution is approximately flat; "H1 fit 3" [90], in which the gluon distribution is more peaked, was used to estimate the sensitivity to the uncertainty in the diffractive PDFs.

The requirement that the two scattered protons were seen in the RP detectors was imposed by weighting the selected events with the RP acceptances.
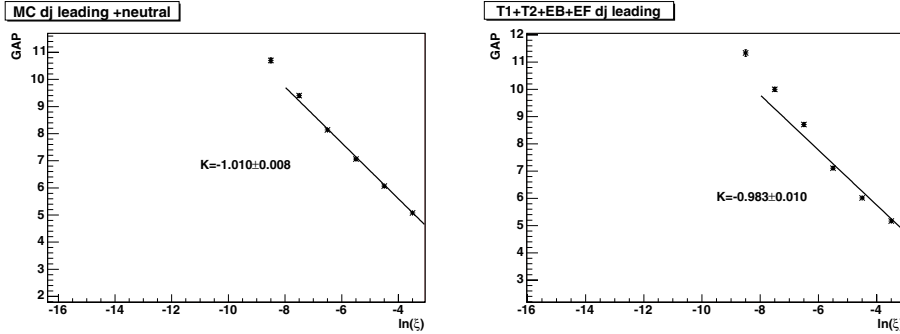
Figure 5.10: Dijets DPE: linear fit of the gap mean value vs ξ, measured on the side of the leading proton at generator level (left) and after reconstruction (right) level.
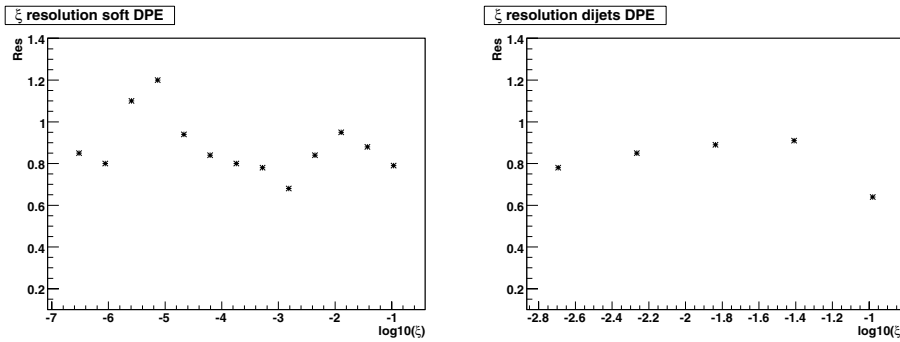
Figure 5.11: Relative ξ resolution from the indirect measurement made with gaps.

Events in the electron channel, $W \rightarrow e\nu$, were selected by requiring a high-energy electron with E_T >30 GeV and a high missing E_T, $\not{E}_T > 20$ GeV. These cuts are tighter than the CMS L1 trigger thresholds. Several thousand events are expected after the selection cuts for 1 fb^{-1}.

Events in the muon channel, $W \rightarrow \mu\nu$, were selected by requiring a high-energy muon with E_T >20 GeV and a high missing E_T, $\not{E}_T$ >20 GeV. Also these cuts are tighter than the CMS L1 trigger thresholds. The expected distributions of the W and muon variables for 1 fb^{-1} are shown in Fig. 5.12. Here again, several thousand events are expected after the selection cuts.

5.2.5 DPE production of low mass mesons

A good environment for the production of known as well as exotic meson states (glueballs, hybrids, etc.) via $gg \rightarrow M$ is expected [91, 92] in the DPE process $pp \rightarrow p + M + p$.

The vacuum quantum numbers of the two colliding colour singlets lead to selection rules on spin J, parity P and charge conjugation C of the state M [93]:

$$J^P = 0^+, 2^+, 4^+; J_z = 0; C = +1 \tag{5.3}$$

(in the limit of $t = 0$). The $J_z = 0$ rule strongly suppresses gg$\rightarrow$ q$\bar{q}$ background because of helicity conservation (this background would totally vanish for massless quarks). The rules can also be used for determining the quantum numbers of a new state observed. Table 5.3 lists two examples for exclusive production of Standard Model mesons. For exclusive dijet and χ_{c0} production, CDF [43] has seen event candidates and set upper limits on the cross sec-
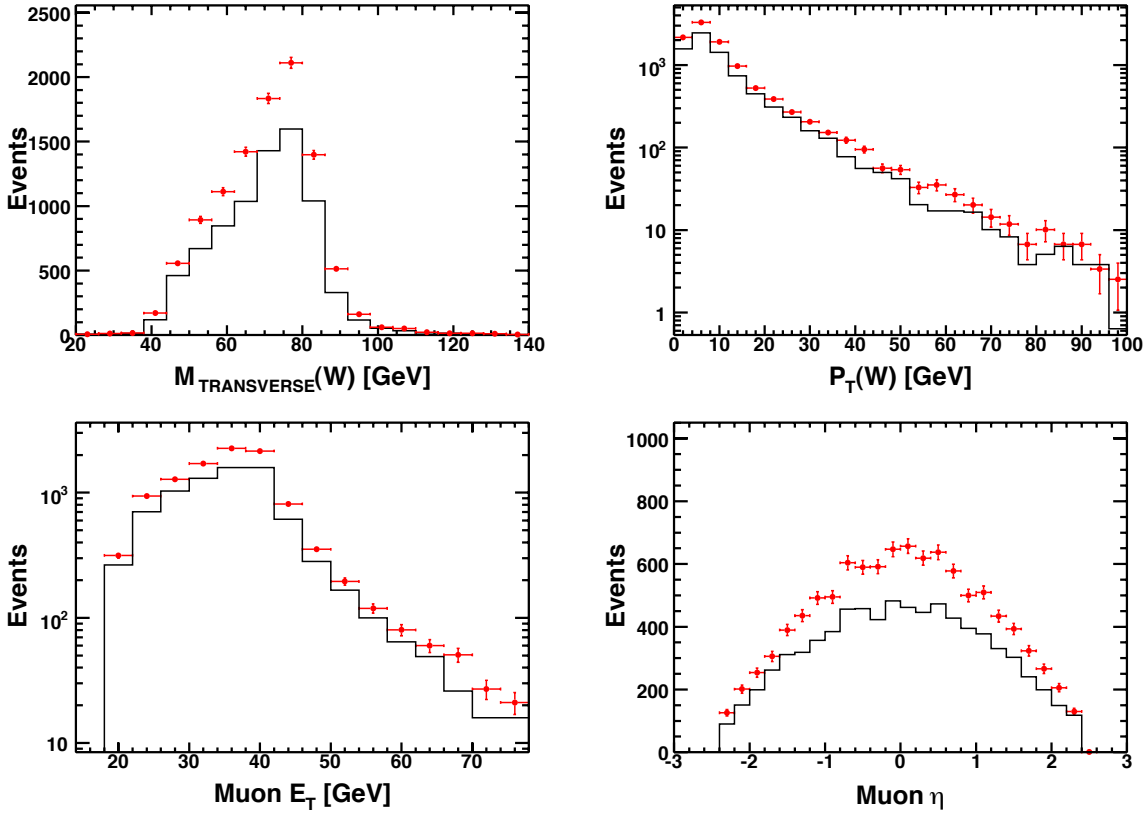
Figure 5.12: Distributions of a) transverse mass of the $W^{\pm}$ boson, b) transverse momentum of the $W^{\pm}$, c) transverse momentum of the muon, d) pseudorapidity of the muon for $W \to \mu\nu$; luminosity=1 fb^{-1}. Full points: approximately flat gluon density; histograms: more peaked gluon density (see text).

tion. At LHC, the χ_{c0} could be within reach, whereas the observability of the χ_{b0} is doubtful because the branching ratio for its muonic decay is unknown (upper limit: 1.5×10^{-3}).

Table 5.3: Examples for meson production by exclusive DPE. For cross sections see e.g. [44], [85].

State M	σ	Decay channel	BR	$\sigma \times$ BR	Events at $\mathcal{L}_{int} = 0.3$ pb^{-1} with 25 % proton accept.
χ_{c0} (3.4 GeV)	3 μb	$\gamma J/\psi \to \gamma\mu^+\mu^-$ $\pi^+\pi^- K^+K^-$	6×10^{-4} 0.018	1.8 nb 60 nb	$5.4 \times 10^3 \times 0.25 = 1.4 \times 10^2$ $180 \times 10^3 \times 0.25 = 45 \times 10^2$
χ_{b0} (9.9 GeV)	4 nb	$\gamma Y \to \gamma\mu^+\mu^-$	$\leq 1.5 \times 10^{-3}$	≤ 6 pb	$\leq 18 \times 0.25 = 0.5$

A strong coupling could be expected for glueballs and hybrids as a result of the assumed two-gluon exchange. The evidence for glueballs thus far has been weak at best. Being central to QCD, discovery of glueballs would be of the greatest importance. The very high statistics studies possible with the 'gluon collider' mode of operation at the LHC would provide this possibility. In this case, azimuthal correlations with the quasielastic pair of leading protons can be particularly significant [94–96].

The measurement of soft, exclusive DPE interactions requires tagging the leading diffractive

protons (or their diffractive excitations) and/or rapidity gaps between the produced systems and the central system. Identification and measurement of central activity, leptons, c- and b-quarks increases the physics potential of the LHC and helps in rejecting QCD backgrounds. Forward coverage is important in filtering out the contamination expected from the inclusive DPE processes.

For the case of low mass DPE interactions, relatively short runs with the $\beta^* = 90\,\text{m}$ optics can be used.

The absence of large p_T presents a challenge for triggering on these final states; low multiplicity and the presence of the rapidity gaps and the pair of leading protons should help in tagging the events.

5.3   Inclusive and semihard Single Diffraction (SD)

In single diffractive dissociation, SD, $pp \rightarrow p + X$, where the + sign denotes a rapidity gap, an initial proton is excited into a final state system with mass, M_X.

The SD processes with large M_X are theoretically problematic if the Regge model is strictly followed and the Pomeron intercept suggested by the experimental measurements of σ_{tot} is used for the predictions. Both the triple-Pomeron based description and the prediction of "multi-Reggeon" events, i.e. for events with a few large rapidity gaps, lead to σ_{SD} that grows faster than σ_{tot}. A measurement of σ_{SD} and the cross section of multiple large rapidity gaps at the LHC will test the proposed models.

For understanding the asymptotics of the strong interaction amplitude, it is crucial to measure the t-dependence of σ_{SD} . A vanishing triple-Pomeron coupling, G_{3P}, at $t \rightarrow 0$, would cure the problem of excessive σ_{SD}, and favour the asymptotic "weak coupling" prediction of equal cross sections at high energies. Measurement of the cross section $d\sigma_{SD}/dt$ at $t \rightarrow 0$, would put the 'weak coupling' scenario to test.

Measurement of the location of the diffractive minimum, predicted for the $d\sigma_{SD}/dt$ as a result of the destructive interference between the pole and cut contributions, would allow further testing of the "weak coupling" scheme.

Another possible solution for the σ_{SD} vs σ_{tot} cross section dilemma could be provided by the "screening corrections" due to multi-loop Pomeron graphs, i.e. by the gap survival factor $S^2 \rightarrow 0$ when c.m.s. energy, s$\rightarrow \infty$, or the gap size $\Delta\eta \rightarrow \infty$. It is important to investigate the dependence of S^2 on c.m.s. energy, gap size and the number of gaps.

Since SD is supposedly dominated by the periphery of the interaction disk, characteristics of the particles produced within the diffractive system should be distinguishable by, e.g., their smaller average transverse momenta as compared to the inclusively produced secondaries at energies $\sqrt{s} \approx M_X$. It is important to test this experimentally.

The measurement of soft diffractive processes is based on tagging leading protons and rapidity gaps in inelastic events. The cross sections are typically large, and short special runs with the $\beta 1540$ scenario yield excellent statistics for these types of events. The run scenarios $\beta 90, \beta 2$, planned for the initial stages of the LHC operation, are well suited for measurements of semihard diffractive scattering.

TOTEM registers, independent of its momentum loss ξ, 85% (50%) of the diffractive protons

with the $\beta 1540$ ($\beta\,90$) optics, over almost the full azimuthal angle. An acceptance better than 50% can be achieved down to the lowest masses of about $3\,\mathrm{GeV}$.

5.3.1 Inclusive single-diffractive dijet production

Semihard SD diffractive reactions are characterised by soft diffractive dynamics combined with a hard-scale process leading to the production of e.g. high E_T jets, heavy quarks, heavy bosons and possibly new heavy particles. By measuring these objects up to rapidities of $\eta=6.5$, the diffractive PDFs of the proton can be measured. In these events, Bjorken x can be evaluated as:

$$x_{Bj} = \frac{1}{\sqrt{s}}\Sigma_i E_T^i e^{-\eta_i},\tag{5.4}$$

where E_{T_i} is the transverse energy of object i (a jet or another heavy object within the diffractive system) and η_i its pseudorapidity. The ratio $\beta = x_{Bj}/\xi$ can then be interpreted as the momentum fraction of a parton within the diffractive exchange. We focus here on SD dijet production. The diagram of the process is shown in Figure 5.13. The cross section can be calculated by convoluting the PDFs and dPDFs of the proton with the cross section of the 'hard' subprocess; the result will have to be scaled by the rapidity gap survival probability. The expected cross sections are large, of the order of 1μb for $p_T >20\,\mathrm{GeV}$. The measurement of SD dijet production, pioneered by CDF [28], gives thus access to the diffractive PDFs of the proton and to the rapidity gap survival probability. CMS and TOTEM have the potential of greatly expanding the kinematic range of the measurement. The scale at which diffractive PDFs are probed is $Q^2 \approx E_T^{jet1} \times E_T^{jet2} \gtrsim 400\,\mathrm{GeV}^2$ at LHC, while $\langle Q^2 \rangle \approx 75\,\mathrm{GeV}^2$ for the CDF data; it will be possible to probe values as large as $160{,}000\,\mathrm{GeV}^2$.
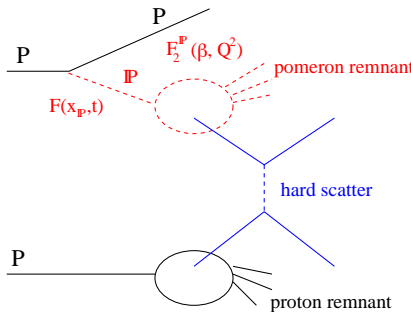
Figure 5.13: Single Diffractive production of dijets as simulated in POMWIG.

It is of great advantage for a clean SD selection that the presence of the scattered proton be required already at trigger level, independently of ξ. This is possible if the data are taken in the $\beta 90$ configuration. An integrated luminosity of $\sim 1\,\mathrm{pb}^{-1}$ can be accumulated within a few days, offering ample statistics. Large ξ values are directly measured with the RP detectors, whereas lower ξ values can be estimated from the calorimeter information (see Sec. 5.2.2). SD events triggered by demanding a proton tag are ideal to study the energy flow on the proton side and also the rapidity gap survival probability. The expected energy density distributions for the signal and background events are shown in Fig. 5.14. The peak in the pseudorapidity region around $\eta = -10$ corresponds to the scattered proton.

In the present study, the signal events,

$$pp \to p\,2j\,X,\tag{5.5}$$

were generated with the POMWIG (version 1.2) MC package [45], using the H1 diffractive structure function [90]. POMWIG does not include the rapidity gap survival probability S^2, which for SD processes may be of order 0.1. The background consists mostly of dijet production by hard two-parton scattering in non-diffractive events. The background events were generated with HERWIG (version 6.5) [97].
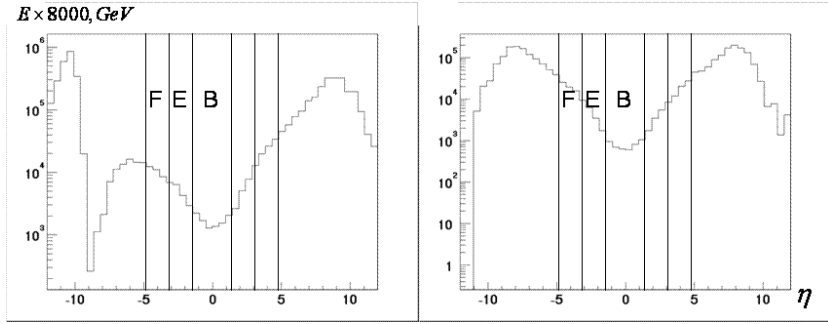
Figure 5.14: Energy density distributions vs pseudorapidity for diffractive (left panel) and non-diffractive (right panel) dijet events. The coverage of the Forward (F), Endcap (E) and Barrel (B) CMS calorimeters is shown.

The CMS detector simulation and event reconstruction were performed for both the non-diffractive dijet background and the signal events by using the FAMOS MC package (version 1.4.0) [71]. Jets were reconstructed using the iterative cone algorithm (cone radius $R < 0.7$).

Process (5.5) is characterised by 2 jets and a rapidity gap between the leading proton and the other products of the reaction. Low energy deposition in the forward calorimeters may reflect the presence of a rapidity gap. Figure 5.14 compares the energy deposition of diffractive and non-diffractive dijet production; a small energy deposition is expected in the hemisphere that contains the outgoing proton. Distributions of energy deposition in the different pseudorapidity regions, plotted in Fig. 5.15 for diffractive and non-diffractive dijet production, illustrate the fact that low energy deposition in the calorimeters covering high rapidity regions (HF calorimeter, for example) could be used for effective background suppression of non-diffractive jet production.

5.4 Diffractive production of B mesons

Inclusive SD and DPE production of B mesons, with $B \rightarrow J/\psi X$ and $J/\psi \rightarrow \mu^+\mu^-$, was studied using the generator DPEMC 2.4 [46] in conjunction with the fast CMS simulation code FAMOS, version 1.3.1 [71]. As discussed earlier, this process is sensitive to the dPDFs of the proton. Single diffractive production of b-hadrons [36] and of J/psi mesons [37] has been measured by CDF at the Tevatron, and used to derive a value 0.59 ± 0.15 for the gluon fraction of the diffractive PDF of the proton.

Events were selected which had at least one pair of oppositely charged muons. If two pairs were found, the one with invariant mass closer to that of the J/ψ meson was taken to be the one originating from the J/ψ decay.

Events were selected if $|\Delta\phi| < 0.635$, $|\Delta\eta| < 0.8$, $2.7 < M_{\mu\mu} < 3.5$ GeV, with $M_{\mu\mu}$ the invariant mass of the muon pair, and p_t^μ threshold for the dimuons – for the L1 trigger $p_t^\mu > 3$ GeV and for the HLT $p_t^\mu > 7$ GeV. In addition, the detection of a proton on either side of the
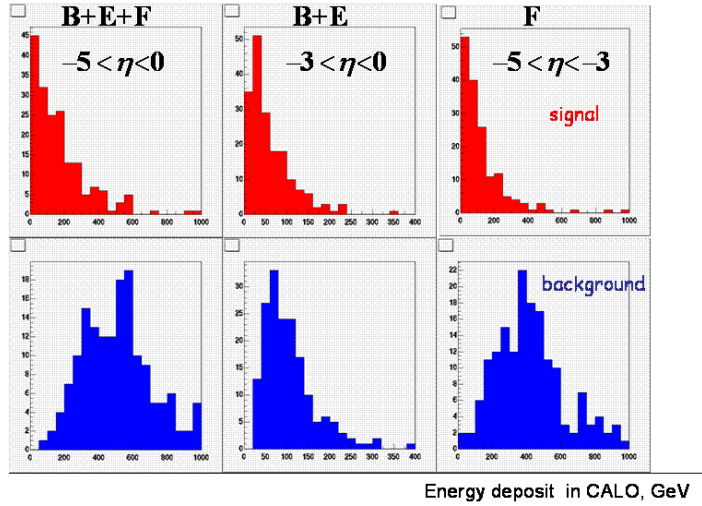
Figure 5.15: Energy deposit in the different CMS calorimeters for diffractive (upper panels) and non-diffractive (lower panels) dijet production.

interaction point was required for the SD events and on both sides for the DPE events. Both the 220 m RP stations and the 420 m stations were assumed in the simulation.

The estimated event yield, after the cuts, for an integrated luminosity of $1\,\mathrm{fb}^{-1}$ is of hundreds of SD events and a few DPE events. Figure 5.16 presents the $\mu^+\mu^-$ invariant mass for the signal in the SD case.
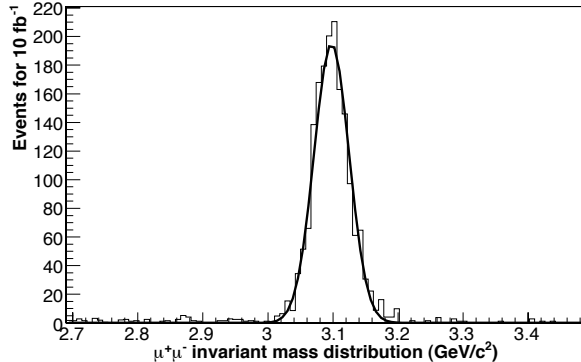
Figure 5.16: $\mu^+\mu^-$ invariant mass distribution for the SD events, after all cuts.

5.5   Exclusive Two-Photon Production in CMS

The exclusive process $pp \to p + \gamma\gamma + p$, with no hadrons produced, is very closely related [98, 99] to central exclusive Higgs boson production, $pp \to p + H + p$, discussed in Sec. 7.2; in fact the QCD part of the Feynman diagrams is identical. In one case we have a top loop $t\bar{t} \to H$ and in the other case mainly $u\bar{u} \to \gamma\gamma$ and $c\bar{c} \to \gamma\gamma$. Therefore if we can measure the exclusive $\gamma\gamma$ production cross section we "calibrate" the theoretical calculations of exclusive Higgs. The main differences are (1) $Ht\bar{t}$ coupling vs $\gamma q\bar{q}$ coupling, both of which are well-known in the Standard Model; (2) The accessible $M(\gamma\gamma)$ is less than $M(H)$ and so Q^2 is

lower; (3) x_i, x_i' would be somewhat different. Key parts of the calculation, such as (1) the Sudakov suppression of *all* hadron emission and (2) the probability of another parton parton interaction ("gap survival probability") are identical. For the same reasons, central exclusive production of χ_c and χ_b mesons, $pp \to p + \chi + p$, is also very interesting.

An observation of $pp \to p + \gamma\gamma + p$ with a statistical error of 10% would translate into a prediction for the central exclusive production cross section of a Standard Model Higgs with about 20% uncertainty.

CDF finds [100] three events with $p_T(\gamma) > 5\,\text{GeV/c}$ and $|\eta| < 1.0$ with an estimated background of < 0.2 events. The corresponding cross section is $0.14^{+0.14}_{-0.04}(stat) \pm 0.03(sys)$ pb, while the theoretical cross section [99] is 0.04 pb with a factor 3-5 uncertainty. This calculation, referred to as KMRS in the following, is the only one available of *exclusive* 2-photon production, and is fully consistent with the CDF measurement. The CDF study used 530 pb^{-1} of delivered luminosity where the *effective* luminosity (single interactions) was only 45 pb^{-1}.

The cross section $\sigma_{\gamma\gamma}(E_T > 5\,\text{GeV}, |\eta| < 2.0)$ at the LHC is 600 fb with a factor 2-4 uncertainty [99].

The measurement is challenging: In runs with nominal LHC optics, i.e. with $\beta^* = 0.55$, the near-beam detectors at 220 m and 420 m do not have acceptance for the process; hence the event selection has to be based on the two photons; absence of pile-up is a prerequisite; the L1 trigger poses a special challenge and would need to be based on the presence of an electromagnetic cluster with $E_T \gtrsim 5\,\text{GeV}$ in conjunction with rapidity gaps.

The feasibility of measuring this reaction at CMS needs to be investigated in detail. This is likewise the case for central exclusive production of χ_c and χ_b mesons.

Chapter 6

Triggering on Diffractive Processes at High Luminosity

6.1 Objective

Diffractive/forward processes typically have values of p_T smaller than those of most hard processes studied at the LHC. Only in those CMS L1 trigger conditions that utilise L1 muon candidates are the p_T thresholds low enough to retain sizable numbers of diffractive events. Conversely, the foreseen L1 jet thresholds are generally too high for diffractive processes. It is hence necessary to introduce a dedicated forward detectors trigger stream in which combining L1 jet conditions with conditions on forward detectors further downstream of the IP makes it possible to lower the jet E_T thresholds substantially.

A case in point is the central exclusive production of a Higgs Boson, $pp \rightarrow pHp$, with Higgs mass close to the current exclusion limit. The dominant decay of a Standard Model Higgs Boson of mass $\sim 120\,\mathrm{GeV}$ is into two b-quarks and generates 2 jets with at most $60\,\mathrm{GeV}$ transverse momentum, p_T, each. The L1 trigger tables of CMS are optimised for events with high p_T; the necessity of keeping the overall L1 rate at acceptable levels requires thresholds in two-jet events above $p_\mathrm{T} = 100\,\mathrm{GeV}$ per jet.

This chapter demonstrates the feasibility of a dedicated forward detectors trigger stream with an output rate of $\mathcal{O}(1)$ kHz for the L1 trigger and of $\mathcal{O}(1)$ Hz for the HLT. In addition, the selection efficiency for several exemplary diffractive processes are presented, both for the dedicated forward detectors trigger stream and for the already foreseen CMS muon trigger. For further details see [101–105].

The proposed forward detectors trigger stream combines the information from the central CMS detector with that from detectors further downstream of IP5. The forward detectors considered are the TOTEM T1 and T2 tracker telescopes as well as the TOTEM Roman Pot detectors up to 220 m downstream of CMS. Information from TOTEM will be available to the CMS L1 trigger. We also consider the FP420 detectors. They cannot be included in the L1 trigger without an increase of the L1 latency of 3.2 μs, though a special, long-latency running mode might be feasible at lower luminosities.

The studies discussed in the following assume that the near-beam detectors are 100% efficient in detecting all particles that emerge at a distance of at least $10\sigma_{beam} + 0.5$ mm from the beam axis (1.3 mm at 220 m and 4 mm at 420 m). Their acceptance was calculated by means of a simulation program that tracks particles through the accelerator lattice [64]. This has been done for the nominal LHC optics, the so-called low-β^* optics ($\beta^* = 0.55$ m), version V6.5 [106, 107]. See Chapter 3 for details.

All Monte Carlo samples used in the following assume LHC bunches with 25 ns spacing. The results presented below do not depend on the specific hardware implementation of the TOTEM T1, T2 and near-beam detectors; they hold for any tracker system with the T1, T2 η coverage in conjunction with near-beam detectors at 220 m from the IP.

6.2 Level-1 Trigger Rates for Forward Detectors Trigger Stream

6.2.1 2-Jet Conditions

As mentioned above, the jets from the reaction $pp \to pHp$, $H \to b\bar{b} \to jj$, with a Higgs mass $M_H = 120\,\text{GeV}$, have transverse energies of at most $60\,\text{GeV}$. In order to retain as large a signal fraction as possible, a low threshold is desirable. In practice, the threshold value cannot be chosen much lower than $40\,\text{GeV}$ per jet. The L1 trigger applies cuts on the calibrated E_T value of the jet. Monte Carlo studies indicate that the uncalibrated value corresponds on the average to about 60% of the calibrated value. Thus, a threshold of $40\,\text{GeV}$ corresponds to $20 - 25\,\text{GeV}$ in reconstructed E_T, i.e. to values where noise starts becoming sizable.

For luminosities of $10^{32}\,\text{cm}^{-2}\,\text{s}^{-1}$ and above, the rate from standard QCD processes for events with at least 2 central jets ($|\eta| < 2.5$) with $E_T > 40\,\text{GeV}$ exceeds by far the target output rate of $\mathcal{O}(1)$ kHz. Thus additional conditions need to be employed in the L1 trigger to reduce the rate from QCD processes. The efficacy of several conditions was investigated and, in the following, the corresponding rate reduction factors are always quoted with respect to the rate of QCD events that contain at least 2 central jets with $E_T > 40\,\text{GeV}$ per jet.

The QCD background events were generated with the PYTHIA Monte Carlo generator. In order to assess the effect when the signal is overlaid with pile-up, a sample of 500,000 pile-up events was generated with PYTHIA. This sample includes inelastic as well as elastic and single diffractive events. The correction to the PYTHIA leading proton spectrum described in [108] was used to obtain the results discussed in the following. However, recent theoretical results indicate that this correction overestimates the rate of final state protons in the acceptance range of the near-beam detectors at 220 m and 420 m by a factor 3 [109]. Hence, all rates obtained in the following can be read as upper limits of the expected rates.

In the following we describe the trigger conditions studied:

- Condition based on central CMS detector quantities

  In addition to the E_T values of individual L1 jets, the CMS Calorimeter Trigger has at its disposal the scalar sum, H_T, of the E_T values of all jets. Requiring that essentially all the E_T be concentrated in the two central L1 jets with highest E_T, i.e. $[E_T^1 + E_T^2]/H_\text{T} > 0.9$ (H_T condition), corresponds to imposing a rapidity gap of at least 2.5 units with respect to the beam direction. This condition reduces the rate of QCD events by approximately a factor 2, independent of the presence of pile-up and with only a small effect on the signal efficiency.

- Condition based on TOTEM detectors T1 and T2

  Using T1 and T2 as vetoes in events with 2 central L1 jets imposes the presence of a rapidity gap of at least 4 units. This condition suppresses QCD background events by several orders of magnitude. At luminosities low enough so that not more than one interaction takes place per bunch crossing, the signal efficiency is very high ($> 90\%$). In the presence of pile-up, the signal efficiency falls rapidly. The non-diffractive component in pile-up events tends quickly to fill in the rapidity gap in

the Higgs production process. Only about 20 (5) % of the signal events survive in the presence of 1 (2) pile-up event(s) [110].

- Condition based on near-beam detectors

Demanding that a proton be seen in the near-beam detectors at 220 m results in excellent suppression of QCD background events in the absence of pile-up, see Fig. 6.1. At $2 \times 10^{33}\,\mathrm{cm}^{-2}\,\mathrm{s}^{-1}$, where on the average 7 pile-up events overlay the signal event, the diffractive component in the pile-up causes the reduction to decrease to a factor ~ 4, and at $10^{34}\,\mathrm{cm}^{-2}\,\mathrm{s}^{-1}$ to a factor ~ 2. For completeness, conditions based on the near-beam detectors at 420 m from the interaction point are included as well. Their coverage in ξ is complementary to that of the detectors at 220 m, and hence the reduction factors obtained with them are of interest both in the L1 trigger for special, long-latency runs and, in normal running conditions, for the HLT.
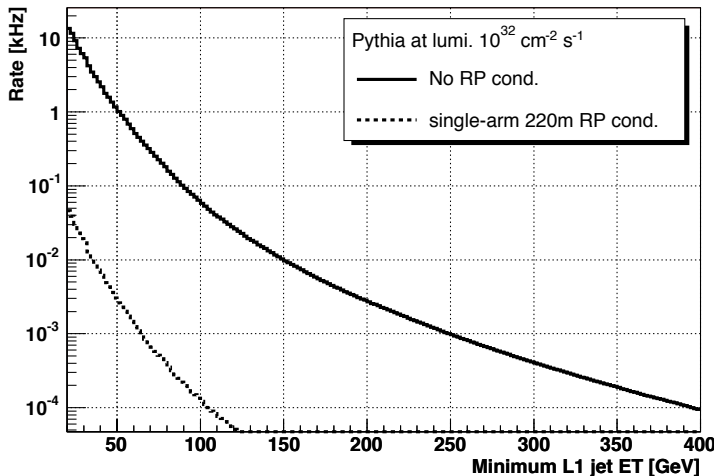
Figure 6.1: L1 rate for the QCD background at a luminosity of $10^{32}\,\mathrm{cm}^{-2}\,\mathrm{s}^{-1}$ and in the absence of pile-up as function of the L1 threshold value when at least 2 central L1 jets with E_T above threshold are required.

Table 6.1 summarises the reduction factors achieved with different near-beam detector conditions: a track in the near-beam detectors at 220 m on one side of the IP (single-arm 220 m), without and with a cut on ξ, a track at 420 m on one side of the IP (single-arm 420 m), a track at 220 m and 420 m (asymmetric). Because the detectors at 220 m and 420 m have complementary coverage in ξ, the last condition in effect selects events with two tracks of very different ξ value, in which one track is seen at 220 m on one side of the IP and a second track is seen on the other side at 420 m. On the HLT, these asymmetric events can be identified and are thus of highest interest.

A collimator located in front of the LHC magnet Q5, planned to be operative at higher luminosities, will have an effect on the acceptance of the near-beam detectors resembling that of a ξ cut. This effect has not been taken into account in Table 6.1.

- Topological conditions

A further reduction of the QCD rate could be achieved with the help of a topolog-

ical condition. The 2-jet system has to balance the total momentum component of the two protons along the beam axis. In signal events with asymmetric ξ values, the proton seen on one side in the near-beam detectors at 220 m distance is the one with the larger ξ and thus has lost more of its initial momentum component along the beam axis. Hence the jets tend to be located in the same η-hemisphere as the near-beam detectors that detect this proton. A trigger condition requiring that $[\eta^{jet1} + \eta^{jet2}] \times \text{sign}(\eta^{220m\ det}) > 0$ reduces the QCD background by a factor 2, independent of pile-up, and with no loss in signal efficiency.

Table 6.1 summarises the situation for luminosities between $10^{32}\,\mathrm{cm^{-2}\,s^{-1}}$ and $10^{34}\,\mathrm{cm^{-2}\,s^{-1}}$. Given a target rate for events with 2 central L1 jets of $\mathcal{O}(1)$ kHz, a total rate reduction between a factor 20 at $1 \times 10^{33}\,\mathrm{cm^{-2}\,s^{-1}}$ and 200 at $1 \times 10^{34}\,\mathrm{cm^{-2}\,s^{-1}}$ is necessary. The first row calculated for a luminosity of $1 \times 10^{32}\,\mathrm{cm^{-2}\,s^{-1}}$ illustrates the reduction potential of the near-beam detectors in the limit of vanishing event pile-up. It can therefore be interpreted as the portion of QCD events with a track observed in the near-beam detectors. Note that this rate is significantly lower for high p_T dijet events than the corresponding rate for minimum bias events. The expected average number of additional proton-proton interactions per bunch crossing of 0.35 at this luminosity will reduce the achievable reduction factor. Beam induced backgrounds may limit the reduction factor further (see Sec. 6.4), however without compromising the Level-1 rate limit in this luminosity regime. It is interesting to note that the L1 2-jet rate (third column of Table 6.1) is directly proportional to the luminosity (and not to its square, as would be expected for pile-up); this is because pile-up events are typically too soft to contribute jets in the central detector; however, they contribute protons in the near-beam detectors.

Table 6.1: Reduction of the rate from standard QCD processes for events with at least 2 central Level-1 jets with $E_T > 40\,\mathrm{GeV}$, achievable with requirements on the tracks seen in the near-beam detectors. Additional rate reductions can be achieved with the H_T condition and with a topological condition. Each of them yields, for all luminosities listed, an additional reduction by about a factor 2.

Luminosity $[\mathrm{cm^{-2}\,s^{-1}}]$	Pile-up events per BX	Level-1 2-jet rate [kHz] for $E_T > 40\,\mathrm{GeV}$	Total reduction needed	Reduction when requiring track in det at					
				220 m $\xi < 0.1$		420 m	220 & 420 m (asymmetric)	$\xi < 0.1$	420 & 420 m
1×10^{32}	–	2.6	2	370					
1×10^{33}	3.5	26	20	7	15	27	160	380	500
2×10^{33}	7	52	40	4	10	14	80	190	150
5×10^{33}	17.5	130	100	3	5	6	32	75	30
1×10^{34}	35	260	200	2	3	4	17	39	10

In summary, a reduction of the QCD rate to levels compatible with a L1 output target rate of $\mathcal{O}(1)$ kHz by including near-beam detectors at a distance of 220 m from the CMS IP thus appears feasible for luminosities up to $2 \times 10^{33}\,\mathrm{cm^{-2}\,s^{-1}}$, as long as a ξ cut can be administered in the L1 trigger. This option is currently under investigation by TOTEM.

6.2.2 Other Conditions

The effect of combining the standard CMS L1 trigger conditions [111] with conditions on the near-beam detectors is illustrated in Table 6.2. The table entries marked with a '(c)' indicate that thresholds have to be implemented in conjunction with the $\xi < 0.1$ condition. Conditions requiring that a proton be seen on one side (both sides) are marked 's' ('d').

Table 6.2: Estimated E_T thresholds that result in a L1 output rate of ~ 1 kHz, for various conditions on central CMS detector quantities and on tracks seen in the near-beam detectors at 220 m and 420 m. '(c)' indicates that thresholds have to be implemented in conjunction with the $\xi < 0.1$ condition. Conditions requiring that a proton be seen on one side (both sides) are marked 's' ('d').

L1 condition	L1 E_T or p_T threshold [GeV] at $\mathcal{O}(1)$ kHz L1 output rate for luminosity [cm^{-2} s^{-1}]			
	1×10^{33}	2×10^{33}	5×10^{33}	1×10^{34}
1 Jet	115	135	160	190
2 Jet	90	105	130	150
1 Jet+220s	90	115	155	190
2 Jet+220s	65	90	125	150
1 Jet+220d	55	85	130	175
2 Jet+220d	30	60	100	140
1 Jet+220s(c)	70	90	150	185
2 Jet+220s(c)	60	70	115	145
1 Jet+220d(c)	30	65	110	155
2 Jet+220d(c)	20	45	85	125
1 Jet+420s	65	90	125	165
2 Jet+420s	45	70	100	130
1 Jet+420d	20	40	80	115
2 Jet+420d	< 10	30	60	90
1 μ+220s	12	16	23	> 100
1 μ+220d	4	9	17	80
1 μ+220s(c)	–	11	22	100
1 μ+220d(c)	–	6	13	30
1 μ+420s	7	11	14	37
1 μ+420d	< 2	4	7	14

A further rate reduction by approximately a factor two can be obtained at luminosities with negligible pile-up by imposing a rough large rapidity gap cut at L1. This was implemented by requiring that there be no forward jets, i.e. jets in the CMS HF, in either hemisphere in the event.

6.3 Level-1 Signal Efficiencies

Of the L1 conditions discussed so far, only those based on the near-beam detectors have a significant impact on the signal efficiency. Of further interest is the question how many signal events are being retained by the already foreseen trigger streams, notably the muon trigger.

6.3.1 Central Exclusive Higgs Production $H(120\,\text{GeV}) \to b\bar{b}$

In order to study the effect of the L1 trigger selection on the Higgs signal, signal samples of 100,000 events with central exclusive production of a Higgs Boson were generated with the Monte Carlo programs EDDE [112] (version 1.1) and EXHUME [68] (version 1.0).
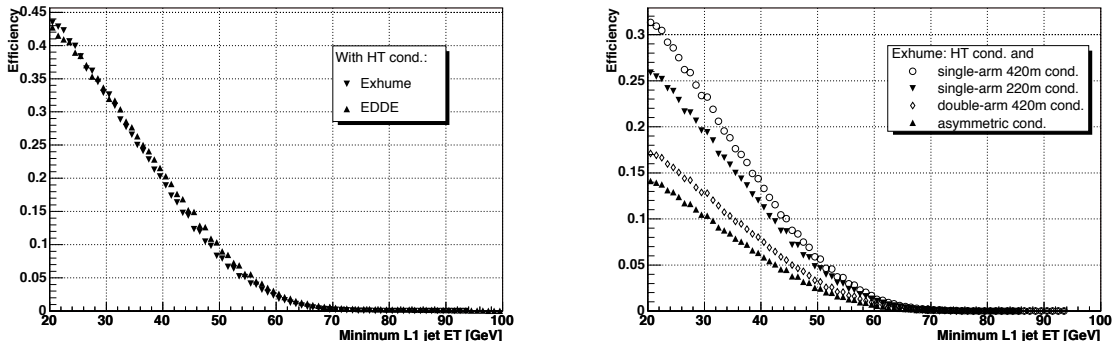

Figure 6.2: L1 selection efficiency for $pp \to pHp$ and $H(120\,\text{GeV}) \to b\bar{b}$ as function of the E_T threshold value when requiring at least 2 central L1 jets with E_T above threshold. All plots are for the non-pile-up case and the H_T condition (see text) has been applied. Left: Comparison between the EDDE and EXHUME Monte Carlo generators, without applying any additional near-beam detector conditions. Right: Comparison of the effect of different near-beam detector conditions on the efficiency in the EXHUME Monte Carlo sample.

Condition based on near-beam detectors

Figure 6.2 shows the L1 selection efficiency as a function of the E_T threshold values when requiring at least 2 central L1 jets with E_T above threshold. The plot on the left-hand side compares the efficiency curves obtained for EDDE and EXHUME. For a threshold of $40\,\text{GeV}$ per jet, EXHUME and EDDE both yield an efficiency of about 20%. The plot on the right-hand side overlays the efficiency curves obtained with Exhume when including four different near-beam detector conditions in the L1 2-jet trigger: single-arm 220 m, single-arm 420 m, double-arm 420 m and the asymmetric 220 & 420 m condition. At an E_T threshold of $40\,\text{GeV}$ per jet, the single-arm 220 m (420 m) condition results in an efficiency of the order 12% (15%), the double-arm 420 m condition in one of 8% and the asymmetric condition in one of 6%. This also means that, even without the possibility of including the near-beam detectors at 420 m from the CMS IP in the L1 trigger, 6% of the signal events can be triggered with the single-arm 220 m condition, but will also have a track also in the 420 m detectors which can be used in the HLT.

Condition based on Muons

An alternative trigger strategy is to exploit the relatively muon-rich final state from B-decays: about 20% of the events have at least one muon in the final state. Several conditions have been studied [105]. The resulting rates in the following are always quoted at a luminosity of $10^{33}\,\text{cm}^{-2}\,\text{s}^{-1}$.

- At least 1 muon. A p_T threshold of $14\,\text{GeV}$ corresponds to an efficiency of 6% at a rate of approximately 2 kHz.
- At least 2 muons. A p_T threshold of $3\,\text{GeV}$ on the lower p_T muon, as in the CMS

DAQ-TDR [113], gives an efficiency of 2% and a rate of approximately 1.5 kHz.

- At least 1 muon and 1 jet, the latter with $E_T > 40\,\text{GeV}$. This condition is not yet foreseen in the CMS trigger tables. For a muon p_T threshold of $3\,\text{GeV}$, the rate is slightly less than 3 kHz, with a signal efficiency of 9%.

In summary, about 20% of the $H \to b\bar{b}$ events have a muon in the final state. Of these, about half can be triggered by implementing a 1 muon + 1 jet trigger with thresholds of $3\,\text{GeV}$ on the muon p_T and $40\,\text{GeV}$ on the jet E_T. The rate would then be approximately 3 kHz at a luminosity of $10^{33}\,\text{cm}^{-2}\,\text{s}^{-1}$; no condition on the forward detectors is assumed.

6.3.2 Central Exclusive Higgs Production $H(140\,\text{GeV}) \to WW$

We limit ourselves to a few remarks on the L1 selection efficiency. For SM Higgs masses above $120\,\text{GeV}$, the $H \to WW$ branching ratio becomes sizable; in this case the final state contains high-p_T leptons, and triggering is easier.

Efficiencies are in general high. About 23% of the events have at least one muon in the final state. Approximately 70% of these (i.e. 16%) are retained by requiring at least one muon with a p_T threshold of $14\,\text{GeV}$. An extra $\approx 10\%$ (i.e. 2%) would be retained by implementing the muon/jet slot discussed above with thresholds of $3\,\text{GeV}$ on the muon p_T and $40\,\text{GeV}$ on the jet E_T.

6.3.3 Single diffractive hard processes

Double-Pomeron exchange processes constitute only a small part of the diffractive cross section. Hard single-diffraction, $pp \to pX$, where only one proton remains intact have much higher cross sections than hard double-Pomeron exchange events. Efficiencies have been studied for $pp \to pX$, with X containing a W or a Z boson that decays to jets and to muons, as well as with X containing a dijet system. Samples of 100,000 signal events each were generated with the POMWIG Monte Carlo generator [45] (version 1.3).

For four example processes, Fig. 6.3 shows the efficiency as a function of the L1 threshold value, normalised to the number of events (in the muon rate case to the number of events with a muon in the final state) where for the diffractively scattered proton $0.001 < \xi < 0.2$ holds [104]. Three different trigger conditions are considered: trigger on central detector quantities alone (i), trigger on central detector quantities in conjunction (ii) with the single-arm 220 m condition, and (iii) with the single-arm 420 m condition. Also shown is the number of events expected to pass the L1 selection per pb^{-1} of LHC running. There, a gap survival probability of unity was assumed. However, at the LHC this factor is expected to be $\mathcal{O}(0.1)$. As the Tevatron results summarised in Sec. 1.2.4 indicate, the survival probability is the same for events selected with rapidity gap methods and for events selected by requiring a leading proton.

6.4 Effect of beam induced backgrounds

Pile-up effects are included in all rate and efficiency studies presented so far.

The rate of a L1 trigger stream that makes use of near-beam detectors at 220 m is also affected by machine induced background. This background is discussed in Ch. 4. It should be noted that at this stage the simulation and thus estimating this type of background is subject to large uncertainties. The effect from beam-halo and beam-gas events on the L1 rate is not yet
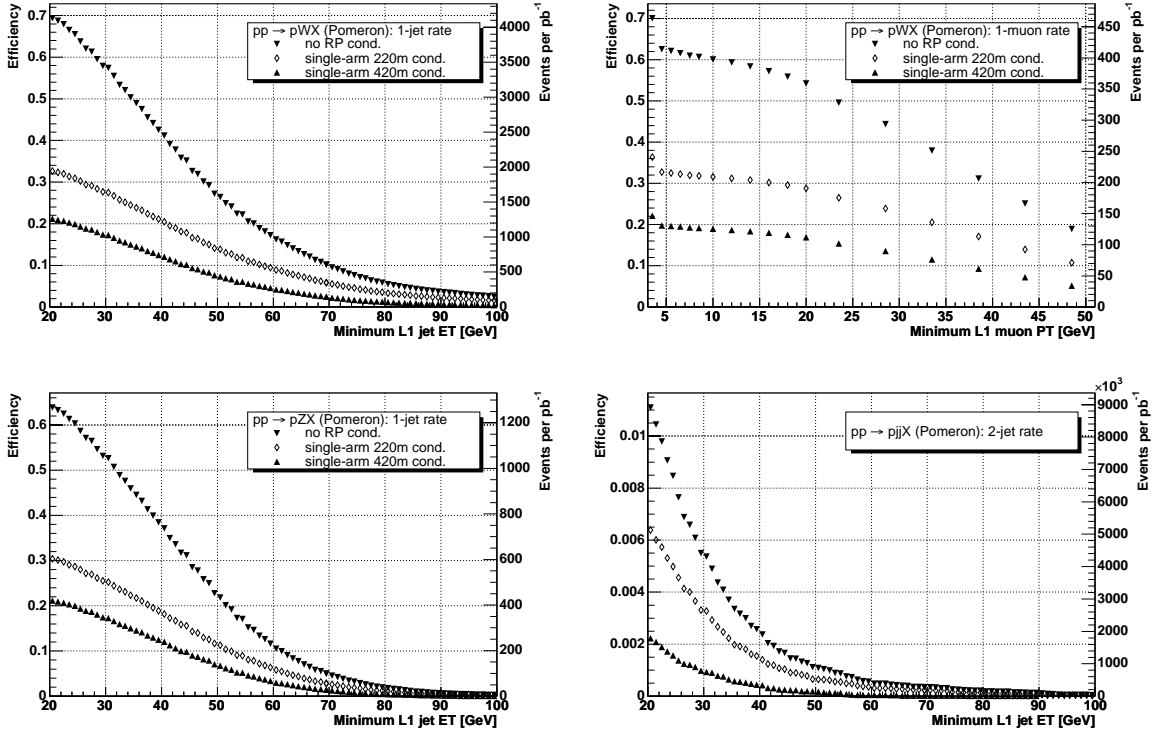
Figure 6.3: Selection efficiency as function of the threshold value for $pp \rightarrow pWX$ (upper left and upper right), $pp \rightarrow pZX$ (lower left), $pp \rightarrow pjjX$ (lower right). At least one L1 jet with E_T above threshold is required (upper and lower left), at least two L1 jets with E_T above threshold are required (lower right), at least one L1 muon with p_T above threshold is required (upper right). The normalization of the efficiency curves (left y-axis) is explained in the text. The number of events expected to pass the L1 selection per pb^{-1} of LHC data (right y-axis) does not take into account the gap survival probability which at the LHC is expected to be $\mathcal{O}(0.1)$. All plots are for the non-pile-up case.

included in the studies discussed here. Preliminary estimates suggest that they are chiefly a concern for any trigger condition based solely on the forward detectors. For any trigger condition that includes a requirement on central CMS detector quantities the size of their contribution is such that they do not lead to a significant increase of the L1 output rate.

Proton-proton interactions lead also to signals in the near-beam detectors. Currently available estimates result in probabilities between 1.4% and 6.3% that a proton-proton interaction produces a fake proton in either of the two arms of the near-beam detectors at 220 m. This ratio is independent of the running scenario because both the physics signal rate and the proton-proton background rate scale with the luminosity. As a numerical example, assuming an average probability of 4%, the achievable reduction factor (see Table 6.1) would be limited to approximately 25 at $10^{32} \, \text{cm}^{-2} \, \text{s}^{-1}$.

We conclude that the required L1 reduction factor can be achieved up to luminosities of the order of $10^{33} \, \text{cm}^{-2} \, \text{s}^{-1}$. However, more detailed and refined studies of the beam induced background are necessary to improve the accuracy and to consolidate our conclusions.

6.5   HLT strategies for a diffractive trigger stream

Section 6.2.1 demonstrated that the default CMS L1 dijet thresholds can be lowered substantially, to about $E_T > 40\,\text{GeV}$, when the dijet condition is combined with the requirement that a proton be seen in the near-beam detectors at 220 m on one side. The L1 output rate for this condition is of the order 1 kHz for luminosities up to $2 \times 10^{33}\,\text{cm}^{-2}\,\text{s}^{-1}$. This section addresses the question if the output rate of a dedicated forward detectors trigger stream based on this condition can be kept to $\mathcal{O}(1)$ Hz on the HLT.

Jets are reconstructed at the HLT with an iterative cone ($R < 0.5$) algorithm. The L1 selection cuts are repeated with the HLT which employs much more sophisticated reconstruction algorithms, as described in [113]. Given the physics interest of central exclusive production of $H \to b\bar{b}$, the option of a b-tag is investigated as well. The b-tagging algorithm relies on the track impact parameter information. A jet is considered a b-jet candidate if it contains a minimum number of tracks with impact parameters consistent with coming from a B decay. For details of this method see Chapter 15.6 of [113].

The following conditions are considered [104]:

A   The events pass the single-arm 220 m L1 condition with $\xi < 0.1$ cut. As demonstrated in Table 6.1, this condition reduces the L1 output rate to below $\mathcal{O}(1)$ kHz. Additional rate reduction factors of ~ 300 (~ 1000) at $1(2) \times 10^{33}\,\text{cm}^{-2}\,\text{s}^{-1}$ are needed to reach the HLT target output rate of $\mathcal{O}(1)$ Hz.

B   The two jets are back-to-back in the azimuthal angle ϕ ($2.8 < \Delta\phi < 3.48$ rad), and have $(E_T^1 - E_T^2)/(E_T^1 + E_T^2) < 0.4$, and $E_T > 40\,\text{GeV}$ for each jet.

C   The proton fractional momentum loss ξ is evaluated with the help of calorimeter quantities:

$$\xi_{+-} = (1/\sqrt{s})\Sigma_i E_{Ti}\, e^{\pm\eta_i}, \tag{6.1}$$

where the sum runs over the two jets and the $+, -$ signs denote the two hemispheres. The result is compared with the ξ value measured by the near-beam detectors. Events are rejected if the difference between the two values of ξ is larger than $2\,\sigma$. At present, no simulation of the near-beam detector reconstruction in the HLT is available. As estimate of the ξ resolution, 15% (10%) is assumed at 220 m (420 m).

In the presence of pile-up, this condition is effective in rejecting fake single diffractive events where the proton came from a pile-up event. For a more detailed discussion of this method, see Chapter 7.

D   At least one of the two jets is b-tagged.

E   A proton is seen at 420 m.

The case without pile-up presents no difficulty: essentially no QCD background events survive the selection. For luminosities up to $2 \times 10^{33}\,\text{cm}^{-2}\,\text{s}^{-1}$, the combination of conditions A+B+C+E leads to the targeted HLT output rate of $\mathcal{O}(1)$ Hz, as is clear from Table 6.3. This combination of conditions is effective for any double-Pomeron exchange process with production of two central jets.

As in the case of the L1 trigger, the channel $pp \to pHp$ with $H(120\,\text{GeV}) \to b\bar{b}$ would profit substantially from a diffractive trigger stream with lowered jet E_T thresholds also on HLT. If conditions A+B+C are applied, the signal efficiency is at 11% essentially unchanged with respect to the L1 selection, but the HLT output rate exceeds the target output rate. If b-tagging

is required but no ξ matching (conditions A+B+D), the efficiency drops to 7%, without any improvement in the rate reduction. The combination of conditions A+B+C+E leads to the targeted HLT output rate of $\mathcal{O}(1)$ Hz without any loss in signal efficiency compared to L1.

Table 6.3: Results of HLT selection.

HLT selection condition	A+B+C	A+B+D	A+B+C+E
HLT rate at $1 \times 10^{33}\,\mathrm{cm}^{-2}\,\mathrm{s}^{-1}$	15 Hz	20 Hz	< 1 Hz
HLT rate at $2 \times 10^{33}\,\mathrm{cm}^{-2}\,\mathrm{s}^{-1}$	60 Hz	80 Hz	1 Hz
Signal eff. $H(120\,\mathrm{GeV}) \to b\bar{b}$	11%	7%	6 %

6.6 Conclusion

Combining trigger conditions based on the CMS central detector with information from near-beam detectors at 220 m and 420 m increases substantially the potential for retaining diffractive events in the trigger, notably for the case of central exclusive production of a Higgs Boson with mass around 120 GeV.

The default CMS dijet trigger thresholds can be lowered substantially, to $E_T > 40$ GeV for each jet, when in addition a proton candidate is required in the near-beam detectors at 220 m. At the HLT, conditions can be used that are based on the match between the invariant mass produced in the interaction as calculated from the jets in the central CMS detector and as calculated from the fractional momentum loss, ξ, of the detected proton candidates in the near-beam detectors.

A dedicated diffractive trigger stream hence is found feasible, with output rates of $\mathcal{O}(1)$ kHz on L1 and $\mathcal{O}(1)$ Hz on the HLT.

The conclusions reached in this chapter were obtained using a cross section for leading proton production which recent theoretical estimates [109] suggest is overestimated by a factor 3. All rates obtained can therefore be read as upper limits of the expected rates.

Chapter 7

Hard Diffraction at High Luminosity

The high luminosities available at the LHC will give unprecedented access to rare diffractive processes. This chapter presents two analyses of high luminosity data: central exclusive production of a Higgs boson and DPE production of top quarks. A light Higgs ($\sim 120\,\mathrm{GeV}$) mainly decays to $b\bar{b}$, but its detection in non-diffractive events is hopeless because of non-resonant $b\bar{b}$ production, which leads to a minute signal-to-background ratio. Most of this background disappears in central exclusive production, $pp \to pHp$, which may offer signal-to-background ratios of order unity in the SM case and much larger in some MSSM scenarios. In the latter case, central exclusive production would be a discovery channel. Diffractive production of t quarks would give access to diffractive PDFs and to the rapidity gap survival probability.

While interesting in their own right, these channels are taken as exemplary of the main experimental challenge at high luminosity along with the trigger: the pile-up. The problem is the following: at high luminosity, in a given bunch crossing, many collisions occur. Some portion of these events have leading protons within the acceptance of the near-beam detectors used for tagging diffractively scattered protons. This is notably true for diffractive events in the pile-up ($\sim 20\%$ of the total). It may thus happen that a non-diffractive event appears as diffractive because it is overlaid with one (or more) diffractive pile-up events. The size of the problem is quantified by the fact that the cross section for a given hard process at the LHC is expected to be typically ≈ 100 times higher than that of the corresponding diffractive process.

The two processes chosen for detailed analysis, central exclusive production of a SM Higgs and inclusive DPE production of top pairs, are among the most challenging because of the low cross section and high background. We show that in both cases the pile-up background can be reduced by several orders of magnitude with relatively simple requirements. The potential is discussed of further, more elaborate requirements which can bring the signal-to-background ratio to values significantly larger than unity. In the Higgs case, already with the present cuts, certain MSSM scenarios give a signal-to-background ratio of 10-100 and about 1000 expected signal events for an integrated luminosity of $30\,\mathrm{fb}^{-1}$ at an instantaneous luminosity of $2 \times 10^{33}\ \mathrm{cm}^{-2}\,\mathrm{s}^{-1}$. For a SM Higgs, alternative lower background channels, e.g. $H \to WW$, are being studied.

The Higgs analysis assumes near-beam detectors both at 220 m and at 420 m from the interaction point. The top analysis only assumes the 220 m detectors. Both analyses presented are still in progress; their main point is to demonstrate that the issue of pile-up is being studied in detail and with appropriate tools. These studies are stimulating the theoretical community to produce reliable estimates not only for the hard-diffractive, low cross section processes,

but also for the large cross section, soft reactions that lead to pile-up. They are also helping to define some of the measurements that will need to be made in the early days of LHC running – the leading proton spectrum from soft events among them.

The present studies show that high-luminosity measurements of rare, hard diffractive processes at the LHC are feasible.

7.1 Pile-up

The unprecedented high luminosities at the LHC come at the cost of event pile-up, i.e. each hard scatter will be overlaid with a luminosity-dependent number of generally soft events. At an instantaneous luminosity of $2 \times 10^{33}\,\mathrm{cm}^{-2}\,\mathrm{s}^{-1}$, the average number is 7 events per crossing, at $1 \times 10^{34}\,\mathrm{cm}^{-2}\,\mathrm{s}^{-1}$ it is 35. Of these pile-up events, of the order of 3% (1%) contain a proton within the acceptance of near-beam detectors at 220 m (420 m).

For the selection of diffractive events at the LHC at high luminosities, these leading protons from pile-up are a major background source. To illustrate the point, we consider the case of central exclusive production (CEP) of a Higgs boson with 120 GeV mass, $pp \to pHp$, that decays into a pair of b-jets. This is discussed in more detail in Sec. 7.2. For the non-diffractive production of a Higgs boson of this mass and decay channel, the background from inclusive dijet production is overwhelming. Quantum number selection rules in the case of CEP suppress this background to a large extent (see Sec. 7.2). However, inclusive dijet events, when they occur in coincidence with pile-up events that have leading protons within the acceptance of the near-beam detectors, appear to have the same signature as the signal. Simple combinatorics yield an estimate at $2 \times 10^{33}\,\mathrm{cm}^{-2}\,\mathrm{s}^{-1}$ that of the order of a few per mill of inclusive dijet events are being mistaken as signal events. Given the much larger cross section of inclusive dijet events compared to the signal, this is the most important source of background.

This background can be reduced by exploiting the correlations between quantities measured in the main detector and those measured with the near-beam detectors. One possibility is to estimate the fractional momentum loss, ξ, of the protons with the help of the dijet system as $\xi_{1,2} = \frac{1}{\sqrt{s}}[\Sigma E_T^{jet} e^{\pm\eta}]$, where the sum is over the two jets and η denotes their pseudorapidity (see Chapter 5), and then compare it with the value found with the near-beam detectors.

Another possibility is the use of fast timing detectors that determine whether the protons seen in the near-beam detectors came from the same vertex as the hard scatter. Fast timing detectors with an expected vertex resolution of better than 3 mm are part of the FP420 project. Preliminary Monte-Carlo studies indicate that with nominal LHC running conditions a rejection of about 97% is possible of events that appear to be double Pomeron exchange events, but where the protons in reality originated from coincidences with pile-up events.

7.1.1 The leading proton spectrum

A key ingredient in the determination of the pile-up background is the ξ and p_T^2 spectrum of the protons produced in soft SD and DPE interactions.

For the studies presented in this chapter, PHOJET [66] was used to simulate the SD and DPE leading proton spectra. Figure 7.1 compares the predictions of PHOJET (for $\sqrt{s} = 14\,\mathrm{TeV}$) and the spectra measured at ZEUS [114, 115] as a function of $x_L = 1 - \xi$. Vertex factorisation and limiting fragmentation imply that the spectrum measured at HERA should be equal to that
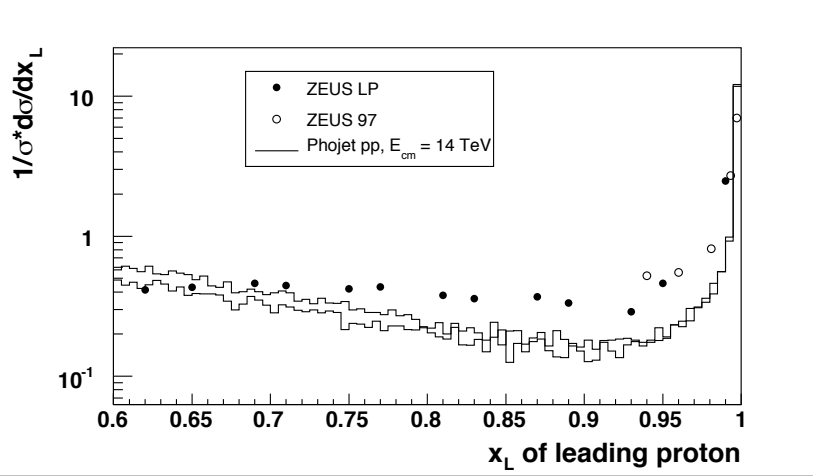
Figure 7.1: Leading proton x_L spectrum as measured at HERA [114, 115] and predictions of PHOJET for $\sqrt{s} = 14$ TeV. PHOJET describes the high-x_L data satisfactorily in the region of coverage of the 420 m detectors ($x_L > 0.98$); it underestimates the data by a factor about 2 in the region covered by the 220 m detectors. Based on the predictions in [109], the PHOJET normalisation for the LHC should be lowered by a factor 3 in the 420 m region and should be taken at face value in the region covered by the 220 m detectors.

at the LHC. However, recent theoretical estimates [109] suggest that in the region of interest here, $\xi < 0.2$, the leading proton spectrum at the LHC should be obtained by scaling the HERA data down by a factor ~ 3. This takes into account the energy dependence of the rapidity gap survival probability. Figure 7.1 shows that PHOJET gives a fair description of the HERA data in the diffractive-peak region ($\xi < 0.01 - 0.02$), while it underestimates the data by a factor ~ 2 for $0.02 < \xi < 0.2$. The pile-up rate as predicted by PHOJET will therefore have to be reduced by a factor 3 in the diffractive-peak region covered by the 420 m detectors (a factor 9 for DPE events in which both protons are detected at 420 m). We will take the PHOJET prediction to be correct in the ξ region covered by the 220 m detectors. Unless stated otherwise, the correction factors just discussed are applied to all PHOJET results presented in this chapter.

In the trigger studies presented in Chapter 6, pile-up events were instead simulated with PYTHIA [116], reweighted so as to reproduce the ZEUS data over the whole ξ spectrum [108]. The leading proton rates there are therefore overestimated by a factor approximately 3.

The diffractive pile-up rates are currently affected by a large uncertainty, probably at least a factor 2-3. The signal-to-background ratios presented in this chapter should therefore be taken with care. It is imperative that the leading proton spectrum at the LHC be measured as soon as possible. Ideally, this should be done in one of the special-optics, low-luminosity runs in which the ξ coverage of the TOTEM detectors is largest.

7.1.2 Rapidity gap detection vs pile-up at high luminosity: the CDF experience

As just discussed, the study of hard single diffraction (HSD) at high luminosity, where the average number of events per crossing is $\gtrsim 1.0$, is plagued by pile-up. The situation is better for exclusive double pomeron exchange (DPE) processes with both protons measured and a

fully measured central state, as one has kinematic, spatial and timing constraints not present in HSD – even there though pile-up is the most significant background source at high luminosity. If we take the Tevatron as an example, the reason is basically that of all central dijets (or W- and Z-bosons) only about 1% are from HSD [28, 32, 33, 35], while about 10% of all interactions are diffractive and have a leading proton. When triggering on a central dijet, if there happened to be two or more interactions it is more likely that a forward proton came from another interaction than from the dijet interaction.

Experience from the Tevatron demonstrates this point. In CDF two triggers can be compared, a central (inclusive) dijet trigger 'JJ' and the same trigger with a coincident forward antiproton 'pJJ'. The ratio of rates pJJ/JJ at very low luminosity is $\approx 1\%$ but it rises with increasing luminosity (as $\mathcal{L}^2$) and exceeds 10% at $\mathcal{L} \approx 2 \times 10^{31}$ cm^{-2} s^{-1} at which the average number of interactions per bunch crossing is still only $\bar{n} = 0.75$. Even though $\bar{n} < 1$ about 90% of the events are pile-up. This is remedied in CDF using forward detectors in the direction of the forward anti-proton. One possibility is to simply require a forward gap $\Delta \eta \gtrsim 1.0$ with no hadrons. CDF employs a method using more information, the E_T and η of all particles (or calorimeter showers) detected in CDF, excluding the leading anti-proton. From energy E and p_z conservation one can derive [86] the following estimator of ξ:

$$\xi' = \frac{1}{\sqrt{s}} \sum_{particles} E_T e^{+(-)\eta}. \tag{7.1}$$

In CDF the detected anti-proton has a negative η value. The accompanying particles also with large negative η count heavily in the sum; the particles on the far side (large positive η) are irrelevant. At low luminosity with no pile up, $\xi_{\bar{p}} \approx \xi'$, where $\xi_{\bar{p}}$ is obtained from the Roman pot detectors, i.e. ξ' is a good estimator of ξ. When $L = 0.6 \times 10^{31}$ cm^{-2} s^{-1} and $\bar{n} \approx$ 0.2, pile-up and signal are about equal. Off-line one can require $\xi_{\bar{p}} \approx \xi'$, which is similar to requiring no particles with large negative η. Other off-line pile-up rejection techniques used by experiment UA8 at the CERN $Sp\bar{p}S$ collider used [23] event timing from central counters, a single central reconstructed vertex and p_{tot}, the sum of the proton p_z and the longitudinal energy in the UA2 calorimeter on the proton side, which should not be more than p_{beam}.

A consequence of having to require no pile-up for HSD is that the effective luminosity for single interactions, $\mathcal{L}_\mathrm{eff}$, is lower than the delivered luminosity $\mathcal{L}_\mathrm{del}$. In a CDF study needing single interactions, $\mathcal{L}_\mathrm{del}$ was $530\,\mathrm{pb}^{-1}$ while $\mathcal{L}_\mathrm{eff}$ was only $45\,\mathrm{pb}^{-1}$, as Tevatron stores typically start with $\bar{n} \approx 5$ and are dumped when $\bar{n} \approx 1$.

The situation at the LHC is summarised in Table 7.1 for certain assumptions on running conditions. In certain cases, in particular for high luminosity as expected for the nominal LHC running condition at $\beta^* = 0.55$ m, only a fraction of the delivered luminosity consist of collisions with a single proton-proton interaction. The expected total luminosity usable for HSD is limited and will be collected during the start-up phase of the collider. Even though it is unlikely to exceed $1\,\mathrm{fb}^{-1}$, it will still take us well into the regime of single diffractive W- and Z-boson and even $t\bar{t}$ production.

Central exclusive production of Higgs, W^+W^- and ZZ pairs with both protons detected is not, of course, immune to pile-up but there are many more handles. Calorimetric rapidity gaps cannot be used as the cross sections are small and we must live with pile-up. However precise ($\approx$ 10-20 ps) timing on the forward protons will provide a z_{vertex}^{pp} with $\sigma_{pp}(z) \approx$ 2-5 mm to match with the central (b$\bar{\mathrm{b}}$, W$^+$W$^-$, ZZ) vertex, and there are also kinematic constraints (missing mass M_X in p + p $\to$ p + X + p, and p_T and p_z balance). Timing detectors

Table 7.1: Effective luminosity and average number of interactions per beam crossing for different running conditions at the LHC. The last column indicates the fraction of effective luminosity when requiring a single interaction.

$\beta^*(m)$	N(bunches)	$\mathcal{L}_{\mathrm{del}}\,[\,\mathrm{cm}^{-2}\,\mathrm{s}^{-1}]$	$\bar{n}$ /crossing	$\mathcal{L}_{\mathrm{eff}}/\mathcal{L}_{\mathrm{del}}$
18	43	3×10^{29}	0.07	0.95
2	156	2×10^{31}	1.26	0.40
2	156	1×10^{32}	6.30	0.01
2	936	1×10^{32}	1.05	0.46
0.55	2808	2×10^{33}	7	0.006

of this type are planned for the FP420 project (see Sec. 2.3).

7.2 SM and MSSM central exclusive Higgs production

7.2.1 Introduction

As the delivered luminosity reaches tens of fb^{-1}, the central exclusive production process becomes a tool to search for new physics [117].

By central exclusive, we refer to the process $pp \rightarrow p\phi p$, where there are large rapidity gaps between the outgoing protons and the decay products of ϕ. There are three primary reasons why this process is attractive. Firstly, if the outgoing protons remain intact and scatter through small angles, then, under some general assumptions, the central system ϕ is produced in the $J_Z = 0$, C and P even state. Secondly, the mass of the central system can be determined from a measurement of the transverse and longitudinal momentum components of the outgoing protons alone [118]. This means a potentially accurate determination of the mass irrespective of the decay mode of the centrally produced particle. Thirdly, the process delivers potentially very good signal to background ratios, due to the combination of the $J_Z=0$ selection rules, the mass resolution, and the simplicity of the event in the central detectors. An additional attractive property of central exclusive production is its sensitivity to CP violating effects in the couplings of ϕ to gluons.

In the following, we discuss the central exclusive production of a light Higgs boson, focussing on the $H \rightarrow b\bar{b}$ decay channel. By light we mean here $M_H \gtrsim 120\,\mathrm{GeV}$. Observing a SM Higgs of such a relatively low mass poses a serious challenge for the LHC: it decays preferably into $b\bar{b}$, a channel for which the QCD background is overwhelmingly large. Recent theoretical calculations (see [44] for a review) show that the QCD background is drastically reduced in the central exclusive reaction $pp \rightarrow pHp$, in which the final-state protons have energies close to that of the beam, and the Higgs is at central rapidities. Central exclusive production may be a discovery channel in some regions of the MSSM parameter space, where the cross section is larger than that of a SM Higgs by factors of up to 1000. Trigger issues are discussed in Chapter 6.

More generally, central exclusive production is an attractive way of searching for any new particles that couple to glue. An example studied in [44] is the scenario in which the gluino is the lightest supersymmetric particle. In such models, there should exist a spectrum of gluino-gluino bound states which can be produced in the central exclusive channel. Likewise, central exclusive production of radions, the fields introduced in the Randall-Sundrum model of five-dimensional quantum gravity, has been studied [119].

7.2.2 Monte Carlo generators for central exclusive production of a SM Higgs boson

Three generators are available for the simulation of central exclusive production of a SM Higgs boson: DPEMC [46], EDDE [112] and ExHuME [68]. A detailed comparison is presented in [120]. Using the default settings, the total cross sections for central exclusive production of a 120 GeV Higgs boson are 3.0, 1.9 and 2.8 fb for DPEMC with the Boonekamp-Peschanski-Royon (BPR) model, EDDE and ExHuME, respectively. In spite of the similarity of these values, there are important differences in the predictions of these generators.

Figure 7.2a) shows the cross section for central exclusive production of a Standard Model Higgs, with $H \rightarrow b\bar{b}$ and $H \rightarrow WW$, as a function of the Higgs mass for the three generators. It is apparent that the $b\bar{b}$ mode is particularly interesting for masses close to the current exclusion limit. The increasing branching ratio to WW as M_H increases compensates for the falling central exclusive cross section. The M_H dependence of the cross section is much faster in ExHuME and EDDE than in DPEMC. Figure 7.2b) shows the $\sqrt{s}$ dependence of the cross section for a 120 GeV Higgs. For fixed central mass, an increase in centre-of-mass energy implies a decrease in ξ; the flatter $\sqrt{s}$ dependence of DPEMC and EDDE thus reflects in the flatter ξ distributions compared to ExHuME (see Fig. 7.3a)). The distributions of ξ as well as of the Higgs rapidity (see Fig. 7.3b)) have a direct impact on the acceptance. The more central rapidity distribution of ExHuME is due to the gluon distribution falling more sharply than the Pomeron flux parameterisation present in DPEMC. The choice of the PDFs in ExHuME also influences the ξ distribution, with CTEQ6M giving a flatter ξ distribution than the default MRST 2002 set; this implies a broader peak and sharper fall in rapidity distribution, and hence a larger cross section of 3.7 fb.

Figure 7.4 shows the acceptance assuming various combinations of detectors at 220 m and 420 m. Both protons can be detected in the 220 m stations only for Higgs masses larger than 280 GeV; this reflects the fact that the 220 m detectors have acceptance for relatively large ξ values, $0.02 < \xi < 0.2$. However, asymmetric events with one proton at low ξ and another at large ξ can be detected by the combination of the 220 and 420 m detectors, which have coverage for $0.002 < \xi < 0.02$. Figure 7.4 shows that the differences in the ξ and rapidity distributions for the three generators reflect into different acceptances. Acceptances were obtained by means of FAMOS [71], which includes a parameterisation of the near-beam detectors acceptance in terms of ξ and p_T of the proton. Only geometrical acceptance was assumed; detector efficiency was taken to be 100% – see [106] and Chapter 3 for details. The total acceptance, including both the 420+420 and the 220+420 configurations, rises as the mass of the central system increases, with the relative difference between the predictions from the three generators decreasing (from about 40% down to 15% for the most extreme relative differences). For a Higgs boson of mass of 120 GeV, the total acceptances are predicted to be 46, 50 and 57% by EDDE, DPEMC and ExHuME, respectively. The corresponding acceptances for the 420+420 mode are 24, 25 and 32%, respectively.

7.2.3 $H \rightarrow b\bar{b}$

At $M_H = 120$ GeV, the three generators predict similar values of the cross section times the branching ratio for the central exclusive production of Higgs boson decaying into $b\bar{b}$, namely 2.0, 1.3 and 1.9 fb for DPEMC, EDDE and ExHuME, respectively.

The signature for this channel consists of three main ingredients: 1) two scattered protons, one in each arm of the near-beam detectors, 2) two well-collimated jets in the central detec-
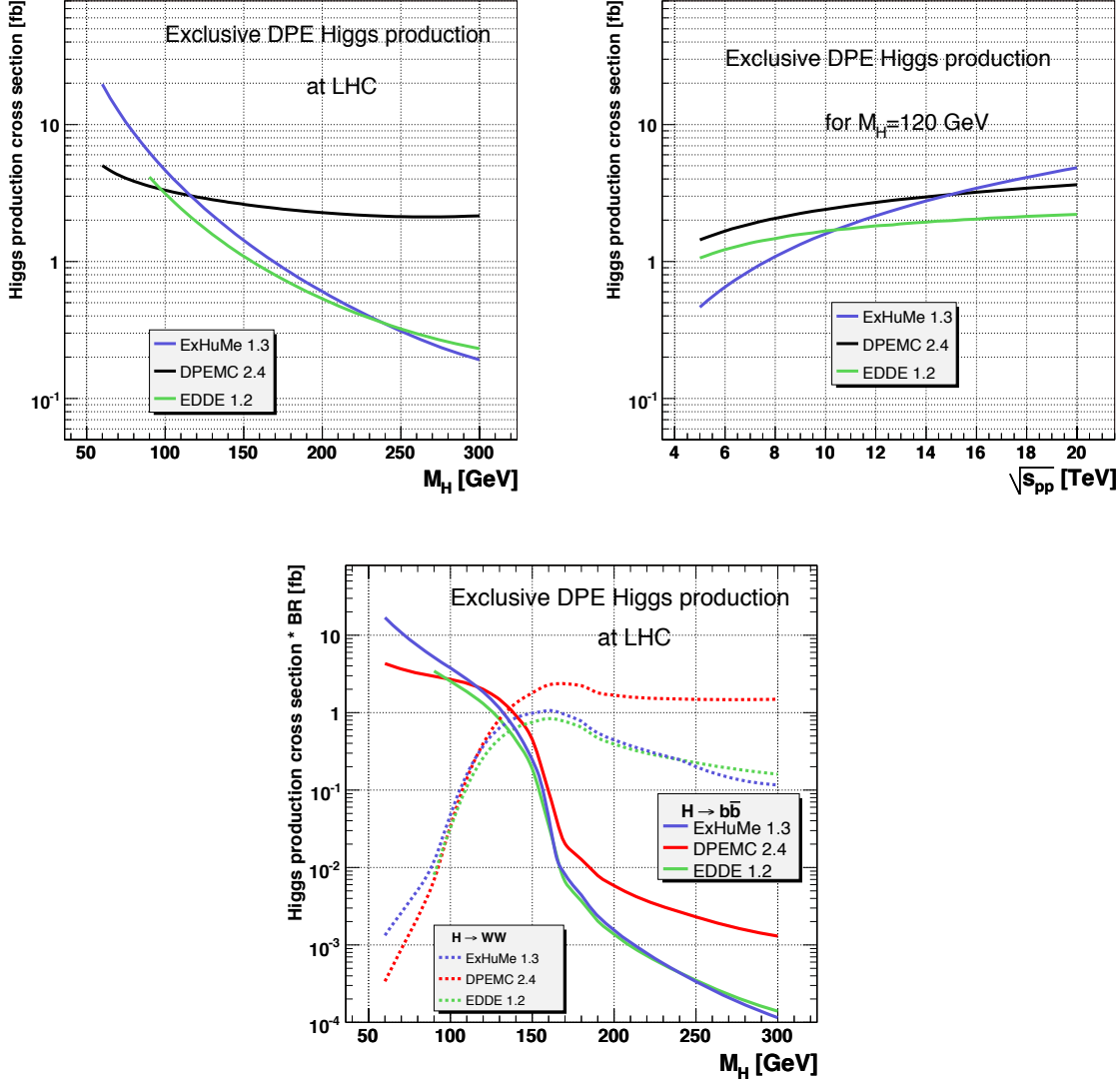
Figure 7.2: The cross section for the central exclusive production of the Higgs boson as a function of (a) the Higgs boson mass, (b) the pp centre-of-mass energy, (c) the Higgs boson mass for $H \to WW$ and $H \to b\bar{b}$.

tor and 3) consistent values of the central mass as evaluated from the momenta of the two protons ("missing mass") and as evaluated from the central detectors.

The following cuts are used to select Higgs boson candidates with mass of 120 GeV:

1. Both scattered protons have to be detected in the near-beam detectors at opposite sides from the interaction point. As explained earlier, this can happen in three different configurations: 420+420, 420+220 and 220+420. The latter two will be kept separate from the 420-only configuration and will be generically referred to as 220+420.

2. Two back-to-back b jets are required. An iterative cone jet algorithm with a cone radius $R = 0.7$ is used. We take the two highest E_T jets ($E_{T,1} > 45\,\text{GeV}$, $E_{T,2} > 30\,\text{GeV}$), require that they are well-contained in the central detector ($|\eta_{1,2}| < 2.5$), are back-to-back ($165° < |\phi_1 - \phi_2| < 195°$) and are b-tagged. In the following, these cuts, without
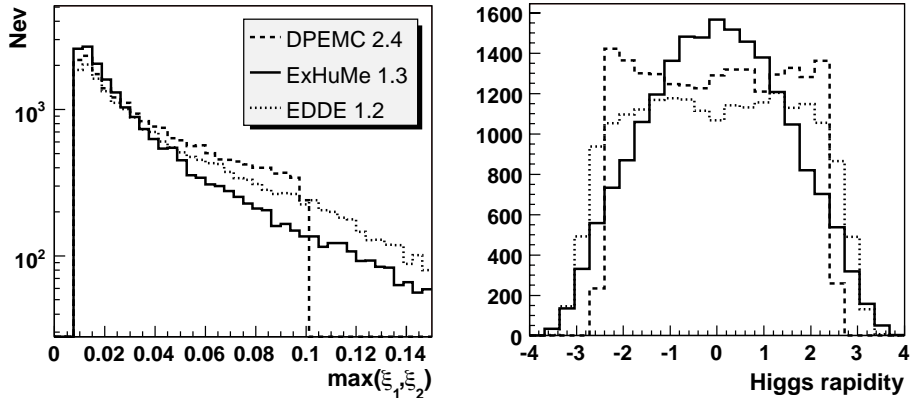
Figure 7.3: The distribution of a) $\max(\xi_1, \xi_2)$, where ξ_1 and ξ_2 are the fractional momenta of the two scattered protons, and b) the Higgs boson rapidity. A cut $\xi_{\max} = 0.1$ is applied in DPEMC, since the model which it implements ceases to be valid for larger values of ξ.
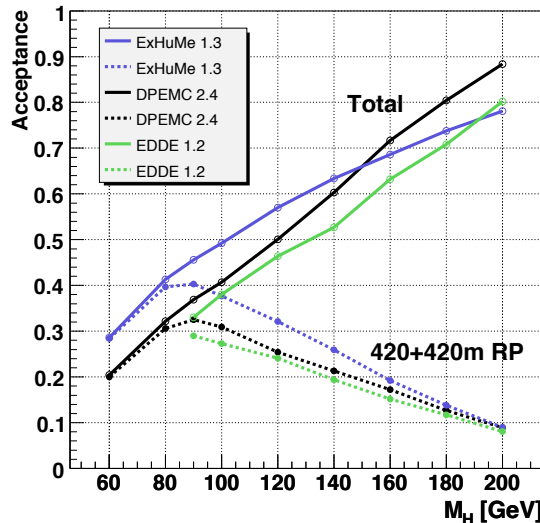
Figure 7.4: Acceptance for events in which both protons are measured in the 420 m detectors ("420+420 RP") and for events in which the two protons are seen in any combination of detectors ("Total").

the b-tag requirement, will be referred to as "jet cuts".

3. ξ and hence the central mass can be measured using information either from the central detector or from the near-beam detectors. As discussed earlier, calorimeter quantities give $\xi_{\mp} = (1/\sqrt{s}) \sum_i E_{T,i} \exp(\mp \eta_i)$, where the sum runs over the two highest E_T jets and the signs $+, -$ denote the two hemispheres. The results are compared with the ξ values measured by the near-beam detectors, ξ_{RP}. For both hemispheres we require $(\xi_{\mp} - \xi_{RP})/\xi_{RP} < 0.3$.

Events are accepted if $0.85 < M_{j1j2}/M_{mm} < 1.15$ (420+420 configuration), where M_{j1j2} is the dijet mass and M_{mm} is the missing mass obtained from the two protons. For the 220+420 configuration, for which the missing-mass resolution is worse, the cut is $0.8 < M_{j1j2}/M_{mm} < 1.2$.

In Fig. 7.5, correlations between $\xi_{\mp}$ and ξ_{RP} are shown along with the mass ratios defined above for the signal and two types of background. These latter two cuts have negligible effect on the signal when applied after all cuts including the mass windows and take 20% of signal when the mass windows are not considered. The figure also shows that there are no signal events at large ξ; the cut $0.002 < \xi < 0.04$ was shown to maximise the signal-to-background ratio.

In the following, these cuts will be referred to as "correlation cuts".
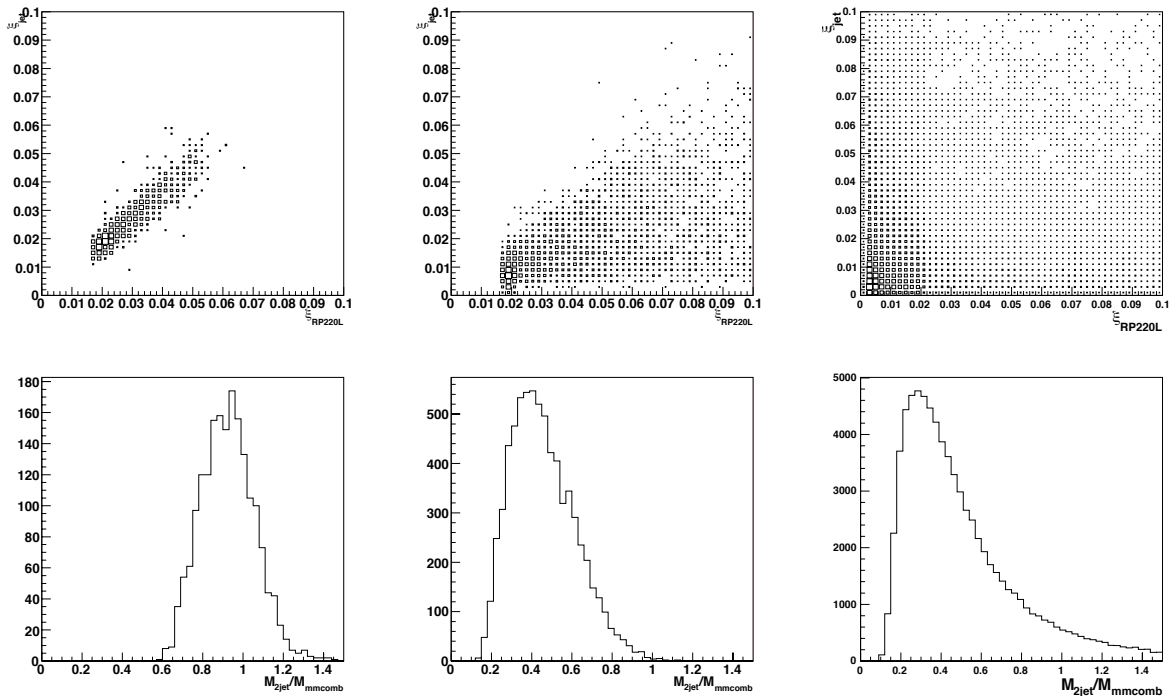
Figure 7.5: Comparison of quantities that relate the central detector and the near-beam detectors (RPs) as obtained using DPEMC 2.4. a) ξ calculated from the jets vs ξ and from the RPs (signal). b) and c) show the same type of plot as a) for the inclusive DPE production of dijets and for non-diffractive dijet production mixed with 35 pile-up events per bunch crossing, respectively. In d) the ratio of the central mass measured in the calorimeter and the missing mass is shown for signal; e) and f) show the same type of plot as d) for the background processes of b) and c).

After all the above cuts, and including the effect of L1 trigger efficiency for L1 jet and muon conditions, 0.6 events are expected, according to ExHuME, for the 420+420 configuration in the mass range 118-122 GeV and 0.9 for the 220+420 configuration in the mass range 115-125 GeV for 30 fb^{-1}. As discussed in the next section, these mass windows are chosen to quantify the S/B ratio in the region of interest; they are different for the 420+420 and the 220+420 configurations, since the mass resolution is different in the two cases. A few remarks are in order. As discussed in Sect. 7.2.5, the number of signal events, with the present cuts, can be as large as of order 1000 in some MSSM scenarios. In addition, different analysis strategies are possible, in which some of the cuts discussed above are released (e.g. the b-tag) thereby increasing the number of signal events, and new cuts are applied to keep the background under control, notably on the multiplicity of charged tracks in the central region and on the vertex (see Sect. 7.2.3.2). These studies are in progress.

7.2.3.1 Background due to central exclusive production of $b\bar{b}$ jets and inclusive DPE dijets

The question of background for $pp \to pHp$ and $H \to b\bar{b}$ is elaborated from the theoretical point of view in [117, 121]. The b-jet background is controlled by the $J_z = 0$ selection rule, which strongly suppresses central $b\bar{b}$ production at leading order. But the LO contributions are only fully suppressed in the limit of massless quarks and forward going protons. There is an admixture of $|J_z| = 2$ production, arising from non-forward going protons and also contributions of order m_b^2/E_T^2 from massive quarks. There are also indications that the NLO contributions are non-negligible, though they still need to be calculated.

Here we focus on two background processes:

1. central exclusive (i.e. exclusive DPE) production of $b\bar{b}$ jets, $pp \to pb\bar{b}p$;

2. inclusive DPE dijet production, $pp \to pjjXp$.

For the $b\bar{b}$ channel, DPEMC and EXHUME give similar results, while EDDE gives a factor of 10 smaller background due to a 10 times smaller cross section. For the second process, for $\hat{p_T} > 30$ GeV, the Cox and Forshaw model [122, 123], also implemented in DPEMC [1], gives a cross section of 13.2 fb. Here, $\hat{p_T}$ indicates the p_T of the hard interaction.

In order to quantify the S/B ratio in the region of interest, we define mass windows and consider the 420+420 and the 220+420 configurations separately, since the mass resolution is different in the two cases. So for $M_H = 120$ GeV, where the resolutions are about 1.6% and 5.6%, respectively, the mass windows chosen are 4 and 10 GeV.

Table 7.2: Cross section and event yield for 30 fb^{-1}. For the signal, $H \to b\bar{b}$, EXHUME 1.3.1 was used. The first of the two background numbers corresponds to $pp \to pb\bar{b}p$, the second to $pp \to pjjXp$, obtained with DPEMC with the Cox and Forshaw model.

M_H[GeV]	σ^S[fb]	$N_{ev}^S/N_{ev}^B(\Delta M)$	
		420+420	220+420
120	1.87	0.6/(1+6)	0.9/(8+8)

Table 7.2 shows the number of selected events, within the mass window, after all cuts for the signal and for the two background processes mentioned above.[2] The background numbers quoted in the table were obtained from samples which had to be rescaled by a factor 0.3 and 6, respectively, to arrive at the yield at 30 fb^{-1}.

It should be noted that the contribution from inclusive DPE production of dijets has a significant theoretical uncertainty and depends critically on the dPDFs at high β, where they are poorly known. In addition, more stringent cuts on the correlation between the central event and the momenta of the scattered proton, not applied in the present analysis, can reduce this background further. As discussed in Sect. 7.2.5, the number of signal events, with the present cuts, can be as large as of order 1000 in some MSSM scenarios.

---

[1]It was checked that this implementation of the model gives identical results to those in POMWIG [122].

[2]This prediction depends critically on the dPDFs at high β, where they are poorly known. A reduction of the inclusive dijet background by a factor about 10 is expected when the most recent dPDFs from H1 [29] are used [124].

The total event selection efficiency for the signal was found to increase by a factor of approximately 3 when going from 120 GeV to 200 GeV in the Higgs mass, while the total background from the two processes described above decreases by a factor of about 4. The b-tag requirement is important for suppressing the $pp \rightarrow pjjXp$ background; it provides a reduction factor by about 500.

7.2.3.2 Pile-up effects to $H \rightarrow b\bar{b}$

Coincidences with pile-up are by far the most prominent source of background in this channel at high luminosity. For the non-diffractive production of a light Higgs boson decaying to $b\bar{b}$, the background from inclusive dijet production is overwhelming. Quantum number selection rules suppress this background to a large extent (see Sec. 7.2.1). However, inclusive dijet events, when they occur in coincidence with pile-up events that have leading protons within the acceptance of the near-beam detectors, again appear to have the same signature as the signal.

The size of the effect depends principally on three factors:

- The probability of misidentifying a background event as a signal event based on the selection cuts applied to central detector quantities.
- The probability, at a given luminosity, of obtaining a fake DPE signature in the near-beam detectors caused by protons from pile-up events.
- The efficacy of requiring a correlation between the 2 jets in the central detector and the protons detected in the near-beam detectors against background events in coincidence with a fake DPE signature caused by pile-up.

The effect of the second factor is independent of the signal channel under study, but depends crucially on the normalisation of the leading proton ξ spectrum.

A large-statistics background sample of inclusive dijet events and a pile-up sample of 200,000 inclusive minimum bias events were used to quantify the effect of these factors on the Signal-to-Background (S/B) ratio. The dijet background was generated with PYTHIA 6.4 in the two most relevant bins for the hard scale, with $30 < \hat{p_T} < 50$ GeV (cross section 156 μb) and $50 < \hat{p_T} < 80$ GeV (cross section 20 μb). The pile-up sample was generated with PHOJET 2.1, where the total pp cross section is 118 mb. The generated sample comprises non-diffractive, elastic, single diffractive, DPE as well as double dissociation events, and was reweighted as discussed in Sec. 7.1.1.

Proper mixing of events with pile-up was done in FAMOS. FAMOS takes into account that the number of pile-up events is given by a Poisson distribution with an average value that depends on the luminosity. The quantitative effect of the overlaid pile-up events was assessed for the signal sample, for the diffractive background sources discussed in the preceding section and for the inclusive dijet background in the two $\hat{p_T}$ bins given above.

From any of these mixed samples one can extract the channel-independent probability of obtaining a fake DPE signature in the near-beam detectors caused by protons from pile-up events. The result is summarized in Table 7.3. The numbers there correspond to the full acceptance range of the near-beam detectors, without any further cuts in ξ.

At a luminosity of $1 \cdot 10^{33}$ cm^{-2} s^{-1}, where the average number of pile-up events is 3.5, the probability of an event to have a fake DPE signature caused by pile-up protons is a few per mill for the 420+420 case, about 2% for the 220+220 case, and about 1.5% for the 220+420

Table 7.3: Probability of obtaining a fake DPE signature, caused by protons from pile-up events, as a function of luminosity. The case where the two protons are seen on both sides in the detectors at 420 m (220 m) is denoted as "420+420" ("220+220"); the other configurations are denoted by "220+420". The numbers in this table were obtained without the rescaling of PHOJET discussed in Sec. 7.1.1.

lumi	$\langle N^{PU} \rangle$	420+420	220+220	220+420	Total
$1 \cdot 10^{33}$	3.5	0.003	0.019	0.014	0.032
$2 \cdot 10^{33}$	7.0	0.008	0.052	0.037	0.084
$5 \cdot 10^{33}$	17.5	0.033	0.205	0.153	0.300
$7 \cdot 10^{33}$	25.0	0.063	0.280	0.246	0.417
$1 \cdot 10^{34}$	35.0	0.101	0.480	0.380	0.620

configuration. These probabilities increase dramatically with luminosity. At $1 \cdot 10^{34}\,\mathrm{cm}^{-2}\,\mathrm{s}^{-1}$, where the average number of pile-up events is 35, 60% of all events will be accompanied by a fake DPE signature, where 10% stem from the 420+420 configuration, 50% from the 220+220 configuration, and about 40% from 220+420.
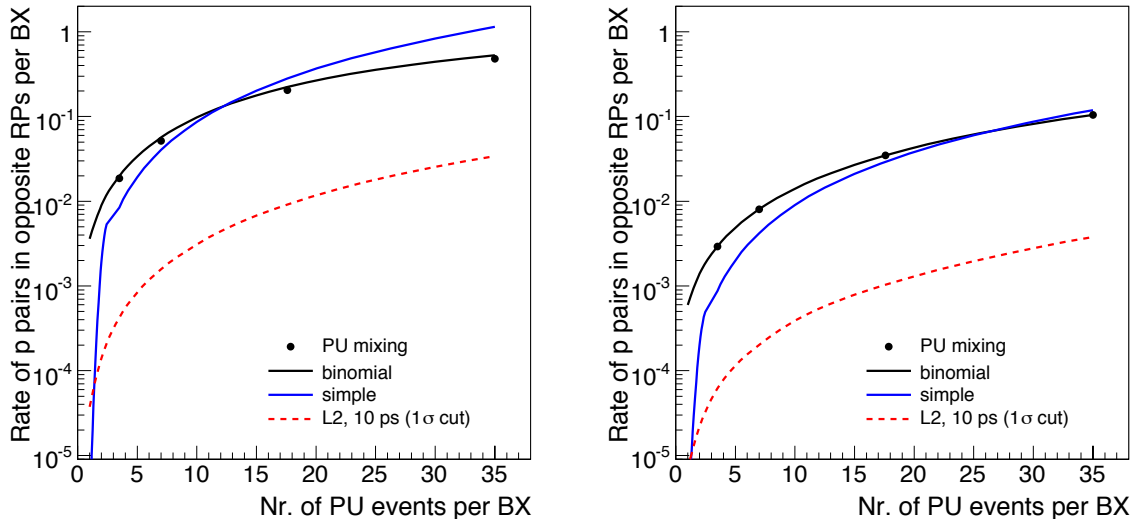
Figure 7.6: Probability of obtaining a fake DPE signature, caused by protons from pile-up events, as a function of the average number of overlaid pile-up events, for the 220+220 configuration (left) and the 420+420 configuration (right). The circles correspond to the numbers in Table 7.3, the continuous line describing the circles best to Eq. (7.2), the second continuous line to a simple-minded approximation of Eq. (7.2) (see text). The dashed curve indicates the additional reduction that can be achieved with the help of fast timing detectors (see text). Curves taken from [125].

The numbers in Table 7.3 are of purely combinatorial nature and are well described by the following formula [125]:

$$N^{RP}/BX = 2e^{-\mu_{SS}}(\cosh(\mu) - 1) + 1 - e^{-\mu_{DS}}. \tag{7.2}$$

Here, $\mu_{SS} = A_{SS} \cdot N^{PU}$ and $\mu_{DS} = A_{DS} \cdot N^{PU}$, where N^{PU} is the average number of pile-up events per bunch crossing, and A_{SS} and A_{DS} denote the percentage of pile-up events

with protons within the acceptance of the near-beam detectors either on one side only ("SS", single-sided) or on both sides ("DS", double-sided). The high statistics PHOJET sample of minimum bias events gives 1.0% and 3.1% for A_{SS} at 420 m and 220 m, respectively, and 0.05% and 0.27% for A_{DS} at 420 m and 220 m, respectively. As shown in Fig. 7.6, the analytical formula above ("binomial") describes successfully the results from Table 7.3. The differences are below 4% for 420+420 and below 10% for 220+220. Also shown in the figure is how well the following simple-minded approximation of Eq. (7.2) performs: $N^{RP}/BX = N^{PU}(N^{PU} - 1)A_{SS}A_{SS}$.

The dashed line in Fig. 7.6 indicates the possible effect of fast timing detectors that determine whether the protons seen in the near-beam detectors came from the same vertex as the hard scatter. Fast timing detectors with an expected vertex resolution of better than 3 mm are part of the FP420 project. Preliminary Monte-Carlo studies indicate that with nominal LHC running conditions a rejection of about 40 is possible of events that appear to be double Pomeron exchange events, but where the protons originated from different interactions [125, 126].

In order to quantify the background that arises from inclusive dijet events with a fake DPE signature from pile-up protons, samples of inclusive dijet events with large statistics were mixed with the appropriate number of pile-up events for several luminosity values and the same cuts used to select the signal sample (see Sec. 7.2.3) were applied. The double b-tag requirement is independent of all the other cuts and was found to lead to a reduction by a factor 560 in the bin $30 < \hat{p_T} < 50\,\mathrm{GeV}$ and 310 in $50 < \hat{p_T} < 80\,\mathrm{GeV}$. A reduction factor of 40 was applied as well to take into account the effect of fast timing detectors on the background numbers.

Figure 7.7 illustrates how the S/B ratio for the pile-up related background evolves when several families of cuts are applied sequentially. The power of those cuts that correlate the measurement in the central detector with those in the near-beam detectors ("correlation cuts") is apparent.

The signal-to-background ratio when including both the pile-up related background and the background from the sources discussed in Sec. 7.2.3.1 is listed in Table 7.4. Not included is the effect of tracking cuts, notably on the charged multiplicity measured in the central detector, expected to reduce the pile-up background by an extra factor 10-100 [127]. Also not included is a further reduction by a factor of order 10-100 which may be obtained by exploiting the CMS vertex resolution of better than 100 μm: events with more than one vertex in the few mm window given by the timing detectors (presumably due to pile-up) can then be rejected [128].

7.2.4 $H \rightarrow WW$

This channel does not suffer from a number of the difficulties discussed for the $H \rightarrow b\bar{b}$ case. The suppression of the dominant backgrounds does not rely primarily on the mass resolution of the near-beam detectors, the corresponding cross sections are known with sufficient precision and, in the semi-leptonic decay channel, level 1 triggering is not a problem.

From the experimental point of view, there are three main categories of events with two W bosons in the final state:

1. **Dilepton.** Events in which at least one of the W bosons decays in either the e or μ are
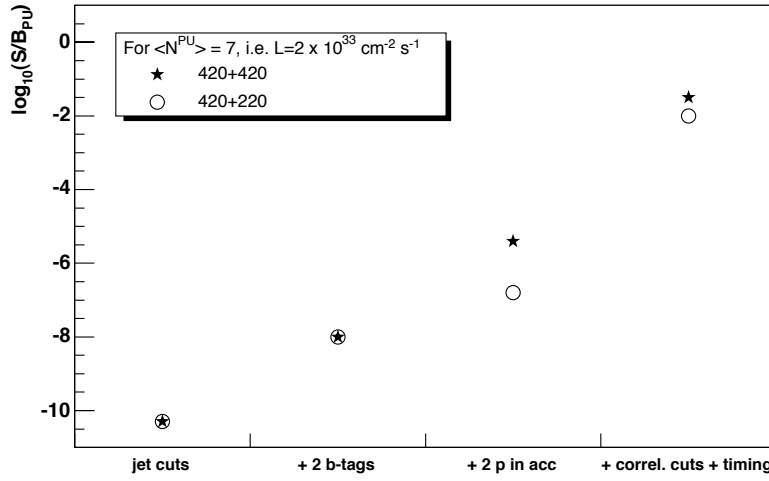
Figure 7.7: Effect of cuts on the S/B ratio for the pile-up related background. The numbers are normalised to an integrated luminosity of $30\,\mathrm{fb}^{-1}$. Not included is the effect of tracking cuts expected to reduce the pile-up background by an extra factor 10-100, nor that of cuts on the vertex coordinates (see text).

Table 7.4: S/B ratios as a function of the instantaneous luminosity for an integrated luminosity of $30\,\mathrm{fb}^{-1}$. The background numbers are the sum of the contributions expected for $pp \to pb\bar{b}p$, $pp \to pjjXp$ and for pile-up events. Not included is the effect of tracking cuts expected to reduce the pile-up background by an extra factor 10-100, nor that of cuts on the vertex coordinates (see text).

lumi	$\langle N^{PU} \rangle$	S/B	
$[\,\mathrm{cm}^{-2}\,\mathrm{s}^{-1}\,]$		420+420	220+420
$1 \cdot 10^{33}$	3.5	0.6/20	0.9/40
$2 \cdot 10^{33}$	7.0	0.6/30	0.9/120
$5 \cdot 10^{33}$	17.5	0.6/190	0.9/340
$1 \cdot 10^{34}$	35.0	0.6/900	0.9/1900

the simplest and will usually pass the level 1 trigger thresholds due to the high p_T final state lepton.

2. **Lepton+jets.** If one of the W bosons does not decay in the e or μ channel, the event can still pass the level 1 trigger thresholds if one W decays in the τ channel, with the τ subsequently decaying leptonically.

3. **All jets.** The 4-jet decay mode occurs approximately half of the time, but it is unlikely to pass the level 1 trigger thresholds without information from the near-beam detectors. In addition the QCD background is expected to be overwhelming.

The CMS level 1 trigger has a single (double) electron threshold of 29 (17) GeV with a pseudorapidity coverage of $|\eta| < 2.5$, falling to 14 (3) GeV for a single (double) muon, with a

coverage of $|\eta| < 2.1$. In the semi-leptonic decay channel, two jets are required to have $p_T > 25\,\text{GeV}$ and $|\eta| < 2.5$ and at least one e (μ) to have $p_T > 20$ (10) GeV.

As an order-of-magnitude estimate, Table 7.5 shows the event yields for $30\,\text{fb}^{-1}$ as obtained with EXHUME, assuming the above cuts and the near-beam detector acceptances. Similar results were obtained for the ATLAS level 1 trigger thresholds [129]. A discussion of the non-pile-up backgrounds is presented in [129]. The evaluation of the pile-up background is in progress.

Although the SM yields are small, exclusive WW production ($p + p \rightarrow p + W^+W^- + p$) has very striking features. The mass resolution on M_{WW} is far better ($\sigma_M \approx 2\,\text{GeV}$ for 420+420 even when jets and neutrinos are involved) than any other measurement. In the dilepton case the two leptons, oppositely charged but not necessarily the same flavour, come from a vertex with no other charged tracks, but with large missing E_T. As the associated charged multiplicity in generic W^+W^- production is generally high, the observation of only about 3 or 4 such events with $z_{\text{vertex}} = z_{\text{vertex−from−pp−timing}}$ and with the same (to $\sim 2\,\text{GeV}$) missing mass could be a significant discovery. There is a control channel, namely $\gamma\gamma \rightarrow W^+W^-$ which gives a continuum in $M(W^+W^-)$ with a known cross section (see Chapter 8). As discussed earlier, exclusive W^+W^- production also has the potential of measuring the quantum numbers (spin etc.) of the state through angular distributions, including azimuthal correlations between the forward protons. We note also that beyond the SM theory [130] expects prolific production of WW and ZZ in double pomeron events, not necessarily exclusive.

Table 7.5: Cross sections, total RP acceptances and event yields for $30\,\text{fb}^{-1}$ for the $H \rightarrow WW$ decay channel as obtained with EXHUME 1.3.

M_H[GeV]	σ[fb]	Acc[%]	semi-lept	fully-lept	Total
120	0.37	57	1.2	0.2	1.3
135	0.77	62	3.1	0.6	3.4
140	0.87	63	3.5	0.6	3.8
150	1.00	66	4.9	1.0	5.3
160	1.08	69	6.0	1.0	6.6
170	0.94	71	5.4	1.0	5.9
180	0.76	74	4.5	0.8	4.9
200	0.44	78	2.9	0.6	3.2

7.2.5 Central exclusive production of a MSSM Higgs boson

There are various extended models predicting a variety of Higgs-like bosons with different masses, coupling and CP-parities. The most elaborate extension of the SM up to now is the Minimal Supersymmetric Standard Model (MSSM) [131–133], in which there are three neutral (h, H and A) and two charged (H^+, H^-) Higgs bosons. At lowest order, the Higgs sector of the MSSM is CP-conserving, with the CP-even states h and H ($M_h < M_H$) and the CP-odd state A. As was realised in [134, 135] (see also [136]) there are certain regions of the MSSM parameter space which can be especially 'proton tagging friendly'. For instance, in the region of large $\tan \beta > 20$ and $M_H \lesssim 250\,\text{GeV}$ the situation becomes exceptionally favourable.

It seems reasonable to define benchmarks in which all SUSY parameters are fixed and only

the two tree-level parameters, M_A and $\tan\beta$, are varied. Three most relevant scenarios in this context are the following.

- The M_h^{max} scenario:

  This scenario was designed to obtain conservative $\tan\beta$ exclusion bounds [137] at LEP [138]. The parameters are chosen such that the maximum possible Higgs-boson mass as a function of $\tan\beta$ is obtained (for fixed M_{SUSY}, and M_A set to its maximal value, $M_A = 1\,\mathrm{TeV}$). The parameters are:

  $$m_t = 172.7\,\mathrm{GeV}, \quad M_{\mathrm{SUSY}} = 1\,\mathrm{TeV}, \quad \mu = 200\,\mathrm{GeV}, \quad M_2 = 200\,\mathrm{GeV},$$
  $$X_t = 2\,M_{\mathrm{SUSY}} \quad A_b = A_t, \quad m_{\tilde{g}} = 0.8\,M_{\mathrm{SUSY}}\,. \tag{7.3}$$

- The no-mixing scenario:

  This scenario is the same as the m_h^{max} scenario, but with vanishing mixing in the $\tilde{t}$ sector and with a higher SUSY mass scale to avoid the LEP Higgs bounds [138, 139]:

  $$m_t = 172.7\,\mathrm{GeV}, \quad M_{\mathrm{SUSY}} = 2\,\mathrm{TeV}, \quad \mu = 200\,\mathrm{GeV}, \quad M_2 = 200\,\mathrm{GeV},$$
  $$X_t = 0 \quad A_b = A_t, \quad m_{\tilde{g}} = 0.8\,M_{\mathrm{SUSY}}\,. \tag{7.4}$$

- The small α_{eff} scenario:

  The decays $h \rightarrow b\bar{b}$ (and also $h \rightarrow \tau^+\tau^-$) can be strongly affected by changes in α_{eff} [140]. If α_{eff} is small, these two decay channels can be heavily suppressed in the MSSM due to the additional factor $-\sin\alpha_{\mathrm{eff}}/\cos\beta$ compared to the SM coupling. Such a suppression occurs for large $\tan\beta$ and not too large M_A for the following parameters:

  $$m_t = 172.7\,\mathrm{GeV}, \quad M_{\mathrm{SUSY}} = 800\,\mathrm{GeV}, \quad \mu = 2.5\,M_{\mathrm{SUSY}}, \quad M_2 = 500\,\mathrm{GeV},$$
  $$X_t = -1100\,\mathrm{GeV}, \quad A_b = A_t, \quad m_{\tilde{g}} = 500\,\mathrm{GeV}\,. \tag{7.5}$$

Cross sections for the $b\bar{b}$ and $\tau\tau$ channels are enhanced most in the M_h^{max} scenario. The enhancement increases with rising $\tan\beta$ and reaches a value of about 2000 for $M_H \approx 180$–300 GeV and $\tan\beta = 50$ in case of $H \rightarrow b\bar{b}$. In the case of the $h \rightarrow b\bar{b}$ and $h \rightarrow \tau\tau$ channels, the largest enhancement (about 60 for $b\bar{b}$ and about 12 for $\tau\tau$) is observed in the region of $M_h \approx$ 90–130 GeV and $\tan\beta \approx 40$.

The most favourable scenario for the $h \rightarrow WW$ channel is the small α_{eff} scenario where $h \rightarrow b\bar{b}$ and $h \rightarrow \tau\tau$ can heavily be suppressed for large $\tan\beta$ and for $M_h \sim 120\,\mathrm{GeV}$. The enhancement reaches a value of 4 but only in the narrow region of $M_h \sim 121$–123 GeV.

7.2.6 Conclusions

Central exclusive production of a light SM or MSSM Higgs boson has been studied. By light we mean here $M_H \gtrsim 120\,\mathrm{GeV}$. Observing a SM Higgs of such a relatively low mass poses a serious challenge for the LHC: it decays preferably into $b\bar{b}$, a channel for which the QCD background is overwhelmingly large. The measurement may become possible in the central exclusive reaction $pp \rightarrow pHp$, in which the QCD background is drastically reduced. One of the most dangerous background source here is that from pile-up events.

The signal event yields after cuts, for an integrated luminosity of $30\,\mathrm{fb}^{-1}$, vary from a few events for a SM Higgs with mass between 120 and $200\,\mathrm{GeV}$, to several thousands for some MSSM scenarios. The current theoretical uncertainty of the predictions is not negligible. Measurements in progress at HERA (notably of exclusive production of vector mesons and dijets) and CDF (exclusive production of dijets, two-photon states, as well as χ_c and χ_b mesons) will lower this uncertainty significantly in the next few years.

Backgrounds due to non-resonant central exclusive production of $b\bar{b}$ jets have been studied, along with inclusive DPE production of dijets. With the cuts used in the present analysis, these backgrounds contribute less than 10 events for $30\,\mathrm{fb}^{-1}$. The contribution from inclusive DPE production of dijets has a significant theoretical uncertainty and depends critically on the dPDFs at high β, where they are poorly known; the present estimates are expected to be reduced by about a factor 10 if the most recent H1 dPDFs, which have better coverage at high β, are used. In addition, more stringent cuts on the correlation between the central event and the momenta of the scattered proton, not applied in the present analysis, can reduce this background further.

The pile-up contribution was studied for several values of the instantaneous luminosity. For $2 \times 10^{33}\,\mathrm{cm}^{-2}\,\mathrm{s}^{-1}$, the rate of events faked by pile-up is about 100 for $30\,\mathrm{fb}^{-1}$ in the case in which one proton is seen in the 220 m detectors and the other in the 420 m detectors; this assumes that timing devices both at 220 m and at 420 m can give a longitudinal vertex resolution of the order of a few mm, yielding a factor 40 reduction due to timing. The pile-up rate reduces to ~ 20 events for the 420 m + 420 m configuration. Studies in progress indicate that further cuts on the charged-particle multiplicity in the central rapidity region reduce the rate by another factor 10-100, yielding a signal to pile-up background ratio of order unity; a further reduction of similar size may be obtained by rejecting events with multiple vertices in the z window given by the timing detectors. The main uncertainty in the pile-up background prediction is the shape and normalisation of the leading proton spectrum due to soft diffractive processes. It is imperative that this spectrum be measured accurately at the start of the LHC operation.

In summary, we demonstrated that for one of the most challenging channels a reduction of the pile-up background by a factor $\sim 10^9$ can be obtained with relatively simple cuts. Further, more elaborate requirements can give a further 10-100 suppression or larger. This would yield S/B in excess of unity for a SM Higgs and up to 1000 for a MSSM Higgs. This work has stimulated the theoretical community to study the main contributions to the backgrounds; this will hopefully lead to a reduction of the uncertainties in the background estimations – notably that of the pile-up. The results presented are intermediate and detailed studies taking into account full detector simulation and reconstruction are in progress. The discovery-physics potential of adding near-beam detectors at 420 m from the interaction point has also been demonstrated.

7.3   Diffractive DPE $t\bar{t}$ production

7.3.1   Introduction

We present a study of inclusive DPE production of $t\bar{t}$ pairs (see Fig. 7.8), with one top quark decaying leptonically and the other to jets. The reaction was simulated with the generator DPEMC 2.4 [46] in conjunction with the fast CMS simulation code FAMOS, version 1.4.0 [71]. The two models available in DPEMC were used – that by Cox and Forshaw [122, 123] and

that by Boonekamp, Peschanski and Royon (BPR) [141, 142]. [3]
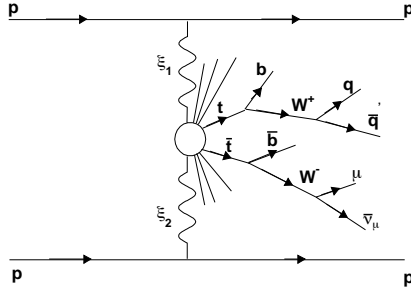
Figure 7.8: Schematic diagram of inclusive DPE production of $t\bar{t}$ pairs, with one t decaying leptonically and the other to jets.

To leading order, top production proceeds by quark-antiquark and gluon-gluon fusion, with the latter dominating ($\sim 90\%$) at the energies considered here. This reaction therefore mainly probes the gluonic component of the dPDFs of the proton.

The top quark decays primarily into a $W + b$ pair (unlike other quarks, the top does not hadronize before decaying). The following decay schemes can be distinguished:

- **Dilepton** ($l\nu b l\nu b$): the two W bosons decay leptonically. This channel is characterised by two high energy leptons, two b-jets and high missing transverse energy. The event is clean but the branching ratio is low ($\sim 5\%$ for $l = e, \mu$).

- **Lepton + Jets** ($l\nu b jjb$): Considerably higher BR ($\sim 30\%$ for $l = e, \mu$), without too much increase in background, especially if b-tagging is available.

- **All jets** ($jjbjjb$): This mode has the highest BR ($\sim 45\%$), but also the highest background.

7.3.2 Selection Cuts and Reconstruction

We concentrate on inclusive DPE $t\bar{t}$ production, with semileptonic (lepton + jets) decay and consider only the muon case. Our selection cuts are:

- As the full trigger simulation was not available for this analysis, we required the p_T of the L3 muons to be above the HLT threshold of $19\,\mathrm{GeV}$. This should simulate the event yield reduction from the trigger.

- We demanded exactly 1 muon with $E_T > 20\,\mathrm{GeV}$ and $\eta < 2.4$. We also required the muon to be isolated, i.e. that the ratio R_{calo} of the muon E_T to the E_T of all calorimeter towers in a cone of 0.3 around the muon, plus the muon E_T itself, be at least 0.9. Figure 7.9 shows the E_T and R_{calo} distributions with the cuts indicated.

- The missing transverse energy, $\not{E}_T$, was required to be at least $20\,\mathrm{GeV}$.

- At least 4 jets with $E_T > 30\,\mathrm{GeV}$ were required, of which at least two were b-tagged. These four jets should be the two b ones and those from the hadronically

---

[3]The model by Cox and Forshaw does not include the rapidity gap survival probability S^2. Unless stated otherwise, the predictions of this model are therefore presented as a number of events or a cross section divided by S^2.
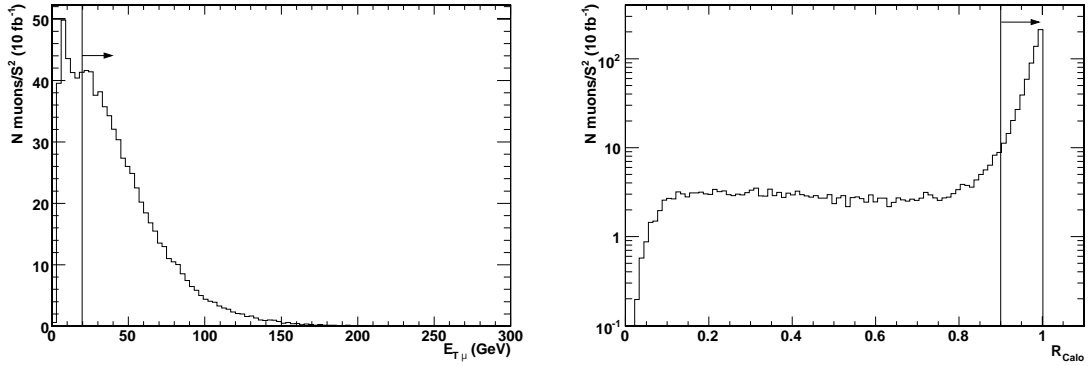
Figure 7.9: E_T and R_{calo} distributions for muons. The symbol S^2 indicates the rapidity gap survival probability.

decaying W. Jets are reconstructed with the standard iterative cone algorithm with cone size 0.5. Figure 7.10 gives the E_T distributions for non b-tagged jets and b-tagged jets.
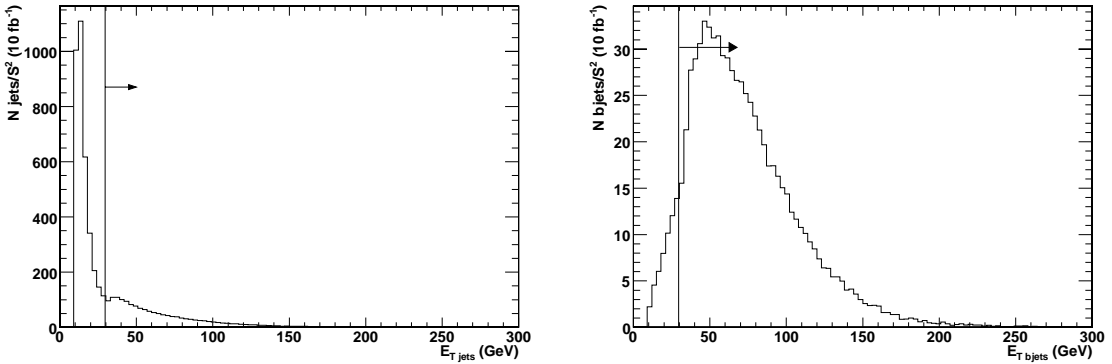

Figure 7.10: E_T distributions for non b-tagged jets (left panel) and b-tagged jets (right panel). The symbol S^2 indicates the rapidity gap survival probability.

- In addition, we demand the detection of at least one proton in both arms of the 220 m RP detectors with $0.02 < \xi < 0.1$. Events were weighted by the RP acceptance as available in FAMOS, which is a function of ξ and t. Figure 7.11 shows the generated ξ spectrum for the signal and the diffractive pile-up protons (cf. discussion below). The rise towards high values of ξ of the signal distribution is a direct consequence of the large centrally produced mass. The cut $\xi > 0.02$ helps in rejecting the pile-up background.

Both t quarks were reconstructed, one with the W decaying into jets and the other with the W decaying leptonically:

1. Hadronic top
    - Step 1: W reconstruction
        - From the non b-tagged jets with the given E_T cut, the pair with invariant mass closest to the nominal W mass was selected.
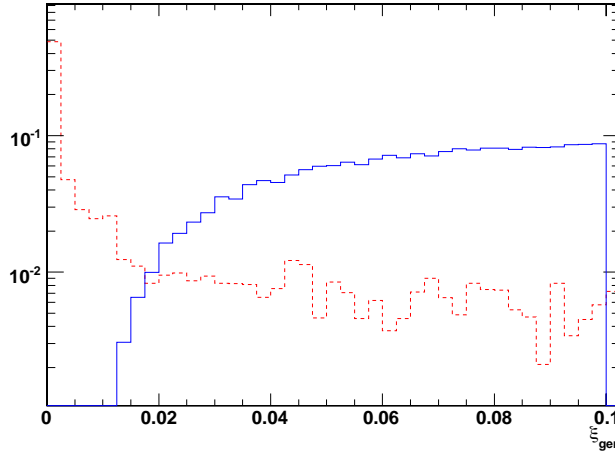
Figure 7.11: ξ spectrum of the signal protons (continuous line) and of the pile-up protons (dashed line). The units on the vertical scale are arbitrary.

- The reconstructed invariant mass of these two jets was required to be between $40\,\mathrm{GeV}$ and $120\,\mathrm{GeV}$.
  - The energy of the two selected jets was rescaled such that their invariant mass equals that of the W.
  - Step 2: Top reconstruction
    - In order to match the b-tagged jets and the W jet, the pair with invariant mass closest to the nominal t mass was chosen.
    - With the b-tagged jet just selected and the W, one of the two t quarks can thus be reconstructed.

2. Leptonic top
   - The transverse mass of the W decaying leptonically was reconstructed using the $\displaystyle{\not}E_T$ and the muon energy. The transverse mass was further required to be less than $120\,\mathrm{GeV}$.
   - The ambiguity due to the unmeasured longitudinal component of the neutrino was resolved by minimising the difference between the reconstructed t mass and the nominal one, when looping over the remaining b-tagged jets. If no solution was found for the longitudinal momentum component of the W, the W was assumed to have the same direction as the muon.
   - It was further required that the mass difference between the two t candidates be less then $50\,\mathrm{GeV}$ and that the cosine of the azimuthal angle between them be less than -0.8.

- ξ reconstruction: As discussed earlier, ξ can be obtained from central detector quantities as

$$\xi_{cen} = \frac{1}{\sqrt{s}} \sum_{\text{particles}} E_T e^{\pm\eta},$$

where the sum is over all particles in the event.

In the present case, ξ can be reconstructed from this formula only in an approximate way: instead of summing over all the particles, the sum is only over the main objects in our event – all the jets, the muon and the reconstructed neutrino.

The variable ξ is also measured with the RP detectors. We then required the difference $\xi_{cen} - \xi_{\mathrm{RP}}$ to be less than 0.02. The cut has to be satisfied for the protons on both sides. This difference should be biased towards negative values, given the approximation used. This cut helps rejecting the pile-up background, in which an event with non-diffractive $t\bar{t}$ production overlaps with soft diffractive events with protons detected in the RPs; in this case, the detected protons are uncorrelated with the central event. Figure 7.12 shows the distribution of $\xi_{cen} - \xi_{\mathrm{RP}}$ for signal and pile-up events. In the case of more than one proton accepted in a given RP, the highest ξ one is taken – assuming that it is possible to reconstruct more than one.
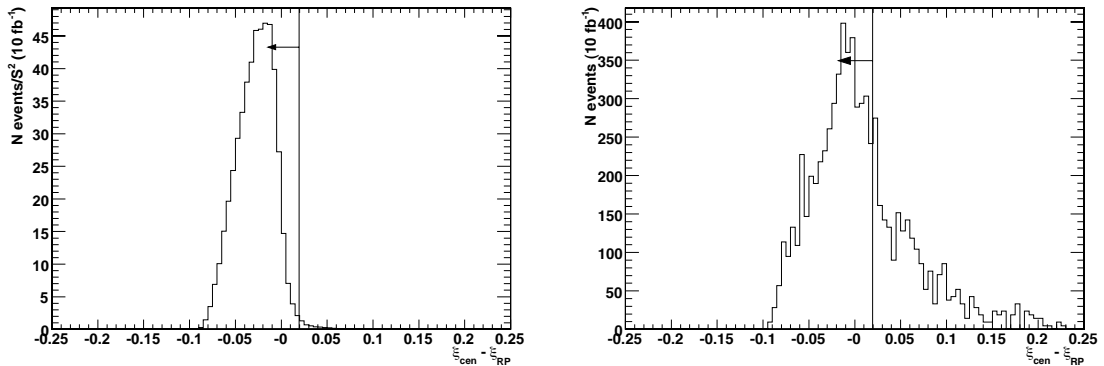

Figure 7.12: Difference between the ξ calculated from the central detector and from the RP detector information, for signal (left panel) and non-diffractive inclusive $t\bar{t}$ (right panel). The symbol S^2 indicates the rapidity gap survival probability.

7.3.3 Pile-up Background, Efficiencies and Event yields

As already discussed, the dominant background source is the accidental overlap of an event with non-diffractive $t\bar{t}$ production and protons due to diffractive pile-up events in the same bunch crossing. The pile-up effect was simulated at the detector level, using the FAMOS package, by combining non-diffractive $t\bar{t}$ events (from PYTHIA) with minimum bias events generated by PHOJET [66]. As discussed earlier, at a luminosity of $2 \times 10^{33}\,\mathrm{cm}^{-2}\,\mathrm{s}^{-1}$, 7 pile-up events are expected on average. FAMOS is used to combine the signal event and a number of pile-up events sampled from a Poisson distribution with mean of 7. The same mixing procedure was also applied to the signal and to the other backgrounds considered. The latter were the inclusive DPE production of $t\bar{t}$ pairs with the top quarks decaying differently than semileptonically. Diffractive $W + j$ production was also studied.

Table 7.6 shows the effect of the cuts for all $t\bar{t}$ decay modes in the case of DPE inclusive $t\bar{t}$ production: semileptonic decay with the W decaying into muon or electron, fully hadronic, dileptonic (e and μ) as well as all modes involving τ leptons. Comparing these efficiencies gives an idea of the efficacy of the cuts in selecting the semileptonic channel. None of the diffractive $W + j$ events survived the cuts: they were all rejected by the b-tag requirement; this corresponds to an upper limit of less than $\sim 3 \times S^2\ W + j$ events after all cuts. The

background from diffractive $W + c\bar{c}$ and $W + b\bar{b}$ remains to be evaluated. Figure 7.13 presents the top mass distribution for all the hadronic decay modes. Approximately 28 x S^2 signal events are expected in the semileptonic decay channel for $10\,\mathrm{fb}^{-1}$. The number of events in the other channels is negligible. For a gap survival probability of 0.05-0.1, appropriate for this reaction [124], the number of signal events would be about 1-3.
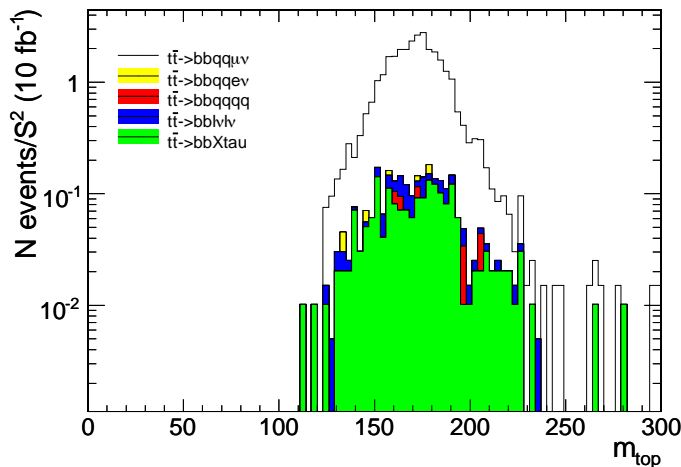

Figure 7.13: Top mass distribution for all the hadronic decay modes. The symbol S^2 indicates the rapidity gap survival probability.

The model by Boonekamp, Peschanski and Royon predicts approximately 270 signal events; the model already includes the appropriate gap survival probability. The BPR prediction is thus a factor about 300 times larger than that of the Cox and Forshaw model.

Table 7.7 gives the effect of the cuts and the expected event yields for the signal evaluated with the Cox and Forshaw model to which the pile-up background was added as described above. Approximately 109 ± 24(stat.) pile-up events are expected.

7.3.4 Conclusions

The event yield for inclusive DPE production of $t\bar{t}$ pairs was evaluated. For $10\,\mathrm{fb}^{-1}$, the Cox and Forshaw model predicts a few events. Perhaps more importantly, the study gives a quantitative assessment of the pile-up background at $2 \times 10^{33}\,\mathrm{cm}^{-2}\,\mathrm{s}^{-1}$, which is of the order of one hundred events in $10\,\mathrm{fb}^{-1}$. Depending on the model, the signal-to-background ratio may vary from 0.01-0.03 to 3. Put differently, a signal-to-background ratio of unity would correspond to a signal cross section times branching ratio of 270 fb.

The signal-to-background ratio can be improved by a more elaborate selection procedure requiring correlations between the protons observed in the RPs and the central part of the event. In addition, if timing detectors are used in the 220 m RPs in order to select protons originating from the correct event vertex, the background can be suppressed by a factor about 40 (assuming a 10 ps resolution), yielding a signal-to-background ratio of order unity for the Cox and Forshaw model even with the present cuts. Furthermore, the vertex cuts outlined for the Higgs case in Sect. 7.2.3.2 may give a further significant reduction.

Table 7.6: Comparison of efficiencies and yields for different $t\bar{t}$ decay modes: effect of the cuts on the efficiencies for inclusive DPE $t\bar{t}$ production generated according to the Cox and Forshaw model in DPEMC. The symbol σ indicates the generator-level cross section, and N is the event yield; S^2 indicates the rapidity gap survival probability, which was not included in the calculations.

Cuts	$t\bar{t} \to b\bar{b}q\bar{q}\mu\nu$	$t\bar{t} \to b\bar{b}q\bar{q}e\nu$	$t\bar{t} \to b\bar{b}q\bar{q}q\bar{q}$	$t\bar{t} \to b\bar{b}\tau X$	$t\bar{t} \to b\bar{b}l\nu l\nu$
L3 pt muon	0.83	0.05	0.05	0.19	0.67
1 muon isol.	0.74	0.003	0.003	0.13	0.46
4 jets	0.26	0.002	0.002	0.02	0.03
2 bjets	0.10	0.0004	0.0005	0.006	0.01
$\not{E}_T$	0.09	0.0004	0.0002	0.005	0.009
lep W $m_\perp$	0.08	0.0003	0.0002	0.005	0.007
had W mass	0.07	0.0003	0.0002	0.004	0.006
Δm_{top} & $\cos\phi$	0.05	0.0002	0.00006	0.003	0.002
RP's acceptance	0.04	0.0002	0.00006	0.003	0.002
$\Delta\xi < 0.02$	0.04	0.0001	0.00006	0.002	0.002
σ/S^2(pb)	0.07	0.07	0.21	0.10	0.02
$N/S^2(10\,\text{fb}^{-1})$	28	0.09	0.12	2.26	0.45

Table 7.7: Effect of pile-up background: effect of the cuts on the number of accepted Monte Carlo events and on the efficiencies for the signal sample (Cox and Forshaw model) and for the pile-up background described in the text. The expected number of events for $10\,\text{fb}^{-1}$ is also given. The meaning of the symbols is the same as in the previous table. The assumed instantaneous luminosity is $2 \times 10^{33}\,\text{cm}^{-2}\,\text{s}^{-1}$

Cuts	$t\bar{t} \to b\bar{b}q\bar{q}\mu\nu$	ϵ_{cuts}	$qq, gg \to t\bar{t} \oplus$ PHO MB	ϵ_{cuts}
N total	46559		1029469	
L3 pt muon	38563	0.83	221924	0.22
1 muon isol.	34526	0.74	149330	0.15
4 jets	12354	0.27	55981	0.05
2 bjets	4547	0.10	19294	0.02
$\not{E}_T$	4088	0.09	17187	0.02
lep W $m_\perp$	3822	0.08	15191	0.02
had W mass	3338	0.07	13357	0.01
Δm_{top} & $\cos\phi$	2082	0.04	6293	0.006
RP's acceptance	2048	0.04	55	0.00005
$\Delta\xi < 0.02$	1833	0.04	23	0.00002
σ(pb)	0.07 x S^2		488	
N($10\,\text{fb}^{-1}$)	28 x S^2		109	

Chapter 8

Photon-photon and Photon-proton Physics

8.1 Introduction

The interpretation of hard diffractive processes in pp collisions in terms of diffractive structure functions and generalised structure functions suffers from the presence of rapidity gap-survival factors S^2 which are due to soft rescattering between the incoming or outgoing protons (see Chapter 1). The small numerical values of S^2 ($S^2 = \mathcal{O}(0.01\text{-}0.1)$) lead to small cross sections for diffractive production of new particles, such as the Higgs (see Sec. 7.2). Diffractive processes happen at modest squared 4-momentum transfers $|t|$ between the incoming and the outgoing proton. It should be therefore of topical interest to investigate pp-collisions at smaller $|t|$ (i.e. larger impact parameters), where QED starts to dominate and strong effects become small – a known procedure for the measurement of the real part of the elastic scattering amplitude. It may thus be possible to reach a better understanding and/or measurement of S^2 from a variation of t for certain processes. [1] One is therefore led to investigate two-photon processes as in e^+e^--collisions and/or single photon exchanges ("photoproduction") as in ep scattering; the LHC can thus be considered as a photon-photon or photon-proton collider [143] reaching invariant photon-photon masses beyond 1 TeV. In the following, some examples of reactions are discussed in the framework of pp collisions; similar arguments hold, however, also for pA and AA-collisions [144]. There should also be a contribution of photon-Pomeron interactions in pA collisions with the pomeron being essentially emitted by the proton, whereas photons should come mainly from the nucleus due to its charge.

In principle the simplest reactions to be studied are the pure QED processes (see Sec. 8.3): $pp \rightarrow (p\gamma\gamma p) \rightarrow pl\bar{l}p$, where $l\bar{l} = e^+e^-, \mu^+\mu^-$. As the theoretical cross section is precisely known [145–147], this reaction may be used for calibrating the pp-luminosity, on condition that the events can be identified in the presence of pile-up. This should be possible thanks to three handles: The leptons have $\Delta\phi \approx 180°$ and $p_T(1) \approx p_T(2)$ and there are no other charged tracks from the l^+l^- vertex. In addition, a calibration of the forward protons' energy measurement can be envisaged, as well as cross checks of acceptance issues.

Of considerable interest are furthermore the exclusive processes $pp \rightarrow (p\gamma\gamma p) \rightarrow pXp$, where $X = \gamma\gamma, WW, ZZ, H, tt$ or a SUSY-pair. The yield of events with sparticle-pairs and masses below about 250 GeV is supposed to be quite substantial [148]; this is not elaborated here

---

[1]Take for instance the process $pp \rightarrow pl\bar{l}p$, where l is a lepton: at small $|t|$, this reaction is exclusively driven by QED, while at larger $|t|$ also strong re-interactions of protons may become significant. In both cases the final state is the same. The measured cross section will therefore contain the square of the pure QED amplitude, the square of the QED+re-interactions amplitude and their interference. A deviation of the measured t-dependence from the QED expectation, which is known theoretically with very good precision, may yield an estimate of S^2.

any further. A measurement of W-pair production is sensitive to anomalous quartic gauge couplings; Z-pair production is suppressed in the standard model. Production of W- and Z-pairs is briefly discussed in Sec. 8.4.

As a final topic, photoproduction of single W and of WH , i.e. $pp \rightarrow (p\gamma p) \rightarrow pWX$ and $pp \rightarrow (p\gamma p) \rightarrow pWHX$ is addressed in Sec. 8.5.

Crucial ingredients for a discussion of these processes are the spectra of virtual photons and of the resulting kinematic configurations of final states. The latter are at the origin of procedures for tagging the desired events and for the suppression of background from strong interactions. This is discussed first in section Sec. 8.2.

8.2   Photon spectra and selection of photon-exchange processes

In order to calculate the QED cross section $d\sigma(pp)$ for photon induced final states in pp collisions, the photon cross sections $d\sigma(\gamma\gamma)$ and $d\sigma(\gamma p)$ have to be convoluted with the photon spectra $dN = dN(w, Q^2, Q^2_{min}, E, F - E, F - M)$, which are functions of beam energy E, photon energy w, virtuality Q and of the proton form-factors; they can be calculated according to the equivalent photon approximation (EPA) [143, 145]:

$$d\sigma(pp) = d\sigma(\gamma\gamma) \cdot dN_1 \cdot dN_2, \tag{8.1}$$

$$d\sigma(pp) = d\sigma(\gamma p) \cdot dN. \tag{8.2}$$

To calculate cross sections for reactions with or without excitations of protons in the final state, one has to use the appropriate inelastic or elastic form factors, respectively. Integration of $dN_1 \cdot dN_2$ over w and Q for fixed photon collision energy $W = 2\sqrt{w_1 \cdot w_2}$ yields the photon luminosities S in [143, 148] as a function of W and integrated over $W > W_0$; they include excitations of single protons to masses below 20 GeV; as motivated below, integrals should be performed for $70\,\text{GeV} < w < E = E_{beam}$ and $Q^2_{min} < Q^2 < 2\,\text{GeV}^2$. Also available are calculations for the "elastic" case (no proton excitation), as well as for pA and light ion interactions [149]. These calculations show that the integrated photon-photon luminosity for $W_0 = 100\,\text{GeV}$ is about 1% of the pp luminosity, while the integrated photon-proton luminosity for $W_0 = 1\,\text{TeV}$ is about 10% of the pp luminosity. Note that the integrated photon luminosities are the probabilities for a photon interaction per pp-collision.

All studies of lepton-pair production are based upon the LPAIR generator [150]. In addition, photon fluxes were integrated into the COMPHEP [151] and SHERPA [152] generators, which were used especially for simulating the process $\gamma p \rightarrow WHX$. Many of the following simulations of the reactions $\gamma\gamma \rightarrow WW$ and $\gamma p \rightarrow WX$ are based upon PHOTIA, which introduces the photon spectra into PYTHIA 6.152 [153] for photon induced interactions; PHOTIA is interfaced to OSCAR/ORCA and also produces event displays. For precision studies, EPA or calculations based on LPAIR, COMPHEP, SHERPA are not sufficient but rapidity gap survival factors S^2 should be accounted for [44, 146].

As mentioned above, $\gamma\gamma$ interactions correspond to small proton scattering angles which turn out to be of the order of the angular divergence of the beams at the interaction vertex. However, protons that lose more than about 1% of their energy to the photons are removed from the beam. At appropriately chosen positions along the accelerator structure, i.e. where
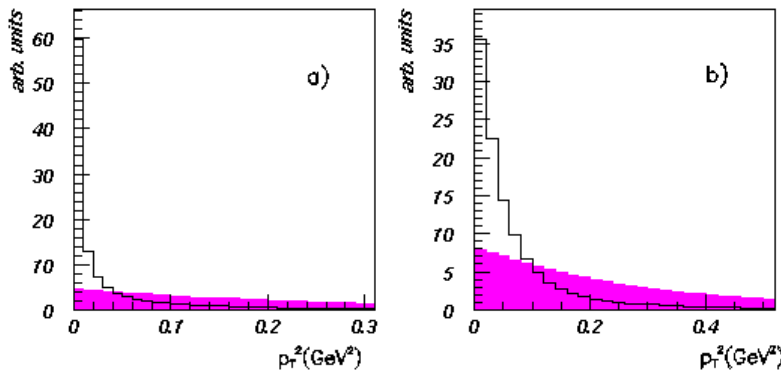
Figure 8.1: The true (a) and observed (b) p_t^2 distributions of the scattered protons in photo-production (line) and in diffraction (filled histogram).

the horizontal beam size is minimal such as at the position of the TOTEM RPs, the horizontal distance D_x of the detected proton impact to the nominal beam spot is large and allows for a safe measurement of the photon energy w via the relation $w = D - x \cdot E/D$, where D is the dispersion of the beam. At the same position the scattering angles in the horizontal and vertical planes, θ_x and θ_y, are proportional to their values $\theta_x^\star$ and $\theta_y^\star$ at the primary vertex. A measurement yields therefore the proton virtuality $Q^2 = p_T^2 = E^2 \cdot \sqrt{\theta_x^2 + \theta_y^2}$. With detectors at about 1 mm from the nominal beam with a horizontal dispersion of about 50μm, the minimal tagged photon energy is about $70\,$GeV, which is therefore to be used as a lower limit for the luminosity integrals. Typical collision energies W are then of the order of or larger than $200\,$GeV, for which consideration of all measurement uncertainties leads to a relative error $dW/W = 5/200$.

Even if forward protons are tagged, i.e. when events without rapidity gaps are suppressed, there remains a substantial number of diffractive events, as e.g. the Double-Pomeron cross section is more than 2 orders of magnitude larger than the photon-photon cross section. Based on Fig. 8.1 one realises how photon induced events can be separated from strong processes assuming equal cross sections for reasonably large energies W: in Fig. 8.1a the distribution of p_T^2 of the produced forward protons is shown both for diffractive and QED processes. The diffractive contribution corresponds to an exponential distribution $e^{-bp_T^2}$ with $b \approx 4\,$GeV^{-2}; Figure 8.1b includes the effects of the finite width of the transverse primary vertex distribution and of the beam divergence for a proton energy loss of $100\,$GeV. Selecting a proton with $p_t^2 < 0.05\,$GeV^2, the diffractive contribution is reduced to about 20% in this case; double tagging gives an even better suppression.

8.3 Photon-photon production of lepton pairs

At low momentum transfers to the proton, lepton-pairs are exclusively produced by double photon exchange, $pp \rightarrow pl^+l^-p$, i.e. by a pure QED process with well known cross section. At smaller impact parameters one or both protons may be excited into heavier mass systems X and/or additional strong re-interactions may happen. In principle, the QED contribution can be enhanced by kinematical selections. All following considerations and results are based upon the event generator LPAIR; COMPHEP gives compatible results. The QED cross section
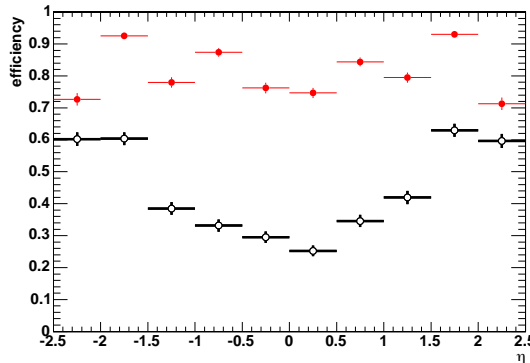
Figure 8.2: Muon reconstruction efficiency as a function of η for $p_t > 3\,\text{GeV}$ (lower points) and $p_t > 5\,\text{GeV}$ (upper points).

for producing 2 leptons, each with a transverse momentum $p_t > 2\,\text{GeV}$, is $\sigma(l\bar{l}; p_t > 2\,\text{GeV}) = 0.129$ nb. Simulations including the CMS detector (using OSCAR) and reconstruction (with ORCA) confirm the expectation that dilepton pairs emerge with small transverse momenta, such that the leptons are emitted at a relative azimuthal angle $\Delta\phi$ close to π. The studies presented do not make use of the near-beam detectors; the potential of using them is however discussed.

8.3.1 e^+e^- pairs

Two photon production of electron pairs, $\gamma\gamma \rightarrow e^+e^-$, has been observed in e^+e^- and ep collisions, and very recently in $p\bar{p}$ collisions by CDF [154] – the first time exclusive 2-photon processes have been seen in hadron-hadron collisions, and the data ($10\,\text{GeV} \le M_{ee} \le 38\,\text{GeV}$) agree with the QED prediction obtained with the LPAIR Monte Carlo.

An analysis of e^+e^- pairs was performed for leptons with $p_t > 2\,\text{GeV}$. Electrons are identified by requiring that their measured energies E and momenta p match: $0.8 < E/p < 1.2$. The average combined reconstruction (tracking) plus identification efficiency per lepton is about 0.16; it increases from about 0.07 at $p_t = 2.5\,\text{GeV}$ to 0.8 for $p_t > 6\,\text{GeV}$ ($|\eta| < 0.8$). The pair reconstruction efficiency is about 0.055 for $\Delta\phi > 3.02$. Due to the low transverse momenta, a dedicated trigger would be needed as well as a veto for background events, for example by tagging forward protons or by a measurement of energy flow by CASTOR. The current CMS L1 trigger conditions do not allow triggering on these events.

8.3.2 $\mu^+\mu^-$ pairs

More straightforward seems to be a measurement based upon μ-pairs. The cross section calculated using LPAIR for events where both muons have $p_t > 3\,\text{GeV}$ is about 50 pb. Such events have been simulated and processed with OSCAR and ORCA. The reconstruction efficiencies for each μ are shown in Fig. 8.2 for $p_t > 3\,\text{GeV}$ and $5\,\text{GeV}$, respectively, as a function of η; in Fig. 8.3 the reconstruction efficiency is given as a function of p_t, levelling off at about 0.9 for $p_t > 6\,\text{GeV}$. The reconstructed μ-pairs correspond to a cross section of 6 pb. The L1 threshold is $3\,\text{GeV}$, but a p_t threshold of $7\,\text{GeV}$ of the HLT reduces the global trigger efficiency of the standard CMS di-μ trigger to about 40%.

Drell-Yan pairs have been considered as a possible background, but can be effectively elimi-
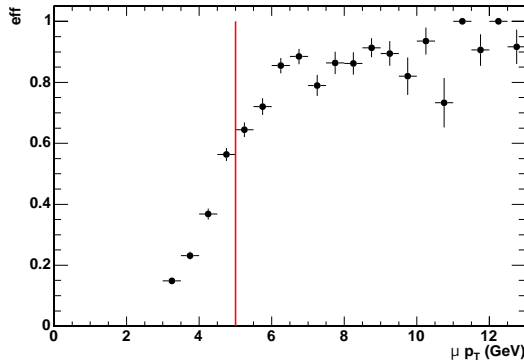
Figure 8.3: Muon reconstruction efficiency as a function of p_t.
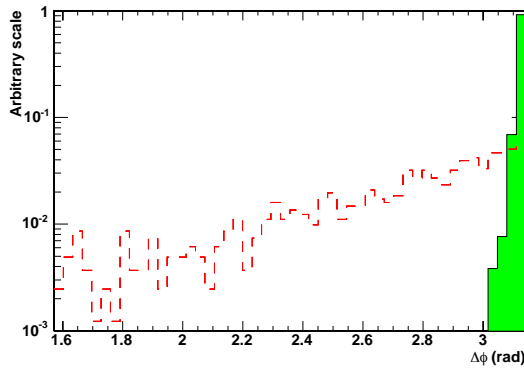
Figure 8.4: Distribution of the difference in the azimuthal angle distribution of muon pairs for Drell-Yan events (dashed histogram) and photon-photon production of dimuon pairs.

nated by requiring no additional charged tracks from the dilepton vertex. In addition, Fig. 8.4 proves that the coplanarity signature of the QED pairs can efficiently be used to suppress this background, which is also not expected to survive an energy veto using the HF calorimeter covering $2.5 < \eta < 5.5$.

An estimation indicates a possible luminosity measurement with a statistical precision of about 2% for about $0.5\,\text{fb}^{-1}$.

Distributions of generated and reconstructed di-μs in Fig. 8.5 indicate a substantial acceptance in the Υ mass region, which may turn out to be useful for calibrating/aligning the near-beam detectors – though the near-beam detector acceptance in this region is small.

Detection of both muons leads to a measurement of both the dimuon invariant mass and rapidity, from which the photon energies and hence both proton energy losses can be calculated. The predicted distribution of proton energy loss, i.e. of the ratio of E_γ/E_{proton}, suggests that this method would be useful for calibrating/aligning the FP420 detectors; at high luminosity, when the statistics at higher masses becomes significant, the 220 m detectors of TOTEM may also profit from it. Finally, the simulated energy resolution of forward protons determined from measured di-muons, i.e. the differences between the generated and inferred values of Feynman-x, shown in Fig. 8.6, is about 10^{-4}, and thus narrower than
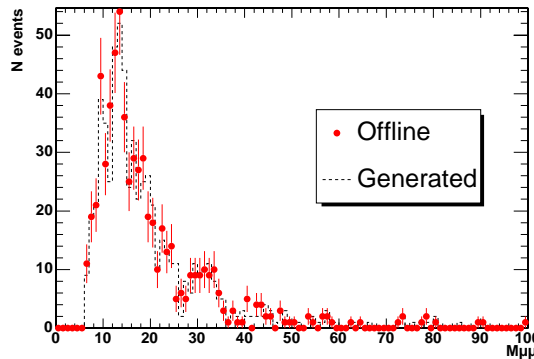
Figure 8.5: Invariant mass distribution of muon pairs for the generated (histogram) and reconstructed (full circles) events.
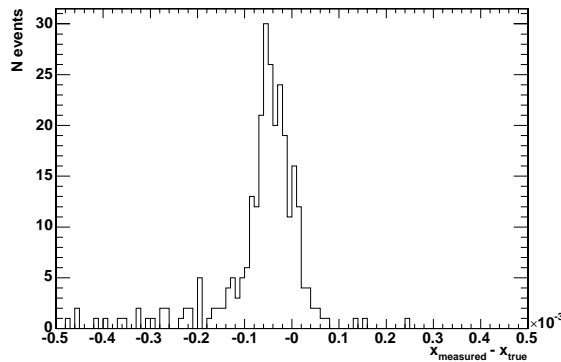

Figure 8.6: Resolution on the reconstructed forward proton momentum using exclusive muon pairs reconstructed in CMS.

the beam dispersion.

In summary, two-photon (exclusive) lepton pair production is an excellent candidate for in situ, data-driven calibration of the proton energy scale and acceptance. Even using standard CMS di-muon triggers, good statistics can be collected: for 100 pb^{-1} about 300 calibration events are expected (this does not include the near-beam detector acceptance). Resolution of proton energy loss is excellent, better than the beam energy uncertainty of 10^{-4}. Backgrounds at low luminosity, when a forward energy veto can be applied, should be negligible.

8.4 Photon-photon production of boson pairs

The production of pairs of γs, Zs, or Ws in $\gamma\gamma$ interactions is either not allowed on tree level ($\gamma\gamma$, ZZ) or sensitive to quartic couplings (WW). A potential measurement would therefore lead to insight into physics beyond the standard model – allowing a clean detection of anomalous WW production as predicted e.g. by a theory of the supercritical Pomeron [130], in which colour sextet quarks couple strongly to W and Z bosons as well as to the Pomeron. As an example, COMPHEP-based predictions of cross sections for WW production as a function of the normalised couplings a_0 and a_c are displayed in Fig. 8.7; similar predictions are
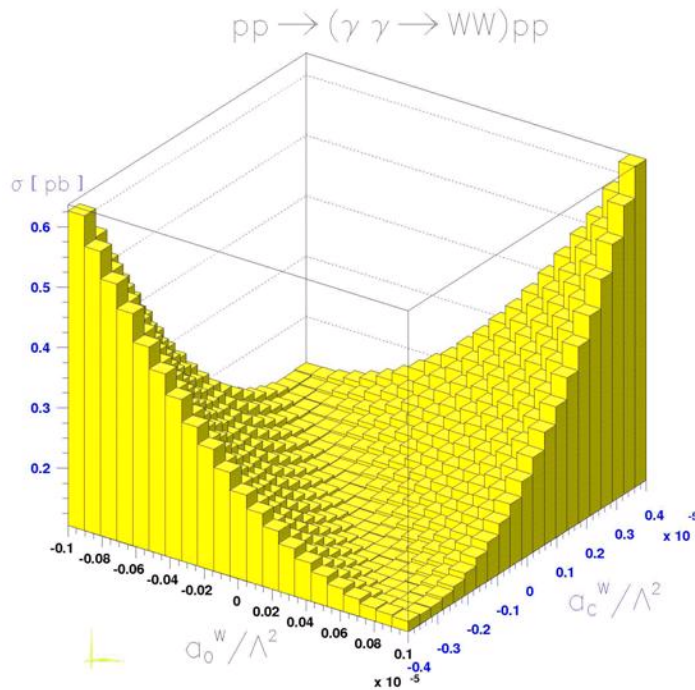
Figure 8.7: COMPHEP-based predictions of cross sections for WW production as a function of the normalised couplings a_0 and a_c.

available for ZZ pairs. In the framework of the standard model and for an integrated luminosity of $10 \, \text{fb}^{-1}$ one expects about 1000 W-pairs and a few Z-pairs (before acceptance and for all types of decays).

In a separate study, events with leptonic decays, i.e. of the type $WW \rightarrow ll$, were selected by requiring at least one "tight" lepton (electron: $E_T > 30 \, \text{GeV}$, muon: $p_T > 20 \, \text{GeV}$) and one "loose" lepton (electron: $E_T > 20 \, \text{GeV}$, muon: $p_T > 10 \, \text{GeV}$); ee, $\mu\mu$ and $e\mu$ combinations were considered. Events with jets with $E_T > 10 \, \text{GeV}$ were discarded. No restrictions for the missing transverse energy $\not{E}_T$ were applied.

The expected distributions of the transverse mass of the WW pair, of the missing E_T, of the invariant ll-mass and of $\Delta\phi$ for the two decay leptons are shown in Fig. 8.8. Superimposed on these are the corresponding generated distributions for leptonically-decaying pairs only. Figure 8.8d shows that a selection $|\Delta\phi(ll)| < 2.4$ removes the background due to non-leptonic WW decays. The resulting distributions are shown in Fig. 8.9.

The expected number of events with lepton pairs from WW-decays for $10 \, \text{fb}^{-1}$, assuming the model of Boonekamp et al. [46] implemented in DPEMC and after the cuts discussed above, is $7.7 \pm 0.4(\text{stat}) \pm 1.5 \, (\text{sys})$. The systematic uncertainty reflects the theoretical uncertainty. For this channel, backgrounds were not yet studied in detail.
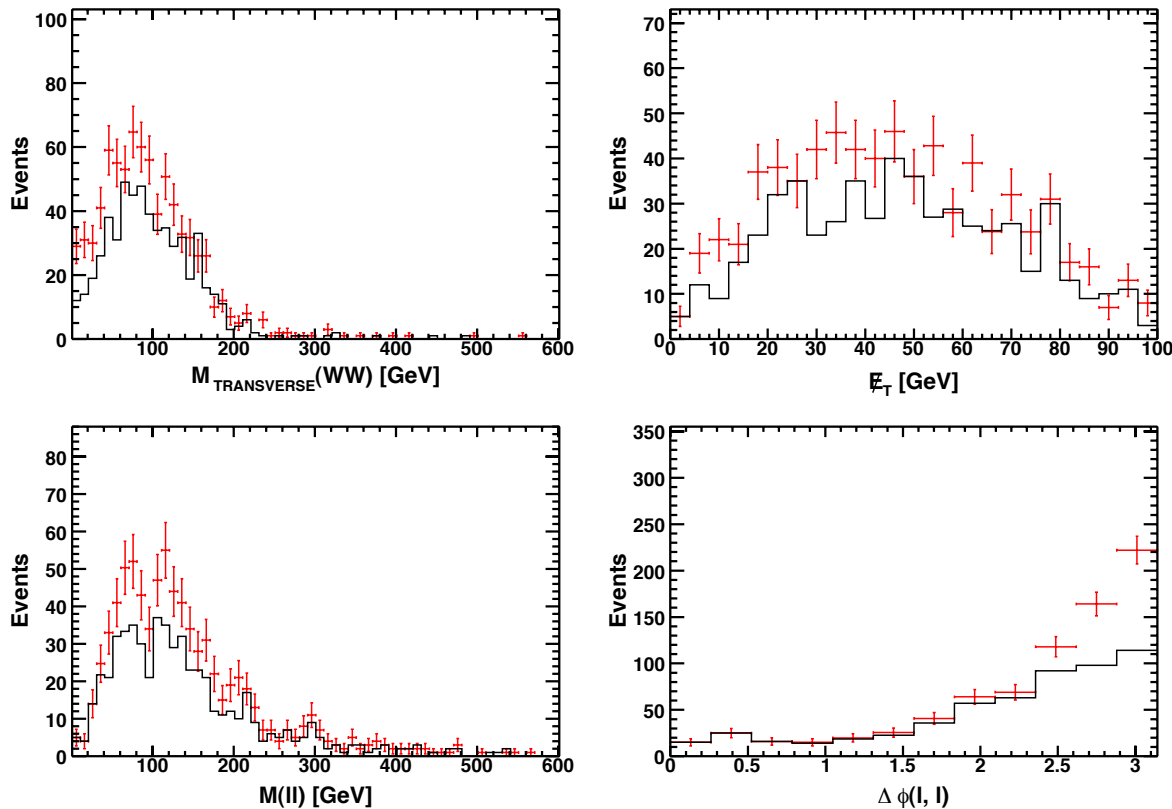
Figure 8.8:   Distributions of a) transverse mass from the lepton and missing transverse energy information, b) missing transverse energy transverse momentum, c) invariant mass of the two leptons, d) azimuthal angle difference between the two leptons. The points correspond to the FAMOS level. The histogram corresponds to the generated level for the leptonic decay modes only. The plots are not normalised to luminosity.

8.5   Photoproduction of single W and of WH

8.5.1   Photoproduction of single W bosons

The PHOTIA generator was used to study production and leptonic decay of single W bosons; the generated events were passed through the ORCA 8.1.22 program to obtain efficiencies for L1 (48%) and HLT (29%); it should be noted that the HLT efficiency is underestimated, as in the ORCA version used no muon endcap detectors were present. The resulting p_t distribution for electrons is shown in Fig. 8.10; it corresponds to about $10\,\mathrm{fb}^{-1}$.

8.5.2   Associated photoproduction of Higgs

Generation of the reaction $pp \rightarrow HWX$ with a Standard Model Higgs H was performed using CALHEP; the cross section as a function of the Higgs mass is shown in Fig. 8.12, indicating a cross section of more than 20 fb. Under study are decays of low mass Higgs bosons into $b\bar{b}$, $\tau\bar{\tau}$ and WW including all relevant backgrounds such as photoproduction of $t\bar{t}$, of WZ or single t (Fig. 8.11). For the $b\bar{b}$ final state a full CMS simulation including the trigger was performed, as well as for the irreducible background. The energy measured in the HF calorimeter can be used to efficiently suppress inclusive background. For a Higgs mass of $115\,\mathrm{GeV}$, of the order of a hundred elastic and quasi-elastic events can be expected for $10\,\mathrm{fb}^{-1}$.
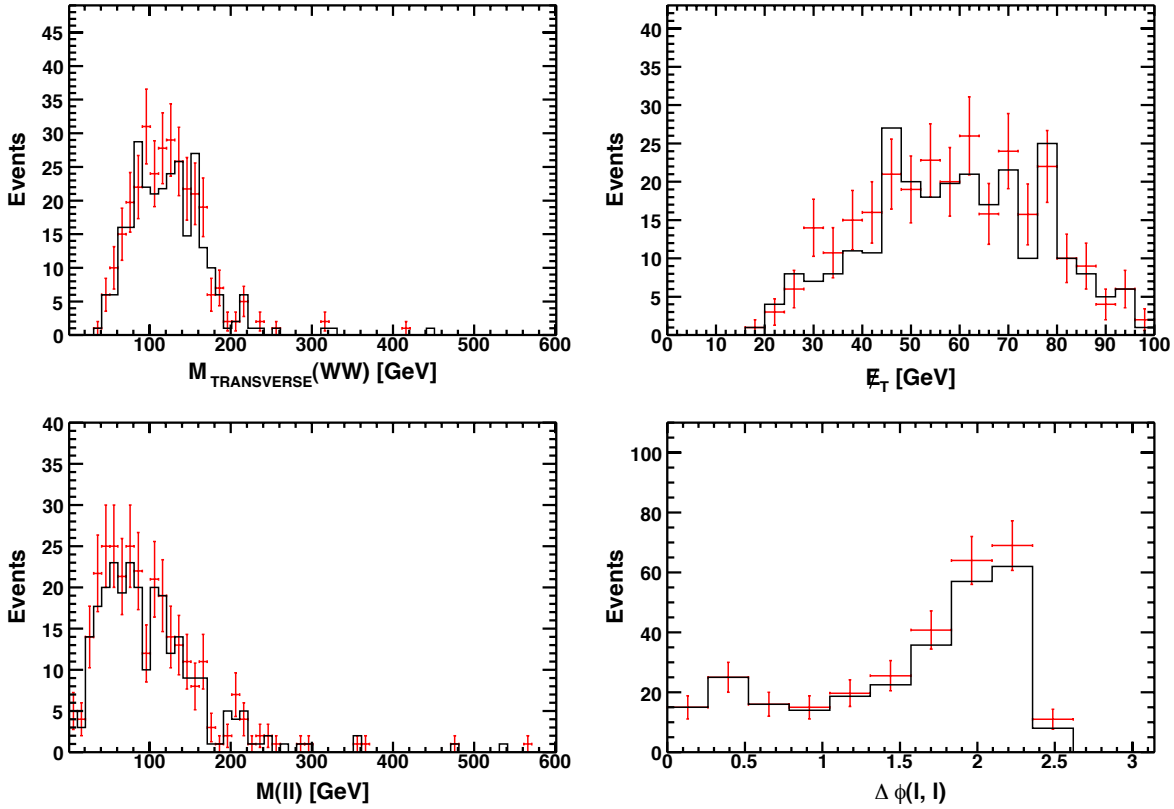
Figure 8.9: Distributions of a) transverse mass from the lepton and missing transverse energy information, b) missing transverse energy transverse momentum, c) invariant mass of the two leptons, d) azimuthal angle difference between the two leptons. The points correspond to the FAMOS level. The histogram corresponds to the generated level for the leptonic decay modes only. A cut $|\Delta\phi(ll)| < 2.4$ has been applied. The plots are not normalised to luminosity.

8.6 Summary

There is potentially a very interesting physics program with photon-induced processes, relevant to:

- absolute luminosity calibration for pp- and AA-collisions;
- precision calibration of the momentum scale of forward proton spectrometers, including a measurement of the momentum resolution;
- measurement and understanding of factorisation breaking mechanisms in hard diffraction.

Also potentially very interesting are the study of anomalous boson couplings and the production of Higgs bosons. For these channels, however, backgrounds were not yet studied in detail.

The necessary event generators have been adapted and/or developed. Many relevant cross sections were calculated and turn out to be rather large. CMS has good acceptance and trigger capabilities for all interesting processes. To suppress undesired background, forward proton detection should be made use of, along with the rapidity gap requirement. Additional
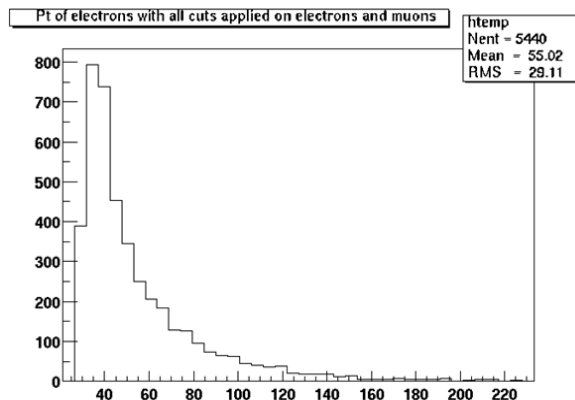
Figure 8.10: The p_t-distribution of electrons from W decay in photoproduction of single Ws.
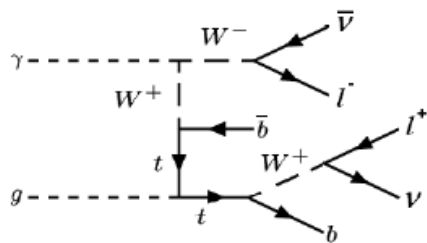
Figure 8.11: Background to associated photoproduction of Higgs due to single t photoproduction.

specialised triggers such as electron- and/or muon-triggers with a rather low p_t-threshold of the order of 2-3 GeV should be investigated. In most cases, detailed studies of efficiencies for the signals and backgrounds, of pile-up effects and trigger questions have to be pursued in more detail.
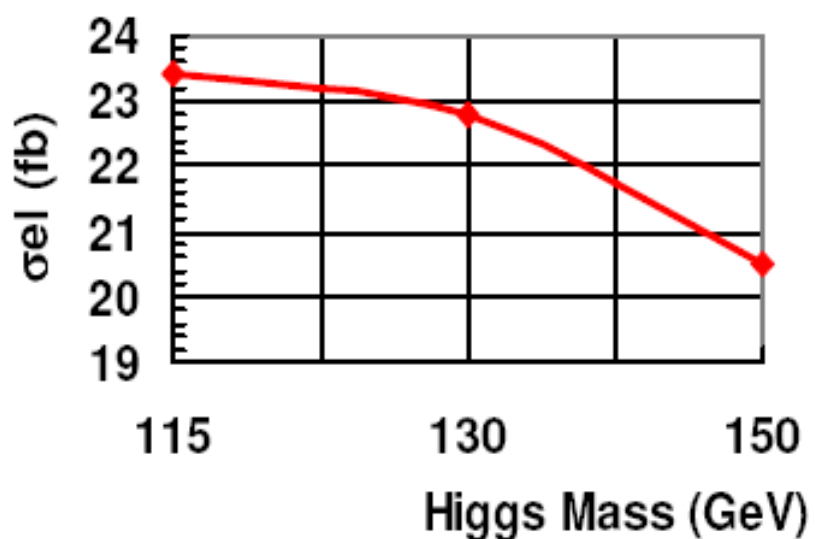
Figure 8.12: Cross section for associated photoproduction of Higgs, $pp \rightarrow p + HWX$, as a function of the Higgs mass.

Chapter 9

Low-x QCD physics

The programme of investigating the structure and the dynamics of QCD at small values of parton fractional momentum in the hadron wave-functions (low-x QCD) is not only appealing in its own right but it is an essential prerequisite for predicting a large variety of hadron-, photon- and neutrino- scattering cross sections at very high energies.

This chapter discusses the potential of forward jet measurements and of forward Drell-Yan production as means to access the parton structure and evolution at low-x in the proton. It also addresses the measurement of events with gaps between jets – a potential window on BFKL dynamics.

9.1   Parton saturation and evolution at low-x

One of the most significant discoveries of deep-inelastic (DIS) ep collisions at HERA is the strong growth of the parton distribution functions (PDF) in the proton for decreasing parton momentum fraction $x = p_{parton}/p_{hadron}$ (Bjorken-x). The gluon density is seen to grow as $xg(x,Q^2) \propto x^{-\lambda(Q^2)}$ with $\lambda \approx 0.1 - 0.3$ logarithmically rising with Q^2 [155]. As long as the densities are not too high, this growth is described by the Dokshitzer-Gribov-Lipatov-Altarelli-Parisi (DGLAP) [156–158] or by the Balitski-Fadin-Kuraev-Lipatov (BFKL) [159–161] evolution equations which govern, respectively, parton radiation in Q^2 and x. Eventually, at high enough centre-of-mass energies (i.e. very low x) the gluon density will be so large that non-linear (gluon-gluon fusion) effects will become important, saturating the growth of the parton densities. Figure 9.1 schematically depicts the different domains of the QCD evolution as a function of $y = \ln(1/x)$ and Q^2. The transition to the regime of saturated PDFs is expected for small x values ($x \lesssim 10^{-4}$) below an energy-dependent "saturation momentum" Q_s intrinsic to the size of the hadron: $Q_s^2 \approx (1\,\text{GeV}^2)\exp(\lambda\eta)$ with $\lambda \approx 0.2\text{-}0.3$ for protons probed at pseudorapidities η at the LHC [162]. In the last 15 years, an effective field theory of QCD in the high-energy (high density, small x) limit has been developed - the Colour Glass Condensate (CGC) [163, 164] - which describes the hadrons in terms of classical fields (saturated gluon wavefunctions) below the saturation scale Q_s. In this framework, hadronic and nuclear collisions are seen as collisions of classical wavefunctions which effectively "resum" all gluon recombinations and multiple parton scatterings. The quantum evolution in the CGC approach is given by the JIMWLK [165–167] non-linear equations (or by their mean-field limit for $N_c \to \infty$, the Balitsky-Kovchegov equation [168, 169]) which reduce to the standard BFKL kernel at higher x.

In hadron-hadron collisions, direct information on the PDF structure and evolution is provided by hard probes - such as jets, Drell-Yan (DY) pairs, prompt γ, heavy quarks, etc. -
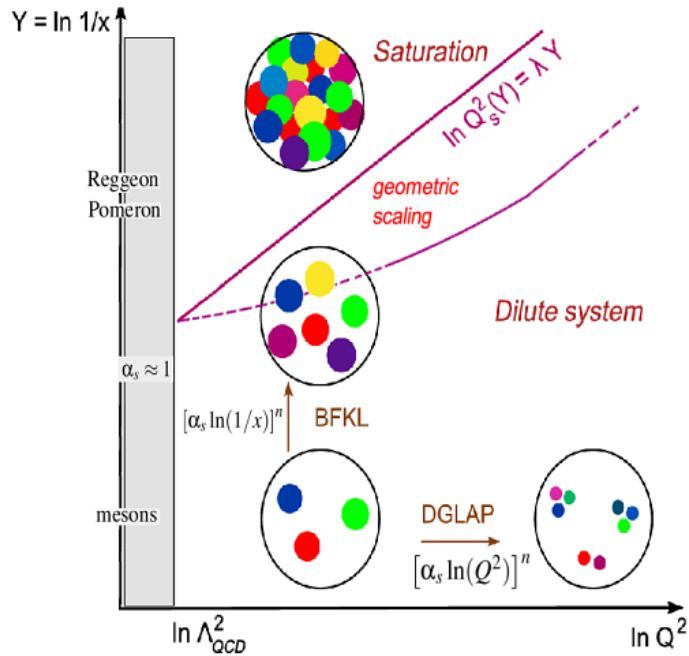
Figure 9.1: QCD "phase diagram" in the $(1/x, Q^2)$ plane (each dot represents a parton with transverse area $\sim 1/Q^2$ carrying a fraction x of the hadron momentum) [170]. Different parton evolution regimes (DGLAP, BFKL, saturation) are indicated. The upper "saturation momentum" Q_s curve separates the linear and non-linear regimes. The "geometric scaling" region covers a range of large Q^2 and moderate x where high gluon density effects still influence parton evolution [171].

which are directly coupled to the parton-parton scattering vertices. The main source of information on the *quark* densities is given by the measurement of lepton pair (Drell-Yan) production (see Section 9.3). The *gluon* densities enter at LO directly in processes with jets (see Section 9.2) and prompt photons in the final state. In addition, the production of heavy vector mesons (J/ψ, Υ) in diffractive photon-induced processes in which the hadron remains intact (or in a low excited state) and separated by a rapidity gap from the rest of the final-state particles [170], is a valuable probe of the gluon density since their cross sections are proportional to the *square* of xg [172, 173] (see Sec. 1.2.3.3). A typical measurement of e.g. direct γ, DY, or jets at central rapidities ($y = 0$) is sensitive to fractional momenta $x_T = 2Q/\sqrt{s}$, where $Q \sim p_T, M$ is the characteristic scale of the hard scattering. However, one can probe smaller x in the "target" by measuring the corresponding cross sections in the *forward* direction. From LO kinematics the rapidities and momentum fractions of the two colliding partons are related via

$$x_2 = (p_T/\sqrt{s}) \cdot (e^{-y_1} + e^{-y_2}) \quad \text{and} \quad x_1 = (p_T/\sqrt{s}) \cdot (e^{y_1} + e^{y_2}). \tag{9.1}$$

The *minimum* momentum fractions probed in a $2 \rightarrow 2$ process with a particle of momentum p_T produced at pseudo-rapidity η are [174]

$$x_2^{min} = \frac{x_T e^{-\eta}}{2 - x_T e^{\eta}} \quad , \quad x_1^{min} = \frac{x_2 x_T e^{\eta}}{2x_2 - x_T e^{-\eta}} \quad , \text{ where } \quad x_T = 2p_T/\sqrt{s} \,, \tag{9.2}$$

i.e. x_2^{min} decreases by a factor of ~ 10 every 2 units of rapidity. Although Eq. (9.2) is just a lower limit at the end of phase-space (in practice, the $\langle x_2 \rangle$ values are at least 10 larger than x_2^{min} [174]) this minimum x_2 value is virtually identical to the x_2 that one obtains from the $2 \rightarrow 1$ kinematics characteristic of parton saturation models where a single particle is produced with momentum p_T at rapidity η as a result of the fusion of two gluons (the overall momentum being "balanced" by the gluon "medium" [175, 176]):

$$x_2^{2\rightarrow 1} = (p_T/\sqrt{s})\, e^{-\eta}. \tag{9.3}$$

The Large Hadron Collider will provide pp, pA and AA collisions at $\sqrt{s}$ = 14, 8.8 and 5.5 TeV respectively with maximum luminosities $\mathcal{L} \sim 10^{34}$, 10^{29} and $5 \cdot 10^{26}\,\mathrm{cm}^{-2}\,\mathrm{s}^{-1}$. From equations (9.2) or (9.3), it follows that a hard probe with momentum p_T = 10 GeV/c emitted at $\eta = 0$ (η = 4) at $\sqrt{s}$ = 14 TeV, will be potentially sensitive to x_2 values as low as 10^{-3} (10^{-5}). The use of nuclear beams will enhance even more the non-linear QCD phenomena since the saturation momentum increases with the radius of the hadron, $Q_s^2 \propto A^{1/3}$, and saturation effects are expected to be enhanced by a factor of $A^{1/3} \approx 6$ in heavy nuclear targets (A = 208 for Pb) compared to protons [162, 170].

The experimental capabilities of CMS+TOTEM have been described in Chapter 2. CMS and TOTEM together are extremely well adapted for the study of low-x phenomena with proton and ion beams at LHC thanks to the unparalleled *forward* physics coverage including the forward hadronic calorimeter (HF, 3< $|\eta|$ <5), TOTEM T1 (3.1 < $|\eta|$ < 4.7) and T2 (5.2< $|\eta|$ <6.5) trackers, and CASTOR (5.3< $|\eta|$ <6.6) and zero-degree (ZDC, $|\eta|$ >8.1 for neutrals) calorimeters. The combination of HF, TOTEM, CASTOR and ZDC (Fig. 9.2) makes CMS the largest acceptance detector ever built at a hadron collider.
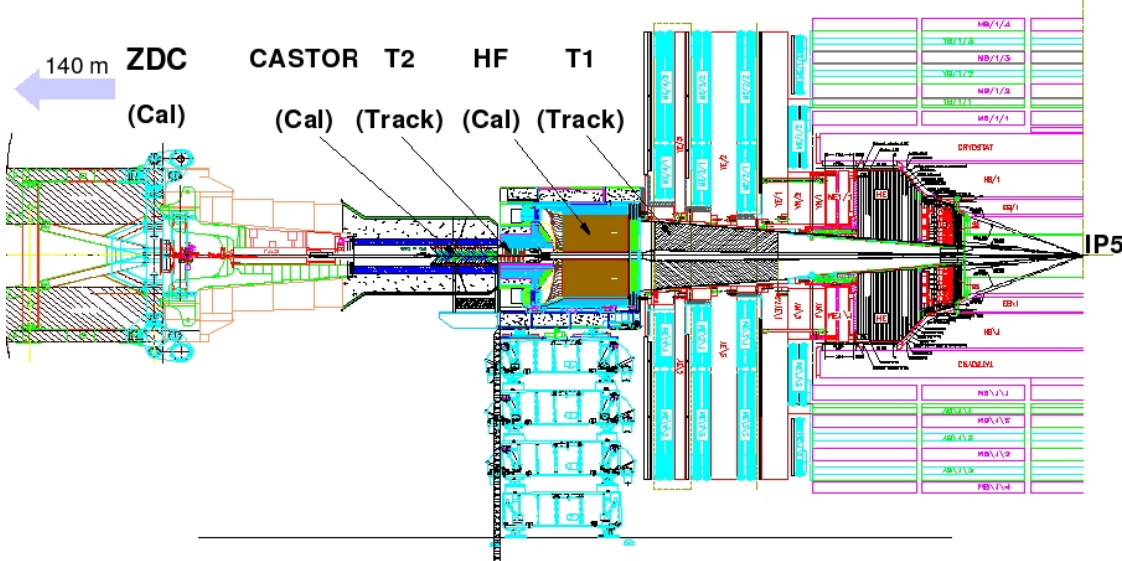

Figure 9.2: Layout of the detectors in the CMS forward region used for the low-x studies.

The following sections present two different CMS measurements accessible in pp (as well as, in principle, in pA and AA) collisions which are sensitive to the low-x high gluon density dynamics:

(i) forward jets in HF (3 < $|\eta|$ < 5), and

(ii) forward Drell-Yan pair in CASTOR-T2 ($5.3 \lesssim |\eta| \lesssim 6.6$).

A final section is devoted to the study of events with a large rapidity gap between high E_T jets, with large values of the four-momentum transfer squared across the gap. These events can be due to the exchange of a BFKL gluon ladder between the interacting partons.

9.2 Forward jets measurement in pp at $\sqrt{s} = 14$ TeV

The goal of this study is to investigate small-x QCD effects in forward-jet production at the LHC. The measurement of jets in $\bar{p}p$ collisions at Tevatron energies has been a standard tool to determine the proton PDFs in global fit analysis (see e.g. [177]). According to Eq. (9.3), the measurement in pp collisions at 14 TeV of jets with $p_T \approx 20$ - 200 GeV/c in the CMS forward calorimeter (HF, $3< |\eta| <5$) allows one to probe x values as low as $x_2 \approx 10^{-4} - 10^{-5}$. Figure 9.3 shows the actual $\log(x_{1,2})$ distribution of two partons scattering in pp collisions at 14 TeV and producing at least one jet within the HF acceptance as computed with PYTHIA 6.403 [178]. As expected in forward scattering, the collision is very asymmetric with x_2 (x_1) peaked at $\sim 10^{-4}$ ($\sim 10^{-1}$). Our analysis aims at the following two different jet measurements in proton-proton collisions at 14 TeV:

1. Single inclusive jet cross-section in HF, $Ed^3\sigma/d^3p|_{3<|\eta|<5}$, at moderately high virtualities ($Q \sim p_T \approx 20$ - 100 GeV/c).

2. "Müller-Navelet" (MN) dijet cross-section, $d\sigma/dy_1dy_2$, where two jets with moderately high and similar p_T are produced with a large relative rapidity separation: specifically, we will consider the case where two back-to-back jets are simultaneously detected in HF$^+$, $3 < \eta < 5$, and HF$^-$, $-5 < \eta < -3$.

The interest of observable (1) is based on the use of such relatively low E_T jets to constrain the low-x proton PDFs by including their cross sections in global fit analyses (note that all jet measurements so far at Tevatron have probed the PDFs at larger values $x \gtrsim 10^{-3}$ than those considered here). The motivation for (2) is based on the fact that the MN dijet cross section is a particularly sensitive measure of the BFKL [179] and small-x [180] evolution in hadronic collisions. We will present *generator-level* estimates of the expected number of jets produced in both measurements for a data sample consistent with the first LHC pp run with integrated luminosity of $1\,\text{pb}^{-1}$. Implementation of a full MC jet reconstruction simulation including detector response, underlying event subtraction, and hadronization corrections will come in a second stage. While these studies do not use any TOTEM detectors yet, their inclusion is potentially very interesting.

9.2.1 Experimental aspects

In the CMS experiment, very forward jets can be identified using the two HF calorimeters ($3< |\eta| <5$). The HF, located 11.2 m away on both sides of the interaction point (IP), is a steel plus quartz-fiber Čerenkov calorimeter segmented into 1200 towers of $\Delta\eta \times \Delta\phi \sim 0.175 \times 0.175$. It has an interaction length of $10.3\lambda_I$ and is sensitive to deposited electromagnetic (EM) and hadronic (HAD) energy. The two HFs have been specifically designed for forward jet and missing-energy measurements. In particular, the HF plays a prominent role in forward jet tagging for the vector-boson-fusion (VBF, $qq \rightarrow qqH$) Higgs production channel [181]. The HFs have an energy (position) resolution of $\sim 20\%$($\sim 10\%$) for typical jets with $E_T \sim 40$ GeV
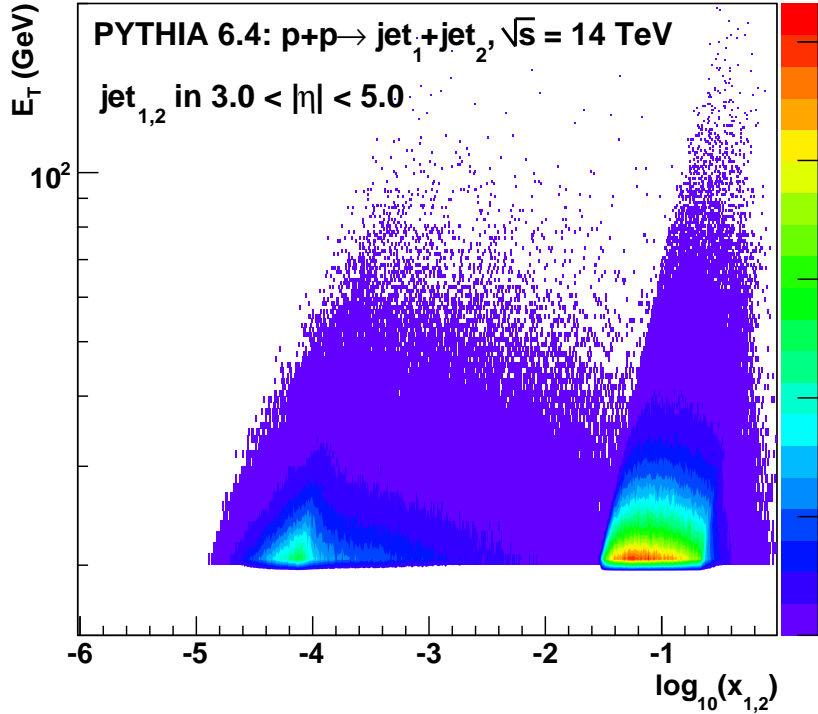
Figure 9.3: $\log(x_{1,2})$ distribution of two partons colliding in pp collisions at $\sqrt{s} = 14$ TeV and producing at least one jet above $E_T = 20$ GeV within HF acceptance ($3 < |\eta| < 5$) as determined with PYTHIA.

(i.e. $E = E_T \cosh \eta \approx 1$ TeV at $\eta = 4$) [48].

Events for this analysis can be selected online with a L1 trigger requirement of a jet candidate with a transverse energy threshold of $E_T \approx 10$ GeV since the default CMS jet L1 algorithm includes as primitives the 2×72 trigger towers in HF$^{+/-}$ (each tower has an $\eta - \phi$ segmentation of about 0.5×0.35). In addition, an HLT trigger currently exists (although with a higher $E_T = 30$ GeV threshold) for the fast jet reconstruction and tagging of forward-backward jets in HF emitted in the Higgs VBF channel [182]. We will consider an integrated luminosity for the trigger of 1 pb^{-1} for the first-year-run 14 TeV sample. Pileup interactions which, in principle, could distort the topology of the event and bias the cross sections, will be infrequent for the low instantaneous luminosity conditions in the startup LHC run ($\mathcal{L} \lesssim 10^{32}$ cm^{-2} s^{-1})

9.2.2 Monte Carlo event generation

PYTHIA 6.403 [178], interfaced via the HIROOT framework [183], was used to generate 10^7 minimum bias events (with soft and hard QCD processes on). Minimum bias (MB), rather than just hard QCD, processes were considered in order to account for the effects from the underlying event background in HF, although no particular tuning (such as e.g. the common PYTHIA-Tune A [184]) was selected. Jets were reconstructed at the generator level in a grid with the same $\Delta\eta \times \Delta\phi \sim 0.175 \times 0.175$ granularity as HF, using an iterative cone algorithm [185] with radius of $\mathcal{R} = 0.5$ in (η, ϕ), $E_{seed} = 3$ GeV and $E_{thres} = 10$ GeV. The cone size of 0.5 was chosen since, for the relatively low E_T jets considered here, it results in better

resolution as it minimises underlying event background. Seed thresholds lower than 2-3 GeV caused an inefficiency for low E_T jets and introduced a larger dependence on the details of jet fragmentation. In order to estimate the effects of the underlying event contributions and the hadronization corrections we computed the jet cross-sections at the particle-level using the iterative cone algorithm with all particles generated by PYTHIA after hadronization, as well as at the parton-level recovering the original outgoing partons directly from the MC "truth".

9.2.3   Single inclusive forward jet measurement

Figure 9.4 shows the single spectrum measured in both HFs (3< $|\eta|$ <5) obtained from PYTHIA after jet reconstruction at the particle-level compared to a NLO calculation (CTEQ6M PDFs, $\mathcal{R} = 0.5$, scales $\mu = 0.5E_T$-$2E_T$) [174]. Although PYTHIA only contemplates LO diagrams, both calculations agree well. This is not unexpected since higher-order corrections play a decreasing role at the large LHC energies [186].
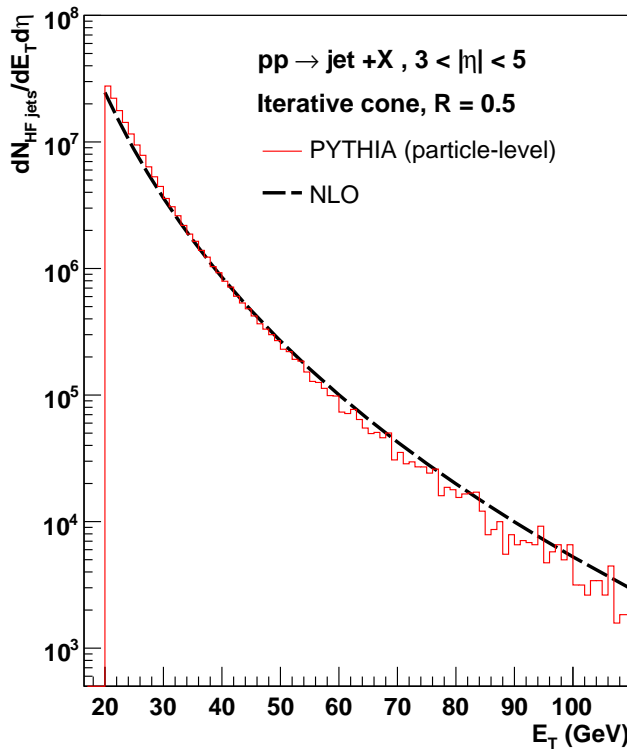
Figure 9.4: Single inclusive jet cross-section in HF ($3 < |\eta| < 5$) in pp collisions at 14 TeV as determined with PYTHIA 6.403 at the particle-level with the cone algorithm ($\mathcal{R} = 0.5$) (histogram) compared to a NLO jet calculation with scale $\mu = E_T$ (scales variations in the range $\mu = 0.5E_T$-$2E_T$ yield only ~15% changes in the spectrum) [187, 188]. [Note that no detector response, underlying event and hadronization corrections have been considered to produce the spectrum].

Although we are not taking into account any detector response in this preliminary study, we do *not* expect very significant changes in the measured spectrum due to: (i) the HF energy resolution, (ii) electronic noise, or (iii) pileup events; inasmuch as the HF jet energy resolution is excellent [48] (thanks to the large forward boost of the produced jets), the expected

electronic noise of $\sim$10 GeV at most [189] is negligible compared to the $\mathcal{O}(1\,\text{TeV})$ energy deposited by the forward-going jets, and we are considering the low luminosity conditions of a first startup run. However, the following effects will likely have a more significant effect in the measured cross-sections: (i) energy scale, (ii) underlying event (and in general final- and initial-state radiations), and (iii) hadronization corrections. The energy scale uncertainty (estimated at $\sim$3% for the first year of operation) will play a smaller role than the other two effects as we are dealing with relatively low E_T jets in this analysis. The effects of (ii) and (iii) can be approximately estimated by the differences observed in Fig. 9.4 between the parton-level and particle-level reconstructed jet cross-sections which can be as large as $\sim$30% especially at low E_T. In a coming analysis we plan to accurately estimate both contributions by rerunning the event generation with a tuned underlying PYTHIA event which reproduces well the Tevatron data [184], by subtracting the average background energy in the towers as described in [189] (this method can also correct for any residual pileup and electronic noise backgrounds), and by using an alternative hadronization scheme to the Lund string model, such as the cluster fragmentation implemented in HERWIG. With real data, one will have to consider also an additional $\sim$5% overall luminosity uncertainty. Having in mind all the caveats above, the measurement of low-E_T forward jets in HF seems feasible (the purely statistical rates are very large as shown in Fig. 9.4) but, any possible use of this measurement to constrain the proton PDFs in the associated range of low-x values will require a careful analysis of the associated cross-section uncertainties.

9.2.4 Müller-Navelet (MN) dijets measurement

Inclusive dijet production at large pseudorapidity intervals in high energy hadron-hadron collisions has been considered an excellent testing ground for BFKL [179] and also for small-x [180] evolution. The colliding partons in the MN kinematics are both large-x valence quarks ($x_{1,2} \approx 0.1$) which produce two jets with transverse energies $E_{T,i}$ with a large rapidity interval between them:

$$Y = \log(x_1\, x_2\, s / (Q_1\, Q_2))\,, \tag{9.4}$$

where $Q_i \approx E_{T,i}$ are the corresponding parton virtualities. The large rapidity separation enhances the available phase space in longitudinal momentum for BFKL radiation. A previous D0 measurement in $p\bar{p}$ collisions [190] indicated a large enhancement in the cross-section between 0.63 and 1.8 TeV but the result was not conclusive mainly because of differences in the kinematics cuts and definitions between the DØ analysis and the original Müller-Navelet proposal [191]. Those differences play a smaller role at LHC where larger values of s and η are reached. Recent works [180] indicate that in the presence of low-x saturation effects (occurring in the gluon dipole wave function or BFKL "ladder" which describes the jet production, *not* in the PDF of the colliding protons), the forward-backward MN dijet production cross section is expected to be suppressed compared to the BFKL prediction (Fig. 9.5). Factors of more than two suppression are expected for jets separated by $\Delta\eta \sim 9$ in pp at 14 TeV which is a range experimentally accessible in CMS for jets measured respectively in HF$^-$ at $\eta \approx$ -4.5 and HF$^+$ at $\eta \approx$ 4.5.

As a proof of principle of the measurement we have reanalysed the generated PYTHIA [1] sample presented in the previous Section, and selecting events with one jet in each one of the

---

[1]We note that hard parton-parton scattering in PYTHIA is computed in a collinear factorisation approach which does not, obviously, include any BFKL (or saturation) effect. The estimates discussed in this preliminary analysis can be just considered as indicative of the expected "standard" leading-order QCD yields.
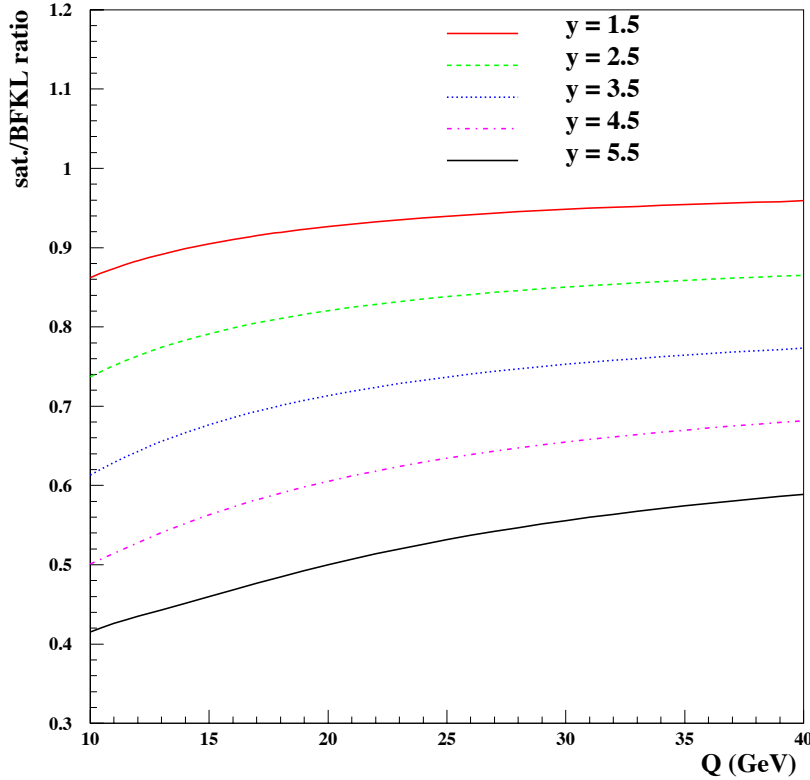
Figure 9.5: Ratio of the saturation over BFKL predictions for the Müller-Navelet forward dijet cross sections in pp collisions at $\sqrt{s}$ = 14 TeV as a function of $Q \equiv Q_1 = Q_2$ for different values of $y \equiv y_1 = -y_2$ [180].

HFs, reconstructing the relevant kinematics for the Mueller-Navelet process and determining the cross-section as a function of Q_2. In particular we applied the following event selection cuts:

- $E_{T,i} > 20$ GeV
- $|E_{T,1} - E_{T,2}| < 2.5$ GeV (similar virtuality, to minimise DGLAP-evolution)
- $3 < |\eta_{1,2}| < 5$ (both jets in HF)
- $\eta_1 \cdot \eta_2 < 0$ (each jet in a different HF)
- $|\eta_1| - |\eta_2| < 0.25$ (almost back-to-back in pseudo-rapidity)

The momentum transfer during the hard scattering is defined as:

$$Q \equiv \sqrt{E_{T,1} \cdot E_{T,2}} \ . \tag{9.5}$$

The requirements $Q \approx E_{T,1} \approx E_{T,2}$ and $\eta \approx |\eta_1| \approx |\eta_2|$ allow one to go higher values in Y (Eq. 9.4) [180]. The longitudinal momentum fractions $x_{1,2}$ carried by the two interacting MN partons can be obtained from the jet $E_{T,i}$ and η_i via Eq. (9.1). As expected dijets passing the chosen MN kinematics cuts have large-x: $0.02 \lesssim x_{1,2} \lesssim 0.3$. The data were divided into 4 equal pseudorapidity bins in HF ($\eta = [3., 3.5], ..., [4.5, 5.0]$) and the dijet cross section in each η bin was computed as

$$\frac{d^2\sigma}{d\eta dQ} = \frac{N_{jets}}{\Delta\eta\Delta Q}\frac{1}{\int \mathcal{L}\mathrm{dt}} \ , \tag{9.6}$$

where N is the observed number of jets in the bin and L is the integrated luminosity for the trigger used.

Fig. 9.6 shows the expected dijet cross-sections passing the MN kinematics cuts as a function of Q for four pseudo-rapidity ranges ([3.0-3.5], [3.5-4.0], [4.0-4.5], [4.5-5.0]) as obtained directly from PYTHIA using the jet iterative cone algorithm on the generated particles after hadronization. The measured yields are large enough for the first $\Delta\eta = 6 - 7$ range but decrease systematically for increasing rapidity separations. The measurement of the MN yields for the largest $\Delta\eta \sim 9$ separation seems challenging, not only because the yields are relatively low but especially because the true jet reconstruction efficiency in HF drops steeply beyond $\eta \approx 4.5$ according to full response studies [103]. The plots shown above should be just considered a first attempt to assess the possibility to perform such an analysis in CMS, but full simulation analyses are needed before reaching any definite conclusion.

9.3 Forward Drell-Yan pairs

In this section we focus on the Drell-Yan process, where the lepton pair originates from the annihilation of a quark-antiquark pair whose fractional momenta, x_1 and x_2, are related to the dilepton mass, M, and rapidity, y, through

$$M^2 = sx_1x_2; \qquad x_{1,2} = \frac{M}{\sqrt{s}}e^{\pm y}, \tag{9.7}$$

with $\sqrt{s} = 14\,\text{TeV}$, the centre-of-mass energy of the colliding protons. In order to be sensitive to the low x regime of the (anti)quark distributions at reasonably large values of M^2, a large imbalance in fractional momenta is required, boosting the lepton pair to large rapidities.

The effect of saturation on the cross section is shown in Fig. 9.7 where a standard parameterisation of the parton density function (CTEQ 5M1) is compared to a "saturated" parameterisation (EHKQS) [192]. In the kinematic range accessible by CASTOR, a 30% decrease of the cross section would be observed.

9.3.1 The CASTOR calorimeter and T2 tracker

The CASTOR calorimeter in CMS (see Chapter 2) is designed for low luminosity studies at very forward rapidities in pp, pA and AA interactions. If approved, this detector will cover the pseudorapidity range $5.3 < \eta < 6.6$, corresponding to Bjorken-x values down to 10^{-7}. It will consist of an electromagnetic and a hadronic section and will have a 16-fold segmentation in azimuth. It will be installed at the beginning of 2008 and operate during the first low luminosity pp phase of the LHC (and full time in the AA and pA running modes), until approximately $10\,\text{fb}^{-1}$ of data have been collected.

With the CASTOR calorimeter alone, it will be possible to trigger on electromagnetic energy deposits and to make a measurement of the electron energies and azimuthal component of the opening angle, yielding a crude estimate of the dilepton mass. As CASTOR does not provide a measurement of the polar angle, the fractional momentum of the low-x parton entering the Drell-Yan process is fully correlated to the dilepton mass through $x = M/\sqrt{s}\exp(-y_{\text{CASTOR}})$.

The TOTEM Collaboration plans to build the T2 tracker in front of CASTOR [51]. This tracker would therefore cover a similar range in pseudorapidity ($5.2 < \eta < 6.5$). It will consist of

Gas Electron Multiplier (GEM) detectors organised in trigger pads with a 2×13-fold segmentation in azimuth.

With the additional information provided by the T2 tracker, one can enhance the signal to background ratio by requiring tracks in association to the electromagnetic energy deposits. As T2 will measure both the azimuthal and polar angles of the tracks, a much more accurate measurement of the opening angle (and therefore the dilepton mass) and a two-dimensional study in M^2 and x will become possible.

9.3.2 Monte Carlo study

A preliminary generator study based on PYTHIA [116] was performed to study the kinematic coverage and trigger rates. Drell-Yan electron pair production was generated with ISUB = 1 ($q\bar{q} \to \gamma^*/Z^0$) whereby all decays of γ^*/Z^0 were disabled except those to e^+e^-. Defined as such, the total cross section for this process at $\sqrt{s} = 14\,\text{TeV}$ and with $M_{ee} > 2\,\text{GeV}$ was found to be 88 nb when using the CTEQ 5M1 parton density parameterisation. However, this cross section reduces to 2.6 nb when the lepton pair is produced within the acceptance of CASTOR, yielding 26 million events for $10\,\text{fb}^{-1}$ (which is the expected pp luminosity which CASTOR will observe).

Figure 9.8 shows the kinematic coverage as a function of Bjorken-x for Drell-Yan events with invariant mass $M_{ee} > 4\,\text{GeV}$ and with both electrons within the CASTOR acceptance. Values of order $x \sim 10^{-6}$ are reached at large rapidities. The corresponding distribution for the electron energies is also shown. The electrons in CASTOR tend to have large energies and can be selected by requiring $E_e > 300\,\text{GeV}$.

The resolution on the reconstructed M^2 and x variables was studied in the framework of FAMOS [71]. In this software package the energies of the leptons detected by CASTOR are smeared using a resolution curve measured in test beam data [193]. The angular resolution of the tracks measured in T2 were taken to be $\Delta\eta \times \Delta\phi = 0.06 \times 0.018\pi$, corresponding to the pad layout of the tracker. The resulting resolutions are shown in Fig. 9.9. On average, the resolutions are given by $(2.17 \pm 0.03)\,\text{GeV}^2$ and $(8.3 \pm 0.1) \times 10^{-8}$ for M^2 and x, respectively.

In order to get an estimate of trigger rates, samples of minimum bias QCD events were generated using PYTHIA with MSEL=2 for luminosities $\mathcal{L} = 10^{32}\,\text{cm}^{-2}\,\text{s}^{-1}$ and $\mathcal{L} = 10^{33}\,\text{cm}^{-2}\,\text{s}^{-1}$. The latter event sample includes the effects of pile-up at the LHC. At higher pp luminosities, CASTOR is not expected to be operational.

The proposed trigger strategy is based on the observation of an energy deposit in the electromagnetic part of CASTOR above threshold in combination with a veto for energy deposits in the hadronic part of the calorimeter. In order to allow for electronic noise, an upper limit for hadronic energy deposits is used. In this strategy the 16-fold azimuthal segmentation of CASTOR is exploited, such that hadronic deposits elsewhere in the calorimeter are still allowed. It was found that the depth of the electromagnetic section of CASTOR needs to be of the order of 30 radiation lengths at least, otherwise leakage of the electromagnetic shower into the hadronic section will spoil the efficiency for triggering Drell-Yan signal events.

A further decrease of the trigger rate at the first level may be obtained by requiring a confirmation from the T2 tracker. This tracker can produce a trigger signal for charged particles travelling parallel to the beam axis, although stray particles may generate a lot of fake triggers. The effect of these stray particles on the trigger rate has not been studied in this contribution.

Table 9.1 summaries the trigger rates and efficiencies for the two luminosity scenarios. Even in the case of pile-up, trigger rates down to $\sim 0.1\,\text{kHz}$ are achievable when using a trigger signal from T2, although the effect of stray particles may be expected to raise the rates. Even so, without a track requirement, the trigger rate is limited to $3\,\text{kHz}$ at $\mathcal{L} = 10^{32}\,\text{cm}^{-2}\,\text{s}^{-1}$ and $60\,\text{kHz}$ at $\mathcal{L} = 10^{33}\,\text{cm}^{-2}\,\text{s}^{-1}$. Raising the electromagnetic energy cut quickly brings down the rate, however at the cost of the efficiency for Drell-Yan signal events at low Bjorken-x.

Table 9.1: Trigger rates and efficiencies for two different luminosity scenarios. The basic trigger strategy always consist of the requirement of an electromagnetic energy deposit above threshold. In addition a veto for hadronic energy and the presence of a charged track may be asked for.

	Trigger conditions	$L = 10^{32}\,\text{cm}^{-2}\,\text{s}^{-1}$	$L = 10^{33}\,\text{cm}^{-2}\,\text{s}^{-1}$
rate	$E_{em} > 300\,\text{GeV}$	30 kHz	3000 kHz
	$+E_{had} < 5\,\text{GeV}$	3 kHz	60 kHz
	$+n_{ch} \geq 1$	< 0.01 kHz	< 0.1 kHz
	$E_{em} > 600\,\text{GeV}$	0.6 kHz	80 kHz
	$+E_{had} < 5\,\text{GeV}$	0.07 kHz	1 kHz
	$+n_{ch} \geq 1$	< 0.01 kHz	< 0.1 kHz
efficiency	$E_{em} > 300\,\text{GeV}$ $+E_{had} < 5\,\text{GeV}$ $+n_{ch} \geq 1$	$> 20\%$	$> 8\%$
	$E_{em} > 600\,\text{GeV}$ $+E_{had} < 5\,\text{GeV}$ $+n_{ch} \geq 1$	$> 3\%$	$> 1\%$

9.4 Large Rapidity Gaps between Jets

An interesting class of events that is subject to a selection based on rapidity gaps is that of dijet events where the two jets are separated by a rapidity gap. Such events were observed at Fermilab [38, 40, 194, 195]: about 1% of events with two forward jets with $\eta_1 \times \eta_2 = -1$ have a large (3 or more units) rapidity gap in between. The t-channel exchange between the scattering partons cannot be a traditional pomeron since the 4-momentum transfer squared $|t| \approx E_T^2 \approx 1000\,\text{GeV}^2$.

The physical mechanism for the process is not yet well determined. One possibility is the exchange of a colour singlet gluon ladder between the scattering partons – this could be evidence for BFKL dynamics [161, 196, 197]. Another possibility is the *Soft Colour Interaction* model [198]; in this case the gap between jets is caused by two independent processes that occur in sequence: (a) A hard qq, qg or gg scatter (exchanging colour as usual) together with (b) a soft (long time-scale, low Q^2) exchange to cancel the colour of (a). There is no high-Q^2 colour singlet; the time-scales of the hard and soft colour exchanges are very different. Understanding these processes should help understanding what to expect in central exclusive production of jets, W^+W^-, H, etc.

Measuring this "Jet-Gap-Jet" (JGJ) process does not require forward proton detectors since there are no leading protons, but can only be done in the absence of pile-up, i.e. at relatively low luminosities ($\lesssim 5 \times 10^{32}\,\text{cm}^{-2}\,\text{s}^{-1}$). As discussed earlier, the total effective integrated

luminosity, $L_{eff}^{(1)}$, i.e. the useful integrated luminosity for single interactions, is likely to be less than about $1\,\text{fb}^{-1}$, depending on the LHC ramp-up scenario. Events would be selected by requiring two forward jets with $E_T \gtrsim 40\,\text{GeV}$ and $\eta_1 > 2$ and $\eta_2 < -2$ (i.e. measured in the CMS endcap and/or HF calorimeters as discussed in the previous section). The distributions of $\sum E_T$ and particle multiplicity n_{ch} in the central region $-1.5 < \eta < +1.5$ will show a broad distribution with an excess at $\sum E_T = 0$, $n_{ch} = 0$. The dependence of the signal on the rapidity interval between the jets and their E_T will test the physics model of the process.

9.5 Conclusion

We have presented an overview of the physics of non-linear QCD and high parton densities at small fractional momenta x accessible with the forward CMS-TOTEM detectors (HF, CASTOR, T2). The quark and gluon proton structure and evolution can be studied down to $x \sim 10^{-6}$ with various hard probes (inclusive jets, dijets, Drell-Yan, etc.) in proton-proton (as well as in proton-nucleus and nucleus-nucleus) collisions. The programme of investigating the dynamics of low-x QCD is not only appealing in its own right but it is an essential prerequisite for predicting a large variety of hadron-, photon- and neutrino- scattering cross sections at very high energies.
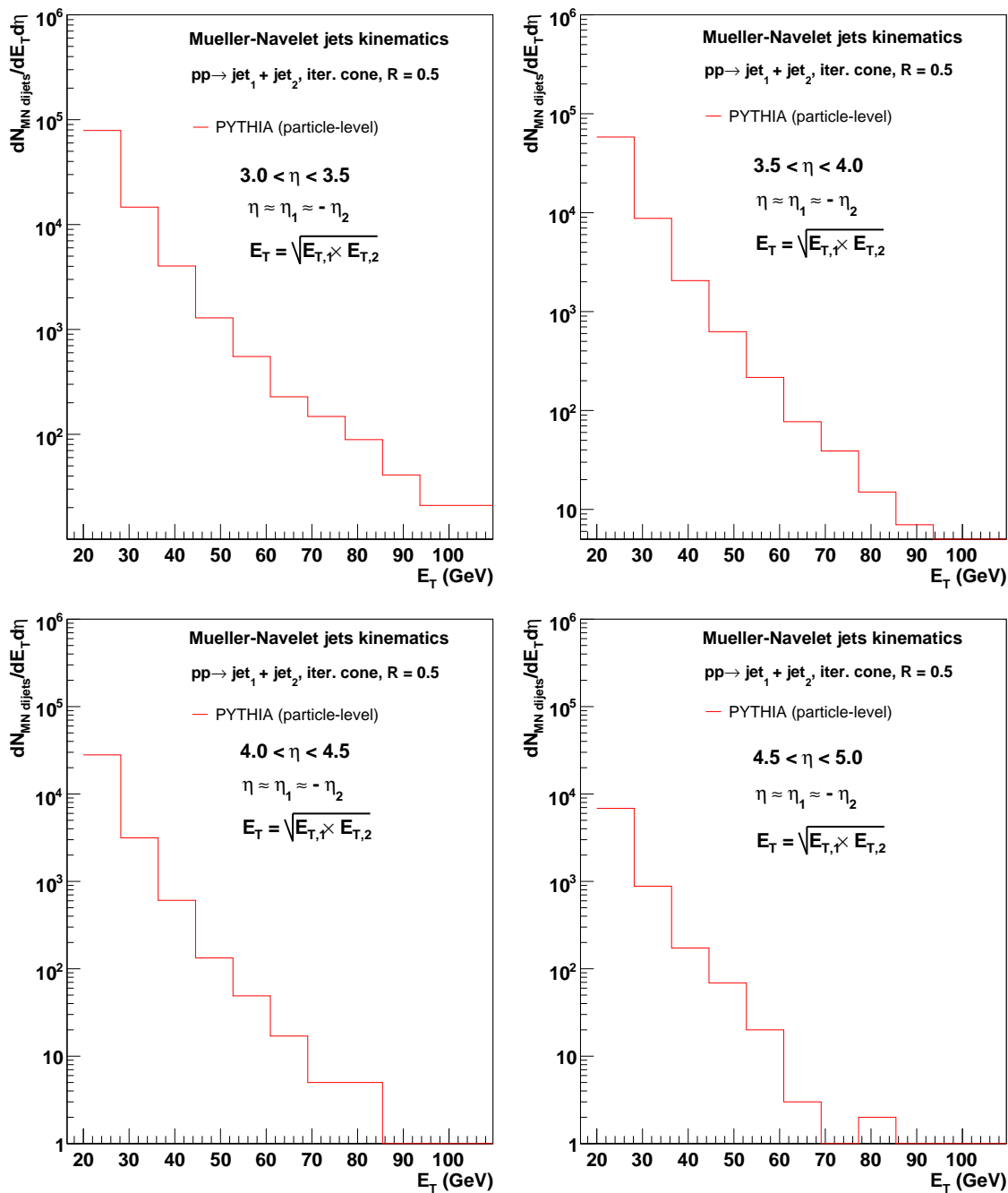
Figure 9.6: Dijet cross sections in pp collisions at $\sqrt{s} = 14$ TeV according to PYTHIA 6.403 with the Müller-Navelet kinematics cuts described in the text, as a function of $Q \equiv E_1 \approx E_2$ for different values of $\eta \equiv \eta_1 \approx -\eta_2$ = [3.0-3.5], [3.5-4.0], [4.0-4.5], [4.5-5.0].
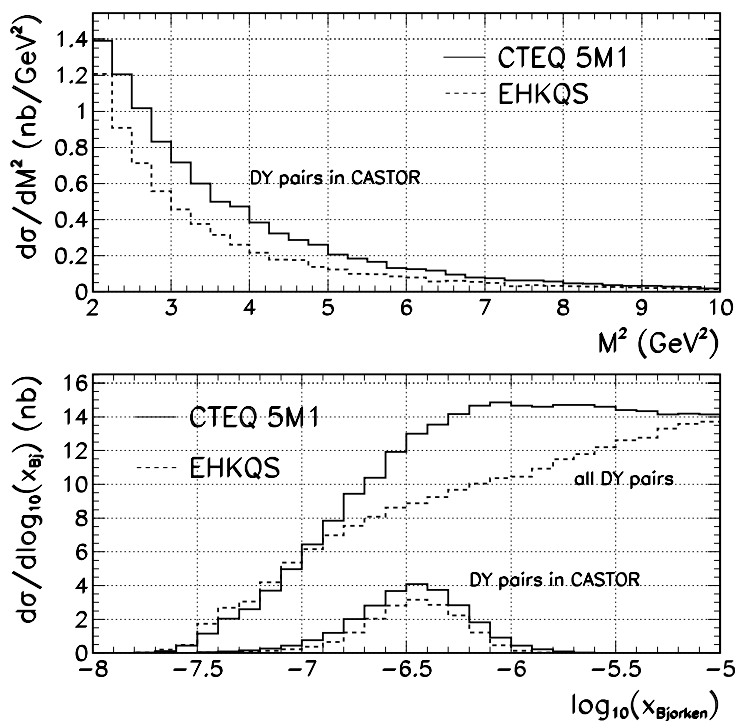
Figure 9.7: The differential cross section for Drell-Yan production of e^+e^- pairs is shown for a standard parameterisation of the parton density (CTEQ 5M1) and for a "saturated" parameterisation (EHKQS) as a function of the dilepton invariant mass (upper plot) and of Bjorken-x (lower plot).
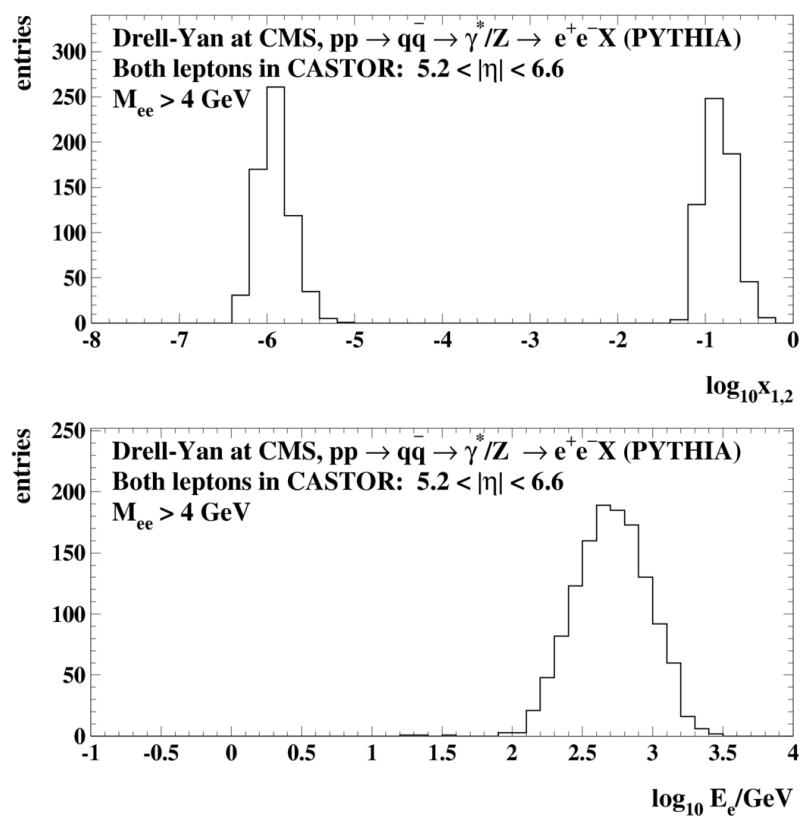
Figure 9.8: Distributions of $x_{1,2}$ (top) and energy (bottom) for Drell-Yan electrons with invariant mass $M_{ee} > 4\,\text{GeV}$, both within the acceptance of CASTOR.
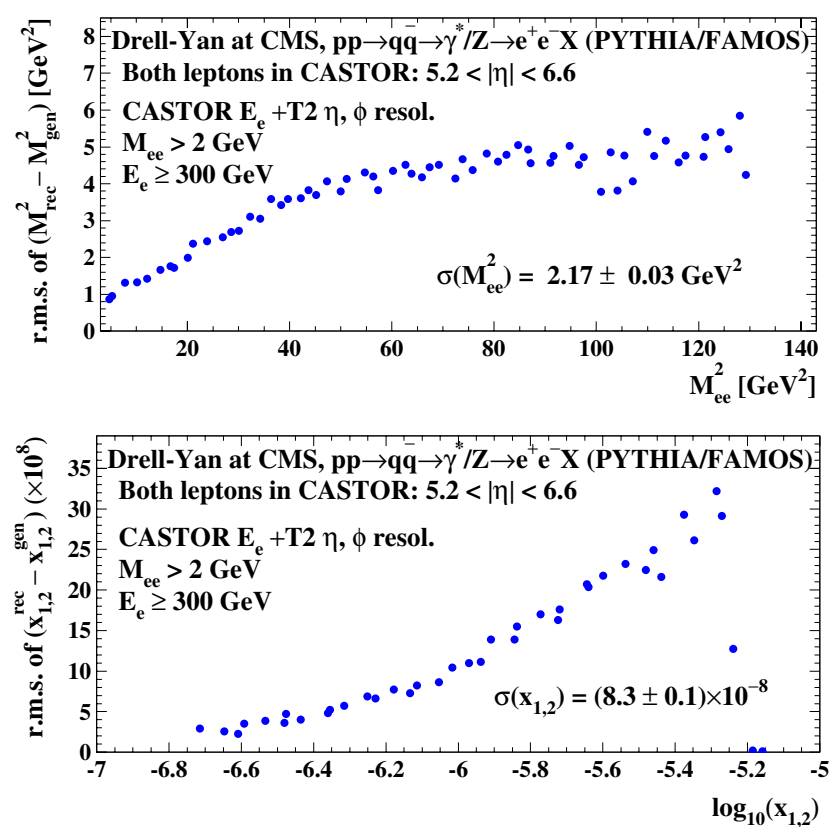
Figure 9.9: Resolutions as obtained from a FAMOS study for M^2 and x are plotted as function of the generated M^2 and x, respectively.

Chapter 10

Validation of Hadronic Shower Models Used in Cosmic Ray Physics

Primary cosmic rays in the PeV (10^{15} eV) energy range are a challenging subject in astrophysics. The origin of cosmic particles of such energy is not clear, nor is the identity of the primaries. The candidates are protons and nuclei as massive as iron, which cause hadronic showers in the air when they enter the atmosphere.

The energy and mass of ultra-high-energy cosmic rays are obtained with the help of Monte Carlo codes which describe the shower development (dominated by forward and soft QCD interactions) in the upper atmosphere. Different high-energy hadronic interaction models exist which predict energy flow, multiplicity and other quantities of such showers. There are differences of factors up to three between the predictions of currently available models, with significant inconsistencies in the forward region ($|\eta| > 5$). Fig. 10.1 shows the transverse and total energy distributions predicted by different Monte Carlo generators for pp collisions at 14 TeV. The approximate coverage of CMS (calorimetry), CASTOR and ZDC (for neutral particles) is also shown.

The rate of cosmic particles above 100 PeV is $\mathcal{O}(10^{-4})$ particles per m^2-year [200], too low for reliable quantitative analysis. Measurements at colliders are therefore very important to tune the models [201]: 100 PeV energy for a fixed target collision in the air is the centre-of-mass energy in pp collision at LHC (see Fig. 10.2).

Several quantities can be measured by CMS and TOTEM and compared with model predictions; among them, energy flow, transverse energy, total/inelastic cross section, fraction of diffractive events, particle multiplicity, ratio of the number of hadronic secondaries to that of leptonic secondaries, distribution of the inelasticity coefficient of the incident nucleon (i.e. the ratio of the energy of the most energetic outgoing particle to the energy of the incident particle; it defines the shape of the shower). Of great interest for the validation of these models is also the study of such quantities in pA (and light AA) collisions. This is not addressed here.

Samples of events obtained with some of the available generators (QGSJET 0.1 [203], SIBYLL 2.1 [204], DPMJET 3 [205], NEXUS 3 [206]) were passed through the simulation of CASTOR (as simulated by OSCAR 365) and the TOTEM detectors T1 and T2. In CASTOR, noise was assumed to have a normal distribution with a standard deviation corresponding to the energy deposition of half a minimum ionising particle (MIP) and noise threshold, in the reconstruction, of half a MIP. To evaluate the energy fraction due to muons in energy flow, the last six layers are used. Two data samples were considered: all inelastic collisions and diffractive events. Diffractive events were defined as those with a leading proton with momentum loss
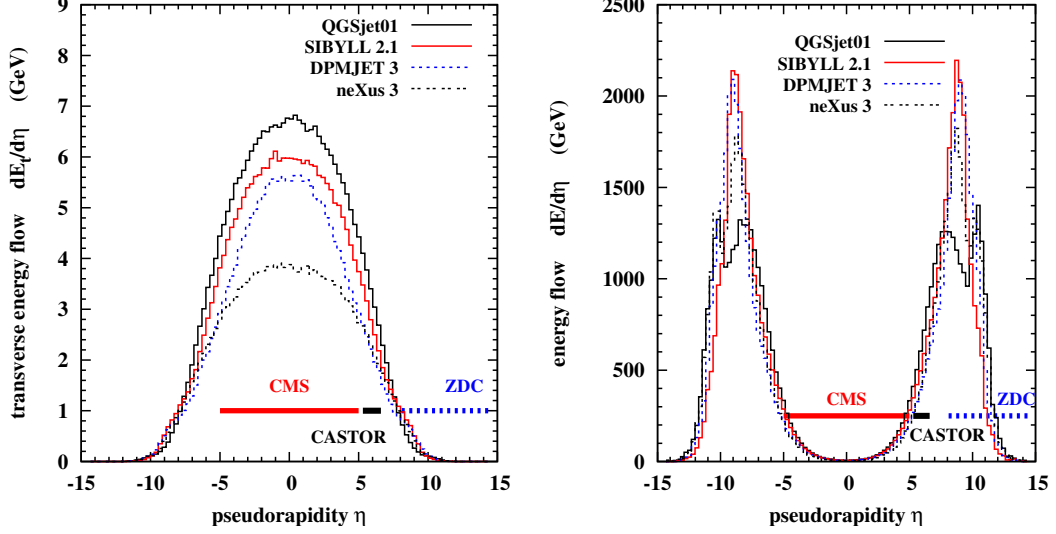
Figure 10.1: Transverse and total energy distributions for pp collisions at LHC energies predicted by four generators typically used to model hadronic showers generated by ultra-high energy cosmic rays [199].
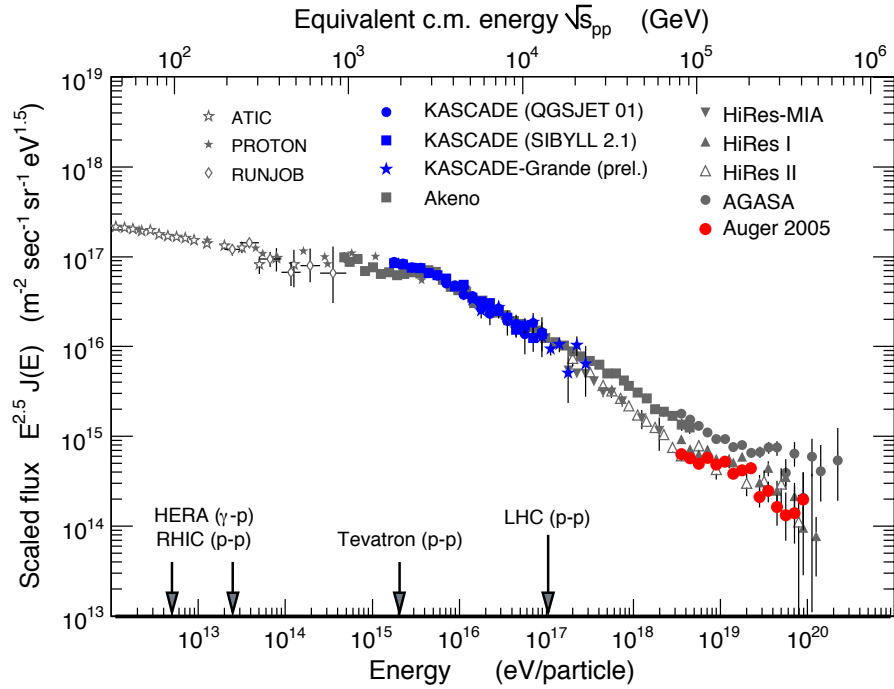

Figure 10.2: Cosmic ray flux scaled by $E^{2.5}$ as a function of energy. Shown is a selection of recent measurements; for more details and all references, the reader is referred to [202].

Table 10.1: Average particle multiplicity in T1, T2 and integrated over all pseudorapidities for proton-proton minimum bias event as expected by the generators quoted in the text.

Particle	QGS-01	SIB-2.1	DPM-3	NEXus3
p	0.73/0.51 / 4.07	0.34/0.24 / 2.66	0.35/0.20 / 2.57	0.32/0.25 / 2.48
p^-	0.7/0.39 / 2.75	0.3/0.16 / 1.26	0.34/0.17 / 1.46	0.3/0.19 / 1.20
n	0.63/0.41 / 3.18	0.33/0.24 / 1.98	0.34/0.20 / 2.02	0.33/0.25 / 1.94
$\pi^+\pi^-$	1.57/0.94 / 7.07	1.45/0.74 / 6.48	1.21/0.65 / 5.69	1.11/0.75 / 5.12
K^+K^-	2.23/1.27 / 9.28	1.61/0.88 / 7.57	1.56/0.84 / 6.81	0.87/0.61 /4.11
K_L			0.75/0.40 / 3.30	0.43/0.30 / 1.98
e^+e^-	0.03/0.015/0.125	0.025/0.013/0.123	0.012/0.007/0.063	0.008/007/0.046
γ	1.67/0.91 / 7.45	2.14/1.06 / 9.8	1.16/0.6 / 5.58	1.05/0.66 / 4.76
$\mu^+\mu^-$			.0004/.001/0.004	.0008/.0002/0.0014
$neutrinos$			0.0/0.0/.0002	
π^0	9.9/5.9 /44.3	8.8/4.6 /39.1	7.2/3.9 /33.6	6.5/4.4 /30.1
$N_{charged}$	19.44/11.56 /87.0	17.0/8.67 /76.4	14.4/7.76 /67.7	12.6/8.56/59.0
N_{total}	34.5/20.4 /153.6	30.4/15.6 /135.9	25.5/13.8/119.7	21.9/14.9/102.5

Table 10.2: Average particle multiplicity in the CASTOR pseudo-rapidity region for minimum bias/diffractive events.

Particles	QGS-01	SIB-2.1	DPM-3	NEXus3
$hadrons$	7.7 / 2.12	6.22 / 3.43	6.0 /5.0	6.25 / 1.91
e, γ	23.0 / 7.43	20.1 / 11.3	17.6 / 14.9	18.7 / 6.35
μ	10.1 / 1.83	8.0 /3.15	7.0 / 5.5	7.1 / 1.87

$0.003 < \xi < 0.05$.

Figures 10.3-10.4 show the predictions of the quoted Monte Carlo generators for the energy flow and the charged particle multiplicity, respectively. Tables 10.1 and 10.2 present the expected multiplicities in the T1, T2 and CASTOR regions; Tab. 10.3 shows the fraction of diffractive events expected in CASTOR. Significant differences in the predictions are apparent. The differences are larger for the diffractive events rather than for inelastic events. Appreciable differences are also observed for the inelasticity coefficient as well as the azimuthal behaviour of the energy flow. The study of the features of diffractive and inelastic events as measured in CASTOR and TOTEM may thus be used to validate/tune the generators.

Furthermore, the CMS Zero Degree Calorimeter (ZDC), located 140 m away from IP5 downstream of the first beam separator dipoles, can measure the energy deposit of neutral particles (e.g. photons and neutrons) for rapidities above $|\eta| \gtrsim 8.1$ and transverse momenta below $\mathcal{O}(2)$ GeV/c. Photons from the decay of very forward neutral pions as well as leading neutrons (produced in proton-proton as well as in collisions involving ions) can thus be measured with 10% (2 mm) energy (position) resolution. The measurements of the neutral energy flow and multiplicity in ZDC can thus be extremely helpful to constrain the models of hadronic shower development in the upper atmosphere, in particular concerning leading baryon and forward pion production.

Table 10.3: Fraction of diffractive events in the CASTOR pseudo-rapidity area.

| QGS-01	SIB-2.1	DPM-3	NEXus3
4.5%	12.4%	13.6%	24.3%
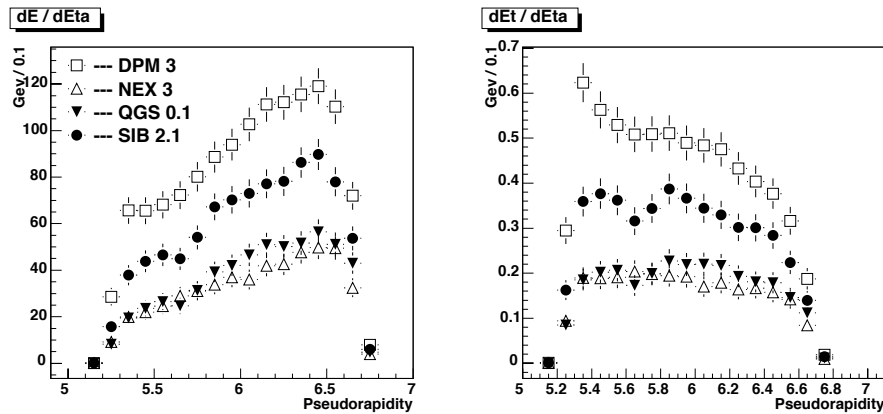
Figure 10.3: Energy flow (left panel) and transverse-energy flow (right panel) distributions in CASTOR for diffractive events as a function of pseudorapidity.
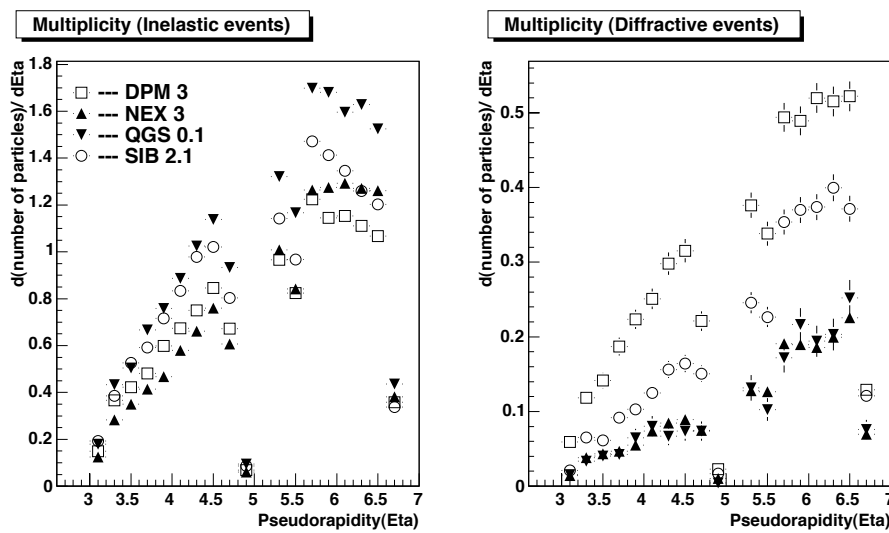

Figure 10.4: Charged particle multiplicity as a function of pseudorapidity for inelastic events (left panel) and diffractive events (right panel).

Glossary

β:
Fraction of pomeron momentum carried by a parton.

SOFT-β:
Pomeron structure function dominated by small $\beta < 0.5$ partons.

HARD-β:
Pomeron structure function dominated by large $\beta > 0.5$ partons.

SUPERHARD-β:
Pomeron structure function dominated by partons with $\beta \approx 1$ partons.

Q^2:
1. Square of the four-momentum of the virtual photon in electron-proton interactions,
2. the dominant four-momentum transfer squared in any subprocess, eg. in qq $\rightarrow$ qq.

ξ:
The ratio $p_{I\!P}/p_{\mathrm{beam}}$: fraction of beam momentum carried by the pomeron; also known as $x_{I\!P}$.

x_{Bj}:
Parton fractional momentum.

Low-x_{Bj}:
Kinematical region where parton fractional momenta are small, e.g. $x_{Bj} < 10^{-4}$.

$x_{I\!P}$:
The ratio $p_{I\!P}/p_{\mathrm{beam}}$: fraction of beam momentum carried by the pomeron; also known as ξ.

BFKL:
Balitski-Fadin-Kuraev-Lipatov (QCD evolution equations in x_{Bj}).

DGLAP:
stands for Dokshitzer-Gribov-Lipatov-Altarelli-Parisi, the authors who first wrote down the QCD evolution equation of the same name. DGLAP was first published by Altarelli and Parisi in 1977, hence DGLAP and its specialisations are sometimes still called Altarelli-Parisi equations. Only later it became known that an equivalent formula had been published in Russia by Dokshitzer also in 1977 and Gribov and Lipatov already in 1972 (in QED).

DIFFRACTION:
In a high energy physics context, any process involving the exchange of the vacuum quantum numbers.

SOFT DIFFRACTION:
A diffractive process with no large Q^2 subprocess.

HARD DIFFRACTION:
A diffractive process with a large Q^2 subprocess (a hard scale).

SINGLE DIFFRACTION (SD):
Only one incoming hadron diffractively dissociates.

DOUBLE DIFFRACTION (DD):
Two incoming hadrons both diffractively dissociate. Note: This term should not be used for Central Diffraction.

CENTRAL DIFFRACTION:
There are two pomerons in series in the t-channel, i.e. one emitted by each colliding hadron; the two pomerons then interact. This process is often called

CENTRAL INCLUSIVE DIFFRACTION (CID):
pp $\rightarrow$ p $+ Y +$ p, where $Y = X + \ldots$ (anything), i.e. there is radiation between the final state protons and the centrally produced system X (see 'central exclusive diffraction'). Sometimes referred to as inclusive double pomeron exchange (DPE).

CENTRAL EXCLUSIVE DIFFRACTION (CED):
pp $\rightarrow$ p $\oplus X \oplus$ p with $\oplus$ signs signifying rapidity gaps on both sides of the central state X, i.e. there is no radiation emitted between the final state protons and the central system X. Sometimes referred to as exclusive double pomeron exchange.

SDD:
Single diffractive dissociation.

DOUBLE DIFFRACTIVE DISSOCIATION:
Both initial state hadrons diffractively dissociate.

SINGLE DIFFRACTIVE DISSOCIATION:
only one of the initial state hadrons diffractively dissociates.

DY:
Drell-Yan scattering
ID'd PARTICLE:
A particle such as γ, e, μ, τ, J/Ψ, $W^{\pm}$, Λ, Δ, etc. identified by the detector systems.
LEADING PROTON:
A final state proton with large longitudinal momentum, e.g. $\xi < 0.15$.
MINIMUM BIAS EVENTS:
Entirety of all pp interactions.
PDF:
Parton Density Function
dPDF:
Diffractive Parton Density Function: conditional probability to find a parton in the proton when the final state of the process contains a fast proton of a given four-momentum. Diffractive parton distributions are accessed in inclusive diffractive events. See Chapter 1.
PILE-UP EVENTS:
At high luminosity, several events occur in the same bunch crossing. Any given event is thus seen overlaid with a number of pile-up events.
POMERON ($I\!P$):
Theory: The highest Regge trajectory, with the quantum numbers of the vacuum, responsible for the growth in hadronic total cross-sections at high energy.
Experimental: The dominant strongly interacting entity exchanged over large rapidity gaps.
The pomeron is now understood in terms of partons from the proton, see Chapter 1.
RAPIDITY GAP (Δy or $\Delta \eta$):
A region of longitudinal rapidity, y, or pseudo-rapidity, η, containing no particles.
DOUBLE POMERON EXCHANGE - DPE:
A diffractive process in which both colliding hadrons emit a pomeron; the two pomerons then interact.
If there are two pomerons in parallel it should be referred to as TWO POMERON EXCHANGE.
TWO POMERON EXCHANGE:
Two pomerons are exchanged in parallel; this is not the same as CENTRAL DIFFRACTION (or DOUBLE POMERON EXCHANGE).
DIS:
Deep Inelastic Scattering: A high energy lepton can probe - in inelastic lepton-proton reactions - distances that are small compared with the proton - that is, deep within the proton.
LO:
Leading Order
NLO:
Next-to-leading order

Keywords on experimental issues:

CASTOR:
Centauro And STrange Object Research: Tungsten plus quartz-plates sampling Cerenkov calorimeter with HAD and EM sections segmented in ϕ, located 14.37 m away from IP5 and covering the pseudo-rapidity range: $5.3 < |\eta| < 6.6$.
CMS FORWARD:
CMS detectors beyond $|\eta| > 2.7$.
CMS CENTRAL:
CMS detectors with acceptance $|\eta| < 2.7$.
HF:
CMS forward hadron calorimeter.
IP:
LHC interaction Point.
T1,T2:
TOTEM forward spectrometers 10 m and 14 m from the CMS interaction point (IP5).
TAN:
Neutral beam absorber located in the LHC tunnel (140 m away from IP5) adjacent to the twin-aperture beam separation dipole on each side of IP5.
TAS:
LHC IP5 front quadrupole (copper) absorbers located just in front of the first inner triplet superconducting quadrupole Q1.
ZDC:
Zero Degree Calorimeter: Tungsten plus quartz-fibre sampling Cerenkov calorimeter with HAD and EM sections located inside the TAN at 140 m from IP5 downstream the first beam separator dipoles. It covers the pseudo-rapidity range $|\eta| \gtrsim 8.3$ for neutral particles.

Main simulation and reconstruction programs:

DPEMC:
Extension of the POMWIG Monte Carlo generator [46]. Includes new models of central production through inclusive and exclusive DPE in pp collisions. Double photon Exchange processes are described as well, both in pp and heavy-ion collisions. In all contexts, various models have been implemented, allowing for comparisons and uncertainty evaluation and enabling detailed experimental simulations.
EDDE:
Monte Carlo event generator, under construction, for different Exclusive Double Diffractive

Events. The program is based on the extended Regge-eikonal approach for "soft" processes. Standard Model and its extensions are used for "hard" fusion processes [112]. An interface to PYTHIA, CMSJET and CMKIN is provided.

HERWIG:
Monte Carlo package for simulating Hadron Emission Reactions With Interfering Gluons [97].

ExHuME:
Exclusive Hadronic Monte Carlo Event (ExHuME) generator. ExHuME implements the perturbative QCD calculation of Khoze, Martin and Ryskin of the process $pp \rightarrow p + X + p$, where X is a centrally produced colour singlet system [68].

PHOJET:
Multiparticle production in high energy hadron-hadron, photon-hadron, and photon-photon interactions (hadron = proton, antiproton, neutron, or pion) [66].

POMWIG:
Pomwig is a modified version of Herwig which is capable of generating diffractive interactions. All standard Herwig hard subprocesses are available in proton - Pomeron, photon - Pomeron and Pomeron - Pomeron collisions. Reggeons are also available [122].

PYTHIA:
Event generator for a large number of physics processes, the latest version 6.409 [116, 207].

FAMOS:
CMS Fast Simulation Program [71].

ORCA:
Object-oriented Reconstruction for CMS Analysis [208].

OSCAR:
Object oriented Simulation for CMS Analysis and Reconstruction [89].

References

Notes:

a) CMS Notes are available at `http://cms.cern.ch/iCMS/` unless otherwise noted.

b) References marked **doi** should be prefixed with `http://dx.doi.org/`.

c) Totem notes are available at `http://www.cern.ch/totem/`.

---

[1] G. Ingelman and P. E. Schlein, "JET STRUCTURE IN HIGH MASS DIFFRACTIVE SCATTERING," *Phys. Lett.* **B152** (1985) 256.

[2] **UA8** Collaboration, R. Bonino et al., "Evidence for Transverse Jets in High Mass Diffraction," *Phys. Lett.* **B211** (1988) 239.

[3] C. A. Piketty and L. Stodolsky, "Diffraction model of high-energy leptonic interactions," *Nucl. Phys.* **B15** (1970) 571–600.

[4] M. Lusignoli, P. Pistilli, and F. Rapuano, "Semiinclusive neutrino scattering and pion structure functions," *Nucl. Phys.* **B155** (1979) 394–408.

[5] V. Barone and E. Predazzi, "High Energy Particle Diffraction". Springer Ed., 2002.

[6] M. Arneodo and M. Diehl, "Diffraction for non-believers," `arXiv:hep-ph/0511047`.

[7] L. Trentadue and G. Veneziano, "Fracture functions: An Improved description of inclusive hard processes in QCD," *Phys. Lett.* **B323** (1994) 201–211.

[8] A. Berera and D. E. Soper, "Behavior of Diffractive Parton Distribution Functions," *Phys. Rev.* **D53** (1996) 6162–6179, `arXiv:hep-ph/9509239`.

[9] J. C. Collins, "Proof of factorization for diffractive hard scattering," *Phys. Rev.* **D57** (1998) 3051–3056, `arXiv:hep-ph/9709499`.

[10] J. C. Collins, L. Frankfurt, and M. Strikman, "Factorization for hard exclusive electroproduction of mesons in QCD," *Phys. Rev.* **D56** (1997) 2982–3006, `arXiv:hep-ph/9611433`.

[11] J. D. Bjorken, "Rapidity gaps and jets as a new physics signature in very high-energy hadron hadron collisions," *Phys. Rev.* **D47** (1993) 101–113.

[12] A. B. Kaidalov, V. A. Khoze, A. D. Martin, and M. G. Ryskin, "Probabilities of rapidity gaps in high energy interactions," *Eur. Phys. J.* **C21** (2001) 521–529, `arXiv:hep-ph/0105145`.

[13] **UA8** Collaboration, A. Brandt et al., "Measurements of single diffraction at $\sqrt{s} = 630$ GeV: Evidence for a non-linear $\alpha(t)$ of the pomeron," *Nucl. Phys.* **B514** (1998) 3–44. `doi:10.1016/S0550-3213(97)00813-4`.

[14] S. Erhan and P. E. Schlein, "Inelastic diffraction data and the Pomeron trajectory," *Phys. Lett.* **B481** (2000) 177–186. `doi:10.1016/S0370-2693(00)00467-6`.

[15] K. Goulianos, "Twenty years of diffraction at the Tevatron," `arXiv:hep-ph/0510035`. Presented at 11th International Conference on Elastic and Diffractive Scattering: Towards High Energy Frontiers: The 20th Anniversary of the Blois Workshops.

[16] G. Giacomelli and M. Jacob, "Physics at the CERN ISR," *Phys. Rept.* **55** (1979) 1–132.

[17] L. Camilleri, "Proton Anti-Proton Physics at the CERN Intersecting Storage Rings," *Phys. Rept.* **144** (1987) 51–115.

[18] **R608** Collaboration, A. M. Smith et al., "Evidence for Pomeron Single Quark Interactions in Proton Diffraction at the ISR," *Phys. Lett.* **B163** (1985) 267.

[19] **R608** Collaboration, T. Henkes et al., "Further evidence for pomeron - quark interactions: Observation of large Lambda0 polarization in p p → (Lambda0 K+) p," *Phys. Lett.* **B283** (1992) 155–160. `doi:dx.doi.org/10.1016/0370-2693(92)91447-H`.

[20] **CCHK** Collaboration, D. Drijard et al., "Double Pomeron Exchange in the Reaction p p → p p pi+ pi- at ISR Energies," *Nucl. Phys.* **B143** (1978) 61.

[21] **Axial Field Spectrometer** Collaboration, T. Akesson et al., "A Search for Glueballs and a Study Of Double Pomeron Exchange at the CERN Intersecting Storage Rings," *Nucl. Phys.* **B264** (1986) 154.

[22] **Ames-Bologna-CERN-Dortmund-Heidelberg-Warsaw** Collaboration, A. Breakstone et al., "The Reaction pomeron-pomeron → pi+ pi- and an unusual production mechanism for the f2 (1270)," *Z. Phys.* **C48** (1990) 569–576.

[23] A. Brandt et al., "The Small angle spectrometer of experiment UA8 at the S p anti-p S collider," *Nucl. Instrum. Meth.* **A327** (1993) 412–426.

[24] **UA8** Collaboration, A. Brandt et al., "Evidence for a superhard pomeron structure," *Phys. Lett.* **B297** (1992) 417–424.

[25] J. C. Collins, L. Frankfurt, and M. Strikman, "Diffractive hard scattering with a coherent pomeron," *Phys. Lett.* **B307** (1993) 161–168, `arXiv:hep-ph/9212212`.

[26] **UA8** Collaboration, A. Brandt et al., "Cross section measurements of hard diffraction at the Spp-barS collider," *Phys. Lett.* **B421** (1998) 395–404, `arXiv:hep-ex/9709015`.

[27] **UA8** Collaboration, A. Brandt et al., "A study of inclusive double-pomeron exchange in p anti-p → p X anti-p at s**(1/2) = 630-GeV," *Eur. Phys. J.* **C25** (2002) 361–377, `arXiv:hep-ex/0205037`.

[28] **CDF** Collaboration, A. A. Affolder et al., "Diffractive dijets with a leading antiproton in $\bar{p}p$ collisions at $\sqrt{s} = 1800$ GeV," *Phys. Rev. Lett.* **84** (2000) 5043–5048.

[29] **H1** Collaboration, A. Aktas et al., "Measurement and QCD analysis of the diffractive deep- inelastic scattering cross section at HERA," *Eur. Phys. J.* **C48** (2006) 715–748, `arXiv:hep-ex/0606004`.

[30] M. Groys, A. Levy, and A. Proskuryakov, "in: HERA and the LHC - A workshop on the implications of HERA for LHC physics: Proceedings Part B," `arXiv:hep-ph/0601013`.

[31] F.-P. Schilling, "in: HERA and the LHC - A workshop on the implications of HERA for LHC physics: Proceedings Part B," `arXiv:hep-ph/0601013`.

[32] **CDF** Collaboration, F. Abe et al., "Observation of diffractive W boson production at the Tevatron," *Phys. Rev. Lett.* **78** (1997) 2698–2703, `arXiv:hep-ex/9703010`.

[33] **D0** Collaboration, V. M. Abazov et al., "Observation of diffractively produced W and Z bosons in $\bar{p}p$ collisions at $\sqrt{s} = 1800$ GeV," *Phys. Lett.* **B574** (2003) 169–179, `arXiv:hep-ex/0308032`.

[34] **CDF** Collaboration, F. Abe et al., "Measurement of diffractive dijet production at the Tevatron," *Phys. Rev. Lett.* **79** (1997) 2636–2641.

[35] **D0** Collaboration, B. Abbott et al., "Hard single diffraction in $\bar{p}p$ collisions at $\sqrt{s} = 630$ GeV and 1800 GeV," *Phys. Lett.* **B531** (2002) 52–60, `arXiv:hep-ex/9912061`.

[36] **CDF** Collaboration, A. A. Affolder et al., "Observation of diffractive beauty production at the Fermilab Tevatron," *Phys. Rev. Lett.* **84** (2000) 232–237.

[37] **CDF** Collaboration, A. A. Affolder et al., "Observation of diffractive J/ψ production at the Fermilab Tevatron," *Phys. Rev. Lett.* **87** (2001) 241802, `arXiv:hep-ex/0107071`.

[38] **CDF** Collaboration, F. Abe et al., "Observation of rapidity gaps in $\bar{p}p$ collisions at 1.8 TeV," *Phys. Rev. Lett.* **74** (1995) 855–859.

[39] K. Terashi, "W/Z + B anti-B / jets at NLO using the Monte Carlo MCFM," `arXiv:hep-ph/0105226`. Proc. of "The XLIst Rencontres de Moriond: QCD and Hadronic Interactions", La Thuile, Italy, March 18-25, 2006.

[40] **D0** Collaboration, S. Abachi et al., "Rapidity gaps between jets in $p\bar{p}$ collisions at $\sqrt{s} = 1.8$ TeV," *Phys. Rev. Lett.* **72** (1994) 2332–2336.

[41] **D0** Collaboration, T. L. Edwards, "Elastic and diffractive scattering at D0,". Prepared for 12th International Workshop on Deep Inelastic Scattering (DIS 2004), Strbske Pleso, Slovakia, 14-18 Apr 2004.

[42] M. Gallinaro, "Diffractive and exclusive measurements at CDF," `arXiv:hep-ex/0606024`. Proc. of the "XIV International Workshop on Deep Inelastic Scattering" DIS2006), Tsukuba, Japan, 20-24 April, 2006.

[43] K. Terashi, "Diffractive measurements at CDF,". Presented at 12th International Workshop on Deep Inelastic Scattering (DIS 2004), Strbske Pleso, Slovakia, 14-18 Apr 2004.

[44] V. A. Khoze, A. D. Martin, and M. G. Ryskin, "Prospects for new physics observations in diffractive processes at the LHC and Tevatron," *Eur. Phys. J.* **C23** (2002) 311–327, `arXiv:hep-ph/0111078`.

[45] B. Cox and J. Forshaw, "Herwig for diffractive interactions," *Comput. Phys. Commun.* **144** (2002) 104–110. `doi:10.1016/S0010-4655(01)00467-2`.

[46] M. Boonekamp and T. Kucs, "Pomwig v2.0: Updates for double diffraction," *Comput. Phys. Commun.* **167** (2005) 217, `arXiv:hep-ph/0312273`.

[47] **FP420** Collaboration, M. Albrow et al., "FP420: A proposal to investigate the feasibility of installing proton tagging detectors in the 420 m region of the LHC," *CERN/LHCC* **2005-025** (2005).

[48] CMS Collaboration, "The CMS Physics Technical Design Report, Volume 1," *CERN/LHCC* **CERN-LHCC-2006-001** (2006). CMS TDR 8.1.

[49] M. Chiu, A. Denisov, E. Garcia, J. Katzy, and S. White, "Measurement of mutual Coulomb dissociation in s(NN)**(1/2) = 130-GeV Au + Au collisions at RHIC," *Phys. Rev. Lett.* **89** (2002) 012302. `doi:10.1103/PhysRevLett.89.012302`.

[50] C. Adler et al., "The RHIC zero degree calorimeters," *Nucl. Instrum. Meth.* **A470** (2001) 488–499, `arXiv:nucl-ex/0008005`.

[51] TOTEM: Letter of Intent, CERN-LHCC 97-49; Technical Proposal, CERN-LHCC 99-7; Technical Design Report, CERN-LHCC-2004-002; and references therein.

[52] G. Bencze et al., "Position and timing resolution of interpolating cathode strip chambers in a test beam," *Nucl. Instrum. Meth.* **A357** (1995) 40–54.

[53] F. Sauli, "GEM: A new concept for electron amplification in gas detectors," *Nucl. Instrum. Meth.* **A386** (1997) 531–534.

[54] M. C. Altunbas et al., "Construction, test and commissioning of the triple-GEM tracking detector for COMPASS," *Nucl. Instrum. Meth.* **A490** (2002) 177–203.

[55] Roman Pot Engineering Specifications, https://edms.cern.ch/file/566420/1/tot-xrp-es-001.pdf.

[56] **TOTEM** Collaboration, M. Deile, "Tests of a Roman Pot prototype for the TOTEM experiment," `arXiv:physics/0507080`.

[57] **TOTEM** Collaboration, G. Ruggiero et al., "Planar edgeless silicon detectors for the TOTEM experiment," *IEEE Trans. Nucl. Sci.* **52** (2005) 1899–1902.

[58] C. Kenney, J. Segal, E. Westbrook, S. Parker, J. Hasi, C. Da Via, S. Watts, J. Morse, "Active-edge planar radiation sensors", to be published in Nucl. Instr. Meth.

[59] TOSTER Project, INTAS Collaborative Call with CERN, INTAS Ref . Nr 05-103-7533.

[60] T. L. S. Group:, "The Large Hadron Collider Conceptual Design," *CERN-AC-95-05* (1995) `arXiv:hep-ph/0601012`.

[61] R. Bailey. Talk at the LHC Project Workshop CHAMONIX XV 23-27 January 2006.

[62] A. Verdier, "TOTEM Optics for LHC V6.5," *LHC-Project-Note-369* **http://cdsweb.cern.ch/search.py?recid=836613ln=en** (2005).

[63] T. Collaboration, "TOTEM Physics," in *Proceedings of 17th Rencontre de Blois:11th International Conference on Elastic and Diffractive Scattering.* Chateau de Blois, Blois, France, 2005. `arXiv:hep-ex/0602025`.

[64] "The MAD-X Program, Methodical Accelerator Design." Information available at `http://www.cern.ch/mad`.

[65] LHC Layout,http://lhclayout.web.cern.ch/lhclayout/.

[66] R. Engel and J. Ranft, "Color singlet exchange between jets and the PHOJET Monte Carlo," *Nucl. Phys. Proc. Suppl.* **75A** (1999) 272–274. `doi:10.1016/S0920-5632(99)00263-7`.

[67] V. Avati and K. Österberg, "Acceptance calculations methods for low–β^* optics," *TOTEM Internal Note 05-2* **http://www.cern.ch/totem** (2005).

[68] J. Monk and A. Pilkington, "ExHuME: A Monte Carlo event generator for exclusive diffraction," *Comput. Phys. Commun.* **175** (2006) 232–239, `arXiv:hep-ph/0502077`.

[69] T. Mäki, Master thesis: Exclusive production of Higgs boson at LHC collider: Higgs mass measurement via leading proton detection, Helsinki University of Technology, 2003, http://totem.web.cern.ch/Totem/theses.html.

[70] **CMS** Collaboration, D. Acosta et al., "CMS Physics TDR Volume 1, Section 8.1," *CERN/LHCC* **2006-001** (2006) 268.

[71] **CMS** Collaboration, D. Acosta et al., "CMS Physics TDR Volume 1, Section 2.6: Fast simulation," *CERN/LHCC* **2006-001** (2006) 55.

[72] M. Ottela and K. Österberg, "Proton resolution studies for $\beta^* = 90$ m optics," *TOTEM Internal Note 06-3* **http://www.cern.ch/totem**.

[73] V. Avati and K. Österberg, "Optical functions parametrization: $\beta^* = 1540$ m," *TOTEM Internal Note 05-1* **http://www.cern.ch/totem** (2005).

[74] M. Deile, "Analytical Studies of Roman Pot Acceptance and Resolution with the $\beta^* = 1540$ m Optics," *TOTEM Internal Note 06-2* **http://www.cern.ch/totem** (2006).

[75] K. Eggert, K. Honkavaara, and A. Morsch, "Luminosity considerations for the LHC,". CERN-AT-94-04-DI.

[76] A. Rossi: Residual Gas Density Estimations in the LHC Insertion Regions IR1 and IR5 and the Experimental Regions of ATLAS and CMS for Different Beam Operations, LHC Project Report 783, Sept. 2004, http://cdsweb.cern.ch/record/794411.

[77] S. Redaelli. Private communication (2005).

[78] V. Avati, M. Deile, D. Macina, V. Talanov: First results of the machine induced background estimation for the forward physics detectors in the IR5 of the LHC, LHC Project Note 360, December 2004, http://cdsweb.cern.ch/record/813913.

[79] M. Deile, "Estimates on Machine-Induced Background in the Roman Pots," *TOTEM Internal Note 06-4* **http://www.cern.ch/totem** (2006).

[80] N. Mokhov, Simulation of pp-induced background at $\beta^* = 0.55$ m in the RP stations at 148 m and 220 m, private communication, May 2006.

[81] N. V. Mokhov, A. I. Drozhdin, I. L. Rakhno, and D. Macina, "Accelerator related backgrounds in the LHC forward detectors," *FERMILAB-Conf-03/086* (2003). Presented at Particle Accelerator Conference (PAC 03), Portland, Oregon, 12-16 May 2003, Additional figures from private communication. Available at `http://lss.fnal.gov/archive/2003/conf/Conf-03-086.pdf`.

[82] **CERN-US to the LHC Project** Collaboration, N. V. Mokhov, I. L. Rakhno, J. S. Kerby, and J. B. Strait, "Protecting LHC IP1/IP5 Components Against Radiation Resulting from Colliding Beam Interactions,". CERN-LHC-PROJECT-REPORT-633.

[83] **CMS** Collaboration, D. Acosta et al., "CMS Physics TDR Volume 1, Section 11.1: Tower definition and thresholds," *CERN/LHCC* **2006-001** (2006) 404.

[84] **ZEUS** Collaboration, S. Chekanov et al., "Exclusive electroproduction of ϕ mesons at HERA," *Nucl. Phys.* **B718** (2005) 3–31. `doi:dx.doi.org/10.1016/j.nuclphysb.2005.04.009`.

[85] V. A. Petrov and R. A. Ryutin, "Exclusive double diffractive events: Menu for LHC," *JHEP* **08** (2004) 013, `arXiv:hep-ph/0403189`.

[86] J. C. Collins, "Light-cone variables, rapidity and all that," `arXiv:hep-ph/9705393`.

[87] **CDF** Collaboration, D. Acosta et al., "Inclusive Double-Pomeron Exchange at the Fermilab Tevatron pbar p Collider," *Phys. Rev. Lett.* **93** (2004) 141601.

[88] R. D. et. al, "Calorimeter cell energy thresholds for jet reconstruction in CMS," *CMS NOTE* **2006/020** (2006).

[89] "OSCAR: CMS Simulation Package Home Page." `http://cmsdoc.cern.ch/oscar`.

[90] **H1** Collaboration, C. Adloff et al., "Inclusive measurement of diffractive deep-inelastic e p scattering," *Z. Phys.* **C76** (1997) 613–629, `arXiv:hep-ex/9708016`.

[91] F. E. Close and G. A. Schuler, "Evidence that the pomeron transforms as a non-conserved vector current," *Phys. Lett.* **B464** (1999) 279–285, `arXiv:hep-ph/9905305`.

[92] **WA102** Collaboration, D. Barberis et al., "Experimental evidence for a vector-like behaviour of Pomeron exchange," *Phys. Lett.* **B467** (1999) 165–170, `arXiv:hep-ex/9909013`.

[93] V. A. Khoze, A. D. Martin, and M. G. Ryskin, "Double-diffractive processes in high-resolution," *Eur. Phys. J.* **C19** (2001) 477, `arXiv:hep-ph/0011393`.

[94] N. I. Kochelev, "Unusual properties of the central production of glueballs and instantons," `arXiv:hep-ph/9902203`.

[95] N. I. Kochelev, T. Morii, and A. V. Vinnikov, "Pomeron fusion and central eta and eta' meson production," *Phys. Lett.* **B457** (1999) 202–206, `arXiv:hep-ph/9903279`.

[96] A. Kirk and O. Villalobos Baillie, "A study of double pomeron exchange in ALICE," `arXiv:hep-ph/9811230`.

[97] G. Corcella et al., "HERWIG 6: An event generator for hadron emission reactions with interfering gluons (including supersymmetric processes)," *JHEP* **01** (2001) 010, `arXiv:hep-ph/0011363`. `doi:10.1088/1126-6708/2001/01/010`.

[98] M. Albrow et al., "A Search for the Higgs Boson using Very Forward Tracking Detectors with CDF," `arXiv:hep-ex/0511057`.

[99] V. A. Khoze, A. D. Martin, M. G. Ryskin, and W. J. Stirling, "Diffractive gamma gamma production at hadron colliders," *Eur. Phys. J.* **C38** (2005) 475–482, `arXiv:hep-ph/0409037`.

[100] **CDF** Collaboration, A. Abulencia, "Observation of exclusive electron positron production in hadron hadron collisions," `arXiv:hep-ex/0611040`.

[101] M. Arneodo et al., "Diffractive Higgs: CMS/TOTEM Level-1 Trigger Studies," in *Proceedings of the HERA-LHC Workshop*. CERN/DESY, January, 2005. Available at `http://www.desy.de/~heralhc/proceedings/wg4arneodo.pdf`.

[102] M. Grothe et al., "Triggering on Forward Physics," *CMS Note* **2006/054** (2006). Also available as TOTEM NOTE 2006-01.

[103] **CMS** Collaboration, M. Della Negra et al., "CMS Physics, Technical Design Report, Vol. 2 Physics Performance," technical report, CMS Collaboration, 2006. CMS-TDR-008-2.

[104] R. Croft, "Emulation of The GCT Jet Processing Chain and Diffractive Trigger Studies for The CMS Experiment". PhD thesis, University of Bristol, 2007.

[105] F. Oljemark, "First level triggering of diffractively produced low-mass Higgs at The Large Hadron Collider," Master's thesis, University of Helsinki, 2006.

[106] V. Avati and K. Österberg, "TOTEM forward measurements: leading proton acceptance," in *Proceedings of the HERA-LHC Workshop*. CERN/DESY, January, 2005. Available at `http://www.desy.de/~heralhc/proceedings/wg4avati.pdf`.

[107] J. Kalliopuska et al., "TOTEM forward measurements: exclusive central diffraction," in *Proceedings of the HERA-LHC Workshop*. CERN/DESY, January, 2005. Available at `http://www.desy.de/~heralhc/proceedings/wg4pXp_heralhc.pdf`.

[108] G. Bruni et al., "Leading proton production in ep and pp, experiments: how well do high-energy physics Monte Carlos reproduce the data ?," in *Proceedings of the HERA-LHC Workshop*. CERN/DESY, January, 2005. Available at `http://www.desy.de/~heralhc/proceedings/wg5lps.pdf`.

[109] V. A. Khoze, A. D. Martin, and M. G. Ryskin, "The extraction of the bare triple-Pomeron vertex: A crucial ingredient for diffraction," `arXiv:hep-ph/0609312`.

[110] F. Ferro, "Diffractive Higgs in CMS/TOTEM: study of L1 trigger conditions from T1 and T2," *TOTEM Note* **04-2005** (2005).

[111] CMS Collaboration, "The TriDAS Project Technical Design Report, Volume 1: The Trigger Systems," *CERN/LHCC* **2000-38** (2000). CMS TDR 6.1.

[112] R. Ryutin, "EDDE Monte Carlo event generator," `arXiv:hep-ph/0409180`.

[113] CMS Collaboration, "The TriDAS Project Technical Design Report, Volume 2: Data Acquisition and High-Level Trigger," *CERN/LHCC* **2002-26** (2002). CMS TDR 6.2.

[114] **ZEUS** Collaboration, S. Chekanov et al., "Leading proton production in e+ p collisions at HERA," *Nucl. Phys.* **B658** (2003) 3–46, `arXiv:hep-ex/0210029`.

[115] **ZEUS** Collaboration, S. Chekanov et al., "Dissociation of virtual photons in events with a leading proton at HERA," *Eur. Phys. J.* **C38** (2004) 43–67, `arXiv:hep-ex/0408009`.

[116] T. Sjostrand, L. Lonnblad, and S. Mrenna, "PYTHIA 6.2: Physics and manual," `arXiv:hep-ph/0108264`.

[117] A. De Roeck, V. A. Khoze, A. D. Martin, R. Orava, and M. G. Ryskin, "Ways to detect a light Higgs boson at the LHC," *Eur. Phys. J.* **C25** (2002) 391–403, `arXiv:hep-ph/0207042`.

[118] M. G. Albrow and A. Rostovtsev, "Searching for the Higgs at hadron colliders using the missing mass method," `arXiv:hep-ph/0009336`.

[119] A. Kisselev, V. Petrov, and R. Ryutin, "5-dimensional quantum gravity effects in exclusive double diffractive events," *Phys. Lett.* **B630** (2005) 100–107. `doi:10.1016/j.physletb.2005.09.059`.

[120] M. Boonekamp et al., "Monte-Carlo generators for central exclusive diffraction," in *Proceedings of the HERA-LHC Workshop*. CERN/DESY, January, 2005. Available at `http://www.desy.de/~heralhc/proceedings/wg4montecarlo.pdf`.

[121] V. A. Khoze, A. B. Kaidalov, A. D. Martin, M. G. Ryskin, and W. J. Stirling, "Diffractive processes as a tool for searching for new physics," `arXiv:hep-ph/0507040`.

[122] B. E. Cox and J. R. Forshaw, "POMWIG: HERWIG for diffractive interactions," *Comput. Phys. Commun.* **144** (2002) 104–110, `arXiv:hep-ph/0010303`.

[123] B. Cox, J. R. Forshaw, and B. Heinemann, "Double diffractive Higgs and di-photon production at the Tevatron and LHC," *Phys. Lett.* **B540** (2002) 263–268, `arXiv:hep-ph/0110173`.

[124] V. Khoze and M. Ryskin. Private communication (2006).

[125] A. Kupčo and M. Taševský. Private communication (2006).

[126] M. Grothe, "Forward proton detectors at high luminosity at the LHC," `arXiv:physics/0610156`.

[127] A. Pilkington. Private communication (2006).

[128] H. Kowalski. Private communication (2006).

[129] B. E. Cox et al., "Detecting the standard model Higgs boson in the W W decay channel using forward proton tagging at the LHC," *Eur. Phys. J.* **C45** (2006) 401–407, `arXiv:hep-ph/0505240`.

[130] A. R. White, "The physics of a sextet quark sector," *Phys. Rev.* **D72** (2005) 036007, `arXiv:hep-ph/0412062`.

[131] H. P. Nilles, "Supersymmetry, Supergravity and Particle Physics," *Phys. Rept.* **110** (1984) 1.

[132] H. E. Haber and G. L. Kane, "The Search for Supersymmetry: Probing Physics Beyond the Standard Model," *Phys. Rept.* **117** (1985) 75.

[133] R. Barbieri, "Looking Beyond the Standard Model: the Supersymmetric Option," *Riv. Nuovo Cim.* **11N4** (1988) 1–45.

[134] A. B. Kaidalov, V. A. Khoze, A. D. Martin, and M. G. Ryskin, "Extending the study of the Higgs sector at the LHC by proton tagging," *Eur. Phys. J.* **C33** (2004) 261–271, `arXiv:hep-ph/0311023`.

[135] J. R. Ellis, J. S. Lee, and A. Pilaftsis, "Diffraction as a CP and lineshape analyzer for MSSM Higgs bosons at the LHC," *Phys. Rev.* **D71** (2005) 075007, `arXiv:hep-ph/0502251`.

[136] M. Boonekamp, J. Cammin, S. Lavignac, R. Peschanski, and C. Royon, "Diffractive SUSY particle production at the LHC," *Phys. Rev.* **D73** (2006) 115011, `arXiv:hep-ph/0506275`.

[137] S. Heinemeyer, W. Hollik, and G. Weiglein, "Constraints on tan(beta) in the MSSM from the upper bound on the mass of the lightest Higgs boson," *JHEP* **06** (2000) 009, `arXiv:hep-ph/9909540`.

[138] **ALEPH** Collaboration, S. Schael et al., "Search for neutral MSSM Higgs bosons at LEP," *Eur. Phys. J.* **C47** (2006) 547–587, `arXiv:hep-ex/0602042`.

[139] **LEP Working Group for Higgs boson searches** Collaboration, R. Barate et al., "Search for the standard model Higgs boson at LEP," *Phys. Lett.* **B565** (2003) 61–75, `arXiv:hep-ex/0306033`.

[140] S. Heinemeyer, W. Hollik, and G. Weiglein, "Decay widths of the neutral CP-even MSSM Higgs bosons in the Feynman-diagrammatic approach," *Eur. Phys. J.* **C16** (2000) 139–153, `arXiv:hep-ph/0003022`.

[141] M. Boonekamp, R. Peschanski, and C. Royon, "Inclusive Higgs boson and dijet production via double pomeron exchange," *Phys. Rev. Lett.* **87** (2001) 251806, `arXiv:hep-ph/0107113`.

[142] M. Boonekamp, R. Peschanski, and C. Royon, "Popping out the Higgs boson off vacuum at Tevatron and LHC," *Nucl. Phys.* **B669** (2003) 277–305, `arXiv:hep-ph/0301244`.

[143] K. Piotrzkowski, "Tagging two-photon production at the LHC," *Phys. Rev.* **D63** (2001) 071502, `arXiv:hep-ex/0009065`.

[144] G. Baur et al., "Hot topics in ultra-peripheral ion collisions," `arXiv:hep-ex/0201034`.

[145] V. Budnev, I. Ginzburg, G. Meledin, and V. Serbo, "The Two photon particle production mechanism. Physical problems. Applications. Equivalent photon approximation," *Phys. Rept.* **15** (1974) 181–281. `doi:10.1016/0370-1573(75)90009-5`.

[146] V. Khoze, A. Martin, and M. Ryskin, "Photon-exchange processes at hadron colliders as a probe of the dynamics of diffraction," *Eur. Phys. J.* **C24** (2002) 459–468, `arXiv:hep-ph/0201301`. `doi:10.1007/s10052-002-0964-4`.

[147] V. A. Khoze, A. D. Martin, R. Orava, and M. G. Ryskin, "Luminosity monitors at the LHC," *Eur. Phys. J.* **C19** (2001) 313–322, `arXiv:hep-ph/0010163`.

[148] K. Piotrzkowski, "High energy photon interactions at the LHC," *AIP Conf. Proc.* **792** (2005) 544–547.

[149] D. Bocian and K. Piotrzkowski, "Very forward two-photon e+ e- production and luminosity measurement for ion collisions at the LHC," *Acta Phys. Polon.* **B35** (2004) 2417–2424.

[150] S. P. Baranov, O. Duenger, H. Shooshtari, and J. A. M. Vermaseren, "LPAIR: A generator for lepton pair production,". In *Hamburg 1991, Proceedings, Physics at HERA, vol. 3* 1478-1482. (see HIGH ENERGY PHYSICS INDEX 30 (1992) No. 12988).

[151] **CompHEP** Collaboration, E. Boos et al., "CompHEP 4.4: Automatic computations from Lagrangians to events," *Nucl. Instrum. Meth.* **A534** (2004) 250–259, `arXiv:hep-ph/0403113`.

[152] T. Gleisberg et al., "SHERPA 1.alpha, a proof-of-concept version," *JHEP* **02** (2004) 056, `arXiv:hep-ph/0311263`.

[153] T. Sjostrand et al., "High-energy-physics event generation with PYTHIA 6.1," *Comput. Phys. Commun.* **135** (2001) 238–259, `arXiv:hep-ph/0010017`.

[154] **CDF and D0** Collaboration, K. Terashi, "New diffraction results from the Tevatron," `arXiv:hep-ex/0605084`.

[155] **H1** Collaboration, C. Adloff et al., "On the rise of the proton structure function F2 towards low x," *Phys. Lett.* **B520** (2001) 183–190, `arXiv:hep-ex/0108035`.

[156] G. Altarelli and G. Parisi, "Asymptotic Freedom in Parton Language," *Nucl. Phys.* **B126** (1977) 298.

[157] V. N. Gribov and L. N. Lipatov, "Deep inelastic e p scattering in perturbation theory," *Sov. J. Nucl. Phys.* **15** (1972) 438–450.

[158] Y. L. Dokshitzer, "Calculation of the Structure Functions for Deep Inelastic Scattering and e+ e- Annihilation by Perturbation Theory in Quantum Chromodynamics," *Sov. Phys. JETP* **46** (1977) 641–653. (In Russian.).

[159] L. N. Lipatov, "Reggeization of the Vector Meson and the Vacuum Singularity in Nonabelian Gauge Theories," *Sov. J. Nucl. Phys.* **23** (1976) 338–345.

[160] E. A. Kuraev, L. N. Lipatov, and V. S. Fadin, "The Pomeranchuk Singularity in Nonabelian Gauge Theories," *Sov. Phys. JETP* **45** (1977) 199–204.

[161] I. I. Balitsky and L. N. Lipatov, "The Pomeranchuk Singularity in Quantum Chromodynamics," *Sov. J. Nucl. Phys.* **28** (1978) 822–829.

[162] D. Kharzeev, E. Levin, and M. Nardi, "Color glass condensate at the LHC: Hadron multiplicities in p p, p A and A A collisions," *Nucl. Phys.* **A747** (2005) 609–629, `arXiv:hep-ph/0408050`.

[163] E. Iancu and R. Venugopalan, "The color glass condensate and high energy scattering in QCD," `arXiv:hep-ph/0303204`.

[164] H. Weigert, "Evolution at small x(bj): The color glass condensate," *Prog. Part. Nucl. Phys.* **55** (2005) 461–565, `arXiv:hep-ph/0501087`.

[165] J. Jalilian-Marian, A. Kovner, A. Leonidov, and H. Weigert, "The BFKL equation from the Wilson renormalization group," *Nucl. Phys.* **B504** (1997) 415–431, `arXiv:hep-ph/9701284`.

[166] J. Jalilian-Marian, A. Kovner, A. Leonidov, and H. Weigert, "The Wilson renormalization group for low x physics: Towards the high density regime," *Phys. Rev.* **D59** (1999) 014014, `arXiv:hep-ph/9706377`.

[167] E. Iancu, A. Leonidov, and L. D. McLerran, "Nonlinear gluon evolution in the color glass condensate. I," *Nucl. Phys.* **A692** (2001) 583–645, `arXiv:hep-ph/0011241`.

[168] I. Balitsky, "Operator expansion for high-energy scattering," *Nucl. Phys.* **B463** (1996) 99–160, `arXiv:hep-ph/9509348`.

[169] Y. V. Kovchegov, "Unitarization of the BFKL pomeron on a nucleus," *Phys. Rev.* **D61** (2000) 074018, `arXiv:hep-ph/9905214`.

[170] D. d'Enterria, "Low-x QCD physics from RHIC and HERA to the LHC," `arXiv:hep-ex/0610061`.

[171] E. Iancu, K. Itakura, and L. McLerran, "Geometric scaling above the saturation scale," *Nucl. Phys.* **A708** (2002) 327–352, `arXiv:hep-ph/0203137`.

[172] M. G. Ryskin, R. G. Roberts, A. D. Martin, and E. M. Levin, "Diffractive J/ψ photoproduction as a probe of the gluon density," *Z. Phys.* **C76** (1997) 231–239, `arXiv:hep-ph/9511228`.

[173] T. Teubner, "Diffractive production of vector mesons and the gluon at small x," *AIP Conf. Proc.* **792** (2005) 416–419.

[174] V. Guzey, M. Strikman, and W. Vogelsang, "Observations on d A scattering at forward rapidities," *Phys. Lett.* **B603** (2004) 173–183, `arXiv:hep-ph/0407201`.

[175] A. Accardi, "Cronin effect from backward to forward rapidity: A tale of two mysteries," *Acta Phys. Hung.* **A22** (2005) 289–299, `arXiv:nucl-th/0405046`.

[176] A. Dumitru, A. Hayashigaki, and J. Jalilian-Marian, "The color glass condensate and hadron production in the forward region," *Nucl. Phys.* **A765** (2006) 464–482, `arXiv:hep-ph/0506308`.

[177] D. Stump et al., "Inclusive jet production, parton distributions, and the search for new physics," *JHEP* **10** (2003) 046, `arXiv:hep-ph/0303013`.

[178] T. Sjostrand, S. Mrenna, and P. Skands, "PYTHIA 6.4 physics and manual," *JHEP* **05** (2006) 026, `arXiv:hep-ph/0603175`.

[179] A. H. Mueller and H. Navelet, "An Inclusive Minijet Cross-Section and the Bare Pomeron in QCD," *Nucl. Phys.* **B282** (1987) 727.

[180] C. Marquet and C. Royon, "Small-x QCD effects in forward-jet and Mueller-Navelet jet production," *Nucl. Phys.* **B739** (2006) 131–155, `arXiv:hep-ph/0510266`.

[181] D. Green, "Vector boson fusion Higgs production at the LHC: Mass variables," `arXiv:hep-ex/0501027`.

[182] **CMS Trigger and Data Acquisition Group** Collaboration, W. Adam et al., "The CMS high level trigger," *Eur. Phys. J.* **C46** (2006) 605–667, `arXiv:hep-ex/0512077`.

[183] "HIROOT: ROOT for Heavy-Ions." Information available at `http://higweb.lns.mit.edu/twiki/bin/view/CMS/HIRootDocumentation`.

[184] **CDF** Collaboration, R. Field and R. C. Group, "PYTHIA Tune A, HERWIG, and JIMMY in Run 2 at CDF," `arXiv:hep-ph/0510198`.

[185] **CMS** Collaboration, D. Acosta et al., "CMS Physics TDR Volume 1, Section 11.2.1: Iterative cone," *CERN/LHCC* **2006-001** (2006) 408.

[186] J. M. Campbell, J. W. Huston, and W. J. Stirling, "Hard interactions of quarks and gluons: A primer for LHC physics," `arXiv:hep-ph/0611148`.

[187] B. Jager, M. Stratmann, and W. Vogelsang, "Single-inclusive jet production in polarized p p collisions at O(alpha(s)**3)," *Phys. Rev.* **D70** (2004) 034010, `arXiv:hep-ph/0404057`.

[188] W. Vogelsang. Private communication.

[189] A. Heister et al., "Jet Reconstruction and Performance in the CMS Detector'," *CMS NOTE* **2005/005** (2005).

[190] **D0** Collaboration, B. Abbott et al., "Probing BFKL dynamics in the dijet cross section at large rapidity intervals in $p\bar{p}$ collisions at $\sqrt{s} = 1800$ GeV and 630-GeV," *Phys. Rev. Lett.* **84** (2000) 5722–5727, `arXiv:hep-ex/9912032`.

[191] J. R. Andersen, V. Del Duca, S. Frixione, C. R. Schmidt, and W. J. Stirling, "Mueller-Navelet jets at hadron colliders," *JHEP* **02** (2001) 007, `arXiv:hep-ph/0101180`.

[192] A. Dainese et al., "in: HERA and the LHC - A workshop on the implications of HERA for LHC physics: Proceedings Part A," `arXiv:hep-ph/0601012`.

[193] P. Katsas et al. *submitted to NIM A* (2006).

[194] **CDF** Collaboration, F. Abe et al., "Dijet production by color-singlet exchange at the Fermilab Tevatron," *Phys. Rev. Lett.* **80** (1998) 1156–1161.

[195] **D0** Collaboration, B. Abbott et al., "Probing hard color-singlet exchange in $p\bar{p}$ collisions at $\sqrt{s} = 630$ GeV and 1800 GeV," *Phys. Lett.* **B440** (1998) 189–202, `arXiv:hep-ex/9809016`.

[196] V. S. Fadin, E. A. Kuraev, and L. N. Lipatov, "On the Pomeranchuk Singularity in Asymptotically Free Theories," *Phys. Lett.* **B60** (1975) 50–52.

[197] G. S. Danilov and L. N. Lipatov, "BFKL pomeron in string models," *Nucl. Phys.* **B754** (2006) 187–232, `arXiv:hep-ph/0603073`.

[198] A. Edin, G. Ingelman, and J. Rathsman, "Soft color interactions as the origin of rapidity gaps in DIS," *Phys. Lett.* **B366** (1996) 371–378, `arXiv:hep-ph/9508386`.

[199] R. Engel and H. Rebel, "Theory of hadronic interactions and its application to modeling of cosmic ray hadronic showers," *Acta Phys. Polon.* **B35** (2004) 321–330.

[200] K. Werner et al., "Ultra-high energy cosmic rays: Some general features, and recent developments concerning air shower computations," *AIP Conf. Proc.* **739** (2005) 385–397, `arXiv:astro-ph/0407165`.

[201] J. Knapp, D. Heck, S. J. Sciutto, M. T. Dova, and M. Risse, "Extensive air shower simulations at the highest energies," *Astropart. Phys.* **19** (2003) 77–99, `arXiv:astro-ph/0206414`.

[202] R. Engel, "Very high energy cosmic rays and their interactions," *Nucl. Phys. Proc. Suppl.* **151** (2006) 437–461, `arXiv:astro-ph/0504358`.

[203] N. N. Kalmykov, S. S. Ostapchenko, and A. I. Pavlov, "Quark-gluon string model and EAS simulation problems at ultra-high energies," *Nucl. Phys. Proc. Suppl.* **52B** (1997) 17–28.

[204] R. Engel, T. K. Gaisser, T. Stanev, and P. Lipari, "Air shower calculations with the new version of SIBYLL." Prepared for 26th International Cosmic Ray Conference (ICRC 99), Salt Lake City, Utah, 17-25 Aug 1999.

[205] S. Roesler, R. Engel, and J. Ranft, "The Event generator DPMJET-III at cosmic ray energies." Prepared for 27th International Cosmic Ray Conference (ICRC 2001), Hamburg, Germany, 7-15 Aug 2001.

[206] F. M. Liu, T. Pierog, J. Aichelin, and K. Werner, "Hadron production in proton proton scattering in NEXUS 3," `arXiv:hep-ph/0307204`.

[207] T. Sjostrand, L. Lonnblad, S. Mrenna, and P. Skands, "PYTHIA 6.3: Physics and manual," `arXiv:hep-ph/0308153`.

[208] "ORCA: CMS Reconstruction Package." Site located at `http://cmsdoc.cern.ch/orca`.